Testing and Aerodynamic Investigation

of a

Tumbleweed Rover for Mars

Andreas Winkler

TECHNISCHE UNIVERSITÄT MÜNCHEN

Lehrstuhl für Aerodynamik
Technische Universität München
Univ. Prof. Dr. Ing. N. Adams

aer

Diplomarbeit Nr. 05/03

für Herrn cand. Ing. Andreas Winkler

Titel: Testing and Aerodynamic Investigation of a Tumbleweed Rover for Mars

Übersicht: A Tumbleweed for Mars is a wind driven rover that can travel over the surface of Mars making atmospheric measurements. It is somewhat like the tumbleweeds found in western USA, but quite different in that it has to be delivered to Mars and have instruments to measure atmospheric and other scientific items while being blown over the surface of Mars. The advantage is that it does not require wheeled propulsion like the traditional Mars Excursion Rovers (MER). Students at NC State University have designed a Tumbleweed Earth Demonstrater and now we need to construct and test it in locations off campus. The proposed locations for the summer of 2005 are the sands at Kitty Hawk, NC, where the Wright Brothers made the first powered flight in 1903, the mountain area in western NC. Several students will compose a test team to test the Tumbleweed in these various locations as to the ability to traverse the terrain and take measurements like pressure, temperature, accelerations and video on board. Included with the tests is the ability of solar panels on the Tumbleweed to provide energy to power the instruments on board.

Aufgabenstellung: As one of the team members Andreas will work during summer 2005 with the team on building the Tumbleweed Earth Demonstrators (TEDs) and conducting the tests. After that period he will proceed with the following research topics.
Some preliminary research on the Tumbleweed's aerodynamic characteristics especially its drag force has been conducted by NASA. However corresponding measurements for the particular TED are missing and hence Andreas will characterize the TED aerodynamic behaviour. A special emphasis thereby is on its aerodynamic drag again. In this context it will also be a task to look into various concepts in order to increase the drag of the sails.
Another field of interest is the wake flow downstream of the Tumbleweed. In order to get a deeper comprehension of this flow its visualization is necessary. Andreas will think about the available possibilities at the NCSU in order to realize this visualization, conduct the corresponding tests and interpret their results.

Betreuung: Prof. Dr. Fred DeJarnette
                Dr.-Ing. Albert Pernpeintner

Raleigh, 15.12.05

Ausgabe: 15.6.05

Einlieferung: 15.12.05

Name: Winkler
Vorname: Andreas
Matr.-Nr.: 2274988

Erklärung

Ich versichere hiermit, dass ich die vorgelegte Diplomarbeit mit dem Titel

Testing and Aerodynamic Investigation of a Tumbleweed Rover for Mars

selbständig verfasst und keine anderen als die angegebenen Quellen und

Hilfsmittelmittel benutzt habe.

Diese Arbeit hat des Weiteren in gleicher oder ähnlicher Form noch keiner

Prüfungsbehörde vorgelegen.

Raleigh, den 15.12.2005

Andreas Winkler

(Unterschrift)

Acknowledgements

TECHNISCHE
UNIVERSITÄT
MÜNCHEN

aer

Table of Contents

I

TECHNISCHE UNIVERSITÄT MÜNCHEN

Lehrstuhl für Aerodynamik
Technische Universität München
Univ. Prof. Dr. Ing. N. Adams

aer

TECHNISCHE
UNIVERSITÄT
MÜNCHEN

Lehrstuhl für Aerodynamik
Technische Universität München
Univ. Prof. Dr. Ing. N. Adams

aer

List of Figures

TECHNISCHE UNIVERSITÄT MÜNCHEN

Lehrstuhl für Aerodynamik
Technische Universität München
Univ. Prof. Dr. Ing. N. Adams

aer

TECHNISCHE
UNIVERSITÄT
MÜNCHEN

Lehrstuhl für Aerodynamik
Technische Universität München
Univ. Prof. Dr. Ing. N. Adams

aer

List of Tables

TECHNISCHE
UNIVERSITÄT
MÜNCHEN

Lehrstuhl für Aerodynamik
Technische Universität München
Univ. Prof. Dr. Ing. N. Adams

aer

Nomenclature

A   area [m^2]; scaling factor [-]

a   speed of sound [m/sec]; zero displacement

B   scaling factor [-]

BF   Blockage Factor [-]

b   breadth [m]; zero shift

C_x force coefficient in x direction [-]

C_y force coefficient in y direction [-]

C_z force coefficient in z direction [-]

C_D drag coefficient [-]

C_f friction drag force coefficient [-]

C_L lift coefficient [-]

C_S side force coefficient [-]

C_l roll coefficient [-]

C_m pitch coefficient [-]

C_n roll coefficient [-]

C_{Mx} moment coefficient around the x-direction [-]

C_{My} moment coefficient around the y-direction [-]

C_{Mz} moment coefficient around the z-direction [-]

C_i i-th integration constant

c   camber [-]; circumference [m]

c'   design camber [-]

D   drag [N]

TECHNISCHE
UNIVERSITÄT
MÜNCHEN

Lehrstuhl für Aerodynamik
Technische Universität München
Univ. Prof. Dr. Ing. N. Adams

aer

d   diameter [m]

E   Young's modulus [N/mm^2]

F   force [N]

f   sail profile thickness [m]; frequency [1/sec]

GF   Gage Factor [-]

g   gravitational acceleration [m/sec^2]

h   height [m]

I   geometrical moment of inertia [mm^4]

K   flow coefficient for orifice flow [-]

k   von Karman's constant [-]; rate of change [various units]

K_t transverse sensitivity factor

L   lift [N]

l   length [m]

M   moment [Nm]

Ma   Mach number [-]

M_b bending moment [Nm]

M_m pitching moment [Nm]

m   mass [kg]

N   number, amount [-]

n   coordinate normal to the flow direction

p   pressure [Pa]

Q   volume flow $\left[m^3/\text{sec} \right]$

q   dynamic pressure [Pa]

R   gas constant [$J/(kg \cdot K)$]; electrical Resistance [Ω]

Re   Reynolds number [-]

TECHNISCHE
UNIVERSITÄT
MÜNCHEN

Lehrstuhl für Aerodynamik
Technische Universität München
Univ. Prof. Dr. Ing. N. Adams

aer

S   surface, area [m^2]

$S_\perp$ sail surface normal to the free stream direction [m^2]

Sr   Strouhal number [-] (dimensionless frequency)

s   coordinate along the flow direction

T   rotational period [sec]; Temperature [K]

TF   turbulence factor [-]

t   time [sec]; thickness [mm]

u   flow velocity in the x-direction

u'   fluctuation velocity in the x-direction

u_* friction velocity [m/sec]

V   flow velocity [m/sec]

v   flow velocity in the y-direction

v'   fluctuation velocity in the y-direction

w   flow velocity in the z-direction

w'   fluctuation velocity in the z-direction

W   section modulus [mm^3]; translational velocity [m/sec]

x   coordinate

y   coordinate

z   coordinate of height [m]

z_0 surface roughness or aerodynamic roughness length [m]

α pitch angle or angle of attack [deg] or [rad]

β yaw angle [deg] or [rad]

γ roll angle [deg] or [rad]

TECHNISCHE
UNIVERSITÄT
MÜNCHEN

Lehrstuhl für Aerodynamik
Technische Universität München
Univ. Prof. Dr. Ing. N. Adams

aer

ε strain [microstrain = $10^{-6}\dfrac{\Delta l}{l}$]

μ dynamic viscosity [Pa sec]

μ_R rolling friction coefficient [-]

ν kinematic viscosity [$m^2/\sec$]

ρ density [kg/m^3]

σ stress [N/mm^2]

τ shear stress [N/m^2]

ω angular velocity [rad/sec]

Abbreviations and Indices

∞	free stream conditions
'	foot
"	inch(es)
atm	atmospheric
amb	ambient
6CB	6-Component Balance (standard balance in the NCSU subsonic wind tunnel)
COTS	Commercial Of The Shelf
E	Earth
ft.	foot
GRAM	Global Reference Atmosphere Model
GN&C	Guidance, Navigation and Control
HP	Horse Power
MIS	Modular Instrument System
M	Mars
NCSU	North Carolina State University
mph	miles per hour
OBS	Obstacle Bypass System
OBB	One Beam Strain Gage Balance (self-made)
psf	pounds per square foot
PBL	Planetary Boundary Layer
R	rolling
r	relative
rpm	revolutions per minute
SC	improvised Smoke Channel
SDRS	Sail Deployment and Retraction System
sg	strain gage
TED	Tumbleweed Earth Demonstrator
tTED	tiny Tumbleweed Earth Demonstrator (first downscale model)
tTED2	tiny Tumbleweed Earth Demonstrator 2 (second downscale model)
TW	actual Tumbleweed Rover for Mars
t	total

TECHNISCHE
UNIVERSITÄT
MÜNCHEN

Lehrstuhl für Aerodynamik
Technische Universität München
Univ. Prof. Dr. Ing. N. Adams

aer

1 Introduction

For centuries the planet Mars is drawing the attention of mankind. From the ancient civilizations of the Babylonians, Egyptians, Greeks and Romans on, the red planet was recognized as a remarkable object on night sky. Consequently they honored the planet by naming it after gods and heroes of their mythology like the Babylonian "Nergal" (the great hero), the Greek "Ares" (god of war) or the Roman "Mars" (god of war). The Babylonians made the first scientific investigations about celestial bodies as early as 400BC. Mainly for the reasons of calendar calculating and religion they mapped the celestial trajectories but never tried to explain the observations they made.

In the Western world it should take almost another 2000 years until in the 16th century astronomers like Nikolaus Copernicus and Tyho Brahe conducted first scientific research on celestial bodies. The Danish Astronomer Tyho Brahe made the first amazingly accurate calculations of the Martian position many years before the telescope was invented. With its invention in the 17th century astronomers like Galileo Galilei or Christiaan Huygens took a closer look on the red planet and features like the Martian southern pole cap or the rotational period were discovered and determined, respectively. With the further development of the telescopes the discoveries became more and more sophisticated but were naturally limited by the vast distance between Earth and Mars.

In the middle of the last century, however, mankind passed the threshold of space travel with the first manmade device ever leaving the Earth - the Russian satellite "Sputnik1". After the launch of this very first artificial satellite on October 10, 1957 it took only another 7 years until on November 28 in 1964 the very first satellite was successfully sent to the red planet - the American satellite "Mariner4". About another seven years later in 1971 the two Russian probes "Mars2" and "Mars3" arrived at Mars in order to land on its surface. "Mars 2" did not survive the entry and "Mars3" only worked 20 seconds after its landing. However both probes marked the very first human artifacts entering the Martian atmosphere. Five years later in 1976 the both American Viking satellites marked the first huge scientific success of in situ data gathering. The landers of Viking 1 and Viking 2 managed to land on Mars and to collect valuable data about the Martian surface and atmosphere. Some more Missions to the red planet followed. Amongst others the American Mars Global Surveyor entered Martian orbit in 1997 and provided a wealth of pictures in order to map the Martian surface. One of the most recognized successes however, was the Mars Pathfinder Mission. After having landed on July

TECHNISCHE
UNIVERSITÄT
MÜNCHEN

Lehrstuhl für Aerodynamik
Technische Universität München
Univ. Prof. Dr. Ing. N. Adams

aer

4 in 1997 it deployed the first Martian rover called "Sojourner" that drove several meters around the landing site. Its pictures together with the pictures from the Pathfinder lander were widely published in the media around the world. Some more Martian rovers and orbiters have followed the successful Pathfinder mission, amongst them the American rovers "Spirit" and "Opportunity" and the European orbiter "Mars Express".

As astonishing the results of these ongoing missions are they however mark the two extreme sides of the technical spectrum of current Martian exploring techniques. The orbiters provide a wealth of data of virtually the whole Martian surface and yet they are limited due to their remote position in orbit. The landers and rovers are able to gather data directly on the Martian surface but are limited due to their non-existing or low mobility. In the cases of the Martian rovers one major issue is the strict energy constraint that does not allow to powering a propulsion that can take the rovers across large distances.

With this issue a new concept ties up. Inspired by the wind driven tumbleweed plant of the American West the Tumbleweed Rover is supposed to combine the advantages of in situ data gathering with a far higher mobility than current rovers. The problem of the lacking propulsion power is overcome by using an energy source that is already available on Mars - its winds. Like the tumbleweed plant the Tumbleweed Rover is supposed to draw energy from the surface winds by exposing an aerodynamic drag to the winds that is as high as possible while considering other technical requirements. Another advantage is its fairly low technical complexity that makes it a cost-efficient concept. While current wheel propelled rovers possess costs in the order of hundreds of millions of dollars per piece the Tumbleweed Rover is supposed to have costs one order of magnitude lower per piece. That means that for the same price about ten times more rovers could be sent to Mars and thus they could explore a very large area of the Martian surface. Moreover some rovers could be stored in orbit as backup and dropped only when scientific interesting areas are identified.

A co-operation between the Langley NASA Research Center in Hampton, VA and the North Carolina State University in Raleigh, NC began in 2001 to development the Tumbleweed concept. Under the supervision of Dr. Fred DeJarnette senior students at NC State University began to think about concepts of a wind driven Mars rover. They considered several designs and shapes but in the end the so called "box-kite" design was chosen (see [21]) and a first prototype was built. It was called "Tumbleweed Earth Demonstrator" (TED).

In the following year the seniors of NC State improved the concept steadily. This process lead to some design changes and finally to the most recent version, the TED3.2. The current

seniors are working right now on the TED3.5. However this thesis is based on the concept and testing of the TED3.2 to TED3.4 so it will be described more closely in chapter 3.

TECHNISCHE
UNIVERSITÄT
MÜNCHEN

Lehrstuhl für Aerodynamik
Technische Universität München
Univ. Prof. Dr. Ing. N. Adams

aer

2 Aerodynamic Fundamentals and Theoretical Background

The research of this thesis requires the introduction of some aerodynamic fundamentals, definitions and research devices. That is why this chapter will deal with the background and definitions that are required in order to understand the subsequent chapters.

2.1 Aerodynamic Fundamentals and Definitions

The Mach number is a measure for the compressibility of a flow.

$$Ma = \frac{V}{a} \tag{2.1}$$

V   flow velocity [m/sec]

a   speed of sound [m/sec]

As a rule of thumb if the Mach number exceeds the value 0.3 compressibility effects must be considered. The TW is supposed to be a wind driven rover. In chapter 2.2.2 it will be shown that the maximum relevant wind speeds on Mars do not exceed the value of $V_M = 30\,m/\sec$. Concluded from [3] and [18] the average speed of sound for the Martian atmosphere at $z = 0\,km$ is given to:

$$a_M = \sqrt{\kappa_M \cdot R_M \cdot T_M} = \sqrt{1.32 \cdot 191.18 \frac{J}{kg \cdot K} \cdot 214K} = 232.39 \frac{m}{\sec} \tag{2.2}$$

Thus the Mach number for the maximum Martian wind speed is

$$Ma_{M,\max} = \frac{30\,m/\sec}{232.29\,m/\sec} = 0.129 \tag{2.3}$$

and hence clearly below the value of M=0.3 . The average wind speeds are even far below this value and consequently *incompressible flow will be assumed*.

$$\rho = const. \tag{2.4}$$

That is why Bernoulli's equation for the incompressible flow holds true:

$$p_{total} = p_{static} + q = const. \tag{2.5}$$

The variable q is well known under the label dynamic pressure and per definition it is:

$$q \equiv \frac{\rho}{2}V^2 \qquad (2.6)$$

In the case of incompressible flow the eq.(2.6) is not only a definition but yields the actual dynamic pressure of the flow.

In this thesis the flow properties about the TW will be investigated by the help of different models. Besides of the already mentioned TED two wind tunnel models called tinyTED (tTED and tTED2, see chapter 4) will be important to determine some aerodynamic properties of the TW. However all models are remarkably smaller than the TW. That is why it has to make sure that both flow fields are similar in spite of their different dimensions. Moreover the TW will operate in a different atmosphere than the models do. That has to be regarded, as weel. As per [8] "two flows in similar geometries are called physically similar when all their similarity parameters are equal." These similarity parameters are gained by introducing reference values into the governing differential conservation equations that means into the momentum, energy and mass conservation equations. The dimensional variables are referenced to a proper set of reference values and hence are made dimensionless. These new dimensionless variables can then be applied to the differential conservation equations. Thus some new dimensionless variables are formed within the equations. These new variables are the so called similarity parameters which may be dimensionless, too.

Two flows are perfectly similar when all of these similarity parameters are equal. However it is very seldom that the physical properties of the model flow can be adjusted so that this requirement is met. Fortunately it is mostly not necessary to match all similarity parameters but only a few. If only these most important parameters are equal the flows are *partially similar*.

In case of the TW the properties of interest for this thesis are foremost the aerodynamic forces and moments that are exerted on the TW. As per [2] the influence of heat transfer and gravity therefore can be neglected. As mentioned above it is assumed that the flow is incompressible. If furthermore only the resting TW is investigated or only one of its possible orientations relative to the free stream, the flow can be assumed to be steady.

TECHNISCHE
UNIVERSITÄT
MÜNCHEN

Lehrstuhl für Aerodynamik
Technische Universität München
Univ. Prof. Dr. Ing. N. Adams

aer

The only similarity parameter that is left for these conditions is the *Reynolds number*:

$$\mathrm{Re} = \frac{\rho \cdot l \cdot V}{\mu} \tag{2.7}$$

The values of the density ρ, the velocity V and the dynamic viscosity μ are commonly taken from the free stream conditions. This approach is also chosen for this thesis. The reference length l is yet to determine. However in case of the TW and its models the most characteristic length certainly is their diameter. Therefore four Reynolds numbers are defined as follows:

$$\mathrm{Re}_{TW} = \frac{\rho_{M,\infty} \cdot d_{TW} \cdot V_{M,\infty}}{\mu_{M,\infty}} \tag{2.8}$$

$$\mathrm{Re}_{TED} = \frac{\rho_{E,\infty} \cdot d_{TED} \cdot V_{E,\infty}}{\mu_{E,\infty}} \tag{2.9}$$

$$\mathrm{Re}_{tTED} = \frac{\rho_{E,\infty} \cdot d_{tTED} \cdot V_{E,\infty}}{\mu_{E,\infty}} \tag{2.10}$$

$$\mathrm{Re}_{tTED2} = \frac{\rho_{E,\infty} \cdot d_{tTED2} \cdot V_{E,\infty}}{\mu_{E,\infty}} \tag{2.11}$$

If rather the rolling than the resting TW is investigated the flow field about the TW cannot be considered as to be steady any more. Instead the rolling motion will occur with a certain frequency f and thus create an unsteady flow field. In that case besides of the Reynolds number the so called dimensionless frequency or *Strouhal number* of the TW and the models should be equal, too.

$$Sr_{TW} = \frac{f_{TW} \cdot d_{TW}}{V_{M,\infty}} \tag{2.12}$$

$$Sr_{TED} = \frac{f_{TED} \cdot d_{TED}}{V_{E,\infty}} \tag{2.13}$$

$$Sr_{tTED} = \frac{f_{tTED} \cdot d_{tTED}}{V_{E,\infty}} \tag{2.14}$$

$$Sr_{tTED2} = \frac{f_{tTED2} \cdot d_{tTED2}}{V_{E,\infty}} \tag{2.15}$$

TECHNISCHE
UNIVERSITÄT
MÜNCHEN

Lehrstuhl für Aerodynamik
Technische Universität München
Univ. Prof. Dr. Ing. N. Adams

aer

Finally the *geometric similarity* of model and TW must be assured as well. That means that the ratios between the governing geometric variables of model and TW are supposed to be constant.

In order to describe the aerodynamic forces and moments it is common to use so called *force and moment coefficients*. These coefficients are defined as follows:

$$C_{F,i} = \frac{F_i}{q_\infty \cdot S}$$ (2.16)

i = space direction

$$C_{M,i} = \frac{M_i}{q_\infty \cdot S \cdot l}$$ (2.17)

i = space direction

F force [N]

M moment [Nm]

q_∞ free stream dynamic pressure [Pa]

S reference surface [m^2]

l reference length [m]

The reference length and surface will again be defined by the most characteristic dimension of the TW and its models that is their diameters.

$$l_i = d_i$$ (2.18)

$$S_i = \frac{\pi}{4} d_i^2$$ (2.19)

i = TW, TED, tTED, tTED2

Lehrstuhl für Aerodynamik
Technische Universität München
Univ. Prof. Dr. Ing. N. Adams

TECHNISCHE
UNIVERSITÄT
MÜNCHEN

aer

It is common in aerodynamics to define two special force components. The lift force L always acts perpendicular to the free stream direction and the drag force D acts always parallel and in the direction of the free stream.

$$C_{D,i} = \frac{D_i}{q_{\infty,i} \cdot S_i} \tag{2.20}$$

$$C_{L,i} = \frac{L_i}{q_{\infty,i} \cdot S_i} \tag{2.21}$$

i = TW, TED, tTED, tTED2

In our case the force and moment coefficients depend on the orientation of the TW/model (the angles will be defined in chapter 2.4), the Reynolds number, the Strouhal number and time. In the case of a steady flow they only depend on the orientation and the Reynolds number.

There are two principally possible kinds of flow that will be described in short. The *laminar flow* is most often just defined as non-turbulent flow. That means that the fluid flows in parallel (laminar) layers that do not mix convectively. Hence the transfer of momentum and heat between the layers is relatively low because it only occurs due to diffusion.

In contrast the *turbulent flow* is characterized by convective mixing between the different flow layers. This mixing is represented by so called eddies of different length and time scales that are superimposed to the translational main motion of the fluid. Hence the transfer of momentum and heat between the layers is larger than for laminar flow. That is why the viscosity in a turbulent flow is enhanced by the so called apparent or eddy viscosity. An approach to describe the variations of the flow variables velocity and pressure are the so called turbulent fluctuations. As per [8] the turbulent motion is decomposed into a mean motion and a fluctuating motion and so is the pressure distribution:

$$u = \bar{u} + u' \tag{2.22}$$

$$v = \bar{v} + v' \tag{2.23}$$

$$w = \bar{w} + w' \tag{2.24}$$

$$p = \bar{p} + p' \tag{2.25}$$

The average values are taken over a sufficiently large time interval and if they are independent of time the whole flow will be regarded to be steady. Similarly other flow variables like density or temperature may be decomposed.

The time averages of the fluctuating variables are zero e.g.:

$$\overline{u'} = 0$$

In contrast the square of the time averaged fluctuating variables need not to be zero. For example in a flow of isotropic turbulence it holds true that:

$$\overline{u'}^2 = \overline{v'}^2 = \overline{w'}^2 \tag{2.26}$$

The special and for this thesis important case of a wind tunnel flow (free stream only along the x-direction) can be assumed to be isotropic turbulent due to the grids within the tunnel's duct. (see chapter 2.3)

The kinetic energy of the turbulent fluctuations is defined as:

$$k = \frac{1}{2}\left(\overline{u'^2 + v'^2 + w'^2}\right) \tag{2.27}$$

With this kinetic energy a measure of turbulence for a free (non-boundary layer) flow can be defined. The so called *turbulence intensity* is given to:

$$Tu = \frac{\sqrt{2/3 \cdot k}}{V_\infty} \tag{2.28}$$

Considering eq.(2.26) the turbulence intensity simplifies to:

$$Tu = \frac{\sqrt{\overline{u'^2}}}{V_\infty} \tag{2.29}$$

Laminar flow is a much less stable state than turbulent flow and may be transformed to turbulent flow by the influence of perturbations. The state between laminar and turbulent flow is known as *transition*. This instability is also the reason why almost every naturally caused flow is turbulent and hence the turbulent flow is more relevant for this thesis.

The criterion that defines if a flow is laminar or turbulent is expressed by the critical Reynolds number Re_{crit}. Dependent on the flow at hand there are different values for these critical Reynolds numbers. Flows whose Reynolds number is below this value are laminar, flows

TECHNISCHE
UNIVERSITÄT
MÜNCHEN

Lehrstuhl für Aerodynamik
Technische Universität München
Univ. Prof. Dr. Ing. N. Adams

aer

whose Reynolds number is above this value are turbulent. About the value of Re_{crit} there is the so called transition region.

From equal experiments in different wind tunnels and under free flight conditions at the same Reynolds number each it is indicated that some corrections are necessary to account for the turbulence in the wind tunnel free stream. As per [2] "it has been argued that this turbulence causes flow patterns in the tunnel to be similar to the flow pattern in free air stream at higher Reynolds numbers. Hence the tunnel test Reynolds number could be said to be a higher 'effective' Reynolds number. The physics of turbulence is far too complex to be captured by this simple concept. There are some phenomena for which it "works" to some extent and others for which is does not." However due to the lack of a more promising approach this concept will be used in this thesis.

For determining this factor in the NCSU Subsonic Wind Tunnel a sphere has been used. It is known that a sphere experiences a sudden drag drop at a well defined critical Reynolds number. Comparing this critical Reynolds number from the wind tunnel to the critical Reynolds number of a free air stream experiment with a plane allows to determining the so called *turbulence factor TF* of the wind tunnel. With this factor the effective Reynolds number can be calculated:

$$\text{Re}_{eff} = TF \cdot \text{Re}_{wind\ tunnel} \qquad (2.30)$$

In the remainder of this thesis all Reynolds numbers that are connected to the wind tunnel are supposed to be regarded as effective Reynolds numbers. Otherwise it will be pointed out.

However this turbulence factor changes with the applied dynamic pressure. Since there is only one known TF-stagnation-pressure-combination for the NCSU wind tunnel (see chapter2.3) new uncertainties may arise.

The *aerodynamic drag* is the variable of the greatest interest for this thesis. Moreover its generation is closely linked to the phenomenon of flow separation and wake flow. That is why its features will be described more closely.

In general there are only two mechanisms by which a force may be communicated from a flow to a rigid body. These are friction and pressure. The drag of a low speed flow exerted on

a body consists of these two components. They are called (skin) friction drag and pressure drag or form drag. In airfoil aerodynamics both are summarized under the term *profile drag*.

In order to describe the *friction drag* briefly reference [26] will be quoted: "... in a manner roughly comparable to that of solid surfaces sliding along each other, a tangential force originates where air or any other fluid moves past the surface of a body. This force is the skin friction drag."

The first approach to describe the frictional stress that is exerted by a flow on the surface of a rigid body is the Newtonian viscosity law:

$$\tau = \mu \frac{dV}{dn} \tag{2.31}$$

τ shear stress $[\,N\!/m^2\,]$

n   coordinate normal to the flow direction

The effect of the friction between body and fluid is to create $V = 0$ at the body surface. This fact is called the *no-slip condition*. However in the external stream further above the surface the flow velocity has a finite value that may be calculated by the means of inviscid flow. Consequently there must be a velocity gradient normal to the flow direction. The region of this velocity gradient is called the *boundary layer*.

The TW may be orientated so that one of its sail planes is parallel to the wind direction. That is why flow past a parallel flat plate will be investigated more closely in terms of its boundary layer and the skin friction. The following phenomena are taken from [31].

Only one side of the flow will be investigated. However for reasons of symmetry the same phenomena occur at the other side, too.

The free stream approaches the thin plate with the velocity V_∞. Due to the no-slip condition the fluid particles touching the surface will have the velocity of zero. Therefore there will be a velocity gradient between these touching particles and the particles in their vicinity and as a consequence of eq.(2.31) also a retarding shear stress at the plate surface. The adjacent particles will be decelerated due to this shear force as they are passing the leading edge of the plate. Due to their retarded velocity, in turn they will retard further particles next to them but farther out from the plate. By this mechanism a velocity profile is formed in the very vicinity of the plate - the boundary layer. With increasing distance from the leading edge the boundary

Lehrstuhl für Aerodynamik
Technische Universität München
Univ. Prof. Dr. Ing. N. Adams

TECHNISCHE
UNIVERSITÄT
MÜNCHEN

aer

layer becomes thicker and the velocity gradient becomes less steep. Assuming that the approaching free stream is a laminar flow this first part of the boundary layer will also be laminar. As mentioned before the laminar flow is an instable state, however. That is why with increasing thickness there will be a point from which on the perturbations in the flow will be big enough to make the boundary layer become turbulent. The eddies will mix more high velocity particles in the regions close to the wall and thus the velocity gradient becomes a lot steeper again. That is also the reason why turbulent boundary layers yield a higher shear stress than laminar boundary layers. Their velocity gradient is larger.
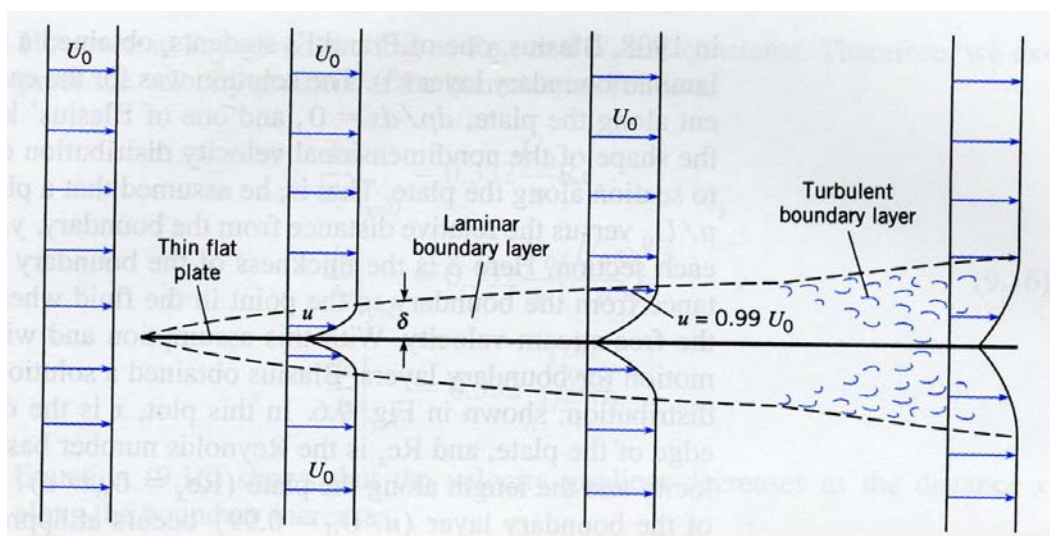
Figure 1 - Boundary Layer Development on a Flat Thin Plate Parallel to the Flow from [31]

As a consequence of the locally different velocity gradients the shear stresses at the plate also depend on the location. Eventually the local shear stress is again represented by a local coefficient:

$$c_f(x) = \frac{\tau(x)}{q_\infty}$$
(2.32)

$\tau(x)$ local shear stress [Pa]

q_∞ free stream stagnation pressure [Pa]

TECHNISCHE
UNIVERSITÄT
MÜNCHEN

Lehrstuhl für Aerodynamik
Technische Universität München
Univ. Prof. Dr. Ing. N. Adams

aer

Integrating these local shear stresses about the whole plate surface yield the coefficient for the friction force on the whole plate:

$$C_f = \frac{F_f}{q_\infty \cdot S_{wetted}}$$ (2.33)

F_f frictional force [N]

S_{wetted} wetted surface [m^2]

As per [31] the local shear stress coefficient and the friction drag coefficient for a laminar boundary layer on a rectangular plate only depends on the plate's Reynolds numbers Re_x and Re_l :

$$c_f(x) = \frac{0.664}{\text{Re}_x^{1/2}}$$ (2.34)

$$C_f = \frac{1.33}{\text{Re}_l^{1/2}}$$ (2.35)

$$\text{Re}_l = \frac{\rho_\infty \cdot l_{plate} \cdot V_\infty}{\mu_\infty}$$ (2.36)

The circumstances of the turbulent boundary layer are much more complex. For example it must be divided into three zones that require different equations for the velocity distributions. However reference [31] provides two equations for the local shear stress and the overall plate resistance that are based only on one power law for the velocity distribution but are supposed to yield reasonable results.

Additionally two different cases have to be distinguished. If the approaching free stream is free of turbulence and the leading edge of the plate is perfectly smooth the flow field from fig.1 will develop. That means that the first part of the boundary layer will be laminar and once the critical Reynolds number is reached the boundary layer will be turbulent. This critical Reynolds number is assumed to be about $\text{Re}_{crit} = \text{Re}_x(x_{crit}) = 5 \cdot 10^5$ and occurs at the point of transition x_{crit} . For this case the stress and drag coefficients are given to:

$$c_f(x) = \frac{0.455}{\left[\ln(0.06 \cdot \text{Re}_x)\right]^2}$$ (2.37)

TECHNISCHE
UNIVERSITÄT
MÜNCHEN

Lehrstuhl für Aerodynamik
Technische Universität München
Univ. Prof. Dr. Ing. N. Adams

aer

$$C_f = \frac{0.523}{\left[\ln\left(0.06 \cdot \mathrm{Re}_l\right)\right]^2} - \frac{1520}{\mathrm{Re}_l} \tag{2.38}$$

It will be seen however that the leading edges of the used TW-models are not smooth. For this case the boundary layer will be tripped from the very beginning and hence be turbulent all over the plate. Reference [31] provides the equations:

$$c_f\left(x\right) = \frac{0.058}{\mathrm{Re}_x^{1/5}} \tag{2.39}$$

$$C_f = \frac{0.074}{\mathrm{Re}_l^{1/5}} \tag{2.40}$$

In addition the local thickness of this turbulent boundary layer may be calculated with:

$$\delta = \frac{0.37 \cdot x}{\mathrm{Re}_x^{1/5}} \tag{2.41}$$

The *form drag* is also closely linked to the viscosity and the boundary layer of the flow namely to the boundary layer separation. If the boundary layer did not separate from the immersed body the subsonic flow field would be symmetric to the direction that is normal to the free stream direction. Thus the pressure distribution would be symmetric, too and no pressure difference that is the condition for a pressure drag could originate. This phenomenon is known in inviscid flow calculations as the d'Alembert paradox. The viscosity of the flow however resolves this paradox.

The preconditions for *flow separation* are the frictional influence of the body and an adverse pressure gradient. Here the assumption must be mentioned that the pressure gradient over the boundary layer is assumed to be zero $\left(\partial p/\partial n = 0\right)$ that means that the outer flow imposes its pressure on the boundary layer.

If a steady flow approaches a blunt body like a cylinder or a flat plate normal to the flow direction the flow will decelerate and one of the streamlines will run into a stagnation point. That means that in this point the velocity is zero and considering Bernoulli's equation (2.5) the static pressure will be maximum there. The other streamlines will pass the body but will be squeezed together upstream of the body. As per [1] the difference in the values of two streamlines given by the stream function represents the mass flow between these two

26

Lehrstuhl für Aerodynamik
Technische Universität München
Univ. Prof. Dr. Ing. N. Adams

TECHNISCHE
UNIVERSITÄT
MÜNCHEN

aer

streamlines. Due to the conservation of mass the squeezing streamlines represent an accelerated flow velocity and hence a decreasing static pressure. The fluid flows along a favorable pressure gradient.

Once the body is passed the streamlines will diverge again in order to return to their initial state before approaching the body. Again due to the conservation of mass diverging streamlines represent a retarding flow velocity and an increasing static pressure. The fluid flows against an adverse pressure gradient form this point on. In addition the viscous forces act on the fluid in the boundary layer, too and dissipate some of the fluids kinetic energy. The fluid particles closest to the body surface (coming from the region around the stagnation point) experience the largest frictional forces due to the largest velocity gradient there. Once the kinetic energy of these particles is completely dissipated they will come to rest at a certain point. The adverse pressure gradient however still acts on them and pushes them in a reverse motion. Faced with the following fluid particles these particles will separate from the body and roll up in vortices. These vortices emerge in the wake of the body. They have a lower static pressure than the upstream flow field (especially the region around the stagnation point) and hence a pressure difference and a force will originate. This force is called the form drag.
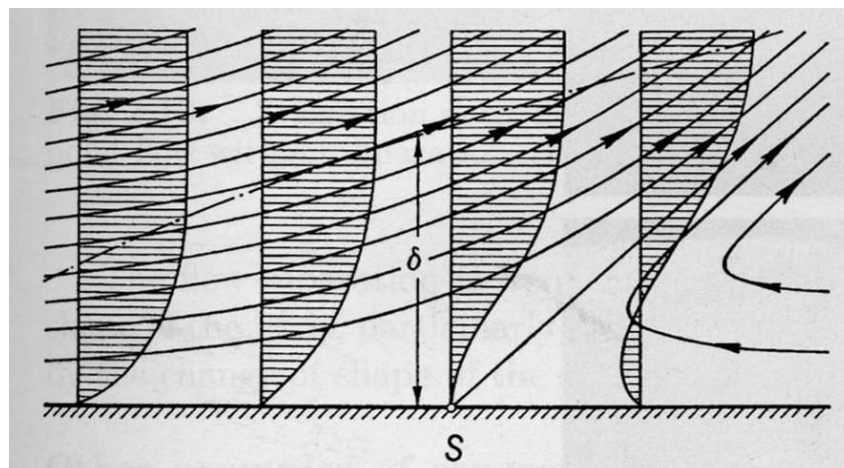
Figure 2 - Retarded Boundary Layer Flow with Separation Point from [8]

Again the flat plate this time normal to the flow will be investigated somewhat closer. The frictional forces will also act on this plate. However they are assumed to be equal and symmetrical to the center line of the plate and hence cancel each other. That is why the drag on a flat plate is only created by the form drag.

TECHNISCHE
UNIVERSITÄT
MÜNCHEN

Lehrstuhl für Aerodynamik
Technische Universität München
Univ. Prof. Dr. Ing. N. Adams

aer

For a two dimensional flat plate the drag coefficient for a perpendicular flat plate is:

$$C_{D,plate} \cong 2 \qquad\qquad (2.42)$$

In the real case of three space dimensions the form drag is always lower than in the two dimensional case. This is due to the fact that the flow can relax in one more space direction and hence the pressure build-up upstream of the body is lower than in the two dimensional case. Consequently the drag coefficient for a flat disk perpendicular to the free stream is lower than two.

Often form drag and friction drag coefficients are referenced to different surfaces. The frictional drag is commonly related to the wetted surface whereas the profile drag's reference surface normally is the projected area normal to the free stream direction.

That is why these two coefficients must not be only summed up normally. Instead the actual drag forces should be added up.

Alternatively the drag coefficient is often measured with a balance in the wind tunnel. Then both drag parts are already included and the stated drag coefficient represents the whole profile drag.

It was mentioned that the boundary layer separation leads to the creation of vortices that evolve in the wake of the body. Since this wake flow will be a part of the thesis the vortices and the wake flow will be described more closely.

As per [31] a "vortex is defined as the motion of a multitude of fluid particles around a common center." Thus a vortex in fluid dynamics is a macroscopic phenomenon. Two types of vortices are defined. In the *forced vortex* the velocity increases linearly from the center of rotation, just like in a solid body rotation. In the *free or potential vortex* the product of the flow velocity and the radial distance from the vortex center is constant $r_{center} \cdot V = const.$. That is why the velocity decreases with increasing distance from the center in a free vortex.

In the real case like downstream of the TW vortices are often a combination of both phenomena. The forced vortex can be found at and around the center of the vortex and the free vortex condition is approximately valid in the outer region towards the edge.

TECHNISCHE
UNIVERSITÄT
MÜNCHEN

Lehrstuhl für Aerodynamik
Technische Universität München
Univ. Prof. Dr. Ing. N. Adams

aer

As per [31] the rotational speed of a fluid element moving in a vortex with circular streamlines is:

$$\omega_z = \frac{1}{2}\left(\frac{dV}{dr} + \frac{V}{r}\right) \qquad (2.43)$$

r distance from the vortex center

For the vortex rotation of the forced vortex, the velocity can be depicted as:

$$V = k \cdot r \qquad (2.44)$$

k   velocity rate of change [1/sec]

and hence the angular velocity of the fluid element is equal to the rate of change of the fluid element velocity:

$$\left|\omega_z = k\right|_{forced\ vortex} \qquad (2.45)$$

If an irrotational vortex flow is demanded the velocity gradient must be:

$$\frac{dV}{dr} = -\frac{V}{r} \qquad (2.46)$$

in order to yield an angular velocity of zero. Integrating this equation yields

$$\ln V + C_1 = -\ln r + C_2 \qquad (2.47)$$

$$\ln V \cdot r = C_3 \qquad (2.48)$$

$$V \cdot r = C_4 = const. \qquad (2.49)$$

$C_{1,} C_{2,} C_3, C_4$ integration constants

This is the condition for a free vortex from which it is concluded that the region of a free vortex represents an irrotational flow.

The vortices downstream of the TW form the so called *wake flow*. Due to the geometry of the TW (see chapter 2.4) its wake flow is expected to be highly complex. As per [24] "the wake flow is the unrestricted flow behind the immersed body which is carried along by mean velocity of the external free stream, and which can be traced very far downstream. (...) The extent of the wake depends on the nature of the flow, whether it is laminar or turbulent, and the shape of the body. (...) Conventionally, two wake regions - near and far wakes - based

TECHNISCHE
UNIVERSITÄT
MÜNCHEN

Lehrstuhl für Aerodynamik
Technische Universität München
Univ. Prof. Dr. Ing. N. Adams

aer

upon the downstream distance form the body surface, are distinguished". For this thesis no means are at hand to investigate the far wake region and hence it will be focused on the very near wake directly behind the TW. It is important to mention however that the wake flow may reach several hundred times the diameter of the TW.

The wake flow can also be divided by lateral distance into a central region and a boundary region. In the central region the magnitudes of the turbulent kinetic energy, the eddy viscosity and dissipation are high and their variation is low. The turbulence is practically homogenous as well as continuous with respect to time. In the boundary region however the turbulent kinetic energy, the eddy viscosity and the dissipation decrease sharply and the turbulence becomes intermittent.

With perfect smooth geometries the state of the wake flow may be determined solely by the Reynolds number. That means that for a laminar boundary layer over the whole body also a laminar wake may develop. However the geometry of the TW and its sail setup is not assumed to be perfect smooth and that is why the boundary layer is assumed to be turbulent form the leading edge on. Therefore the wake flow behind the TW is expected to be turbulent, too.

It will be seen in chapter 4 that the blockage of the wind tunnel test section is an important issue for this thesis. Hence this phenomenon will be described and defined.

The equation for the conservation of mass for an incompressible flow is:

$$V_1 \cdot A_1 = V_2 \cdot A_2 = const. \tag{2.50}$$

$A_{1,2}$ areas perpendicular to the flow direction

An article in the test section has a certain projected area normal to the flow $S_\perp$ that cannot be passed through by the flow. Hence the article reduces the available cross section of the wind tunnel and leads to an acceleration of the flow:

$$V_2 = \frac{A_1}{A_2} \cdot V_1 \tag{2.51}$$

$$A_2 = A_1 - S_\perp$$

As per eq.(2.5) an accelerated flow yields a decreased static pressure and so the flow field will deviate from the real case. For example the form drag of the article is expected to be higher since the lower static pressure provides a larger pressure difference.

Consequently the blockage of the test section is described by the so called blockage factor:

$$BF = \frac{S_{\perp,article}}{A_{test\ section}}$$

(2.52)

$S_{\perp,article}$ \qquad projected surface of the article, normal to the free stream direction [m^2]

$A_{test\ section}$ \qquad cross section of the wind tunnel test section [m^2]

2.2 The Martian Model Atmosphere

The TW will be using the Martian winds as propulsion hence it is very important to define the operational conditions there. Since like on Earth the Martian atmospheric conditions are changing with time it is necessary to define values that may serve as a reference for any further investigations.

2.2.1 Martian Atmosphere Composition

A Mars reference atmosphere from [3] is used to define a model composition for the Martian atmosphere. It has been developed mainly from data of the Viking missions and yields a standard atmosphere like the Earth's GRAM. It is divided into two parts for the northern and southern hemisphere of Mars. Since both Viking landers were sited on the northern hemisphere *the northern standard atmosphere will be applied*.

As per [3] the composition of the lower Martian atmosphere is:

Gas	Abundance [Mass %]
Carbondioxide CO_2	95.32
Nitrogen N_2	2.7
Argon Ar	1.6
Oxygen O_2	0.13
Carbonmonoxide CO	0.07

Table 1 - Composition of the Martian Atmosphere from [3]

Additionally the lower atmosphere of Mars contains traces of the gases Neon, Krypton, Xeon and Ozone as well as water vapor. However it is assumed that the effect of these components on the relevant properties like viscosity and density is small so they will be neglected for this thesis.

Since Mars does not show oceans like the planet Earth a zero reference height like the standard sea level must be determined differently. A reference ellipsoid is defined that contains two semi-major axis. The axis A is located in the equatorial plane and the axis B points in the polar direction. The values for these axis are taken from [27]:

Semi-major axis A	3396.19
Semi-major axis B	3376.2

Table 2 - Reference Ellipsoid from [27]

Consequently the properties at the height z = 0km will be used as the reference data:

z[km]	$T_M[K]$	$\rho_M[kg/m^3]$	$p_M[mbar]$	$\mu_M[Pa\sec]$
0	214	0.0156	6.36	$1.1 \cdot 10^{-5}$

Table 3 - Thermodynamic Reference Values in the Martian Zero Reference Plane

TECHNISCHE
UNIVERSITÄT
MÜNCHEN

Lehrstuhl für Aerodynamik
Technische Universität München
Univ. Prof. Dr. Ing. N. Adams

aer

2.2.2 Martian Winds

Together with the Martian atmosphere composition the winds on Mars define the aerodynamic operational conditions for the TW propulsion system.

In general the atmosphere is divided into the regions troposphere, stratosphere, mesosphere and thermosphere (from bottom to top). For our purposes however only the very lowest part of the troposphere is of interest. It is here where the TW will be exposed to the propelling surface winds. Here the wind is exposed to the frictional influence of the planetary surface. Thus a boundary layer is formed that means that near the planetary surface a significant transfer of heat, momentum and mass between the surface and the flow occurs. In order to provide a phenomenological view on the planetary boundary layer and on the internal layer in particular, a part of reference [17] will be quoted:

"The planetary boundary layer is the layer of air near the ground that responds to spatial and temporal changes in the properties of the surface. This layer is turbulent and well mixed. Its height evolves with time over the course of the day. Its maximum height can reach 3km over deserts, dry fields and boreal forests. Over wetted surfaces the PBL reaches about 1 to 2 km. It consists of a surface layer, a well-mixed layer and a capping entrainment layer."
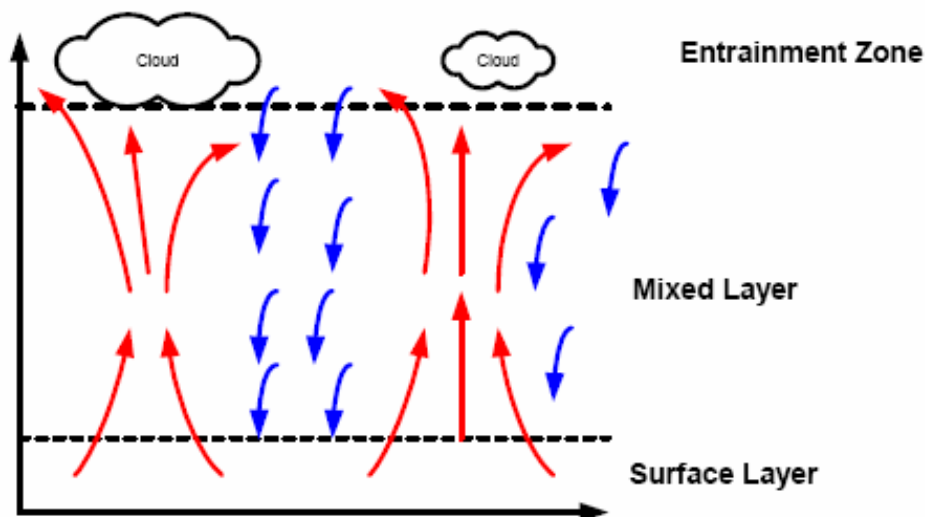
Figure 3 - Conceptual View of the Planetary Boundary Layer from [17]

For the purpose of the TW investigations only the very lowest part of the PBL is of interest that is the surface layer. In order to define this most important region the reference [17] will be quoted again:

TECHNISCHE
UNIVERSITÄT
MÜNCHEN

Lehrstuhl für Aerodynamik
Technische Universität München
Univ. Prof. Dr. Ing. N. Adams

aer

"The surface layer is the lowest layer of the atmosphere. It is the layer where air is in contact with the surface and where strong vertical gradients in temperature, humidity and wind exist. The atmosphere responds to surface forcing on the time scale of an hour or less. Temperature, wind, CO_2, humidity and pollutant concentrations exhibit distinct diurnal patterns over the course of a day in the troposphere.

Wind direction does not change with height and the Coriolis force is neglected. The depth of the surface boundary layer is about 10% of the PBL.

The internal boundary layer is the layer of air with immediate contact with the surface. It is often called the constant flux layer, since the transfer of heat, momentum and mass is invariant with height. The development of the depth of the internal boundary layer is a function of the surface roughness and distance from the edge."

As per [13] the reference case for all investigations of the structure of the atmospheric boundary layer and hence of the surface layer is the neutrally stratified wind over uniform terrain. That means that no effects of temperature or deviation of the surface structure from the ideal (smooth) case are taken into account. They will be described as deviations of this ideal case.

Thereby the influences of temperature and surface roughness are taken into account differently. The effect of surface roughness can be incorporated in the model of the neutrally stratified boundary layer to yield a law for the velocity distribution in the surface layer. The law is valid for about 10% of the height of the planetary boundary layer that is the surface layer. This law is the famous log-law for neutrally stratified boundary layer flow. It will be described below and is the base for our considerations.

The heat influence on the surface layer is modeled in a further step. Therefore the so called stratified atmospheric boundary layer near the ground (i.e. surface layer) will be described by a quote from [13]:

"The diurnal changes in solar radiation set up a cycle of cooling and heating of the planetary boundary layer which is strongly reflected in the wind field. Early in the morning, before sunrise, the stratification of the air layer is stable because the ground is cooler than the air mass above. With the rising sun, on a clear day, solar radiation makes the ground heat up much faster than the overlying air. When the ground is warmer than the air, heat moves from it to the air in contact with the ground. The warm air expands and becomes lighter than the air

TECHNISCHE
UNIVERSITÄT
MÜNCHEN

Lehrstuhl für Aerodynamik
Technische Universität München
Univ. Prof. Dr. Ing. N. Adams

aer

above it. Parcels of heated air tend to move up into cooler air above while cooler air moves down, i.e. the air layer is unstable."

These upward and downward motions obviously affect the velocity profile in the surface layer and so they do on Mars as well. In [10] this effect is modeled by introducing a stability function ψ_m. This stability function is depends on the height z and the so called Monin-Obukov length L. This length in turn is determined by the expression:

$$\frac{z}{L} = Ri \qquad (2.53)$$

in which Ri is the so called Richardson number. It is a measure of the relative importance of mechanical versus thermal turbulence. $Ri = 0$ indicates thermal neutrality where turbulence is completely dominated by the mechanical influences. That is the neutrally stratified boundary layer. The application of this correction procedure in [10] however yields that the corrected values are only slightly different in spite of large temperature gradients near the ground during a Martian day. Moreover the stability function has been developed from Earth measurements and conditions thus the application to Martian conditions is somewhat questionable.

Hence as proposed by [10] and [16] the Martian wind profile near the surface will be modeled with the well known log-law only. It is the standard model for neutrally stratified surface boundary layers of the atmosphere and is given in general form as:

$$V_\infty(z) = \frac{u_*}{k} \ln\left(\frac{z}{z_0}\right) \qquad (2.54)$$

V_∞:   wind speed

z: height coordinate

u_*:   friction velocity

k: von-Karman's constant

z_0:   surface roughness or aerodynamic roughness length

The surface roughness is defined as the height where the wind speed becomes zero. This length is not equal to the individual roughness elements on the ground but there is a one-to-one correspondence between those roughness elements and the aerodynamic roughness length. That means that it is only a function of the surface topography and does not depend on current wind speed or turbulence.

TECHNISCHE
UNIVERSITÄT
MÜNCHEN

Lehrstuhl für Aerodynamik
Technische Universität München
Univ. Prof. Dr. Ing. N. Adams

aer

On the one hand on Mars the surface topography is less complex than on Earth since there is no vegetation or man-made buildings or structures. On the other hand the knowledge about the Martian topography is far less than for the Earth. Hence this thesis will work with data that was measured during the Mars Pathfinder mission with a windsock experiment. A closer look at this experiment is given in [10]. From this reference one can also gain the value for the surface roughness at the Pathfinder landing site: $z_0 = 0.03m$. In [10] it is mentioned that this value might be lower for different Mars regions because Pathfinder landed in an especially rocky area. But since this value is taken from real measurements and no better sources for different values are available it will be worked with this value.

The friction velocity is defined to

$$u_* = \sqrt{\frac{\tau}{\rho_{atm}}}$$

(2.55)

τ :   surface shear stress

ρ_{atm} :   atmospheric density

Thus it changes with the surface shear stress and the atmospheric density. From eq.(2.54) it may be seen that the friction velocity determines the magnitude of the wind speeds at different heights. Consequently the friction velocity is not independent from the current wind speeds. However for this thesis a representative wind profile is desirable. Hence an average value as per [10] is: $u_* = 1\frac{m}{\sec}$.

The value of the von-Karman constant is taken from [8]. Quite apparently there are discussions about this constant ranging from 0.2 up to 0.8 but the most widely accepted value seems to be: $k = 0.4$.

As mentioned above the values are taken from the Pathfinder mission. On the Pathfinder lander the windsock experiment could not be leveled with the actual Martian surface but it was mounted on a baseplate on the lander. Hence a displacement distance of $d = -0.2m$ is estimated in [10] in order to account for this issue.

TECHNISCHE
UNIVERSITÄT
MÜNCHEN

Lehrstuhl für Aerodynamik
Technische Universität München
Univ. Prof. Dr. Ing. N. Adams

aer

Hence the log-law for the Martian wind profile is finally:

$$V_{\infty,M}(z) = \frac{u_*}{k} \ln \frac{(z-d)}{z_0} = \frac{1\,m/\sec}{0.4} \ln \left(\frac{(z+0.2m)}{0.03m} \right) \tag{2.56}$$
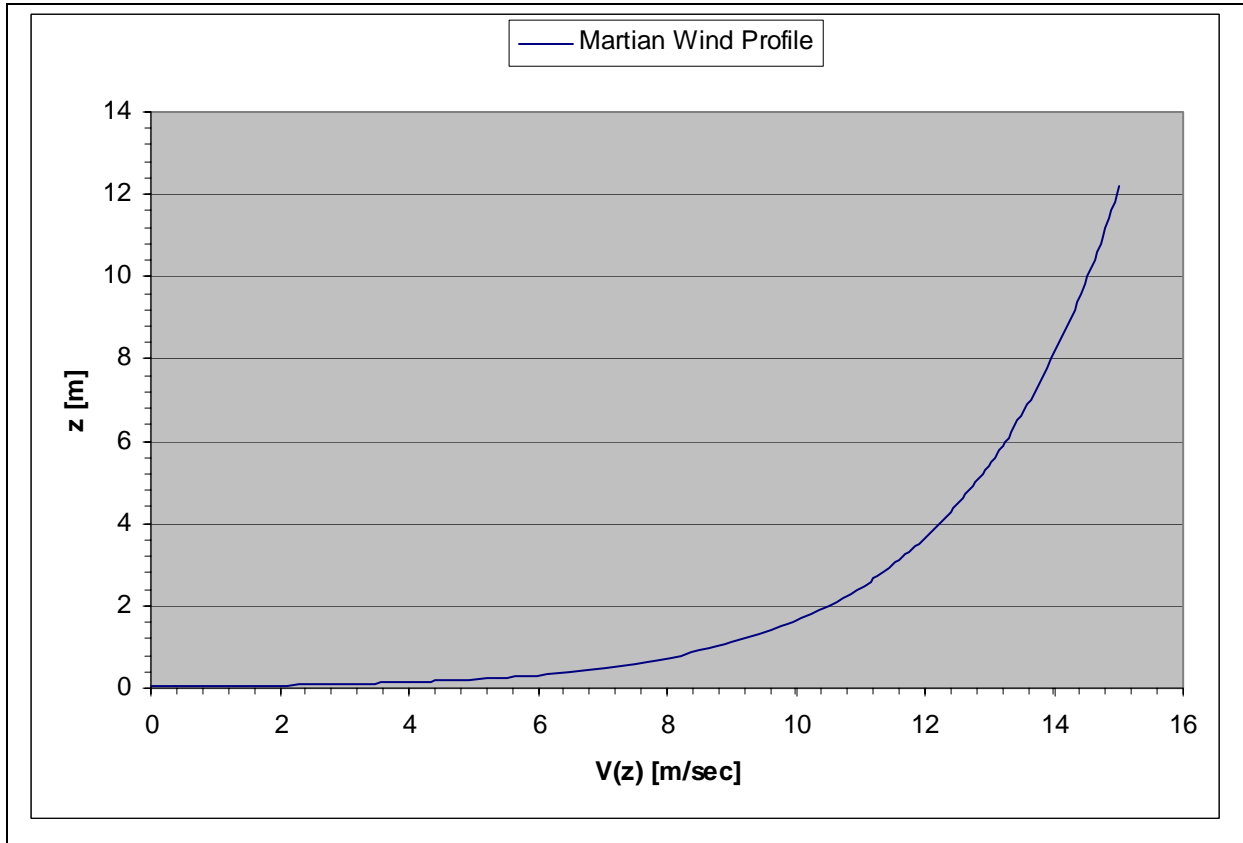
Figure 4 - Martian Wind Profile for u*=1m/sec and z_0=0.03m

Throughout most parts of the accessible literature the average Martian wind speed range is given to 2m/sec to 10m/sec. One example is the website of [28]. In all investigated sources however there is no specification about the height for which these values are related to. Comparing the values of fig.4 to the published average values the assumption is made that this height might be about $z = 1.6m$.

Taking the Martian average dynamic viscosity $\mu_M = 1.1 \cdot 10^{-5} Pa\sec$, the average Martian density $\rho_M = 0.015\,kg/m^3$ and the expected Tumbleweed diameter $d_{TW} = 6m$ lead to a Reynolds number range of: $16363.63 \leq \mathrm{Re}_{TW} \leq 81818.18$. In reference [29] the relevant Reynolds number range for the TW is assumed to be $50000 \leq \mathrm{Re}_{TW} \leq 125000$. Obviously this range accounts also for occasional wind gusts that can achieve wind speeds of

$V = 25\,m/\sec\ to\ 30\,m/\sec$. However reference [29] is still working with an possible Tumbleweed diameter of $d_{TW} = 4m$, too.

In the accessible literature it is written that the very high wind speeds only occur during local dust storms and so called dust devils. The operation under these extreme environmental conditions is not investigated in this thesis, though. That is why a Reynolds number range is chosen that is supposed to include some higher and lower deviations from the calculated average range but no extreme conditions:

$$1.5\cdot10^4 < \mathrm{Re}_{TW} < 1.25\cdot10^5 \tag{2.57}$$

2.3 The NCSU Subsonic Wind Tunnel

Figure 5 - NCSU Subsonic Wind Tunnel

The Department of Mechanical and Aerospace Engineering of the NCSU disposes of a closed circuit subsonic wind tunnel. It is driven by a constant speed fan and hence the flow velocity in the tunnel is regulated by changing the orientation of the fan blades. The fan is powered by a 50HP Westinghouse motor that provides a constant fan speed of 1180rpm.
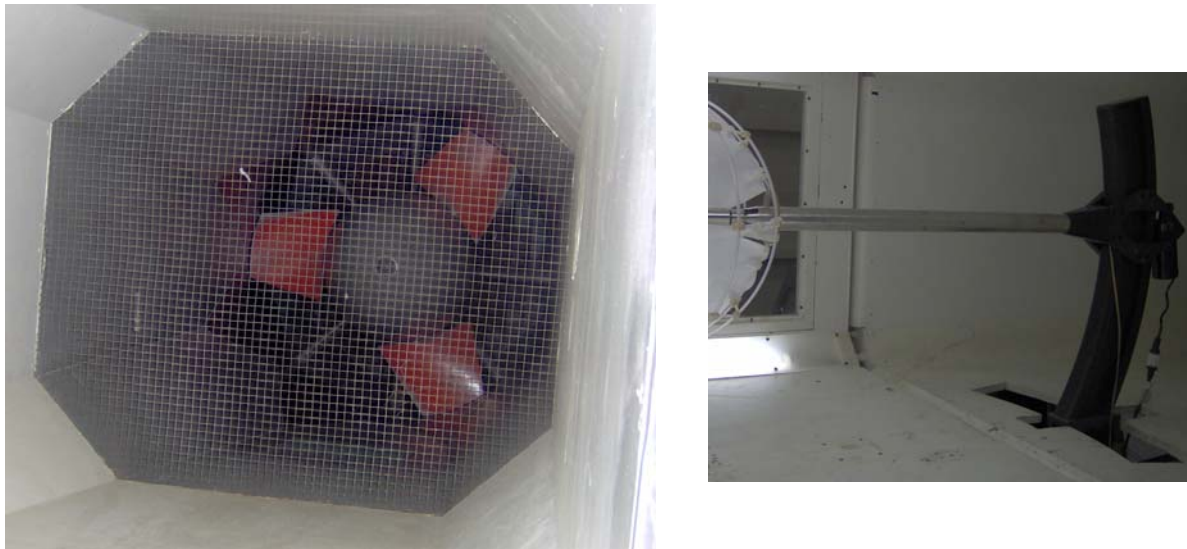
Figure 6 - Constant Speed Fan with Screen (left) and 6-component-balance (right)

2 screens are mounted 1926.6mm [6'3''] in front of the test section and one screen is mounted 2311.4mm [7'7''] after the end of the test section directly in front of the fan. They provide a flow to the test section that shows a turbulence factor of $TF = 1.4$ at a turbulence percentage of 0.5% (measured at a dynamic pressure of $q = 225 Pa$ [$4.7 psf$]).

The test section can be illuminated by four halogen lights. Its dimensions are:

Length [mm]	1168.4
Width [mm]	1143
Height [mm]	812.8
Cross Section [mm^2]	929030.4

Table 4 - Test Section Dimensions

TECHNISCHE
UNIVERSITÄT
MÜNCHEN

Lehrstuhl für Aerodynamik
Technische Universität München
Univ. Prof. Dr. Ing. N. Adams

aer

Figure 7 - Wind Tunnel Test Section

The maximum reachable stagnation pressure is $q = 574.56\,Pa\ to\ 622.44\,Pa\ [12\,psf\ to\ 13\,psf]$.

The lowest reliable that is uniform flow velocity and thus stagnation pressure is somewhat unclear. Unfortunately there is no more documentation available that could clarify this question ultimately. Since the conducted tests are supposed to simulate Martian conditions Reynolds numbers as low as $\mathrm{Re}_{TW} = 1.5 \cdot 10^4$ and hence flow velocities are needed. Therefore tests were run at a stagnation pressure as low as $q = 2.394\,Pa\ [0.05\,psf]$ ($V \cong 2.0\,m/\mathrm{sec}$). The applicability of a stagnation pressure that low is discussed in chapter 4.

The stagnation pressure is set up by a switch at the main control panel that changes the pitch of the fan blades. The stagnation pressure is determined by an internal pitot-static-tube. The final value is shown on a digital display in pounds per square foot at the main control panel. The displayed value is oscillating within $\Delta q = 0.01\,psf$.

Figure 8 - Wind Tunnel Main Control Panel

The ambient air temperature is measured by a thermometer that is mounted next to the test section. The value is displayed digitally and is given in degree Fahrenheit.

The ambient air pressure is determined by a Vernier Scale that is mounted next to one entrance door of the wind tunnel room. Its mode of operation can be looked up at (http://en.wikipedia.org/wiki/Vernier_scale, 11-22-05). The pressure is given in millimeters of mercury.

Figure 9 - Thermometer (left) and Barometer (right) in the Wind Tunnel Room

Knowing the ambient air pressure and temperature allows to determining the current ambient air density after:

$$\rho_{air} = \frac{p_{air}}{R_{air} \cdot T_{air}}$$ (2.58)

$$R_{air} = 287.05 \frac{J}{kg \cdot K} \text{ (gas constant for dry air)}$$

The standard balance of the NCSU wind tunnel is a 6-component-balance (6CB) equipped with strain gages. It measures the forces and moments in and about all three space directions. As can be seen on fig.6 it disposes a certain pitch and yaw ability but no roll ability.

Pitch ability for $\beta = 0°$	$-10° \leq \alpha \leq 20°$
Pitch ability for $\beta \neq 0°$	$-10° \leq \alpha \leq 15°$
Yaw ability	$-15° \leq \beta \leq 15°$

Table 5 - Abilities of Angle Adjustment for the 6-Component-Balance

When changing one or both of these angles the mechanism of the balance makes sure that the article stays in a constant space position of the test section and only changes its orientation. Thus the article is exposed to free stream conditions for every angle combination. The balance is moved by a second control panel.

There is no angle detection included in the balance. That is why the pitch and yaw angle have to be adjusted manually. In terms of the pitch angle this is realized with a portable digital level. Its displayed accuracy is $\Delta\alpha = 0.1°$.

Figure 10 - Pitch Angle Adjustment in the Wind Tunnel

The yaw angle is set up with the help of marks on the wind tunnel base plate. Hence it is estimated that its accuracy is in the order of $\Delta\beta = \pm1°$.

The test articles in this thesis were exposed to pretty low dynamic pressures. Thereby the exerted loads on the balance are relatively small. Unfortunately there is no more documentation of the existing balance available. Hence it is not clear up to what lowest load the balance works reliably. The further assessment of this question is described in chapter 4.

Finally it must be pointed out that the balance support reaches from behind to the test article (see fig.6). However an important issue to investigate will be the wake downstream of the TED or its model, respectively. Here a vortex flow develops that is expected to affect the drag

characteristics to a large extent. Hence it seems possible that this kind of supporting for the test article alters the force and moment characteristics.

2.4 Geometric Relations, Definitions and Transformations

Since the TW-models will be tested in different conditions it is necessary to define the appropriate nomenclature and coordinate systems.

The reference surfaces of the TW and its models for the aerodynamic coefficients are:

$$S_{TW} = \frac{\pi}{4} d_{TW}^2 = 28.274 m^2 \tag{2.59}$$

$$S_{TED} = \frac{\pi}{4} d_{TED}^2 = 7.069 m^2 \tag{2.60}$$

$$S_{tTED} = \frac{\pi}{4} d_{tTED}^2 = 0.126 m^2 \tag{2.61}$$

$$S_{tTED2} = \frac{\pi}{4} d_{tTED2}^2 = 0.0314 m^2 \tag{2.62}$$

These surfaces also represent the maximum sail surface that can be normal to the free stream direction that is one sail plane area. Thereby small surface losses like gaps between the structure and the sails due to mounting are neglected. The structural cross sections are included because they will contribute to the drag creation, too.

The TW and hence also its models show three sail planes that are depicted in the following figure.
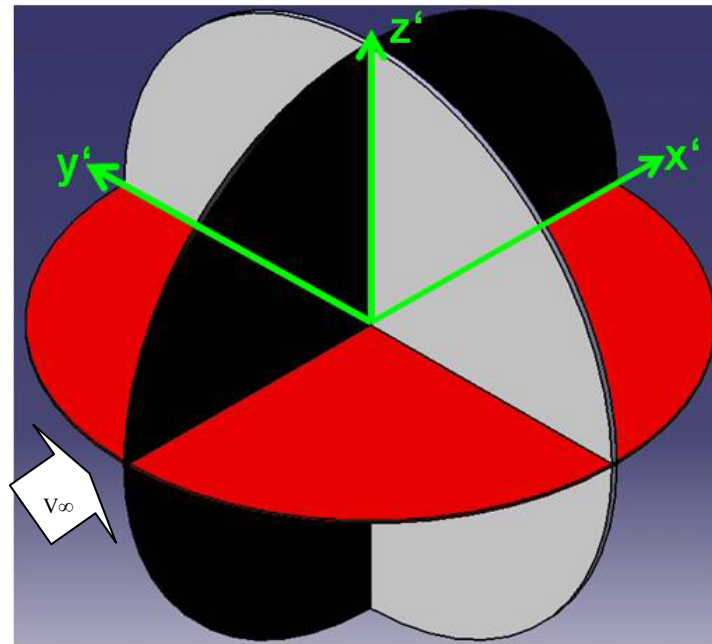
Figure 11 - Tumbleweed Sail Planes and Body Coordinate System

In the figure above the pitch angle, yaw angle and roll angle are zero.

In the static case that is for example at the 6-component-balance not only different pitch angles but also different yaw angles can be measured. The rolling angle remains unchangeable within the means of this thesis. The reference frame fixed in the wind tunnel is:
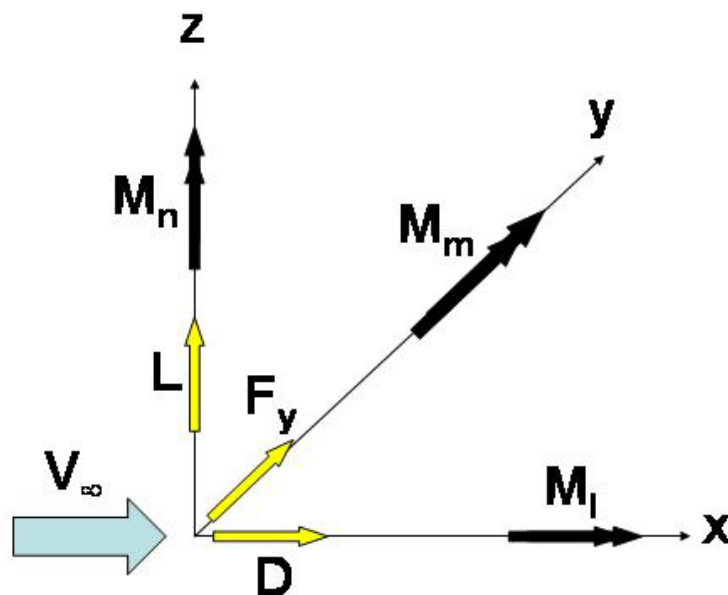
Figure 12 - Reference Frame fixed in the Wind Tunnel

The coordinate directions, forces and moments are labeled as usual in aerodynamics. The drag D acts along the free stream direction and the x-direction. The lift L acts perpendicular to the free stream direction and in positive z-direction. The side force F_y acts perpendicular to the x-z-plane in the positive y-direction.

The moments act along the positive coordinate directions and are counted positive when turning clockwise about the axis. The corresponding force and moment coefficients are:

Force/Moment	Coefficient
D	C_D
L	C_L
F_y	C_y
M_l	C_l
M_m	C_m
M_n	C_n

Table 6 - Force and Moment Coefficients

The relevant angles for this thesis are the pitch angle α (also "angle of attack") and the yaw angle β. A positive pitch angle is caused by a positive pitching moment C_m and a positive yaw angle is caused by a positive yaw moment C_n.
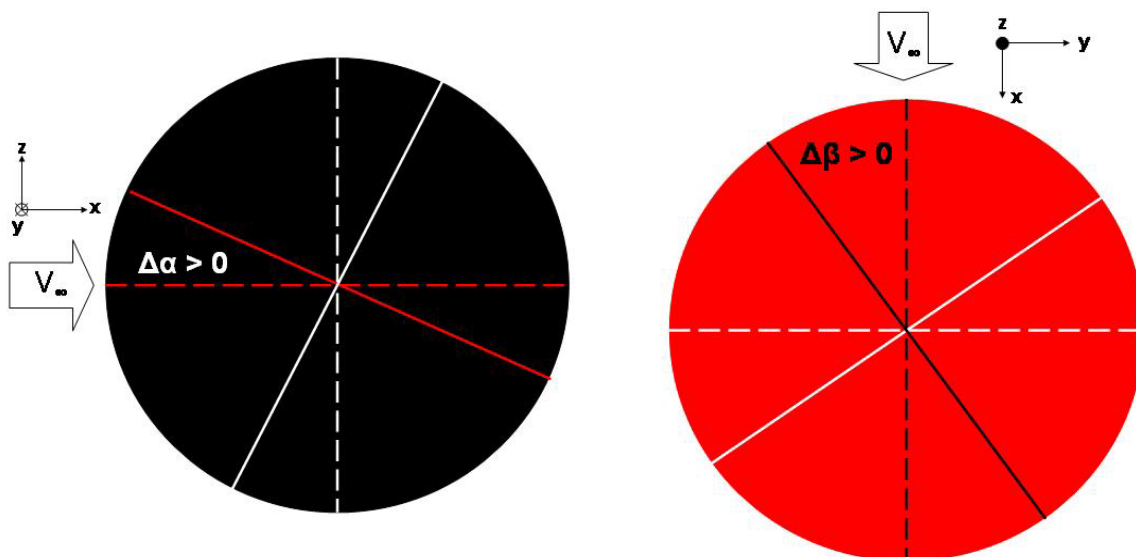
Figure 13 - Definition of Pitch Angle (left) and Yaw Angle (right)

Lehrstuhl für Aerodynamik
Technische Universität München
Univ. Prof. Dr. Ing. N. Adams

TECHNISCHE
UNIVERSITÄT
MÜNCHEN

aer

The angles may also be defined as the angle between the wind tunnel reference frame and the body frame:

$$\text{pitch angle } \alpha = \sphericalangle\left(x - direction,\ x'- direction\right) \text{ in the (black) x-z-plane} \qquad (2.63)$$

$$\text{yaw angle } \beta = \sphericalangle\left(x - direction,\ x'- direction\right) \text{ in the (red) x-y-plane} \qquad (2.64)$$

The dashed lines in figure 13 represent the fixed axis of the x-, y- and z-direction.

The 6-component-balance however measures the forces and moments relative to its fixed coordinate directions. When the model is mounted to the balance the measured values must be transformed from the body system (see figure 11) to the wind tunnel reference system. The forces and moments of the body-system are denominated to: $F_{x'}$, $F_{y'}$, $F_{z'}$ and $M_{x'}$, $M_{y'}$, $M_{z'}$. These measured values are transformed to the reference frame by the equations:

$$D = F_{x'} \cdot \cos\alpha \cdot \cos\beta - F_{y'} \cdot \sin\beta + F_{z'} \cdot \sin\alpha \qquad (2.65)$$

$$F_y = F_{y'} \cdot \cos\beta + F_{x'} \cdot \sin\beta \qquad (2.66)$$

$$L = F_{z'} \cdot \cos\alpha - F_{x'} \cdot \sin\alpha \qquad (2.67)$$

$$M_l = M_{x'} \cos\alpha \cdot \cos\beta - M_{y'} \cdot \sin\beta + M_{z'} \cdot \sin\alpha \qquad (2.68)$$

$$M_m = M_{y'} \cdot \cos\beta + M_{x'} \cdot \sin\beta \qquad (2.69)$$

$$M_n = M_{z'} \cdot \cos\alpha - M_{x'} \cdot \sin\alpha \qquad (2.70)$$

TECHNISCHE
UNIVERSITÄT
MÜNCHEN

Lehrstuhl für Aerodynamik
Technische Universität München
Univ. Prof. Dr. Ing. N. Adams

aer

An important motion for this thesis is the turning about the y'-axis. That is why this motion is described closer considering as an example the TED. During one rotation the projected area normal to the free stream direction $S_\perp$ will change from S_{TED} to $S_{TED} \cdot \cos(45°) = 1/\sqrt{2} \cdot S_{TED}$ and back four times during one period T.
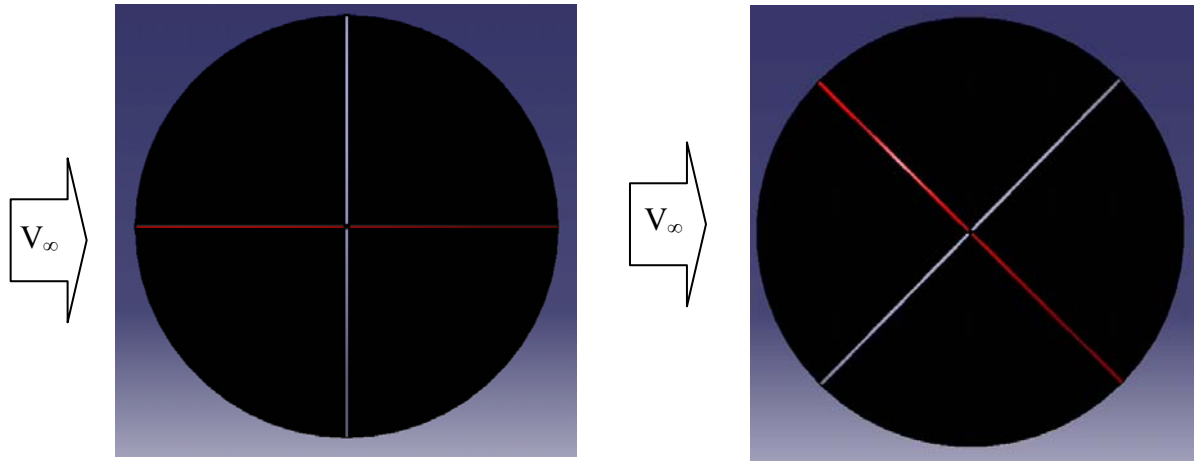
Figure 14 - Maximum (left) and Minimum (right) Sail Surface Normal to the Free Stream

It is defined that one rotation begins at $\alpha = 0°$ and ends at $\alpha = 360°$. That is why the rotation can be depicted by a cosine-function. The non-scaled cosine function with the amplitude S_{TED} has the form:

$$S_{\perp,TED}(\alpha) = S_{TED} \cos(\alpha) \tag{2.71}$$

The general form for scaling and displacing a function $y = f(x)$ is:

$$\frac{y-b}{B} = f\left(\frac{x-a}{A}\right) \tag{2.72}$$

Applying eq.(2.72) to the case at hand yields:

$$S_{\perp,TED}(\alpha) = B \cdot S_{TED} \cdot \cos\left(\frac{\alpha-a}{A}\right) + b \tag{2.73}$$

The calculations of the scaling and displacement parameters can be seen in appendix 04. They are determined to:

$a = 0$:   no phase shift

$A = \dfrac{1}{4}$:   periodicity scaling; four repeats of the geometric features during one

              TED rotation

TECHNISCHE
UNIVERSITÄT
MÜNCHEN

Lehrstuhl für Aerodynamik
Technische Universität München
Univ. Prof. Dr. Ing. N. Adams

aer

$$b = \frac{1}{2} S_{TED} \left(1 + \frac{1}{\sqrt{2}} \right): \quad \text{displacement; calculated from } S_{\perp,\min} \text{ during the rotation and } S_\perp > 0$$

$$B = \frac{1}{2} \left(1 - \frac{1}{\sqrt{2}} \right): \quad \text{scaling of the amplitude}$$

Introducing these terms in eq.(2.73) yields the equation for the normal sail surface dependent on the pitch angle:

$$S_{\perp,TED}(\alpha) = \frac{1}{2} \left(1 - \frac{1}{\sqrt{2}} \right) S_{TED} \cdot \cos(4\alpha) + \frac{1}{2} \left(1 + \frac{1}{\sqrt{2}} \right) S_{TED} \tag{2.74}$$

Introducing the period for one rotation T one gains the time dependent equation for a TED that is rolling steadily about its y'-axis:

$$S_{\perp,TED}(t) = \frac{1}{2} \left(1 - \frac{1}{\sqrt{2}} \right) S_{TED} \cdot \cos\left(4 \cdot \frac{2\pi}{T} \cdot t \right) + \frac{1}{2} \left(1 + \frac{1}{\sqrt{2}} \right) S_{TED} \tag{2.75}$$

The same equations hold true for the TW, the tinyTED and the tinyTED2.
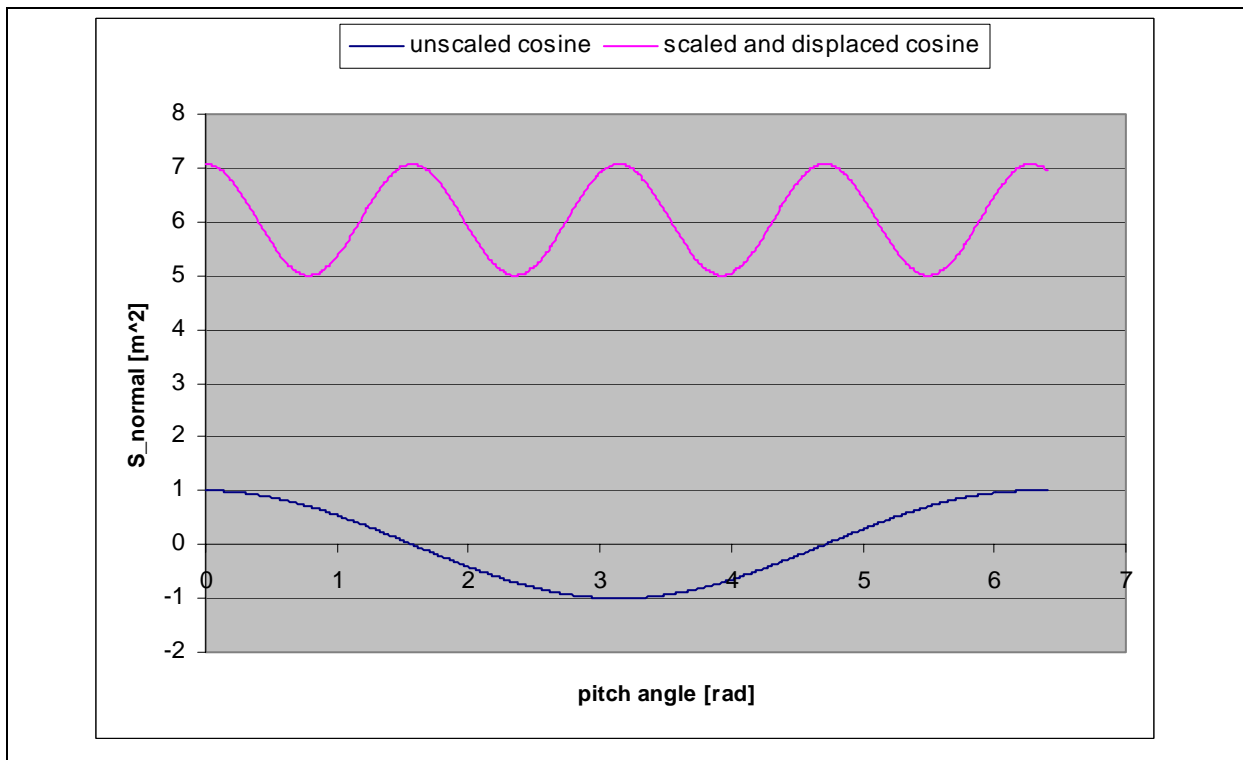
Figure 15 - Function for the TED Sail Surface Perpendicular to the Free Stream for Changing Alpha

After having obtained this equation it also seems to be desirable to enlarge the scope of application of eq.(2.74) to arbitrary pitch and yaw angles. The reason for this is in the determination of the surface normal to the free stream for every possible orientation. In fact

48

this surface will depend only on the pitch and yaw angle but not on the roll angle. Rotating the TW about the x-axis will not change the orientation of the surface normal vector relative to the free stream direction. That is why the surface normal to the free stream direction will not change, either.

The approach in order to determine $S_\perp(\alpha, \beta)$ is basically to use the derivation for $S_{\perp,TED}(\alpha)$ and extent it with the influence of the yaw angle. During the rotation $S_{\perp,TED}$ changes its value from maximum to minimum and back four times during one period. However this time the yaw angle determines the amplitude for the oscillations after $\hat{S}(\beta, S_{TED})$. Additionally the zero shift also depends on the yaw angle after $b(\beta, S_{TED})$. The elaborated derivation may be seen in appendix 04 again. The final equations for the surface perpendicular to the free stream are:

$$S_{\perp,TED}(\alpha, \beta) = \hat{S}(\beta, S_{TED}) \cdot \cos(4\alpha) + b(\beta, S_{TED}) \qquad (2.76)$$

$$\hat{S}(\beta, S_{TED}) = S_{TED}\left[\frac{3}{8}\cos(4\beta) - \frac{1}{2}\frac{1}{\sqrt{2}}\cos(4\beta) + \frac{1}{8} \right]$$

$$b(\beta, S_{TED}) = S_{TED}\left[\frac{1}{8}\cos(4\beta) + \frac{1}{2}\frac{1}{\sqrt{2}} + \frac{3}{8} \right]$$

The same equations hold true for the TW, the tinyTED and the tinyTED2.

TECHNISCHE
UNIVERSITÄT
MÜNCHEN

Lehrstuhl für Aerodynamik
Technische Universität München
Univ. Prof. Dr. Ing. N. Adams

aer

3 Tumbleweed Earth Demonstrator (TED)

During the summer months of 2005 a group of 5 students built and assembled the then latest version of a Tumbleweed Earth Demonstrator (TED) at the NCSU research lab "Research Building II". There several machines and tools are available to conduct most of the works that were necessary. Three demonstrators were built labeled with TED3.2, TED3.3 and TED3.4. The design of TED3.2 to TED3.4 emerged from the preceding senior space design classes of the years 2001 to 2005 and will be described now. *For convenience the demonstrator will be labeled only TED in the remainder of this thesis.*

3.1 TED Components

3.1.1 Outer Sructure

The outer diameter of the TED is $d_{TED} = 3m$ and its outer structure is made out of COTS PVC pipes. Early assessments at NASA have yielded that the minimum size of a promising Tumbleweed concept is $d_{TW} = 6m$. Hence the TED is a $1/2$-downscale model of the actual Tumbleweed Rover.

The pipes have an outer diameter of 33mm and a wall thickness of 4 mm.

They can only be purchased in straight shape. However experiences from the preceding design classes have shown that if shaping the pipes to the outer structure only during the assembly heavy loads are exerted to the pipe connections. That may cause the connections to break and destroy the outer structure. Hence it was decided to bend the pipes to a permanent shape before assembling. That was conducted by putting the pipes in an appropriate rack that forces them to the desired curve. Then boiling water was filled in the pipes so that the pipes' temperature and thus also the pipes' elasticity was increased. The pipes adopted the forced shape and kept it after cooling down again.

Figure 16 - PVC-Pipe Shaping

On the top and the bottom of each TED the pipes were connected by a black iron hub. Thus every main pipe presents about half a circumference of the TED.

Figure 17 - TED Hub

So the main frame of the outer structure consists of 12 semi-pipes and two metal hubs. To increase the rigidity three intersecting auxiliary rings are added. The center ring runs on the central circumference of the TED and thus has got the same length like the main rings namely 9.43m. On 1092.2mm (= 43") below and above the center ring two side rings provide another support for the outer structure. Their circumference is 6.46m. All intersecting pipes are

51

Lehrstuhl für Aerodynamik
Technische Universität München
Univ. Prof. Dr. Ing. N. Adams

aer

connected by commercially available PVC pipe connectors. In order to attach the side rings and the center rings to the main pipes a sleeve-joint-system was designed that was based to a large extent on the use of commercially available PVC cement.

3.1.2 Inner Structure

The actual purpose of the whole Tumbleweed structure is to support an instrument platform for conducting scientific experiments on Mars. Hence a gimbal is place in the very center of the TED sphere. Inside that gimbal the Modular Instrument System (MIS) is mounted that contains all desired scientific instruments, the power supply, the data transmitters and the GN&C system. The gimbal will make sure that the orientation of the MIS is kept nearly constant and it is supported on all six sides (representing all positive and negative space directions) to the outer structure. On the top and the bottom it is mounted to the metal hubs and at the four sides it is mounted to the center ring. The supports are supposed to consist of six metal struts that are reaching from the outer structure to the gimbal.

Figure 18 - Gimbal Supported to the Outer Structure

However after having assembled one TED with a gimbal it became clear that the then current gimbal design did not provide the necessary structural rigidity. It was based on a carbon-fiber layer structure that could not meet the compression requirements of the rolling TED. When rolled around the loads on the gimbal deformed it to such an extent that it could not keep on spinning the whole time. Hence the functionality of the gimbal could not be warranted. It was

tried then to damp the forces on the gimbal by applying some spring-damp-system. However this could not be realized satisfactorily with the means and within the time at hand. Therefore it was decided to replace the gimbal by a simple six-way center piece that allows to supporting the outer structure with PVC struts. Additionally these PVC struts are needed to mount the sails to the TED.

Figure 19 - TED Outer Structure, 6-way Center Piece and Inner Struts

3.1.3 Sails

As per [25] investigations of the Senior Space Design Class of 2004/2005 yielded that the material "rip-stop nylon" combines on the whole the most favorable properties in order to propel the TED. Amongst others these properties include features like highest drag, highest light transmissibility or best rip properties. Thus enough rip-stop nylon was order to produce the sails for all three TEDs.

In reference [25] measurements of the sail drag properties are described. The material was exposed to the free stream in parallel and normal to the free stream direction. The both used dynamic pressures were $q = 0.1 psf$ and $q = 0.5 psf$. Especially the first value raises some doubts about its applicability that are further discussed in chapter 4. The measured drag coefficients are:

TECHNISCHE
UNIVERSITÄT
MÜNCHEN

Lehrstuhl für Aerodynamik
Technische Universität München
Univ. Prof. Dr. Ing. N. Adams

aer

	$C_{D,form}$	C_f
$q = 0.1\,psf$	0.674	0.085
$q = 0.5\,psf$	1.322	0.053

Table 7 - Drag Coefficients of Ripstop Nylon Concluded from [25]

The reference surfaces are: $S_{profile} = S_{frame}$ and $S_{friction} = 2 \cdot S_{frame}$. For the tests the same kind of frame was used like in chapter 5.

The theoretical values for the friction drag coefficient can be approximated with eq.(2.40). The ambient conditions are $T_{amb} = 296K$ and $p_{amb} = 1013\,hPa$. As reference length the value $l = d_{frame}/\sqrt{2} = 0.185\,m$ is taken. Combining these information yields the frame friction Reynolds numbers of $\mathrm{Re}_{friction}(q = 0.1\,psf) = 3.61 \cdot 10^4$ and $\mathrm{Re}_{friction}(q = 0.5\,psf) = 8.08 \cdot 10^4$. Therewith the theoretical approximations are calculated to:

$$C_f(q = 0.1\,psf) = 0.009$$

$$C_f(q = 0.5\,psf) = 0.0072$$

These values deviate by an order of magnitude from the measured data. Besides of the probably not valid lower dynamic pressure the reason for this deviation may also be found in the measuring procedure. For determining the friction force the frame (see chapter 5) was orientated parallel to the free stream. However the frame has got a finite and non-negligible thickness that will produce also a form drag when exposed parallel to the free stream. Therefore the procedure of reference [25] seems not to be capable to measure the real friction drag of the sail material. Hence it stays unknown. However it will be shown in the remainder of this thesis that the contribution of the form drag to the whole TW drag is considered to be significantly higher than that of the frictional forces. That is why it is decided that it is not worthwhile at this phase of the TW investigations to figure out a more sophisticated process for measuring the frictional drag. This effort in cost, work and time is passed over to a later and more elaborated stage of the project.

The sails of the box-kite design are mounted in each of the three space planes that means in the x'-y'-plane, the x'-z'-plane and the y'-z'-plane (see chapter 2.4, figure 11). Therefore every sail plane has to be divided into four quarters and these quarters must be attached to the inner and outer structure.

The requirements of the concept claim that the sails are supposed to be deployable and retractable. By retracting the sails the propulsion of the rover is supposed to be turned off and so it will come to a state of rest. It is in this state when most of the data gathering shall take place. When deploying the sails again the rover is supposed to travel on.

However the SDRS (Sail Deployment and Retraction System) of the TED3.1 that is of the preceding version was very complex. It was driven by several servo engines and required a huge effort in terms of setup and calibration. That is why the versions for the summer testing did not include such a SDRS. The current space design class of 2005/2006 is working on the improvement of such a system and how to provide the TED3.5 with this ability.

Figure 20 - Sail Attachment on the TED

The attachment was carried out by zip ties and grommets that were punched in the edges of every sail.

3.1.4 Modular Instrument System (MIS)

As mentioned before it could not be achieved to get the gimbal working satisfactorily. That is why the MIS could not be assembled to the TED, either. However the MIS includes system elements that are important for the remainder of this thesis. Besides the current space design

class of 2005/2006 is working on improving the structural rigidity of the gimbal so that the MIS can be used in further tests.

The primary power supply of the TED is supposed to be warranted by solar cells. Structurally the MIS just consists of a box that includes the several system elements and instruments and is mounted inside the gimbal.

On top of this box the solar cells are mounted. Through the spinning of the gimbal it is made sure that the solar cells always face to the sky and hence receive as much as sunlight as possible during the TED is rolling around. That is why it is also important that the sails show as much as light transmissibility as possible.

In the center of the top of the wooden box an axle is protruding. On this axle three hollow shells are mounted presenting a self-made anemometer. The turning of the axle induces a voltage that is detected inside the MIS. In order to get the wind speeds out of this voltage the anemometer is calibrated in the NCSU subsonic wind tunnel.
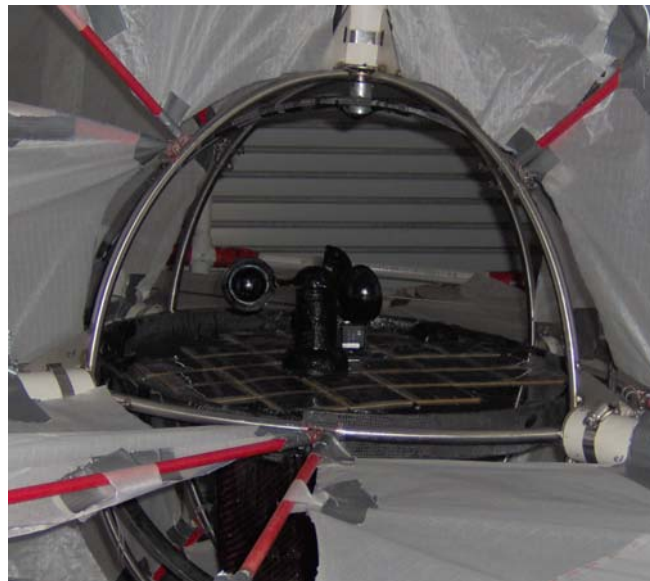
Figure 21- Anemometer and Solar Cells Mounted on the MIS and in the Gimbal

In addition to these elements there are further instruments and system elements inside the MIS. They do not contribute to this thesis but are mentioned for the sake of completeness.

MIS-Element	Purpose
Solar Cells	Power Supply
Batteries	Power Storage
Power Distribution System	Power Distribution
Video Camera	Footage
Magnetometer	Magnetic Field
Anemometer	Wind Speeds
Rocket Data Acquisition System	Data Storage, Accelerations, Pressure, Temperature
GPS-Receiver	TED Position
Inertial Measurement Unit	TED Orientation

Table 8 - MIS-Elements for the TED

For the actual TW further instrumentation is planned like a mineral and water detector.

3.1.5 Obstacle Bypass System (OBS) or Steering Mechanism

A further requirement of the Tumbleweed concept is to provide the rovers with an ability to avoid hazardous obstacles (like big craters or huge rocks) that means to have some steering mechanism. There is some research on this topic by several NCSU students right now. However a somewhat working system has not been developed yet. One idea for example is to change the center of gravity of the rover by moving a mass on the structure. Some students are conducting research on this kind of rolling dynamics under the supervision of Dr Andre Mazzoleni.

TECHNISCHE
UNIVERSITÄT
MÜNCHEN

Lehrstuhl für Aerodynamik
Technische Universität München
Univ. Prof. Dr. Ing. N. Adams

aer

3.1.6 Physical and Design Properties of the TED3.2 to TED3.4

For the sake of clarity the physical properties of the TED3.2 to 3.4 are summarized below.

mass [kg]	52.21
diameter [m]	3
circumference [m]	9.43
d_{PVC_pipes} [mm]	33
wall thickness PVC pipes [mm]	4
sail surface per plane $\left[m^2 \right]$	7.07
number of hubs	2
number of outer main rings [-]	6
number of outer auxiliary rings [-]	1 + 2
number of inner struts	6

Figure 22 - Physical and Design Properties of the TEDs 3.2 to 3.4

3.2 Tests on the Beach of Nags Head

Preliminary tests with all three TEDs were conducted near Research II in order to approve their operability. Since all demonstrators worked satisfactorily they could be taken to the main tests then.

During the summer of 2005 two major tests were conducted with the Tumbleweed Earth Demonstrators (TEDs). The first one took place at the coast of North Carolina on the Outer Banks near Nags Head. Three TEDs were transported to the coast. The purposes of this test were to prove the general operability of the chosen concept and to investigate the rolling behavior as a group. As mentioned before many rovers are supposed to be sent to Mars. Hence the case is thinkable in which an especially interesting area is supposed to be investigated by many rovers. Therefore it is important to get an understanding of their mutual affection while be blown around. Furthermore the deployment mechanism is not determined yet so it is possible that more than one rover is deployed at one spot. That is why it is also interesting to know how they behave when standing very close to each other.

TECHNISCHE
UNIVERSITÄT
MÜNCHEN

Lehrstuhl für Aerodynamik
Technische Universität München
Univ. Prof. Dr. Ing. N. Adams

aer

Unfortunately the wind speeds were never strong enough even at the coast during these days in late July to conduct extensive rolling tests of all TEDs. Only runs of single TEDs could be observed and video-taped. They are attached to this thesis on a CD-ROM.

However measurements of the static flow field about a TED could be conducted while waiting for the wind to rise. One TED was supported on one of his hubs and measurements of the flow velocity in its wake could be conducted with a portable anemometer. Additionally the flow direction could be visualized by a long tuft made out of plastic tape. The measuring procedure was also video-taped and a sample of this is attached to this thesis on a CD-ROM.

The measurements were conducted with a commercially available portable anemometer. It was provided by Jeff Antol, one of the NASA employees that is related to the Tumbleweed project at the NASA Langley Research Center in Hampton, VA. This anemometer had the capability to display real-time data of the wind speeds as well as time averages of a 10-second-period. The latter operation mode was chosen for the flow measurements with the static TED and the real time mode was chosen to catch the gust speeds during the rolling tests. In every case it was tried to orientate the anemometer perpendicular to the wind so that it was measuring the full wind speed.

3.2.1 The Wind Propelled Rolling TED and its Drag Coefficient

Following it is tried to analyze the rolling motion of the TED on the beach. The measured data and the recorded video footage are used to get an approximate average drag coefficient of the rolling TED. During the rotation the area perpendicular to the free stream is changing. So the drag coefficient is expected to be a constant value rather than dependent on time. However it cannot be accounted for this time dependence C_D with the approximate calculations below. So it is tried to determine an average value $\overline{C}_{D,TED}$ for one TED revolution.

It was found that the TEDs would start rolling from their rest state at a wind gust of about 9mph (4m/sec) and would keep rolling at a steady wind speed of at least 7mph (3.11m/sec). These wind speeds were on the very top of the reached wind speeds during this day. Hence it

is assumed that these wind speeds prevailed when the TED started or kept rolling.

The wind speeds were measured with the anemometer mounted on its tripod that is on a height of 1.5m.

The videos "rolling on the beach 01.mpg" and "rolling on the beach 02.mpg" were investigated with the software "Ulead Video Studio 9". The videos can be seen on the attached CD-ROM. The video-taped rolling TED had a big red mark on one of its pipes so the rotational speed could be approximated pretty well.

Figure 23 - Rolling TED with Red Marking

The approximate rotational properties of the TED gained from the videos are:

Rotation	T	$\omega[rad/\sec]$
1	6	1.047
2	8	0.785
3	9	0.698
4	8	0.785
5	9	0.698

Table 9 - Rotational Properties of the Wind Blown TED

Thus the averaged rotational velocity of the TED is $\bar{\omega} = 0.758\,rad/\sec \cong 7.5\,rpm$. Given the Diameter of one TED $d_{TED} = 3m$ the average translational velocity is:

$$\bar{W}_{TED} = \frac{7.5\,rpm \cdot \pi \cdot 3m}{60} = 1.18\frac{m}{\sec}.$$

TECHNISCHE
UNIVERSITÄT
MÜNCHEN

Lehrstuhl für Aerodynamik
Technische Universität München
Univ. Prof. Dr. Ing. N. Adams

aer

As mentioned before the wind speeds were never high enough over a longer period of time in order to conduct extensive rolling tests with all TEDs. Hence the team switched over to conduct flow measurements at one resting TED.

First it was tried to get an idea of the boundary layer profile at the beach. Therefore some measurements were conducted at three different levels upstream of the TED. These levels were the lower side ring (h=0.408m), the center ring (h=1,5m) and the upper side ring (h=2.59m).

Position	Wind Speed [m/sec]			
SR top	2.156	1.545	1.672	1.545
CR	2.024	1.452	1.144	1.452
SR bot.	0.66	0.88	0.66	0.88

$$\overline{V}_{\infty,SRtop} = 1.73\,m/\sec$$

$$\overline{V}_{\infty,CR} = 1.518\,m/\sec$$

$$\overline{V}_{\infty,SRbottom} = 0.77\,m/\sec$$
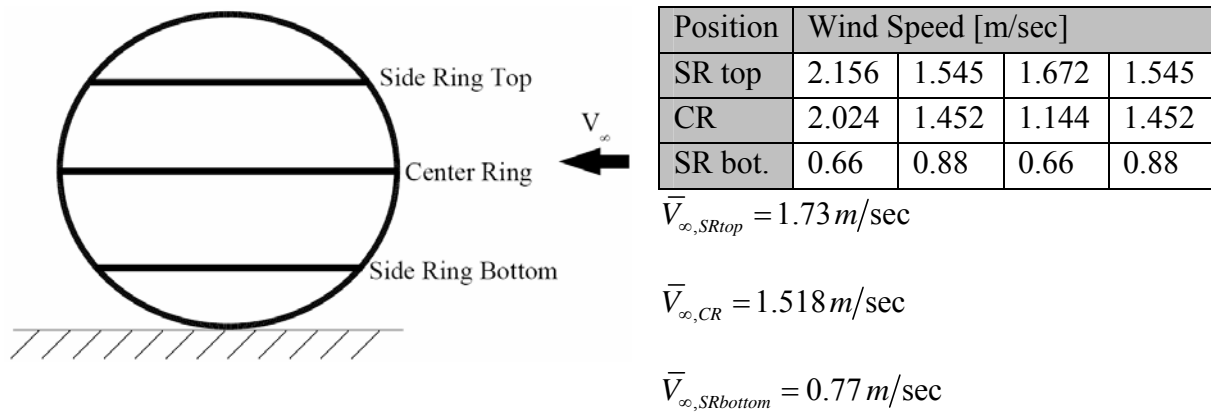
Table 10 - Boundary Layer Measurements on the Beach

Assuming the model of the logarithmical velocity profile of the surface layer (see chapter 2.2.2) the surface roughness on the beach can be calculated from these measurements:

$$V_{\infty}(z) = \frac{u_*}{k} \ln \frac{z}{z_0} \tag{3.1}$$

$$\frac{u_*}{k} = V_{\infty,2} \ln\left(\frac{z_2}{z_0}\right) = V_{\infty,1} \ln\left(\frac{z_1}{z_0}\right) \tag{3.2}$$

$$\ln z_0 = \frac{V_{\infty,1} \cdot \ln z_2 - V_{\infty,2} \cdot \ln z_1}{\left(V_{\infty,1} - V_{\infty,2}\right)} \tag{3.3}$$

$$z_0 = \exp\left(\frac{V_{\infty,1} \cdot \ln z_2 - V_{\infty,2} \cdot \ln z_1}{\left(V_{\infty,1} - V_{\infty,2}\right)}\right) \tag{3.4}$$

TECHNISCHE
UNIVERSITÄT
MÜNCHEN

Lehrstuhl für Aerodynamik
Technische Universität München
Univ. Prof. Dr. Ing. N. Adams

aer

	$V_{\infty,1}\,[m/\sec]$	$z_1\,[m]$	$V_{\infty,2}\,[m/\sec]$	$z_2\,[m]$	$z_0\,[m]$
SRbot, CR	0.77	0.45	1.518	1.5	0.13
SRbot, SRtop	0.77	0.45	1.73	2.55	0.11
CR, SRtop	1.518	1.5	1.73	2.55	0.033

Table 11 - Calculation of Surface Roughness

The first two values for the surface roughness seem to be too big. From reference [33] it is known that for pure sand the surface roughness is in the order of $0.0001m \leq z_0 \leq 0.001m$ and therefore far beyond the calculated values. The wind blew pretty exactly down the beach on that day. In fact it was a very sunny and warm day and hence the beach was crowded with many people and appropriate setups like umbrellas and wind protection tents. This tourist area was several meters upstream of the TED test area and thus it seems to be possible that the real surface roughness is in the order of a rocky area. For this topography the value $z_0 = 0.033m$ is more typical than the larger ones (see chapter2.2.2) and hence it is chosen for the further investigations.

Assuming that the log-law is true the friction velocity can be calculated from applying the surface roughness and the measured wind speed on eq.(3.1):

$$V_{\infty}\left(1.5m\right) = \frac{u_*}{0.4}\ln\left(\frac{1.5m}{0.033m}\right) = 3.11 m/\sec \tag{3.5}$$

$$u_* = \frac{3.11\dfrac{m}{\sec}\cdot 0.4}{\ln\left(\dfrac{1.5m}{0.09m}\right)} = 0.442\dfrac{m}{\sec} \tag{3.6}$$

TECHNISCHE
UNIVERSITÄT
MÜNCHEN

Lehrstuhl für Aerodynamik
Technische Universität München
Univ. Prof. Dr. Ing. N. Adams

aer

Using this friction velocity and the averaged surface roughness a wind profile for the rolling TED can be calculated by an Excel®-Sheet.
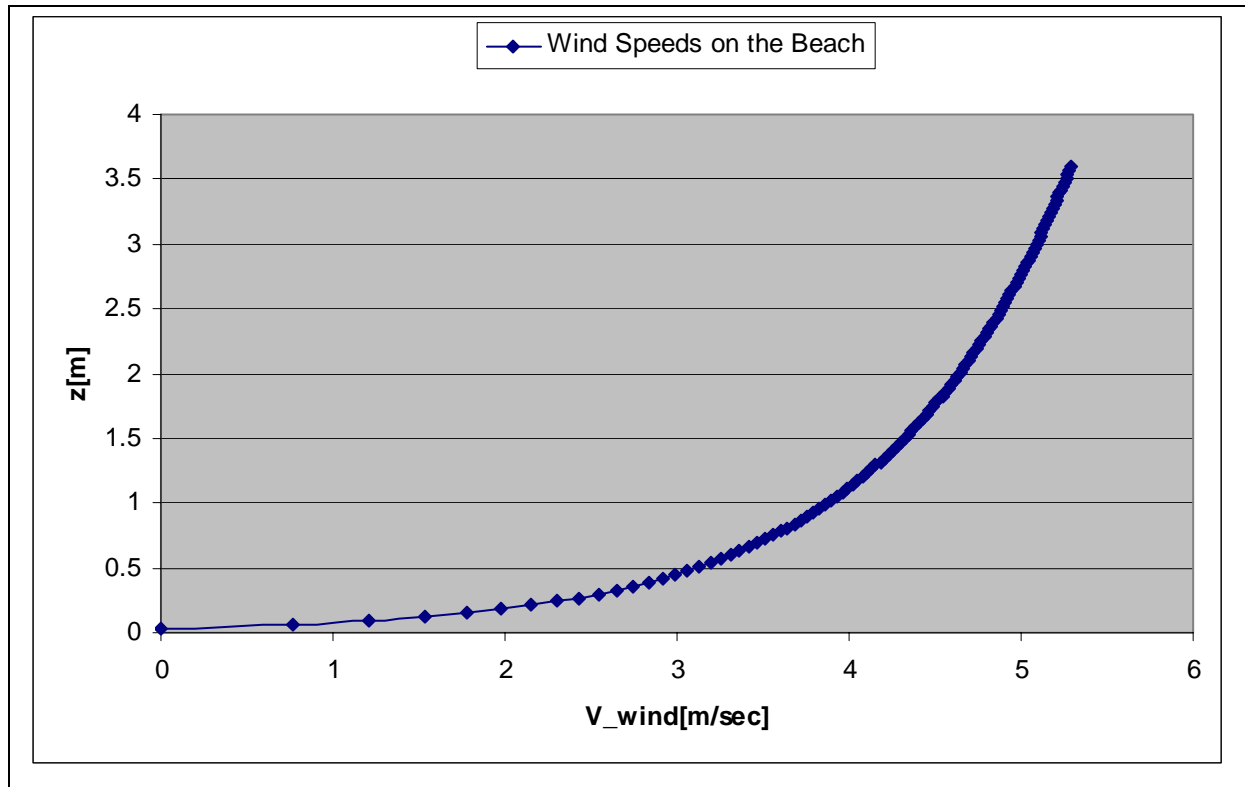
Figure 24 - Wind Profile for the Rolling TED on the Beach

Now an arithmetic average wind speed (free stream) on the rolling TED can be calculated.

Using the Excel®-sheet again yields an average velocity of $\overline{V}_\infty = 4.02 \frac{m}{\sec}$.

The atmospheric temperature and pressure of this particular day and daytime (07-28-05 at 1pm) are gained from the internet website
(http://english.wunderground.com/history/airport/KMQI/2005/7/28/DailyHistory.html?req_city=NA&req_state=NA&req_statename=NA, 08-02-05):

T = 28°C = 301,25K

p=1016hPa

Thus the density during this time was:

$$\rho_{air} = \frac{p_{air}}{RT_{air}} = \frac{1016hPa}{287\frac{J}{kgK} \cdot 301,25K} = 1,175\frac{kg}{m^3} \tag{3.7}$$

As mentioned in chapter 3.1.6 the mass of the TED is: $m_{TED} = 52.21kg$.

63

As per (http://de.wikipedia.org/wiki/Rollwiderstand, 11-17-05) the rolling drag coefficient for a car tire on hardened sand is $\mu_R = 0.04 \; to \; 0.08$. The exact ground composition on the beach is hard to determine. However as can be seen on the videos the TED rolled near the surge. This leads to the assumption that the sand was not yet really dried out by the sun and thus should be in a state of somewhat hardened sand. In addition the surface roughness of the rather smooth PVC-pipes is certainly lower than of a car tire with a defined profile.

Some research was conducted in order to find a more comparable case in terms of the friction pair sand and PVC. However this research did not yield the desired data. Eventually the rolling drag coefficient is chosen to $\mu_R = 0.06$. It must be stressed that this value is somewhat arbitrary.

It is assumed that the drag force and the propelling aerodynamic drag force are in equilibrium during a steady rolling motion:

$$D_{TED} = F_{R,TED} \tag{3.8}$$

$$\bar{C}_{D,TED} \cdot \frac{\rho_{air}}{2} \bar{V}_\infty^2 \cdot S_{TED} = \mu_R \cdot m_{TED} \cdot g_E \tag{3.9}$$

$$\bar{C}_{D,TED} = \frac{\mu_R \cdot m_{TED} \cdot g_E}{\frac{\rho_{air}}{2} \left(\bar{V}_\infty - \bar{W}_{TED} \right)^2 \cdot \frac{\pi}{4} d^2{}_{TED}} \tag{3.10}$$

$$\bar{C}_{D,TED} \left(\mu_R = 0.06 \right) = 0.918 \tag{3.11}$$

The simplest approximation of the TED shape is a flat disk that is orientated perpendicular to the free stream. As per [26] the aerodynamic drag of such an geometry is $C_D = 1.17$. In chapter 2.4 it is shown that the shape of the TED varies during one rotation and so it may be assumed that the flat disk is a maximum value. Consequently the determined value seems to be within a realistic range and further tests under more controllable conditions in the wind tunnel must be conducted.

3.2.2 The Wake Downstream of the Resting TED

While waiting for higher wind speeds the team conducted also wake flow measurements downstream of the TED. Therefore the anemometer was mounted on its tripod and the free stream velocity in front of the TED was measured over a period of several minutes. These

measurements yielded an average free stream velocity of $V_\infty \left(z = 1.5m \right) = 1.95\,m/\sec$. Then the two available measuring tapes were used to place the anemometer on defined locations in the wake of the TED. Thereby the anemometer was mounted on its tripod that is about 1.5m above the ground. In addition a piece of plastic tape that fluttered easily in the wind was used in order to approximate the flow direction. Parts of the measuring procedure may be seen from the attached CD-ROM and the movie "vortex detection on the beach.mpg".

Figure 25 - Wake Measurements on the Beach

The gained local velocities u are following. Thereby a negative sign indicates the backflow towards the TED and a positive and negative sign indicate that the velocity could be measured in both directions. All values are taken approximately 1.5m above the ground that is at $z = 1.5m$. The yellow background marks measurements on the center line and the green background measurements in the lateral direction.

TECHNISCHE
UNIVERSITÄT
MÜNCHEN

Lehrstuhl für Aerodynamik
Technische Universität München
Univ. Prof. Dr. Ing. N. Adams

aer

view from above on the TED
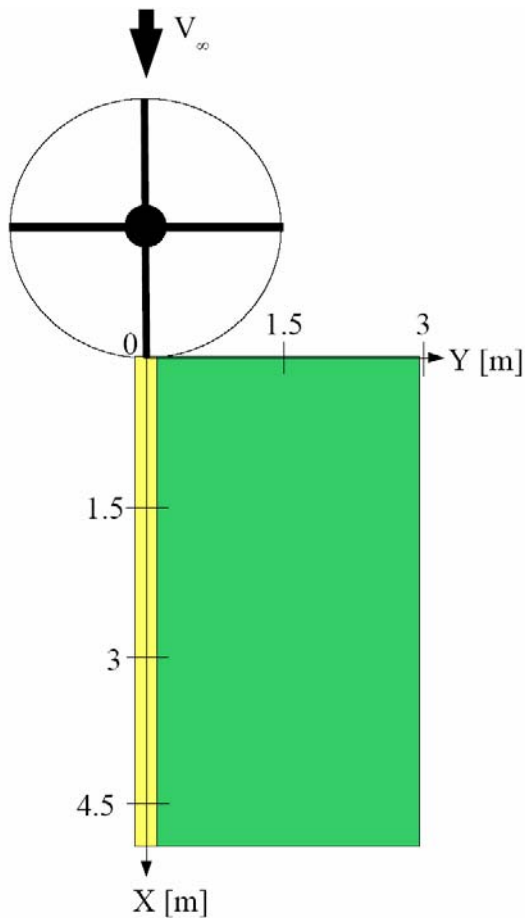
X [m]	Y [m]	u [m/sec]
0	0	0
0.31	0	-0.792
0.61	0	-0.88
0.91	0	-0.968
1.219	0	-1.056
1.52	0	-1.364
3.05	0	-0.968
4.27	0	±0.88
0	1.5	±0.088
0.91	1.5	±0.264
1.83	1.5	±0.484
1.83	0.75	-0.748
2.74	1.5	0.484
2.74	3	2.024
2.74	0.75	-0.748
3.66	1.5	±0.968
3.66	0.75	±0.484
4.57	1.5	0.88
4.57	0.75	±0.264

Table 12 - Local Flow Velocities in the TED Wake Field

As a first approach the geometry of the TED is compared to a simple three dimensional flat plate perpendicular to the free stream. Since the TED was supported on one of its hubs this assumption seems to be justified. The theory for the wake behind a flat plate is taken from [24]. The streamlines are supposed to represent the mean values of the measured velocities in the turbulent wake. If these streamlines are drawn a flow field pattern appears that is somewhat similar to the measured values behind the TED.

TECHNISCHE
UNIVERSITÄT
MÜNCHEN

Lehrstuhl für Aerodynamik
Technische Universität München
Univ. Prof. Dr. Ing. N. Adams

aer
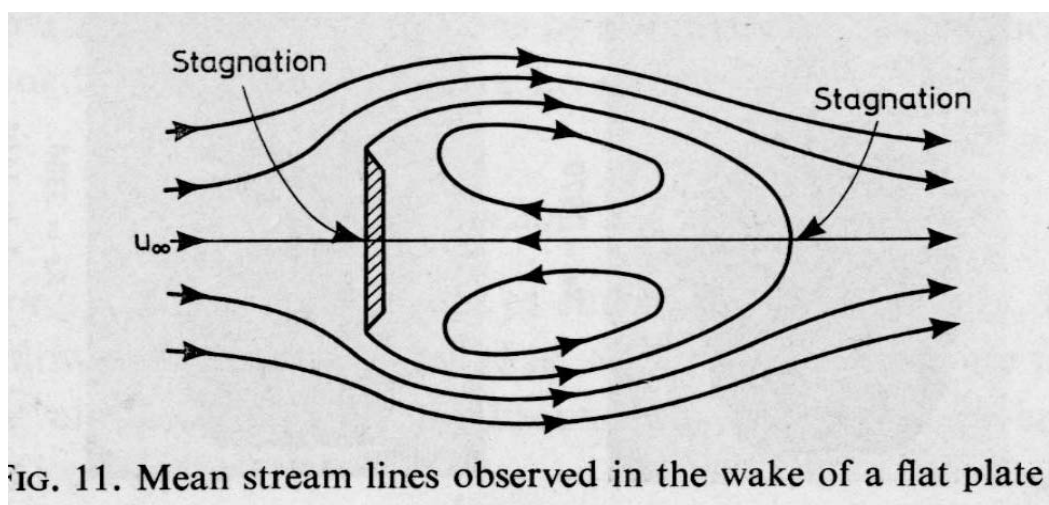
Figure 26 - Streamline Pattern Behind a Flat Pate from [24]

The center streamline behind the plate indicates a purely backflow towards the plate. The same result was obtained at the beach, indicated by the yellow highlighted flow velocities.

In the lateral directions two vortex regions are formed that reach slightly beyond the plate diameter. Many of the flow velocities highlighted green show alternating signs that means flow directions. This fact may be seen as a hint for the presence of turbulent eddies or vortices that are flowing downstream of the TED. As per [24] the frequency of the fluctuations in case of the flat plate is nearly proportional to the free stream velocity and inversely proportional to the diameter of the plate. It will be tried to assess this behavior for the TED under more controllable conditions. (see chapter 6)

Deviations to the flat plate are the two further sail planes that are acting as short tail plates. A tail plate attached to a blunt body is known to be able to prevent the wake pattern and the oscillations. Precondition is a length of five diameters of the blunt body. But only the rear half of the further sail planes are acting as a tail plate. In that case the plates are not able to prevent the wake pattern but decrease the amplitude of the eddies and alter their oscillations.

3.3 Tests in the Mountains near Lake Toxaway

The second test took place in the mountains of North Carolina near Lake Toxaway. Mainly the dynamic rolling characteristics of the TED could be observed there. Hence only one TED was transported to the test site this time.

The TED rolled down a ravine and a pretty steep slope several times.

3.3.1 Rolling Down a Ravine and over Obstacles

When rolling down a ravine the TED overcame obstacles pretty easily. However two observations may cause problems especially for a TED with attached sails. When passing the obstacle the TED's structure shows a clear tendency to deform. It can jump over the obstacle and bounces several times after hitting the ground again. In addition parts of the obstacles like rocks may reach into the outer structure and thus may pose a threat to the sail material. Three appropriate test runs may be seen on the videos "ravine 05.mpg", "ravine 07.mpg" and "ravine 08.mpg" that can be found on the attached CD-ROM.

Figure 27 - TED Rolling Over an Obstacle

3.3.2 Rolling Down a Steep Slope

Again it was found that the structural design at hand tends to bounce remarkably when rolling down a steep slope. However even when damaged the TED kept on rolling pretty much unaffected by the breaks of some joints and members. Two test runs may be seen on the videos "steep slope 01.mpg" and "steep slope 02.mpg".

Figure 28 - TED Bouncing while Rolling down a steep Slope

3.4 Conclusions from the TED Test Phase

First of all it must be stressed that all measurements on the beach were conducted under field conditions that is they all have a kind of approximate character. These field measurements can never be as accurate as under laboratory conditions. For example the sand does not allow to providing a constant height of the anemometer mounted on its tripod because the tripod sank more or less in the sand. Moreover the sand had different composition features ranging from pretty hard wet sand to very loose and deep dry sand. The wind of course did not blow in a steady manner in terms of strength and direction. At least its overall direction was pretty steady that means it blew from North down the beach. Finally the team was not equipped with the instrumentation to guarantee a maximum accuracy of the field measurements. One reason for that was that the main emphasis of the whole test was on the proof that the chosen concept as a whole is working rather than gathering sophisticated aerodynamic and dynamic data.

In the mountains again the interest lay more on the general behavior of the chosen concept. The final structural design of a potential Tumbleweed Rover certainly deviates a lot from the

Lehrstuhl für Aerodynamik
Technische Universität München
Univ. Prof. Dr. Ing. N. Adams

TECHNISCHE
UNIVERSITÄT
MÜNCHEN

aer

current TED design mainly in terms of its materials. For example there will be much more sophisticated materials making the Tumbleweed very much lighter than the TED and hence changing its structural properties.

However some interesting data could be gained from both tests and from that further research demand can be derived.

The problems on the beach in terms of getting the TEDs rolling have shown that an increase in sail performance is very desirable. A brief assessment of the equivalent Martian wind speed is supposed to proof this:

Air Temperature at Manteo on 07-28-05 at 1pm: T = 28°C = 301,25K

Air Pressure at Manteo on 07-28-05 at 1pm: p=1016hPa

(as per

http://english.wunderground.com/history/airport/KMQI/2005/7/28/DailyHistory.html?req_city=NA&req_state=NA&req_statename=NA, 08-02-05)

Calculated Air Density from data above:

$$\rho_E = \frac{p_E}{R_E T_E} = \frac{1016 hPa}{287 \frac{J}{kgK} \cdot 301,25K} = 1,175 \frac{kg}{m^3} \tag{3.12}$$

The wind gust it took to start rolling the TED were about $9 mph \cong 4 \, m/\sec$. Hence the calculated free stream dynamic pressure is:

$$q_E = \frac{\rho_E}{2} V_E^2 = \frac{1}{2} \cdot 1,175 \frac{kg}{m^3} \cdot \left(4 \frac{m}{s}\right)^2 = 9,4 Pa \tag{3.13}$$

The Standard Martian Atmospheric Density is: $\rho_M = 0,0156 \frac{kg}{m^3}$.

The required Martian wind speed for being equivalent to the Earth gust in terms of the same generated drag force is:

$$C_{D,M} \cdot q_M \cdot S_{TW} = C_{D,E} \cdot q_E \cdot S_{TED} \tag{3.14}$$

For this assessment it is assumed that the drag coefficient deviates only slightly with the Reynolds number (what seems to be justified for a blunt body like the TED). So the Martian and Earth drag coefficients are roughly equal: $C_{D,M} \cong C_{D,E}$.

The TED's diameter is half of the TW's diameter. Therefore the area ratio is: $S_{TED}/S_{TW} = 1/4$. This leads to the required Martian wind speed of:

$$V_M = \sqrt{\frac{2}{\rho_M} \cdot q_E \cdot \frac{S_{TED}}{S_{TW}}} = 17.36 \frac{m}{\sec} \qquad (3.15)$$

Considering the average Martian wind speed range of 2m/sec to 10 m/sec this value is very high. Obviously the materials used for the TW will be much lighter than those used for the TED. That in turn leads to a lower rolling friction and consequently to a lower required stagnation pressure and wind speeds. On the other hand the TW will be double in size and thus loose this mass advantage in part.

The drag coefficient of the rolling TED concept on the beach could only be determined in a very approximate manner. Hence it will be interesting to determine the static and dynamic force and moment coefficients of the resting and rolling TED and TW, respectively.

The discovered wake downstream of the TED raises questions concerning its dimensions, structure and flow features. Moreover the wake was measured when the TED was resting. That is why an again different wake is expected for a rolling TED. A first step to a deeper comprehension of the wake properties will be its visualization. However this will not be an easy task since the NCSU wind tunnel is lacking capabilities to visualize the wake flow.

The mountain tests have pointed out that the sails may be damaged by protruding rocks. Moreover their deployment and retraction mechanisms or/and their supports to the structure might fail due to heavy bouncing of the TW or other technical flaws. The effect of these failures on the aerodynamic forces and moments of the TED are interesting to investigate.

Finally the tests could prove successfully that the chosen design concept for the TED3.2 to TED3.4 is working well. Even under pretty harsh conditions like in the mountains the TED keeps on rolling and overcomes obstacles well. So the following senior space design class will

have a constructed TED whose rolling ability is proven and that can serve as a basic design for further developments and tests.

TECHNISCHE
UNIVERSITÄT
MÜNCHEN

Lehrstuhl für Aerodynamik
Technische Universität München
Univ. Prof. Dr. Ing. N. Adams

aer

4 Subscale Models of the TED

In order to use the NCSU subsonic wind tunnel for aerodynamic investigations on the TW a downscale model is necessary. In addition this model is supposed to be used for flow visualization outside of the tunnel because during this thesis there was no possibility to visualize the flow in the NCSU subsonic wind tunnel.

Thereby some requirements and constraints have to be met and considered, respectively. As described in chapter 2.1 the model must be geometrical similar to the TED. That means that the ratios of the most important dimensions of the model to the equivalent lengths of the TED must be held equal or at least similar to the diameter ratio of the model and the TED.

Furthermore it is already known that the Reynolds numbers will be relatively small and hence also the dynamic pressures. However the wind tunnel balance is known not to work reliably for arbitrarily low forces and moments. Indeed the exact minimum values are unknown. Hence the sail surface and therefore the model must not be too small.

On the other hand the solid blockage factor of the wind tunnel must be held below a certain limit. This limit is not fully clear but as per [2] it should not exceed the value of $BF = 0.1$.

Finally the means of building the model are not unlimited. There is only a certain amount of money. The model must be built by the author, at least to the biggest extent since the department's workshops are not available arbitrarily. Most of all there are no machines available that are specialized on producing wind tunnel models. That is why eventually most of the work has been done manually or with the available machines in the workshop of Research II.

Similar constraints in terms of money and machine availability are true for the strain gage balance that is described in chapter 4.2.

4.1 Subscale Model tinyTED

The first subscale model has been labeled tinyTED (tTED). It is a 1/7.5-downscale model of the TED that means that the diameter ratio with the TED is given to:

$$\frac{d_{tTED}}{d_{TED}} = \frac{2}{15} = \frac{1}{7.5} = 0.133 \qquad (4.1)$$

TECHNISCHE
UNIVERSITÄT
MÜNCHEN

Lehrstuhl für Aerodynamik
Technische Universität München
Univ. Prof. Dr. Ing. N. Adams

aer

Consequently the tTED diameter is

$$d_{tTED} = \frac{2}{15} \cdot 3m = 400mm \tag{4.2}$$

From a hobby store plastic pipes could be purchased that have a diameter of $d_{tTED,pipes} = 4.76mm\,(3/16")$ yielding a pipe-diameter ratio of

$$\frac{d_{tTED,pipes}}{d_{TED,pipes}} = \frac{4.76mm}{33mm} = 0.144 \tag{4.3}$$

and thus a very good geometric similarity between the TED and the tTED.

Two sets of circular hubs were designed and constructed. A technical drawing may be seen in appendix 03. The hubs have a diameter of $d_{tTED,Hub} = 50mm$ and the first set is made of balsa wood having a thickness of 10mm. A hub diameter ratio seems to be useless since the TED hubs are made out of welded metal pipes (see fig.17) and hence are based on a different design. However the TED-design seemed not to be feasible for the tTED. Twelve holes are drilled into the hubs laterally having a diameter of $d_{tTED,Hub,holes} = d_{tTED,pipes}$ and the pipes are stuck into these holes. The second set of hubs is made out of standard wood from the DIY-store and each shows a hole of $d_{tTED,Hub,hole} = 11.11mm\,(7/16")$ in its center. The rest is equal to the balsa wood hub. Through the center holes a metal rod is stuck that serves as a support rod in the self-made smoke channel (see chapter 6.1).

For the center ring and side rings appropriate connector pieces were made out of balsa wood. All three rings were made out of pipe pieces exactly like at the TED.

The center struts for the inner structure were made out of standard wood from the DIY-store and have a diameter of $d_{tTED,strut} = 6.35mm\,(1/4")$. The wood was not available in the pipe size. Since these struts must communicate the loads from the outer structure to the support it was decided to go with a larger diameter. As mentioned the hub struts were replaced by a metal rod for the second set of hubs.

In order to mount the tTED on the standard 6-component-balance a standard metal sleeve had to be used. This sleeve has an outer diameter of $d_{balance\,sleeve} = 33mm$ and a length of $l_{balance\,sleeve} = 110mm$. That is why the center piece of the tTED has to account for these dimensions. Moreover the models are mounted to the sleeve by four bolts so that the center

TECHNISCHE
UNIVERSITÄT
MÜNCHEN

Lehrstuhl für Aerodynamik
Technische Universität München
Univ. Prof. Dr. Ing. N. Adams

aer

piece must have four appropriate clearance holes, too. Furthermore the balance reaches in from behind to the tTED. That is why a rod bypass has to be included in the outer structure. This bypass was realized by using a simple piece of circular cardboard.

Figure 29 - Center Piece, Balance Sleeve and Rod Bypass

The sails of the tTED are made out of residues from the TED sails. In order to be able to change the sails quickly the first set of sails was mounted with Velcro® to the structure. However it turned out that this procedure could not tighten the sails satisfactorily. That is why the second set for the rolling experiments in the smoke channel was attached by wool filaments.

The whole area perpendicular to the flow is assumed to be:

$$S_{tTED} = \frac{\pi}{4} \cdot d_{tTED}^{2} = 0.1257 m^{2} \tag{4.4}$$

It has to be mentioned that gaps between the sails and the structure may decrease this surface slightly. However this small effect is neglected. Hence the blockage factor of the tTED in the NCSU wind tunnel is

$$BF_{tTED} = \frac{S_{tTED}}{A_{test\ section}} = 0.1353 \tag{4.5}$$

This value appears to be pretty high. Considering the mentioned constraints however this value seems to be an acceptable trade-off between the assumed maximum blockage factor of

TECHNISCHE
UNIVERSITÄT
MÜNCHEN

Lehrstuhl für Aerodynamik
Technische Universität München
Univ. Prof. Dr. Ing. N. Adams

aer

$BF_{\max} = 0.1$ (taken from [2]) and previous described requirements. Indeed some altering effects must be expected.
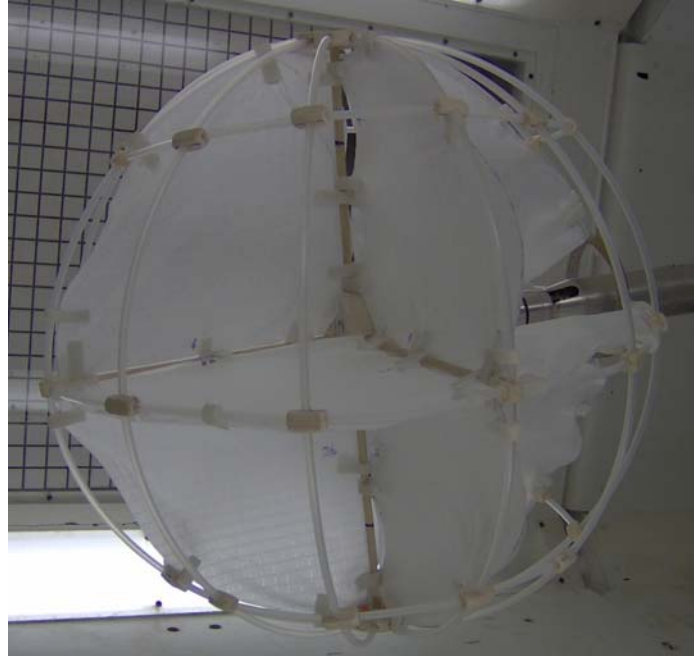
Figure 30 - Final tTED mounted in the Wind Tunnel

4.2 One Beam Strain Gage Balance

(Note: The mechanical equations of this sub-chapter are taken from [9].)

As described previously the standard balances at hand for the NCSU wind tunnel shows some constraints and uncertainties. The support reaches from behind to the test article altering the vortex flow downstream of the article. Additionally it is unknown how large the lowest loads are that can be detected reliably by the balance. The balance is only capable to yaw the article up to $\beta = \pm 15°$. However one interesting yaw angle is $\beta = 45°$ because it marks a distinguished orientation of the TW. (see chapter 2.4)

Finally an aim of this thesis is to investigate different approaches for increasing the sail performance experimentally. Therefore a balance is desirable that allows to mounting a sail in the free stream without disturbing its flow field downstream of the sail.

4.2.1   Balance Design and Construction

Therefore it was decided to build a new balance. Often strain gages are used for realizing wind tunnel balances and hence this approach will be used here as well.

TECHNISCHE
UNIVERSITÄT
MÜNCHEN

Lehrstuhl für Aerodynamik
Technische Universität München
Univ. Prof. Dr. Ing. N. Adams

aer

As per [4] "a strain gage is a device used to measure deformation (strain) of an object. The most common type of strain gage consists of a flexible backing which supports a metallic foil pattern etched onto the backing. As the object is deformed, the foil pattern is deformed, causing its electrical resistance to change. This resistance change, usually measured using a Wheatstone bridge circuit, can be used to calculate the exact amount of deformation by means of the quantity known as the gage factor."

The gage factor of a strain gage relates strain to change in electrical resistance. The gage factor GF is defined by the formula

$$GF = \frac{\Delta R / R_0}{\varepsilon} \tag{4.6}$$

R_0 resistance of the non-deformed gage

ΔR change in resistance caused by strain

ε strain

The most important force component for the Tumbleweed purposes is the created drag force. Hence the approach for building a strain gage balance is the one-beam-balance (OBB) in order to determine this quantity. Therefore a metal rod of circular cross section is chosen as the new center strut for the tTED. It passes through the bottom hub and a hole in the baseplate and reaches under the wind tunnel. For the same reason the sail test frame is mounted on a metal rod of the same diameter (see chapter 5.2). Thus the balance can be used for both the TED model and the sail test frame.

Under the baseplate the rod is connected to a rectangular metal plate by a wooden sleeve. The geometry of this wooden sleeve may be seen from the mechanical drawing in appendix 02. A small hole is drilled into the wooden sleeve and also at various angles into the metal rod. Through these holes the rotational degree of freedom around the vertical axis of the rod can be fixed by putting a bolt through the hole. Thus the yaw angle of the tTED and of the sail frame can be adjusted relative to the balance rack.

TECHNISCHE
UNIVERSITÄT
MÜNCHEN

Lehrstuhl für Aerodynamik
Technische Universität München
Univ. Prof. Dr. Ing. N. Adams

aer

Figure 31 - Yaw Fixing Device in the Wooden Sleeve

Further below two screws attach the wooden sleeve to a metal plate of rectangular cross section. Near the bottom edge of this plate two strain gages are bonded onto the two opposite sides of the plate. Using two strain gages instead of only one for detecting only one strain enables to apply a valuable correction method.

It is known that every material changes its dimensions with temperature that means normally it will expand when heated up and contract when cooled down. However this ability is different for various materials and the strain gage is normally mounted on a specimen of a different material. From this follows that the temperature induced shape change of the specimen will mechanically induce a strain in the strain gage. This phenomenon is known as thermal output.

When the plate is bent it is assumed that the opposed strain gages show values of identical magnitude but different signs. Hence the sum of both strains is supposed to be zero. Every deviation from zero may be interpreted as induced from the thermal output and other error sources and must be subtracted from the measured strain values.

There are more influences that potentially alter the accuracy of a strain gage in a negative manner and a good summary is given in [4]. However after having talked to Dr Kara Peters, one of the strain gage experts at the MAE, it has turned out that none of these influences are

Lehrstuhl für Aerodynamik
Technische Universität München
Univ. Prof. Dr. Ing. N. Adams

TECHNISCHE
UNIVERSITÄT
MÜNCHEN

aer

valid for the strain gage application at hand. This is mainly due to the unproblematic operation conditions of the strain gages in the wind tunnel room. Even the just described thermal influence is probably so small that the results are not heavily affected. However it will turn out further below that this correction method is also good for other error sources.

Finally the metal plate is mounted to a support rack under the wind tunnel and hence the whole balance and the tinyTED are supported to the ground.
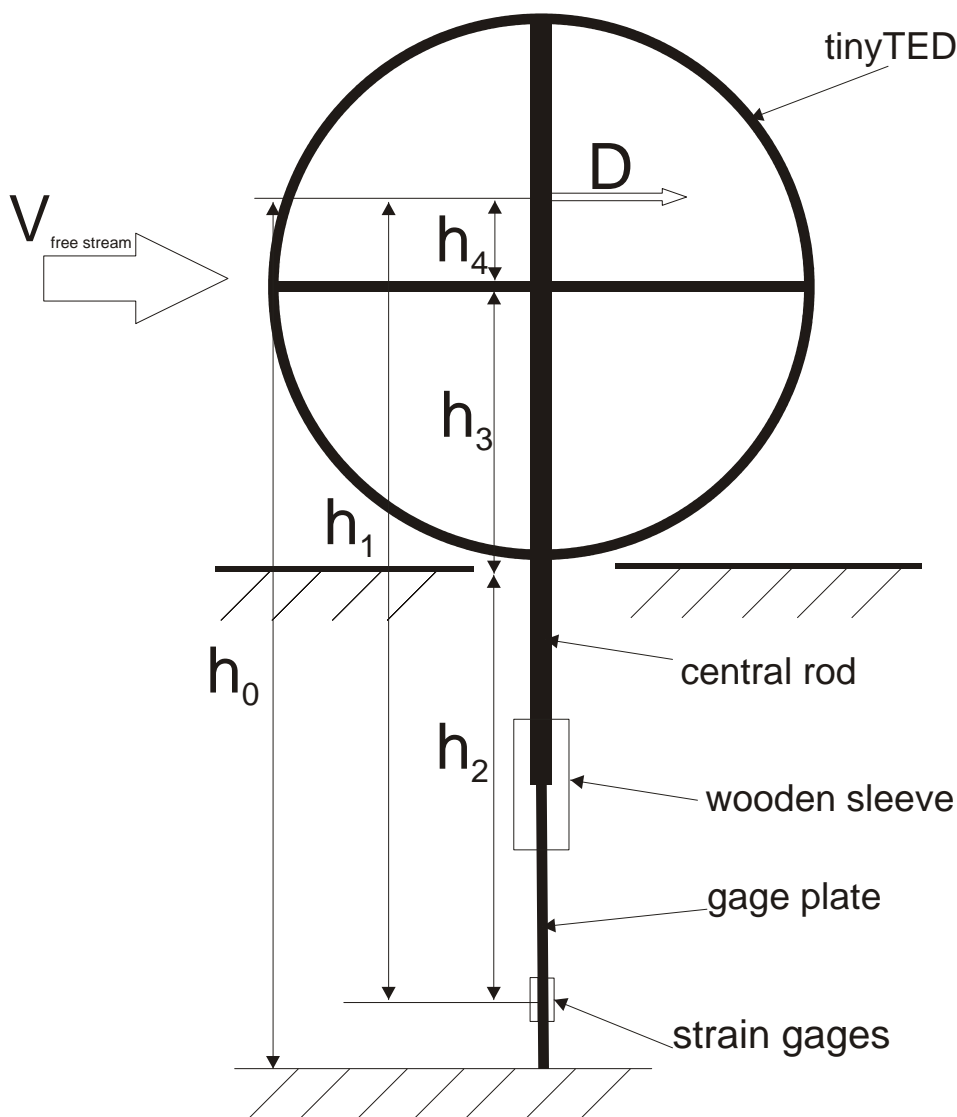
Figure 32 - Geometric Dependencies for the One Beam Balance

The drag component creates a bending moment relative to the strain gage locations:

$$\left(M_b\right)_{sg} = h_1 \cdot D \tag{4.7}$$

TECHNISCHE
UNIVERSITÄT
MÜNCHEN

Lehrstuhl für Aerodynamik
Technische Universität München
Univ. Prof. Dr. Ing. N. Adams

aer

The lever length h_1 consists of the three partial distances:

$$h_1 = h_2 + h_3 + h_4 \qquad (4.8)$$

h_2 :   distance from the tunnel's floor to the strain gages

h_3 :   distance from the tunnel's floor to the center of tinyTED (Assumption: Center of Gravity)

h_4 :   distance form the center of gravity to the drag force's center of effort

The gage plate has a rectangular cross section. Thereby a design rule for this kind of strain gage application is: $t \leq 0.1b$

The rectangular cross section has got the advantage that both strain gages can be mounted pretty exactly parallel to each other and pretty exactly perpendicular to the expected drag force direction. A circular cross section for example could not provide these features that easily.
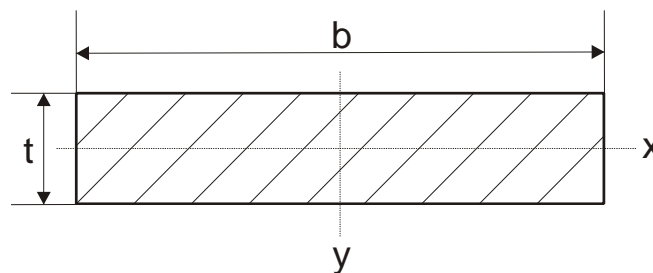
Figure 33 - Gage Plate Cross Section

The final values for the plate cross section are: $t = 3.7mm$ and $b = 50.7mm$.

The strain gages are bonded onto the plate's vertical center line. A further design rule requires that the free distances around the strain gages (e.g. the distance to supports or connections) is supposed to be six times the thickness of the plate: $l_{free} = 6 \cdot t$.

TECHNISCHE
UNIVERSITÄT
MÜNCHEN

Lehrstuhl für Aerodynamik
Technische Universität München
Univ. Prof. Dr. Ing. N. Adams

aer
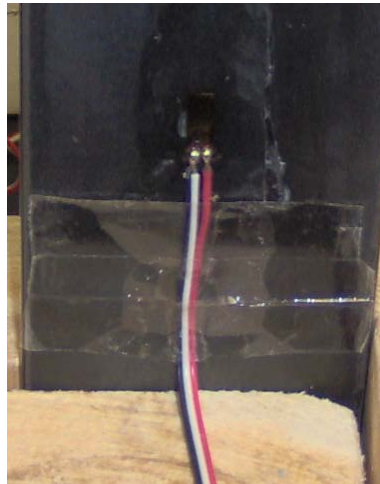
Figure 34 - Bonded Strain Gage

The geometrical moment of inertia of a rectangular cross section relative to the x-axis is:

$$I_{xx} = \frac{b \cdot t^3}{12} \tag{4.9}$$

The bending stress that is experienced by the beam's surface at the location h_1 and hence by the strain gages is given by:

$$\left(|\sigma_b|\right)_{sg} = \frac{\left(M_b\right)_{sg}}{I_{xx}} \cdot e_{max} \tag{4.10}$$

$$e_{max} = \frac{t}{2} \tag{4.11}$$

Combining the equations (4.9), (4.10) and (4.11) yields:

$$\left(|\sigma_b|\right)_{sg} = \frac{6 \cdot \left(M_b\right)_{sg}}{b \cdot t^2} \tag{4.12}$$

Stress and strain are associated by the Young's modulus:

$$\sigma = E \cdot \varepsilon \tag{4.13}$$

Finally the generated drag can be determined by combining the equations (4.7), (4.8), (4.12) and (4.13):

$$D = \frac{\varepsilon_{sg} \cdot E_{gage\ plate} \cdot b \cdot t^2}{6 \cdot \left(h_2 + h_3 + h_4\right)} \tag{4.14}$$

81

TECHNISCHE
UNIVERSITÄT
MÜNCHEN

Lehrstuhl für Aerodynamik
Technische Universität München
Univ. Prof. Dr. Ing. N. Adams

aer

For free stream conditions it is assumed that the resulting drag force attacks exactly in the center of the tTED: $h_4 = 0mm$.

It is assumed that the center of effort of the drag force onto the sail frame is located exactly in the center of the circular frame. Hence the lever length h_1 for the test frame can be measured easily, as well.

Eq.(4.14) still contains an unknown variable. However the strain ε_{sg} can be measured by the strain gage balance. It is related to the strain gages' resistance change by:

$$\varepsilon_{sg} = \frac{\Delta R / R_0}{GF \left(1 - K_t \cdot v_{plate} \right)} \tag{4.15}$$

GF :   gage factor

$\Delta R,\ R_0$:   resistance change, initial resistance

K_t :   factor for transverse sensitivity

v_{plate} :   coefficient of transversal contraction of the gage plate

The term $\left(1 - K_t v_{plate} \right)$ accounts for the fact that by applying a tension or compression load on the gage plate and thus on the strain gage there will also be an induced strain transverse to the main load directions. In order to get the strain only caused by the bending moment the detected strain must be corrected with the term mentioned above.

The resistance change ΔR can be determined with the principle of the so called Wheatstone bridge. Thereby three more resistances are connected to the strain gage (that is the unknown resistance R_x) to form a bridge circuit.

TECHNISCHE
UNIVERSITÄT
MÜNCHEN

Lehrstuhl für Aerodynamik
Technische Universität München
Univ. Prof. Dr. Ing. N. Adams

aer
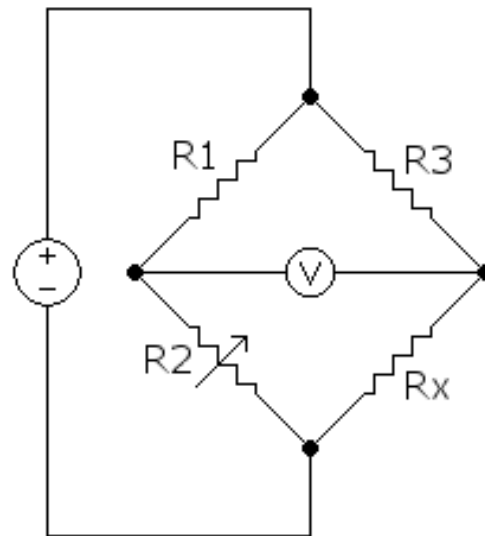
Figure 35 - Wheatstone Bridge from [30]

Now there are various possibilities to determine the unknown circuit. If one of the resistances is adjustable its value can be varied so that no voltage is detectible between the two legs. The unknown resistance then is $R_x = \dfrac{R_3 \cdot R_2}{R_1}$. If alternatively all three resistances are known (but fixed) the detected voltage between the two legs (output voltage) can be used in order to calculate the unknown resistance. This approach is much easier and faster for common microelectronic readout devices than adjusting a resistance.

Another problem evolves from the electrical connection of the strain gages to the readout device. The lead wires represent a further resistance added to the strain gage. This effect is known as desensitization but can be neglected for static measurements. However another effect must not be neglected and its description is again quoted from [4]:

"Temperature-induced leadwire errors are potentially much more serious than desensitization when static measurements are involved. Copper wire has a high temperature coefficient of approximately 0.22%/°F, and changes in temperature which affect the lead wires, will, therefore, cause a resistance offset or zero shift. As an indication of the magnitude of this effect, a temperature change of only 10°F in leadwires with an effective resistance of 1 Ohm would produce a resistance change of 0.022Ohm. This represents a zero shift of about 90 microstrain in a 120Ohm strain gage circuit." It must be added that the leadwires not only react to ambient temperature changes but are also affected by the friction of the flowing current.

TECHNISCHE
UNIVERSITÄT
MÜNCHEN

Lehrstuhl für Aerodynamik
Technische Universität München
Univ. Prof. Dr. Ing. N. Adams

aer

However there is a powerful method in order to deal with this problem. It is called the three-wire system. Hereby the following circuit is used:
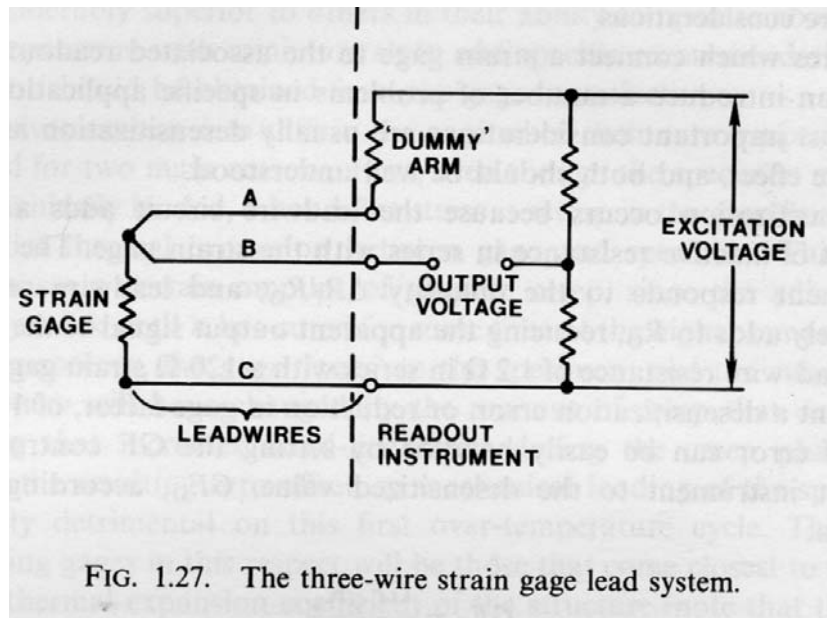
FIG. 1.27. The three-wire strain gage lead system.

Figure 36 - Three-Wire-Circuit from [5]

Wire A and C have to be of the same resistance. Wire A is in series with the active strain gage. Any resistance change that is due to temperature change now occurs simultaneously in the wires A and C and hence in both arms of the bridge. This simultaneous resistance change in the adjacent arms produces no bridge imbalance, however and thus there is no effect on the output voltage.

Fortunately the MAE disposes of a special strain gage read out computer. It is moveable and includes five strain gage interfaces. The whole circuitry is included in this interface device. The three-wire-wiring is also available in the MAE mechatronical lab. That means that eventually only the leadwires have to be soldered to the strain gages and then connected to the strain gage interface properly. The actual 3-wire-system soldered to the strain gage can be seen in fig.34.
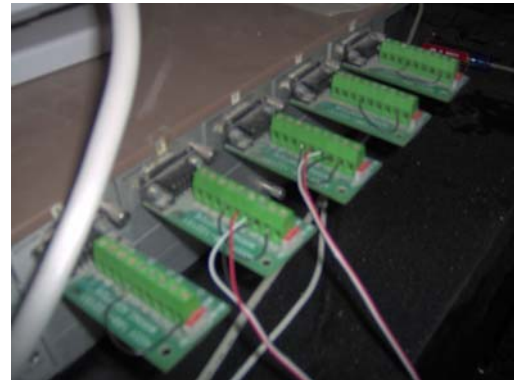
Figure 37 - Readout Computer (left) and Strain Gage Interfaces (right)

The software "StrainSmart™, Version 2.23" from the company Measurement Group Inc. is used to control the strain gage circuitry. This software requires the input of all necessary strain gage features like for example the gage factor or the transverse sensitivity. The features of the used strain gage are summarized in appendix 01. Once the software is provided with the necessary input it allows to translating the electrical signals of the strain gages into various kinds of data. For this thesis the transformation into strain was chosen. The software detected and recorded 10 data points per second during a period of 20 seconds. This data was then written into a text-file and transferred to a proper Excel®-sheet in order to convert it into the desired form. The software also allowed to zeroing the input signal before running the actual tests. Thereby the self-weight of the balance-article-assembly can be accounted for.

Finally the balance plate is supported by a wooden rack and tightened to this rack by a clamp. This rack is again mounted to another wooden rack that is standing on the ground. The yaw angle of the whole assembly is determined by measuring two distances to a row of ground plates that are assumed to be collinear with the wind tunnel.
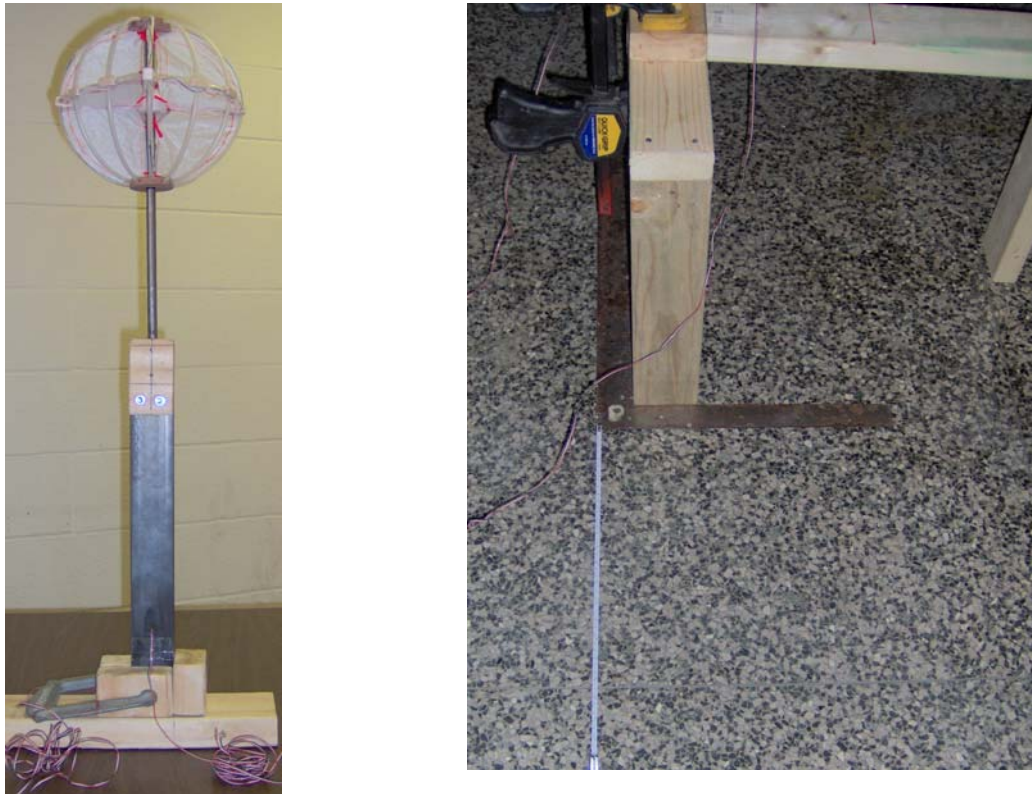
Figure 38 - Final One Beam Balance (left) and Yaw Angle Zeroing (right)

4.2.2 Calibration

For calibrating the balance the following accurate weights are used:

#	Mass [kg]
1	0.01
2	0.02
3	0.05
4	0.1
5	0.2
6	0.5
7	1
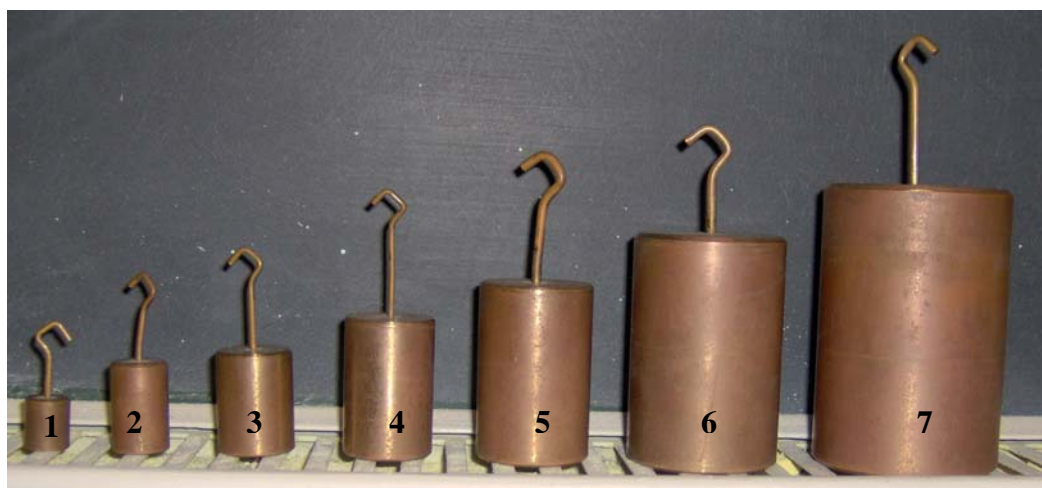
Figure 39 - Accurate Weights for Calibration

TECHNISCHE
UNIVERSITÄT
MÜNCHEN

Lehrstuhl für Aerodynamik
Technische Universität München
Univ. Prof. Dr. Ing. N. Adams

aer

The sail frame (see chapter 5.2) is mounted to the balance plate and a fishing line is mounted to the rod just below the frame. A pulley is mounted on the edge of the test section and the fishing line goes over this pulley through a hole in the wind tunnel test section (where normally the 6-component-balance reaches in). Thus various weights can be applied to the balance.

Figure 40 - Calibration Setup for the OBB

Every weight is applied to the end of the fishing line and a sample of 20 seconds is taken in terms of the measured strain on the gages. In the first place a 20 seconds sample is taken without any weight providing a zero reference. Hence there are two zeroing processes one performed by the software and one with the mentioned zero sample.

From all samples an arithmetic average value is gained. Theoretically the zero sample should provide an average value of zero. However that is not the case. Furthermore the two gages should provide values of equal magnitude but opposite sign. But this is not the case, either. There are several issues that may contribute to these errors.

First of all the strain gage balance was built manually by the author. Although trying very hard to mount two identical gages in terms of location and orientation the two gages are certainly not exactly mutually opposed. The whole balance rack was constructed manually, too and hence there may be deviations from the perfect case that exposes the two gages to slightly different load conditions and cause slightly different strains. The principle of the balance is based on the bending of the balance beam. However when bending the beam changes its orientation and so does the fishing line relative to the balance beam. These angles

87

are considered of being small. Nevertheless they will induce some small axial loads into the beam. Finally the strain gage itself is a very sensitive device and there could be some external boundary conditions that change randomly. For example a railway is passing through the campus whose trains cause some sensible vibrations while passing.

To account for all these error sources two further steps are taken, the first one is based on the thermal output correction method mentioned above. The strain values of each pair of samples are added. If the sum is different from zero this excess is considered as the strain induced by the error sources.

$$\varepsilon_1 + \varepsilon_2 = 0 + 2 \cdot \varepsilon_{error} \qquad (4.16)$$

It is assumed that both gages experience the exact same amount of error strain. Hence the excess is divided by two and this new value is subtracted from the strain value of both gages. These two new strain values are equal of magnitude and opposite in sign.

$$\varepsilon_1' = \varepsilon_1 - \varepsilon_{error} \qquad (4.17)$$

$$\varepsilon_2' = \varepsilon_2 - \varepsilon_{error} \qquad (4.18)$$

$$\varepsilon_1' = -\varepsilon_2' \qquad (4.19)$$

Secondly the average zero strain is subtracted from these strain values.

$$\varepsilon_0 = \frac{\varepsilon_{0.gage1} + \varepsilon_{0,gage2}}{2} \qquad (4.20)$$

$$\varepsilon_1'' = \varepsilon_1' - \varepsilon_0 \qquad (4.21)$$

$$\varepsilon_2'' = \varepsilon_2' - \varepsilon_0 \qquad (4.22)$$

The two strain values are now considered to be the bending strains at each gage.

A comparison between the applied loads and the measured loads is shown in the chart below. The process of calculating the measured load from the measured strains is described in chapter 4.2.1 above.

TECHNISCHE
UNIVERSITÄT
MÜNCHEN

Lehrstuhl für Aerodynamik
Technische Universität München
Univ. Prof. Dr. Ing. N. Adams

aer
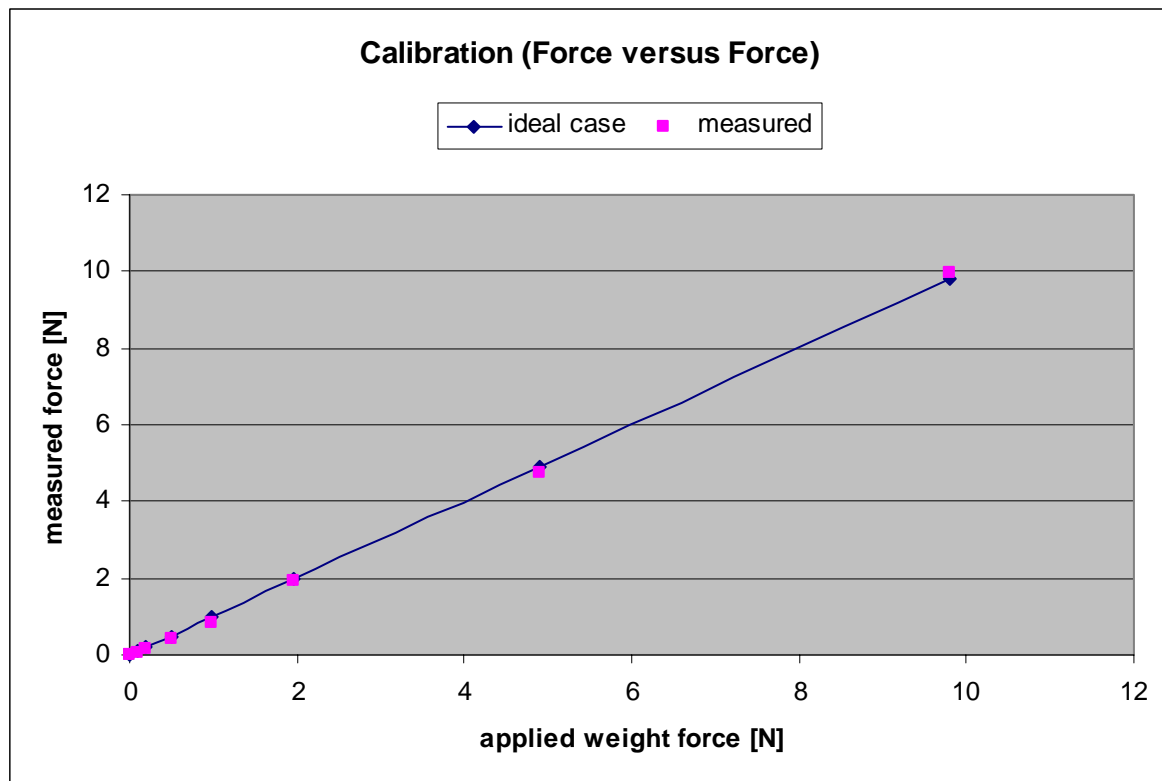
Figure 41 - Calibration Curve (Force versus Force)

The gained accuracy seems to be satisfying when considering the constraints and error sources mentioned above.

In order to get a calibration curve or function of the form $F = f(\varepsilon)$ a linear regression is conducted to the applied weight loads and the corresponding measured or converted strain values, respectively. The linear regression is explained in [23]. This method is able to assess to what extend there is a linear relation between two experimentally determined values. As can be seen from eq.(4.14), however the linear relation between the drag force and the measured strain can be assumed in the first place. That is why the linear regression is rather used to determine the linear function of the two variable strain and force that are already assumed as being mutually linear dependent.

The linear function has the form:

$$F(\varepsilon) = \tilde{a} + \tilde{b} \cdot \varepsilon \tag{4.23}$$

$$\tilde{a} = \bar{F} - \tilde{b} \cdot \bar{\varepsilon} \tag{4.24}$$

$$\overline{F} = \frac{1}{n}\sum_{i=1}^{n} F_i \qquad (4.25)$$

$$\overline{\varepsilon} = \frac{1}{n}\sum_{i=1}^{n} \varepsilon_i \qquad (4.26)$$

$$\tilde{b} = \frac{\sum_{i=1}^{n}\left(\varepsilon_i - \overline{\varepsilon}\right)\left(F_i - \overline{F}\right)}{\sum_{i=1}^{n}\left(\varepsilon_i - \overline{\varepsilon}\right)} \qquad (4.27)$$

The actual calculation is again conducted by an Excel®-sheet. Thus the equation for the calibrating curve is gained to:

$$F\left(\varepsilon\right) = 0.0476\frac{N}{microstrain}\cdot\varepsilon + 0.087N \qquad (4.28)$$
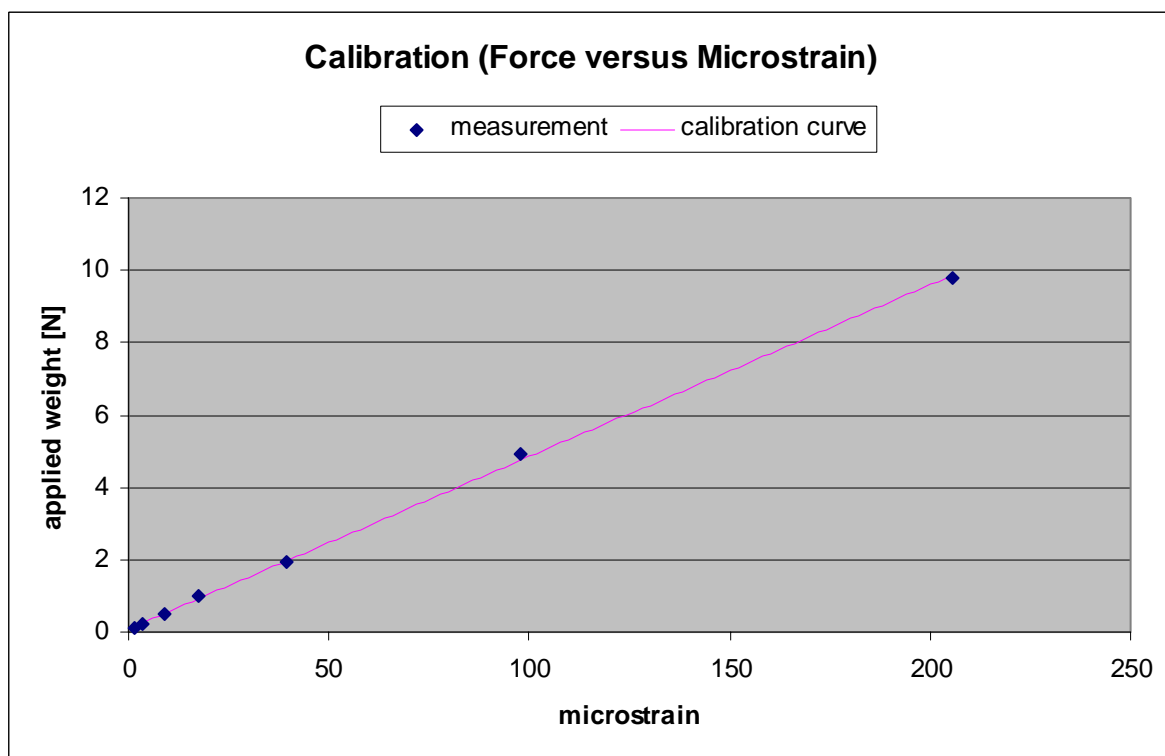
Figure 42 - Calibration Curve (Force versus Microstrain)

TECHNISCHE
UNIVERSITÄT
MÜNCHEN

Lehrstuhl für Aerodynamik
Technische Universität München
Univ. Prof. Dr. Ing. N. Adams

aer

The balance may also be used for setups that have a different lever length than the calibration setup. For example the single frame has got a different lever arm for its resulting drag force than the tinyTED. As a function of the resulting drag force the bending moment depends linearly on the lever arm, though. Hence eq.(4.28) may be adjusted by the ratio of the lever arms:

$$F(\varepsilon) = \left(0.0476 \frac{N}{microstrain} \cdot \varepsilon + 0.087N \right) \cdot \frac{l_{lever\ calibration}}{l_{lever\ new}} \tag{4.29}$$

The lever arm for the calibration process is: $l_{lever\ calibration} = 807mm$.

4.3 tTED in the NCSU Subsonic Wind Tunnel

The two original main purposes for building the tTED were to use it in the NCSU wind tunnel and in an improvised smoke channel. Thus the aerodynamic characteristics like drag or pitching moment were supposed to be measured. Additionally the wake flow field that is the wake vortices were supposed to be visualized by the smoke channel.

The first measurements were conducted in the NCSU wind tunnel using its standard six component balance. The pitch angle was varied from $\alpha = 0°\ to\ -10°$ in steps of $\Delta\alpha = -2°$.

The desired Reynolds number range in order to simulate Martian conditions is given in chapter 2.2.2 to $1.5 \cdot 10^4 < \mathrm{Re}_{TW} < 1.25 \cdot 10^5$ and a condition for the dynamic similarity of the flow is the matching of the Reynolds numbers: $\mathrm{Re}_{TW} = \mathrm{Re}_{tTED}$.

TECHNISCHE
UNIVERSITÄT
MÜNCHEN

Lehrstuhl für Aerodynamik
Technische Universität München
Univ. Prof. Dr. Ing. N. Adams

aer

Therefore the first test runs took place at the following very low dynymic pressures in order to match this Reynolds number range:

q [psf]	q [Pa]
0.02	0.9576
0.03	1.4364
0.05	2.394
0.07	3.3516
0.09	4.3092
0.11	5.2668
0.13	6.2244

Table 13 - Dynamic Pressure Range for the First Wind Tunnel Test Runs

Those are very low dynamic pressures and as mentioned in chapter 2.3 the displayed error tolerance of the stagnation pressure is already $\Delta q = 0.01 psf$. Furthermore the balance accuracy at these low dynamic pressures and forces is unclear and so is the uniformity of the free stream. Consequently the drag coefficients show an oscillating behavior.
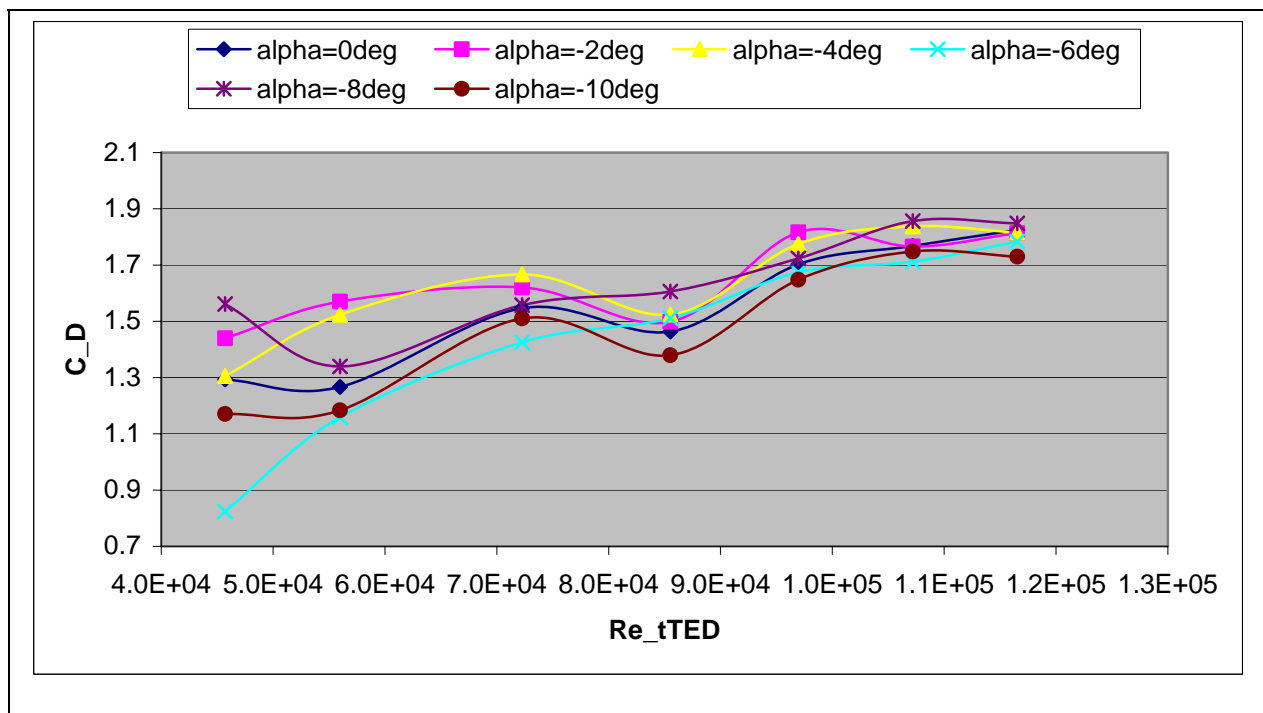
Figure 43 - Drag Coefficient of tTED at Very Low q

TECHNISCHE
UNIVERSITÄT
MÜNCHEN

Lehrstuhl für Aerodynamik
Technische Universität München
Univ. Prof. Dr. Ing. N. Adams

aer

From this chart it is concluded that the chosen dynamic pressure range does not yield reasonable results. The values oscillate a lot and the drag coefficient is rising with increasing Reynolds number. Hence it was decided to increase the dynamic pressure range considerably.

q [psf]	q [Pa]
0.05	2.394
0.3	14.364
0.6	28.728
0.9	43.092
1.2	57.456
1.5	71.82
1.8	86.184
2.1	100.548
2.4	114.912

Table 14 - Dynamic Pressure Range for Second tTED Test Runs

These numbers correspond to a Reynolds number range of about $7.2 \cdot 10^4 < \mathrm{Re}_{tTED} < 5 \cdot 10^5$
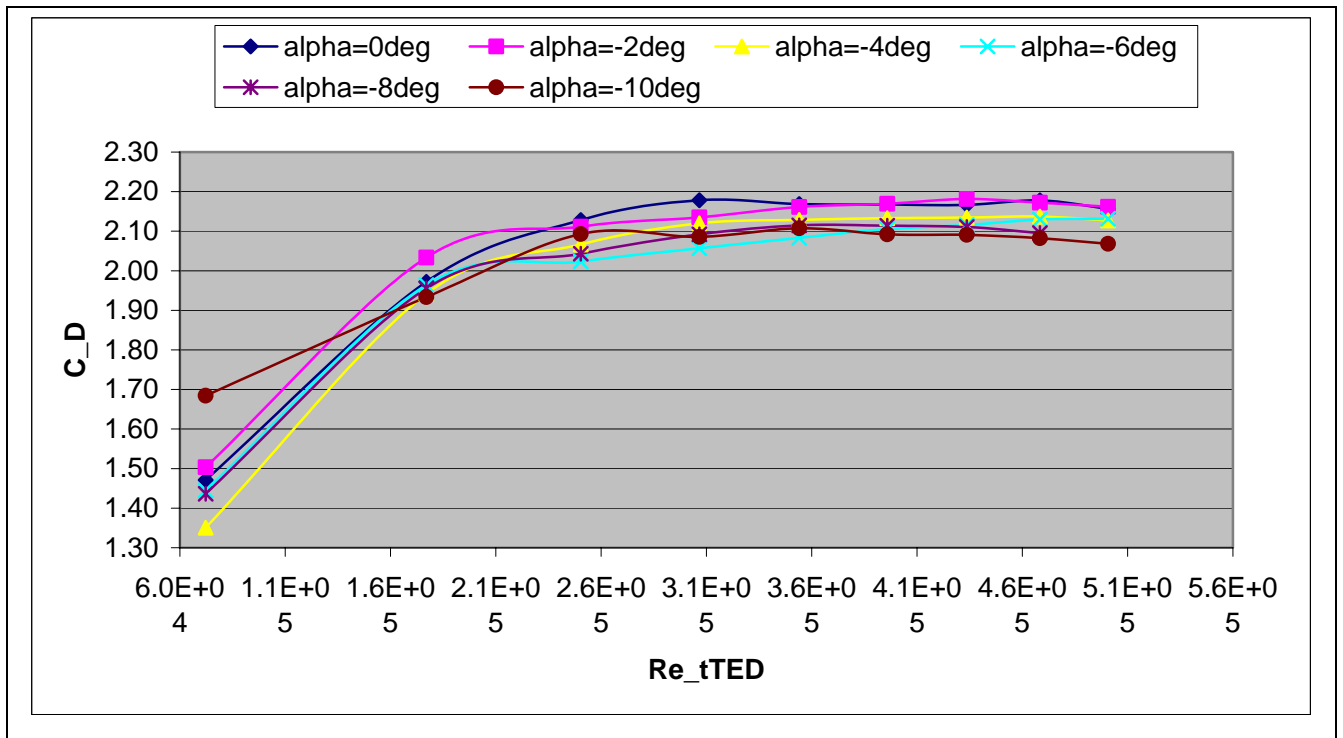
Figure 44 - Drag Coefficients of tTED for different Pitch Angles

TECHNISCHE
UNIVERSITÄT
MÜNCHEN

Lehrstuhl für Aerodynamik
Technische Universität München
Univ. Prof. Dr. Ing. N. Adams

aer

These curves look more reasonable. Though the achieved Reynolds number range is beyond the expected Martian range a special feature of blunt bodies gives rise to the assumption that the results may be realistic. Therefore it is assumed that the tTED will behave similar to a flat disk perpendicular to the free stream. From reference [26] a typical drag coefficient curve for a flat disk normal to the free stream is shown:
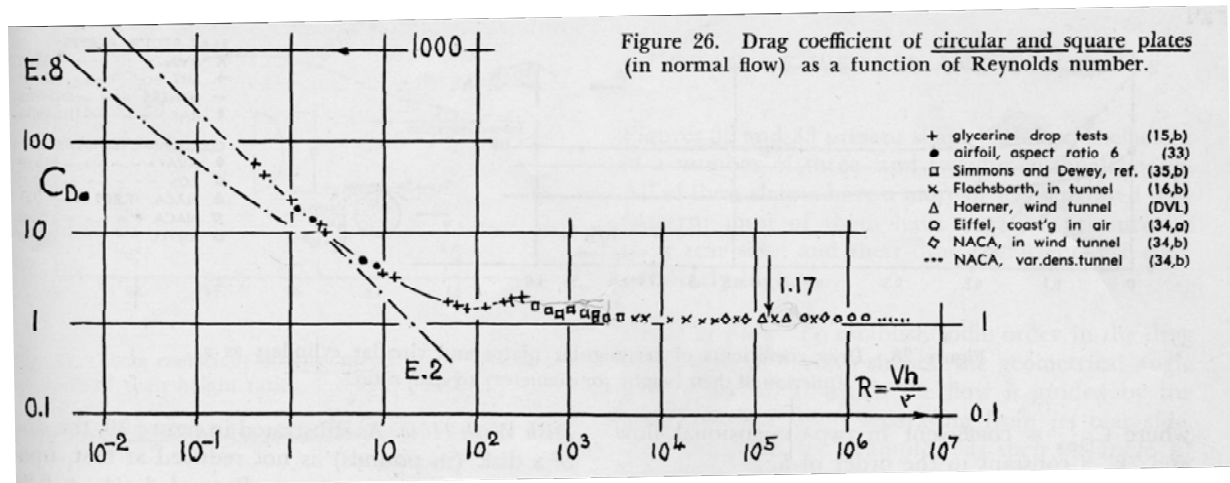
Figure 45 - Typical Drag Coefficient Chart for a Disk Perpendicular to the Free Stream from [26]

Comparing the both charts two attributes stand out. Figure 45 shows that from a sufficiently high Reynolds number on the drag coefficient becomes independent from the Reynolds number. This behavior can also be observed in figure 44 from $q = 0.6\,psf$ on. However for $q = 0.3\,psf$ the drag coefficient does not deviate too much. Hence it is not clear if the deviation is due to the balance constraints or the non-uniform free stream.

The second striking attribute is the large magnitude of the drag coefficient in figure 44. Leaving out the both lowest stagnation pressures (the reason for that is given in chapter 4.5) the average drag coefficient for a pitch angle of zero is $\bar{C}_D \left(a = 0° \right) = 2.16$. Compared to the values from reference [26] these values appear to be far too high even when considering that the material of the sails and the geometry of the tTED deviate from the ideal case of a flat disk.

This difference between the reference values and the measured values seems to violate the previous assumption that even a blockage factor of $BF_{tTED} = 0.1353$ may yield somewhat meaningful results. The maximum value from [2] might be too high for the NCSU wind tunnel and after a consultation with Dr. Pernpeintner from the Department of Aeroydnamics

Lehrstuhl für Aerodynamik
Technische Universität München
Univ. Prof. Dr. Ing. N. Adams

TECHNISCHE
UNIVERSITÄT
MÜNCHEN

of the Technical University of Munich the new maximum blockage factor was assumed to be $BF_{\max} = 0.05$.

Hence it seemed to be necessary to design and build a second model that meets this new important requirement.

4.4 Subscale Model tinyTED2 (tTED2)

The search for appropriate materials for the first subscale model, the tinyTED has shown that it is not easy to find good materials for a reasonable price. Furthermore the geometry of the TED gives reason to the assumption that the most important scale ratio concerns the sail planes. The ratio between the pipe diameter and the model diameter seems to be of less importance. Moreover the aerodynamic relevance of the side rings of the outer structure appears to be small.

For all these reasons it was decided to build another smaller subscale model on the base of the previous tTED. The pipe, strut, hub and connector materials are the same like at the tTED. In addition the hub design and construction is copied from the tTED and so is the center piece design and the rod bypass for the 6CB. Taking the same pipes like for the tTED enlarges the coverage of the sail planes by the pipes' cross section. Therefore it was decided to abandon the side rings at the tTED2.

In the version for the OBB again the wooden center strut was replaced by a metal center strut that reaches trough one of the hubs. At the end of this strut three holes were drilled in. They allow to adjusting the yaw angle of the tTED2 to $\beta_{tTED2} = 0°$, $\beta_{tTED2} = 22.5°$ and $\beta_{tTED2} = 45°$.

The tTED2 has got an outer diameter of $d_{tTED2} = 0.2m$ and thus a diameter ratio relative to the TED of:

$$\frac{d_{tTED2}}{d_{TED}} = \frac{0.2m}{3m} = \frac{1}{15} = 0.0667 \qquad (4.30)$$

The ratio of the pipe diameters is still

$$\frac{d_{tTED,pipes}}{d_{TED,pipes}} = \frac{4.76mm}{33mm} = 0.144 \qquad (4.31)$$

TECHNISCHE
UNIVERSITÄT
MÜNCHEN

Lehrstuhl für Aerodynamik
Technische Universität München
Univ. Prof. Dr. Ing. N. Adams

aer

That is why the geometric similarity has worsened.

The tTED2 reference sail surface is calculated to

$$S_{tTED2} = \frac{\pi}{4} d_{tTED2}^2 = 0.0314 m^2 \tag{4.32}$$

yielding a new blockage factor of

$$BF_{tTED2} = \frac{S_{tTED2}}{A_{test\ section}} = 0.034 \tag{4.33}$$

This new blockage factor stays clearly below the assumed maximum of $BF_{max} = 0.05$ and gives reason to the expectation that this time the test results should yield more reasonable values.

Figure 46 - Second Subscale Model tinyTED2

4.5 tinyTED2 in the NCSU Subsonic Wind Tunnel

The tinyTED2 was mounted on the 6-component balance and measurements were conducted. Since the values of the force and especially the drag coefficient appeared to be much more realistic this time the test extent was broadened. With the 6-component balance a wider range of pitch and yaw angles was tested and additionally the tTED2 was mounted on the OBB near the wind tunnel baseplate. The initial state at this balance is a pitch angle of $\alpha = 0°$ and a defined yaw angle. In order to determine this pitch angle before the tests a digital level was used. If the angle deviated more than $\Delta\alpha_{tTED2} = 0.1°$ from the zero state the orientation of the

TECHNISCHE
UNIVERSITÄT
MÜNCHEN

Lehrstuhl für Aerodynamik
Technische Universität München
Univ. Prof. Dr. Ing. N. Adams

aer

wooden balance rack was changed by using wooden wedges on the floor. Thus the initial pitch angle was very close to zero every time. However as described in chapter 4.2 the OBB is based on the bending of a metal plate. That is why also the tTED2 changes its orientation slightly with increasing stagnation pressure. However the optical observation during the tests gave reason to the assumption that this change is only very small.

Figure 47 - Initial Pitch Angle Determination and Adjustment of the tTED2

4.5.1 Assessment of the 6-Component-Balance Data

The tests with the tTED2 in the NCSU wind tunnel were conducted at the following dynamic pressures:

q [psf]	q [Pa]
0.2	9.576
0.4	19.152
0.6	28.728
0.8	38.304
1.0	47.88
1.2	57.456
1.4	67.032
1.6	76.608
1.8	86.184

Table 15 - Dynamic Pressures for the tTED2

These pressures correspond to a Reynolds number range of about $7 \cdot 10^4 < \mathrm{Re}_{tTED2} < 2.2 \cdot 10^5$.

With the 6-component-balance the following drag coefficients were measured for $\alpha = 0°$ and $\beta = 0°$. That is why the measured drag force equals the measured force in the x-direction:
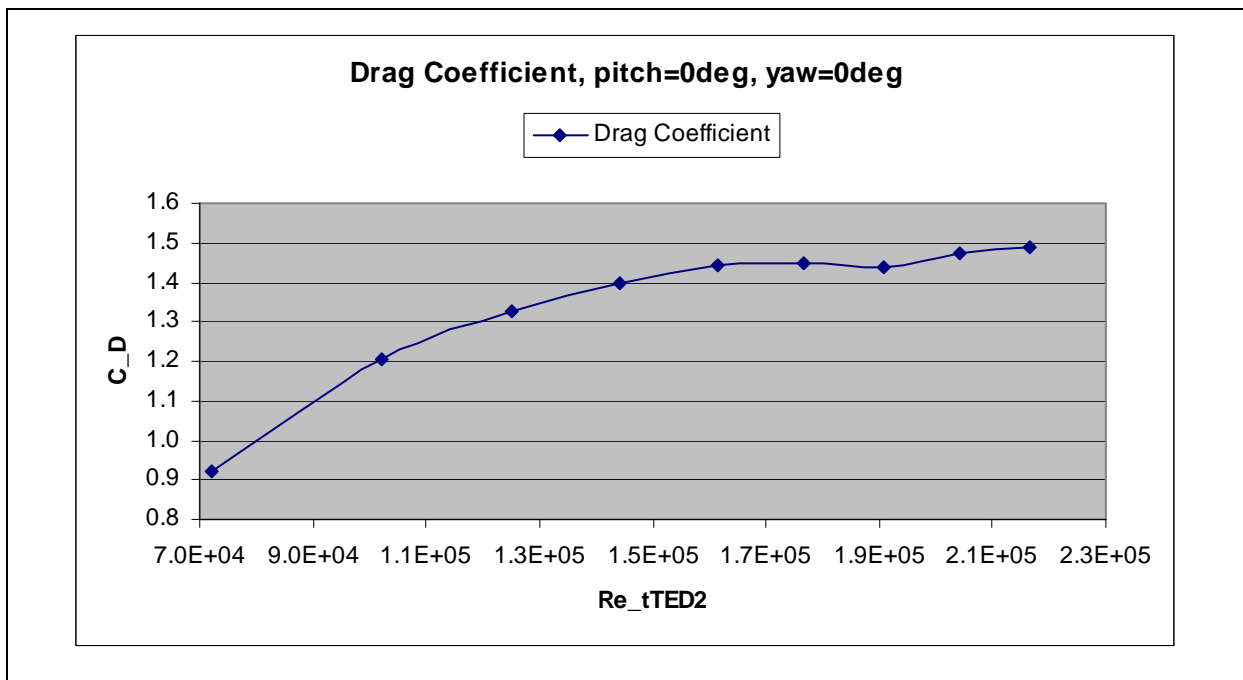
Figure 48 - Drag Coefficient of the tTED2 on the 6CB, Alpha=0°, Beta=0°

TECHNISCHE
UNIVERSITÄT
MÜNCHEN

Lehrstuhl für Aerodynamik
Technische Universität München
Univ. Prof. Dr. Ing. N. Adams

aer

In order to assess the accuracy of the 6-component-balance in terms of the reliably detectable minimum force the drag coefficients of the tTED and the tTED2 are compared with respect to the applied dynamic pressure.
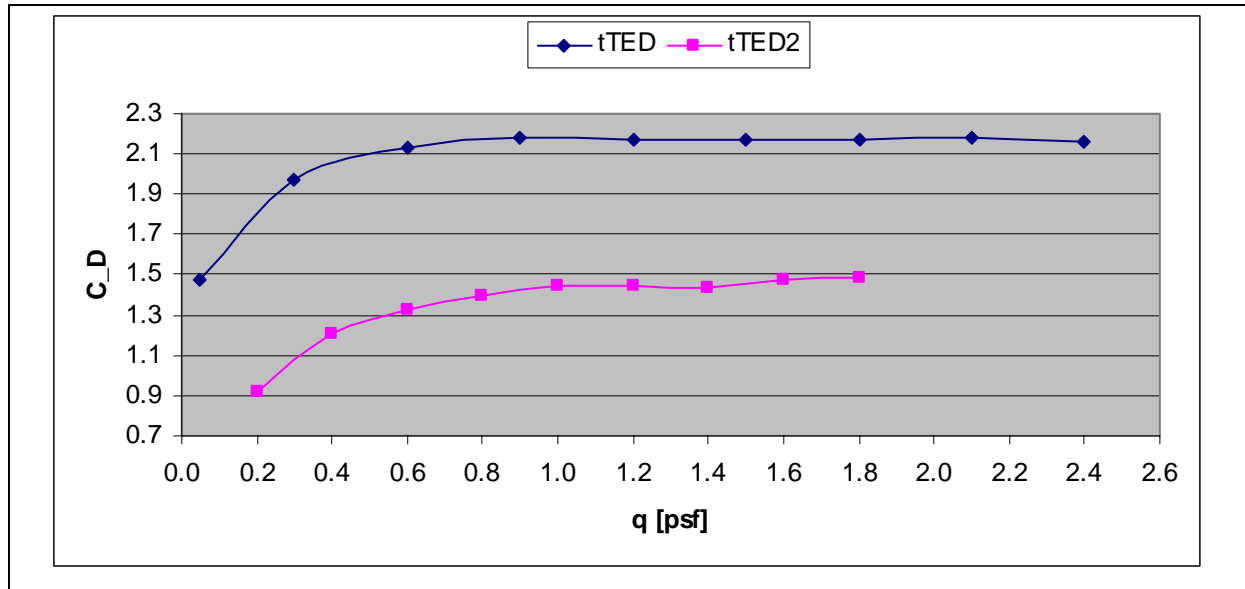
Figure 49 - Drag Coefficients of the tTED and tTED2 at Alpha=0° and Beta=0°

As criterion for the minimum detectible force the Reynolds number independence of the drag coefficient form fig.45 is chosen. In the chart above this independence seems to be achieved for the stagnation pressures of $q_{tTED} = 0.6 psf$ and $q_{tTED2} = 1.0 psf$. The corresponding measured forces are $D_{tTED}(q = 0.6 psf) = 7.68N$ and $D_{tTED2}(q = 1.0 psf) = 2.17N$. These values differ considerably. It is assumed that the reason for this behavior is in the flow field that can be provided for the different stagnation pressures. Additionally the 6-component-balance rod is disturbing the wake flow of the models. In order to account for these influences and in order to evaluate them the equivalent run with the OBB is consulted.

TECHNISCHE
UNIVERSITÄT
MÜNCHEN

Lehrstuhl für Aerodynamik
Technische Universität München
Univ. Prof. Dr. Ing. N. Adams

aer
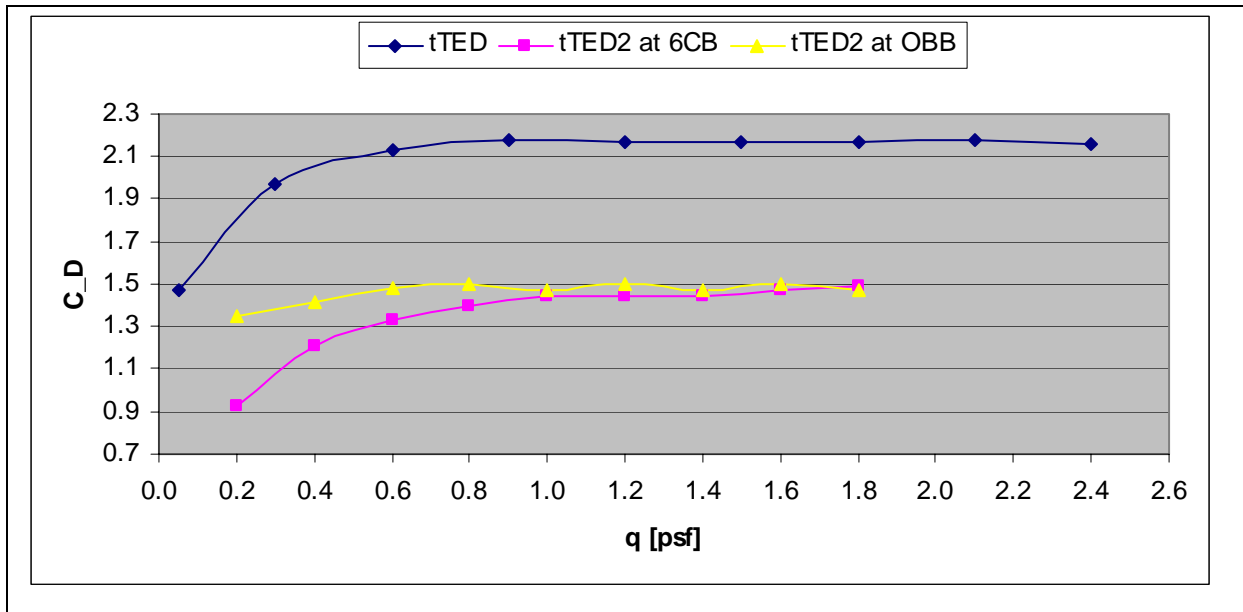
Figure 50 - C_D for tTED and tTED2 at Different Balances at Alpha=0° and Beta=0°

From this chart the following conclusions are drawn:

The drag coefficient for the investigated Reynolds number regime ($7 \cdot 10^4 < \mathrm{Re}_{tTED}, \mathrm{Re}_{tTED2} < 5 \cdot 10^5$) is assumed to be Reynolds number independent. From this fact it is concluded that the wind tunnel provides a sufficiently uniform flow from $q_{\min} = 0.6\,psf$ on, concluded from the tTED chart and the OBB-tTED2 chart. Especially below the value of $q = 0.3\,psf$ it seems not to be justified to assume an uniform flow. The tTED2-chart for the 6-component-balance however only shows the desired Reynolds number independence from $q = 1.0\,psf$ on. The force magnitude at this dynamic pressure is $D_{tTED2,6CB}\left(q = 1.0\,psf\right) = 2.17N$. The dynamic pressure value from which on the 6CB yields a solid force measurement may be somewhere between $q = 0.8\,psf$ and $q = 1.0\,psf$. Therefore it is approximated that the 6-component-balance is able to reliably detect a minimum force of $F_{6CB,\min} = \pm 2.0N$. These both values for the minimum dynamic pressure and the minimum force are the base for the further investigations.

TECHNISCHE
UNIVERSITÄT
MÜNCHEN

Lehrstuhl für Aerodynamik
Technische Universität München
Univ. Prof. Dr. Ing. N. Adams

aer

The investigated dynamic pressures that are assumed to be able to yield solid data for the tTED2 are:

q [psf]	q [Pa]
0.6	28.728
0.8	38.304
1.0	47.88
1.2	57.456
1.4	67.032
1.6	76.608
1.8	86.184

Table 16 - Dynamic Pressures Assumed to Provide an Uniform Flow Field for the tTED2

Especially the minimum force has a major impact on the 6CB measurements. The balance is actually capable to measure forces in all three space directions and moments about all three space directions. The accuracy of the moment coefficients for the test conditions at hand is also unclear. Since there is no means that could be conducted within the scope of this thesis to determine this accuracy the moment coefficients will not be investigated.

As per chapter 2.4 the aerodynamic forces drag, lift and side force must be calculated from the measured values of the corresponding axial forces $F_{x'}, F_{y'}, F_{z'}$. Thereby the actual condition for a solid coefficient for the drag, lift and side force would be that every contributing force component matches or exceeds the minimum force $\left| F_{6CB,\min} \right| = 2N$. A corresponding assessment is conducted in appendix 05. It shows that in no case all three components reach the minimum value at the same time. Moreover the component in the z'-direction even never reaches the minimum value. Hence *the following decisions are made in order to relax the minimum force condition*:

As per eq.(2.65) the drag coefficient depends mainly on the component $F_{x'}$ for the yaw and pitch angles at hand. That is why the drag coefficient is taken into account for every orientation that meets the minimum force requirement for $F_{x'}$.

As per eq.(2.66) the side force coefficient depends mainly on the component $F_{y'}$ for the pitch and yaw angles at hand. That is why the side force coefficient can only be considered to yield

TECHNISCHE
UNIVERSITÄT
MÜNCHEN

Lehrstuhl für Aerodynamik
Technische Universität München
Univ. Prof. Dr. Ing. N. Adams

aer

realistic data for all cases in which the component $F_{y'}$ meets the requirement of the minimum force.

As per eq.(2.67) the lift force coefficient depends mainly on the component $F_{z'}$ for the pitch and yaw angles at hand. Therefore it is decided not to investigate the lift coefficient because the component $F_{z'}$ can never meet the requirement of the minimum force.

After this somewhat complicated assessment of the solid data gained by the 6-component-balance the force coefficients of the drag and side force will be presented now.

4.5.2 Drag Force Coefficients for the tTED2

The average drag coefficients $\bar{C}_D$ are taken over the Reynolds number ranges or dynamic pressure ranges, respectively for the given orientation. The reason for this averaging process is again the theoretical prediction from fig.45 that the drag coefficient of a blunt body does not change with increasing Reynolds number from a certain Reynolds number on. This assumption is approved by some of the following charts, too.
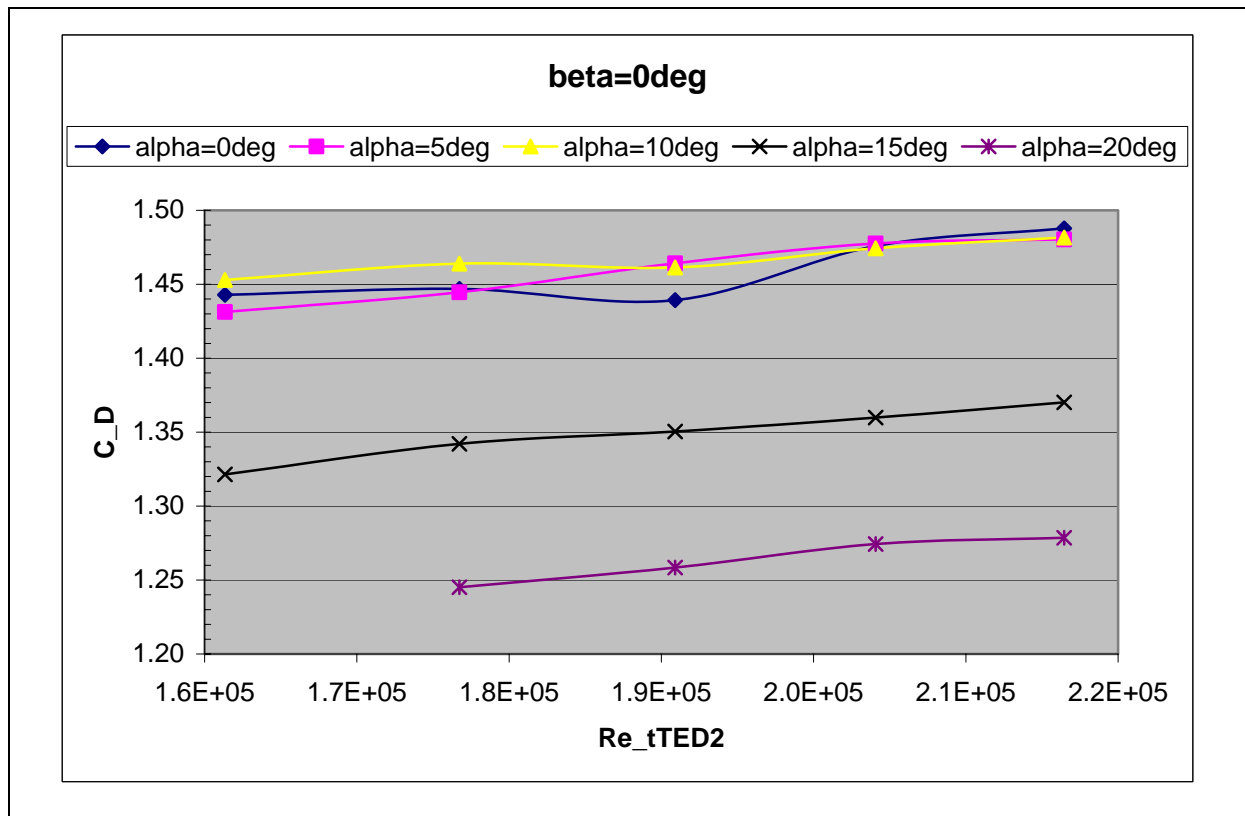
Figure 51 - C_D tTED2 for Beta=0°, Changing Re, Changing Alpha, measured with the 6CB

TECHNISCHE
UNIVERSITÄT
MÜNCHEN

Lehrstuhl für Aerodynamik
Technische Universität München
Univ. Prof. Dr. Ing. N. Adams

aer

In the figure above it stands out that the drag coefficient is still rising slightly with increasing Reynolds number. Therefore the basic assumption to reduce the TW design to a simple flat plate normal to the free stream does not hold true completely. Of course the two other planes that are not perpendicular but rather in parallel to the free stream (at least for $\alpha = 0°$ and $\beta = 0°$) certainly alter the flow field.

It is pointed out again that the tTED2 was constructed manually and so were the sail attachments. Even though an effort was made to attach the sails as tight as possible they still deformed and camber a little with increasing stagnation pressure. In chapter 5 it is described that the drag coefficient rises for a cambered plate perpendicular to the free stream. This cambering effect might be the reason for the still rising drag coefficient with rising Reynolds number.

In terms of the absolute magnitude however the results seem to be reasonable.

For this assessment also a chart from reference [29] will be quoted. In this paper the aerodynamic investigation of different tumbleweed designs is presented. It must be mentioned that the relevant boxkite model had not the same zero orientation like in this thesis. In fact it was mounted like in the following picture. Hence it will approach the initial state of the tTED2 ($\alpha = 0°, \beta = 0°$) with increasing pitch angle.
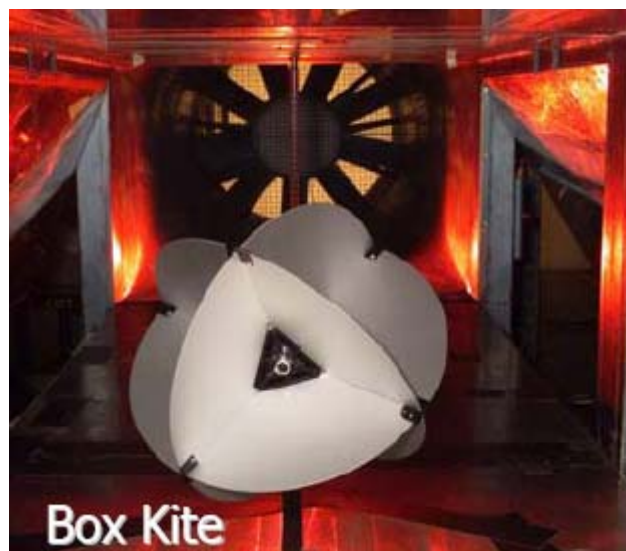
Figure 52 - Boxkite Model from [29]

The model was investigated for a flow velocity of $V = 12.192\,m/\sec\,(40\,ft/\sec)$ and it had a diameter of $d_{model} = 304.8mm\,(1ft)$.
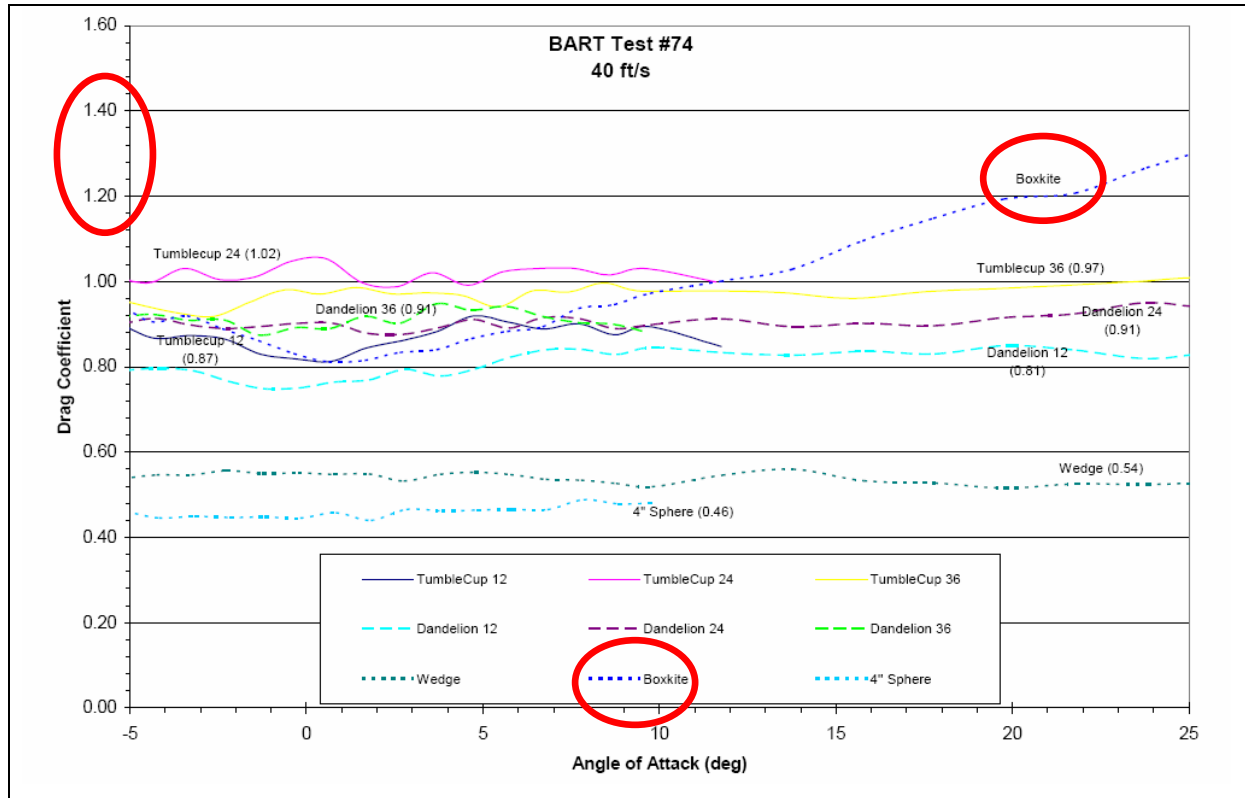
Figure 53 - Drag Coefficient for Different Tumbleweed Models from [29]

It can be seen that the drag coefficient approaches the tTED2-values for a rising pitch angle and therefore for approaching the zero orientation $(\alpha = 0°, \beta = 0°)$ of the tTED2. Due to the lack of a better knowledge about the initial orientation of the model a closer comparison between this data and the tTED2 is not pursued. Indeed it is interesting to see that the boxkite drag coefficient approaches the range of the $C_{D,tTED2}$ with increasing angle of attack. The magnitude of the drag coefficient measurements for the tTED2 seems to be realistic.

Another striking feature of fig.51 is the behavior of the curves for $\alpha = 0°, \alpha = 5°$ and $\alpha = 10°$. There is hardly any difference between their developing. Although it is expected that the orientation of $\alpha = 0°$ should yield a maximum drag because then the surface normal to the free stream is maximum. The reason for this may again be seen in the manual construction of the model. From that a certain lack in the required symmetry could result and hence the maximum could be shifted. Then however a pronounced drop occurs for $\alpha = 15°$ and

104

TECHNISCHE
UNIVERSITÄT
MÜNCHEN

Lehrstuhl für Aerodynamik
Technische Universität München
Univ. Prof. Dr. Ing. N. Adams

aer

$\alpha = 20°$. The assumed explanation for this behavior is given further below. Taking the averages allows to depicting the behavior in an even more clearly manner.

$\alpha\,[°]$	$\bar{C}_D$
0	1.459
5	1.46
10	1.47
15	1.35
20	1.26

Table 17 - C_D_avrg tTED2 for Beta=0°

Additionally it must be pointed out that the absolute difference between $\alpha = 0°$ and $\alpha = 10°$ in terms of the drag coefficient is only $\Delta \bar{C}_D = 0.011$. So the reason for this unexpected behavior may also be found in the constraints and uncertainties of the used balance that is described in the subchapter above.
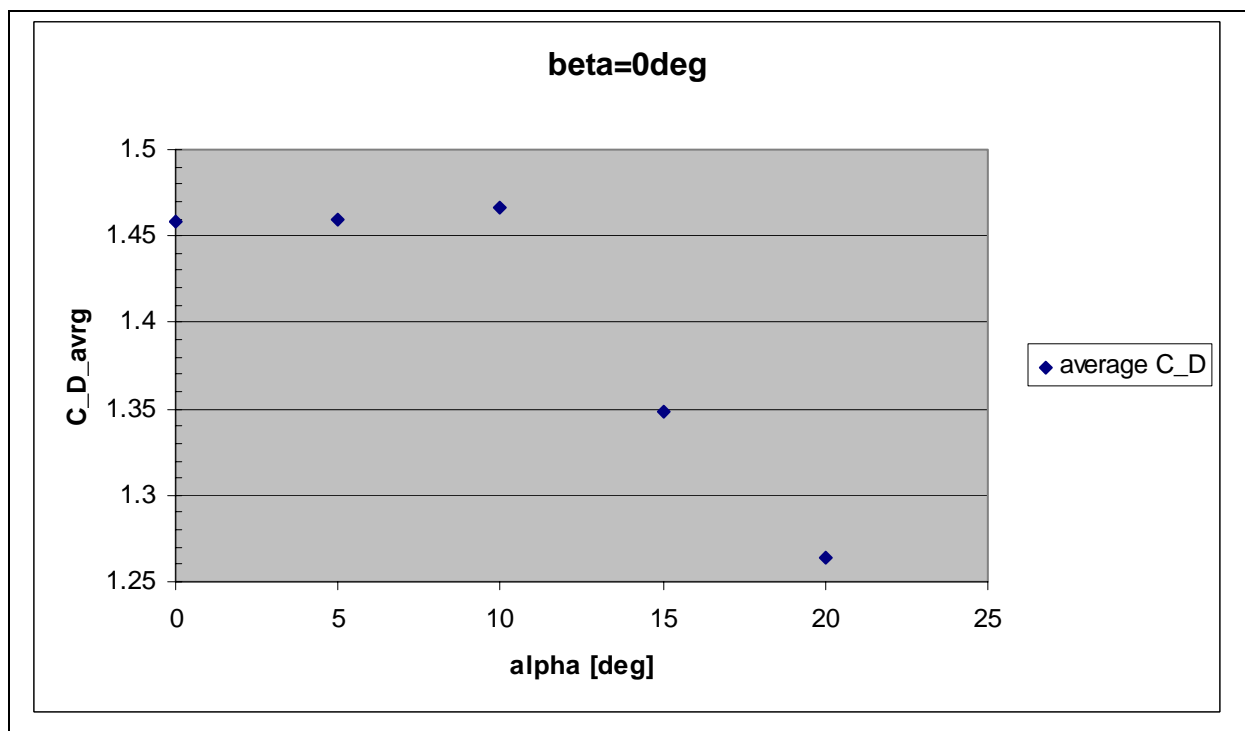
Figure 54 - C_D tTED2 for q=1.2 and Beta=0deg, Changing Alpha
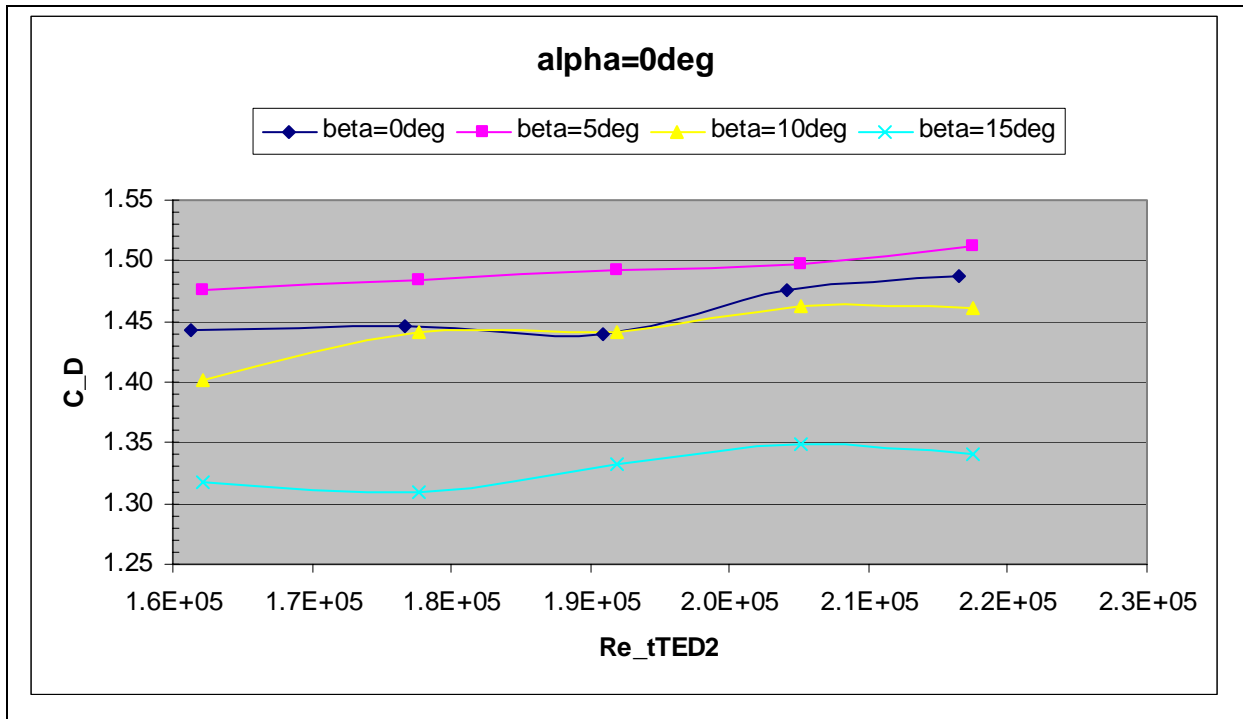
Figure 55 - C_D tTED2 for Alpha=0°, Changing Beta, Changing Re_tTED2, Measured with 6CB

For reasons of symmetry the general behavior of the drag coefficients for the cases $\beta = const., \Delta\alpha$ and $\alpha = const., \Delta\beta$ should not be different at all. However the figure above shows a somewhat larger drag coefficient for a yaw angle of $\beta = 5°$ than for the adjacent orientations of $\beta = 0°$ and $\beta = 10°$. In addition to the reasons given for the α-deviation above this time the angle adjustment mechanism must be considered, too. As mentioned in chapter 2.3 its accuracy is expected to be within $\Delta\beta = \pm 1°$. Thus all these factors may contribute to the unexpected drag coefficient developing between $\beta = 0°$ and $\beta = 5°$.

$\beta[°]$	$\bar{C}_D$
0	1.459
5	1.49
10	1.44
15	1.33

Table 18 - C_D_avrg tTED2 for Alpha=0°

Taking the average drag coefficients it can be shown again that the absolute difference between the two orientations $\beta = 0°$ and $\beta = 5°$ is relatively small namely $\Delta\bar{C}_D = 0.021$.

TECHNISCHE
UNIVERSITÄT
MÜNCHEN

Lehrstuhl für Aerodynamik
Technische Universität München
Univ. Prof. Dr. Ing. N. Adams

aer
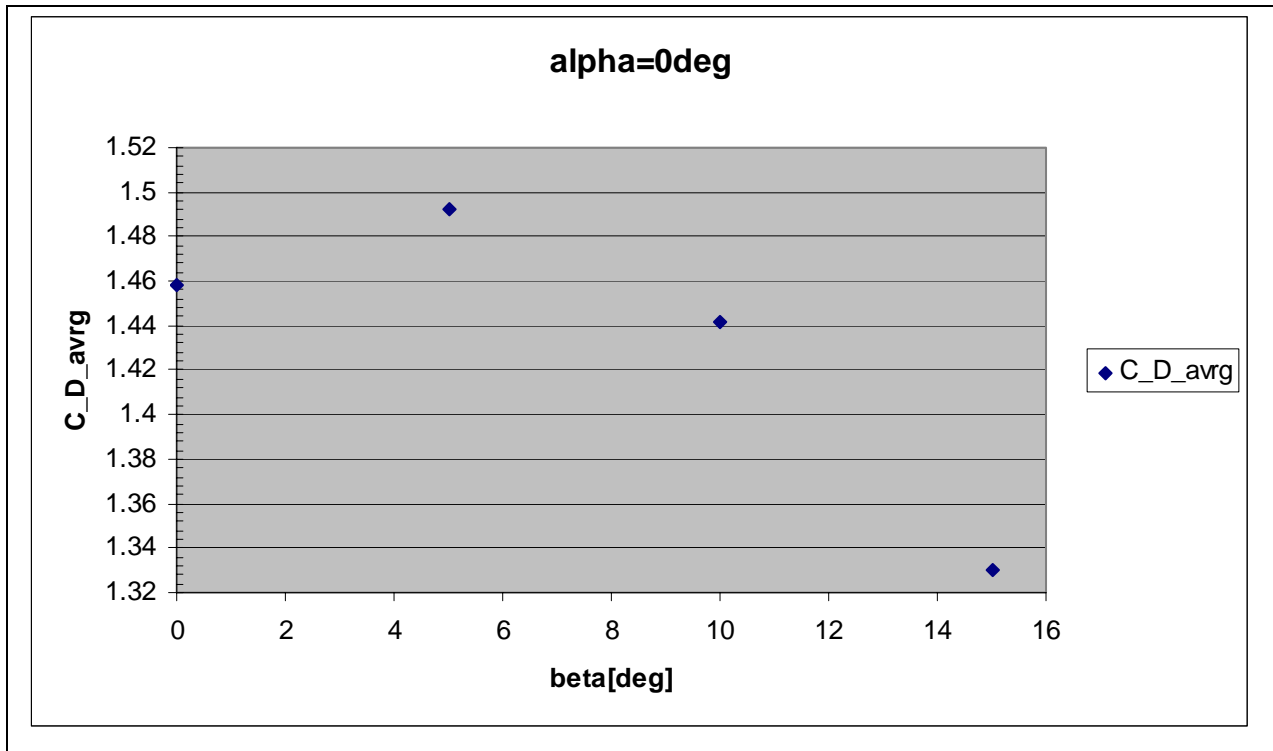
Figure 56 - C_D_avrg tTED2 Alpha=0°, Changing Beta

Again it can be seen that there is a pronounced drop between $\beta = 10°$ and $\beta = 15°$. In spite of the described deviations there is a good congruence between the average values of the cases $\beta = const, \Delta\alpha$ and $\alpha = const., \Delta\beta$.

$\alpha[°], \beta = 0°$	$\overline{C}_D$	$\beta[°], \alpha = 0°$	$\overline{C}_D$
0	1.459	0	1.459
5	1.46	5	1.49
10	1.47	10	1.44
15	1.35	15	1.33

Table 19 - C_D_avrg Comparison between Alpha and Beta for the 6CB

These results lead to the following hypothesis: *The drag coefficient of the TW in the boxkite configuration behaves to a very good extent like the projected surface normal to the free stream if pitch or yaw angle are fixed at zero degree.*

This hypothesis will be used to derive a function for the drag coefficient that depends only on the TW orientation $\overline{C}_D(\alpha)$ or $\overline{C}_D(\beta)$ respectively. This function is then supposed to be compared to the experimental results and thus be validated.

TECHNISCHE
UNIVERSITÄT
MÜNCHEN

Lehrstuhl für Aerodynamik
Technische Universität München
Univ. Prof. Dr. Ing. N. Adams

aer

The equations for calculating the surface normal to the free stream $S_\perp$ for a constant rolling axis (that is $\alpha = 0°, \Delta\beta$ or $\beta = 0°, \Delta\alpha$) are given in chapter 2.4 and will be repeated in terms of the tTED2:

$$S_{\perp,tTED2}(\alpha) = \frac{1}{2}\left(1 - \frac{1}{\sqrt{2}}\right)S_{tTED2} \cdot \cos(4\alpha) + \frac{1}{2}\left(1 + \frac{1}{\sqrt{2}}\right)S_{tTED2} \qquad (4.34)$$

$$S_{\perp,tTED2}(t) = \frac{1}{2}\left(1 - \frac{1}{\sqrt{2}}\right)S_{tTED2} \cdot \cos\left(4 \cdot \frac{2\pi}{T} \cdot t\right) + \frac{1}{2}\left(1 + \frac{1}{\sqrt{2}}\right)S_{tTED2} \qquad (4.35)$$

The hypothesis made above now allows to substituting the reference surface with the maximum drag coefficient. However the results of the 6CB are showing somewhat inconsistent values about the maximum drag coefficient and the angle of its emergence. That is why the measurements of the OBB will be consulted:
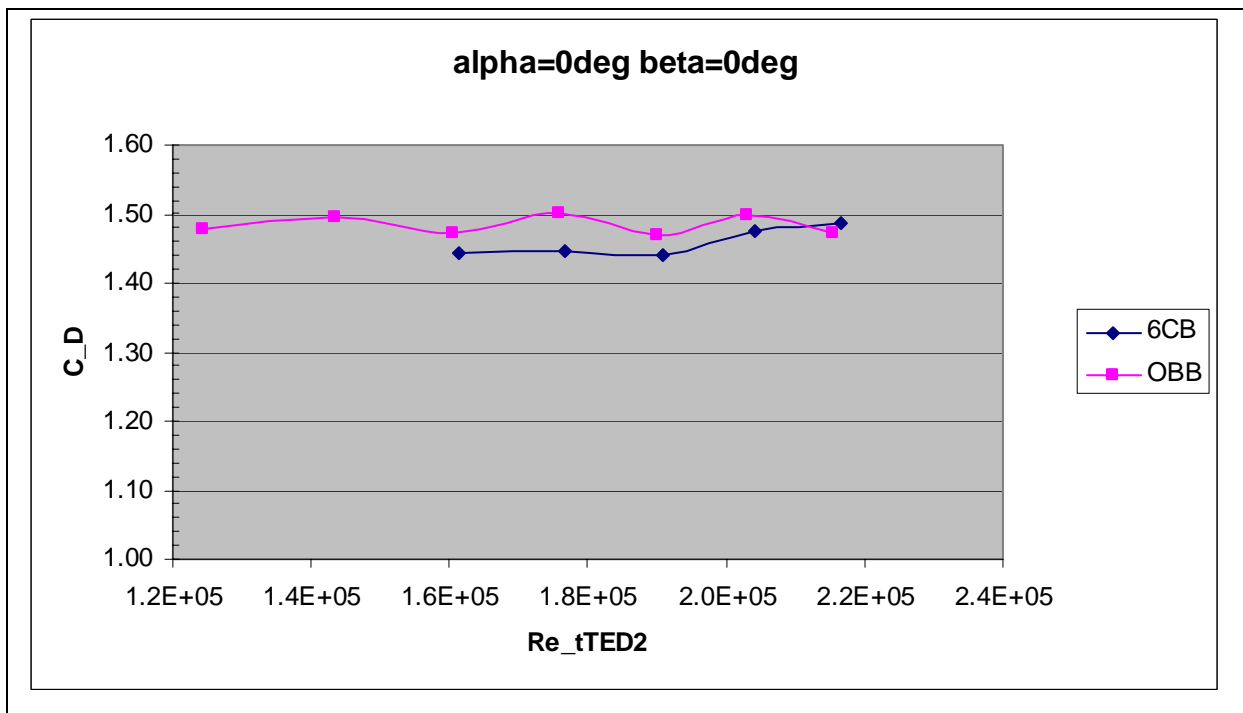
Figure 57 - C_D for tTED2 Measured with the OBB and the 6CB for Alpha=0° and Beta=0°

The comparison between the 6CB and the OBB shows a more reasonable and expected behavior for the OBB. The reason for this may be that the OBB is calibrated especially for the low forces at hand and it is equipped with different strain gages. So the average drag coefficient of the OBB measured for $\alpha = 0°$ and $\beta = 0°$ will be taken as the maximum value:

$$\bar{C}_D(\alpha = 0°, \beta = 0°) = 1.48$$

Applying this maximum to eq.(4.34) yields the following equations for the average drag coefficient when steadily turning about the y'-axis:

$$\overline{C}_D\left(\alpha\right)=\frac{1}{2}\left(1-\frac{1}{\sqrt{2}}\right)\cdot 1.48\cdot\cos\left(4\alpha\right)+\frac{1}{2}\left(1+\frac{1}{\sqrt{2}}\right)\cdot 1.48 \tag{4.36}$$

$$\overline{C}_D\left(t\right)=\frac{1}{2}\left(1-\frac{1}{\sqrt{2}}\right)\cdot 1.48\cdot\cos\left(4\cdot\frac{2\pi}{T}\cdot t\right)+\frac{1}{2}\left(1+\frac{1}{\sqrt{2}}\right)\cdot 1.48 \tag{4.37}$$

With this equation two expected dynamic drag profiles in terms of angle or time can be generated.
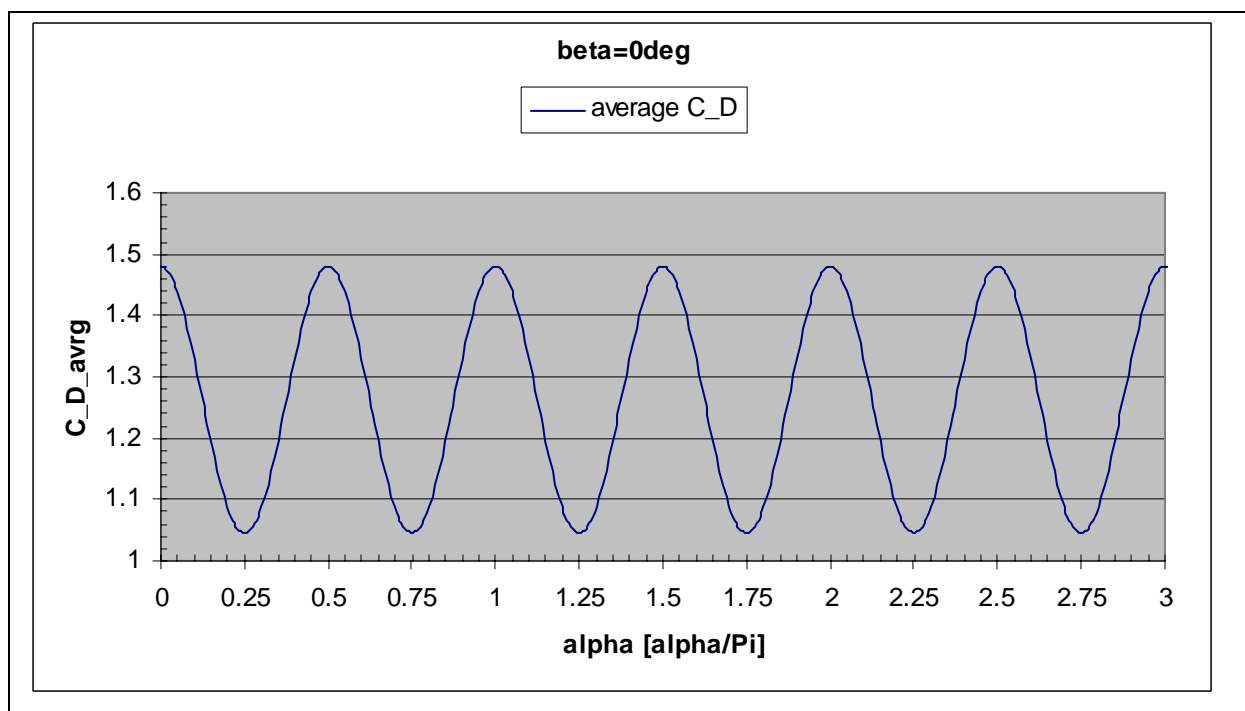
Figure 58 - Dynamic Drag Profile for Beta=0 and Changing Alpha

TECHNISCHE
UNIVERSITÄT
MÜNCHEN

Lehrstuhl für Aerodynamik
Technische Universität München
Univ. Prof. Dr. Ing. N. Adams

aer
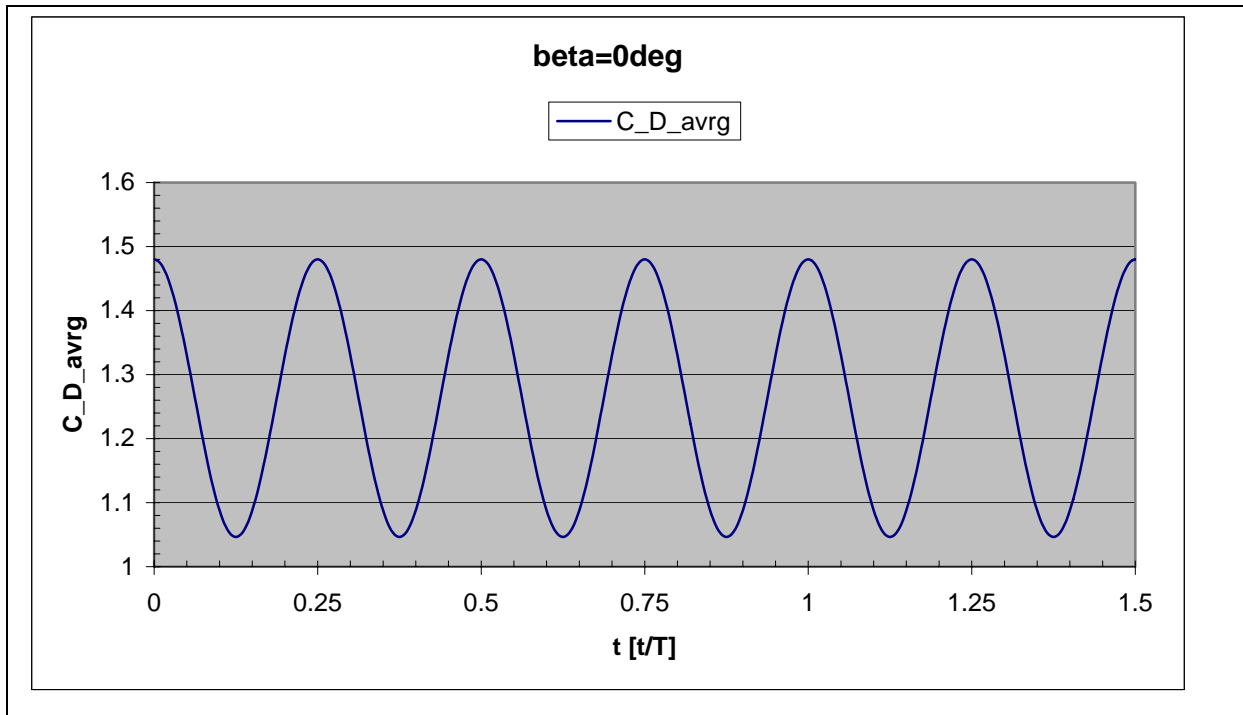
Figure 59 - Dynamic C_D_avrg for Beta=0° and Changing Time

In order to evaluate the gained function it will be compared to the corresponding experimental values. Therefore several values measured with the 6CB and OBB are available. With the 6CB both the pitch and the yaw angle can be measured. However it is restricted to a certain angle range each. The OBB is not able to adjust the pitch angle but it has geometrically no limitations concerning the yaw angle. So also the very interesting extreme value of $\beta = 45°$ can be measured.
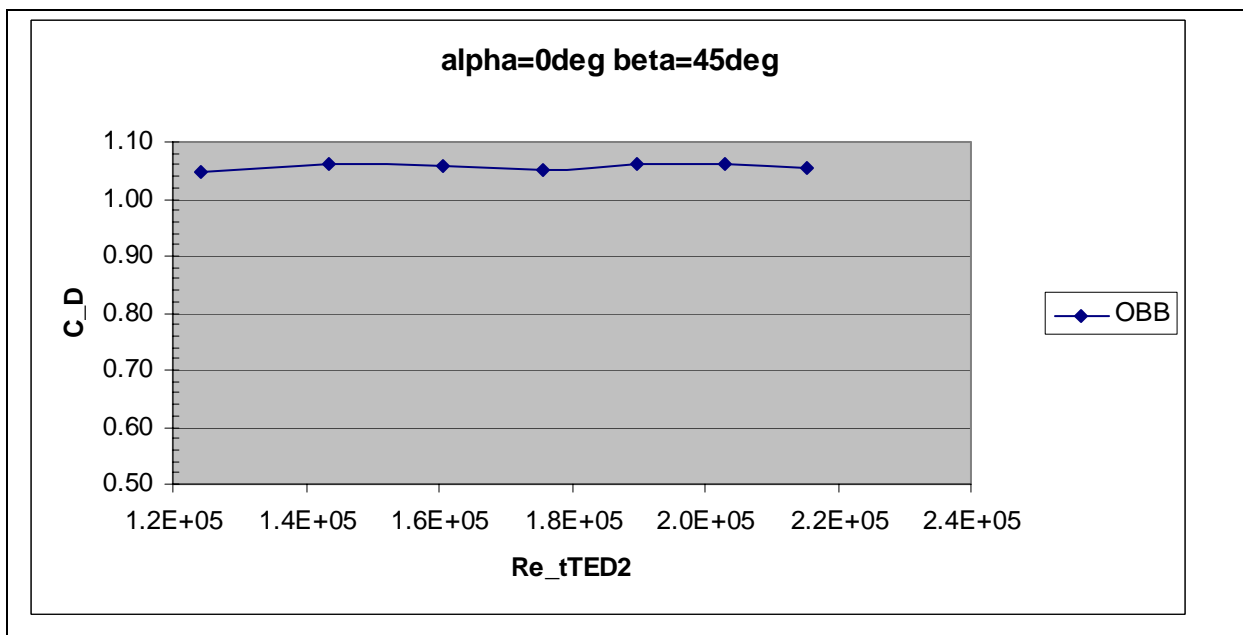
Figure 60 - C_D tTED2 Measured by the OBB for Alpha=0° and Beta=45°

TECHNISCHE
UNIVERSITÄT
MÜNCHEN

Lehrstuhl für Aerodynamik
Technische Universität München
Univ. Prof. Dr. Ing. N. Adams

aer

The average drag coefficient measured in this chart is:

$$\overline{C}_D\left(\alpha = 0°, \beta = 45°\right) = 1.06$$

It would also be very desirable to measure more yaw angles with the OBB especially those that are out of the 6CB range. However as described in chapter 4.2 the OBB is based on the assumption that the balance plate is only bent. If the loading case deviates too much from this assumption it must be expected that the measured values are wrong. This deviating loading case will appear for an asymmetric orientation of the tTED2 towards the free stream. Then it is assumed that also significant side forces and torque moments are exerted on the balance plate. In order to assess this effect the OBB was also used for a yaw angle of $\beta = 22.5°$. This value is compared to the closest yaw angle of the 6CB that is $\beta = 15°$.
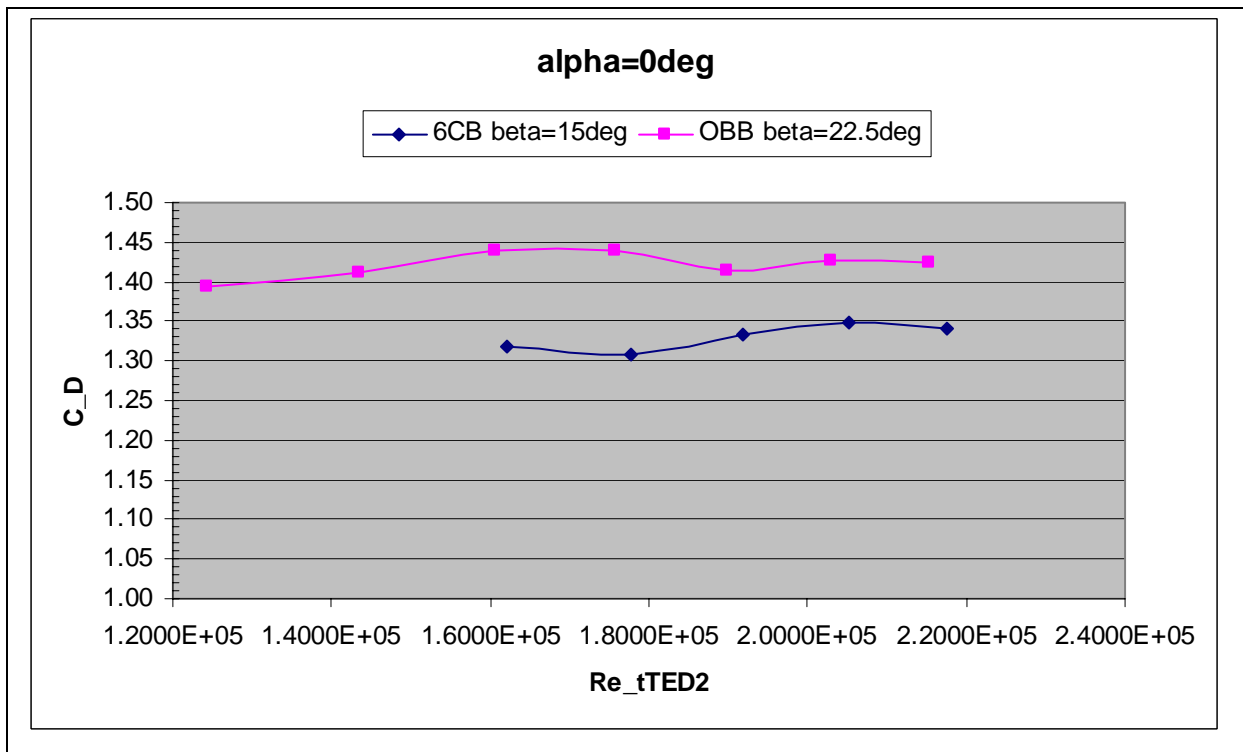
Figure 61 - C_D tTED2 Measured by 6CB and OBB for Alpha=0 and Similar Beta

From this chart it gets clear that the asymmetric cases cannot be measured with the OBB reliably. The measured drag coefficient is even bigger than the drag coefficient for a lower yaw angle. The table 19 shows that this result is unrealistic and therefore further measurements of this kind are ruled out.

With all this available data a comparison can be realized which will take place by a curve-data-point chart. It includes all relevant measured data and the functional drag curve for a

little more than a quarter-rotation. The cases of $\alpha = 0, \Delta\beta$ and $\beta = 0, \Delta\alpha$ are regarded as equivalent and so both angles will appear in the chart.
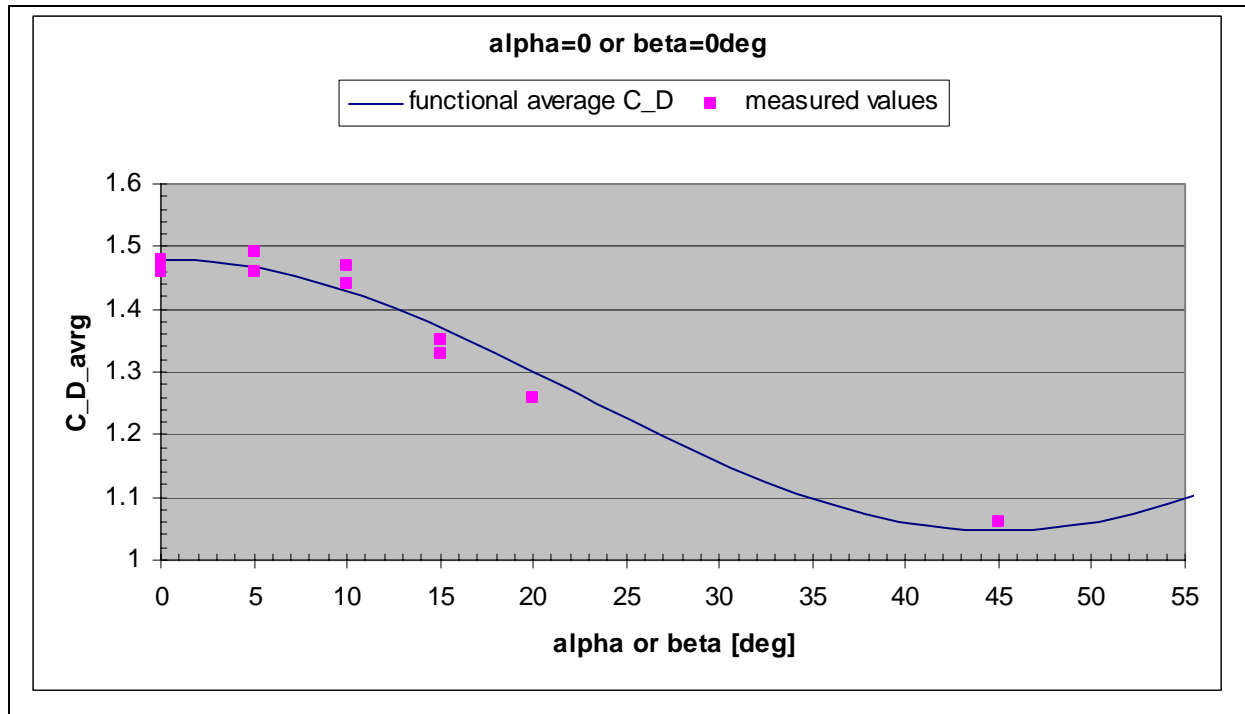
Figure 62 - Comparison between Calculated and Measured Drag Coefficients

This comparison confirms to a good extent the hypothesis made above. With this encouraging result the next obvious question is if the hypothesis also holds true for an even more general description of the drag coefficient that is for arbitrary values of α and β at the same time.

In order to assess this question the next characteristic chart will be shown. It contains the drag coefficients for the same pitch and yaw angles that is $\alpha = \beta$.
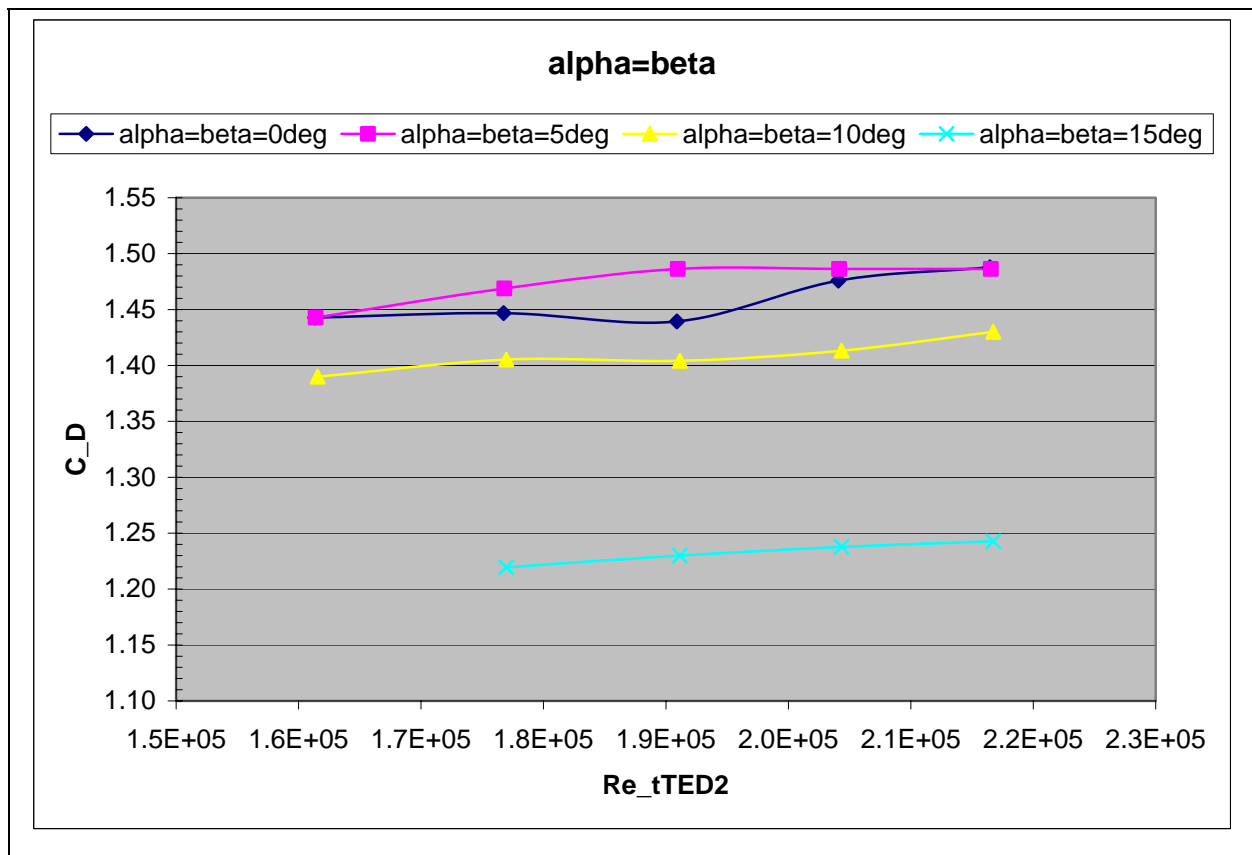
Figure 63 - C_D tTED2 for Alpha=Beta, Changing Re_tTED2, Measured with the 6CB

Again the averages are taken:

$\alpha = \beta \ [°]$	$\bar{C}_D$
0	1.459
5	1.474
10	1.41
15	1.235

Table 20 - C_D_avrg tTED2 for Alpha=Beta

TECHNISCHE
UNIVERSITÄT
MÜNCHEN

Lehrstuhl für Aerodynamik
Technische Universität München
Univ. Prof. Dr. Ing. N. Adams

aer
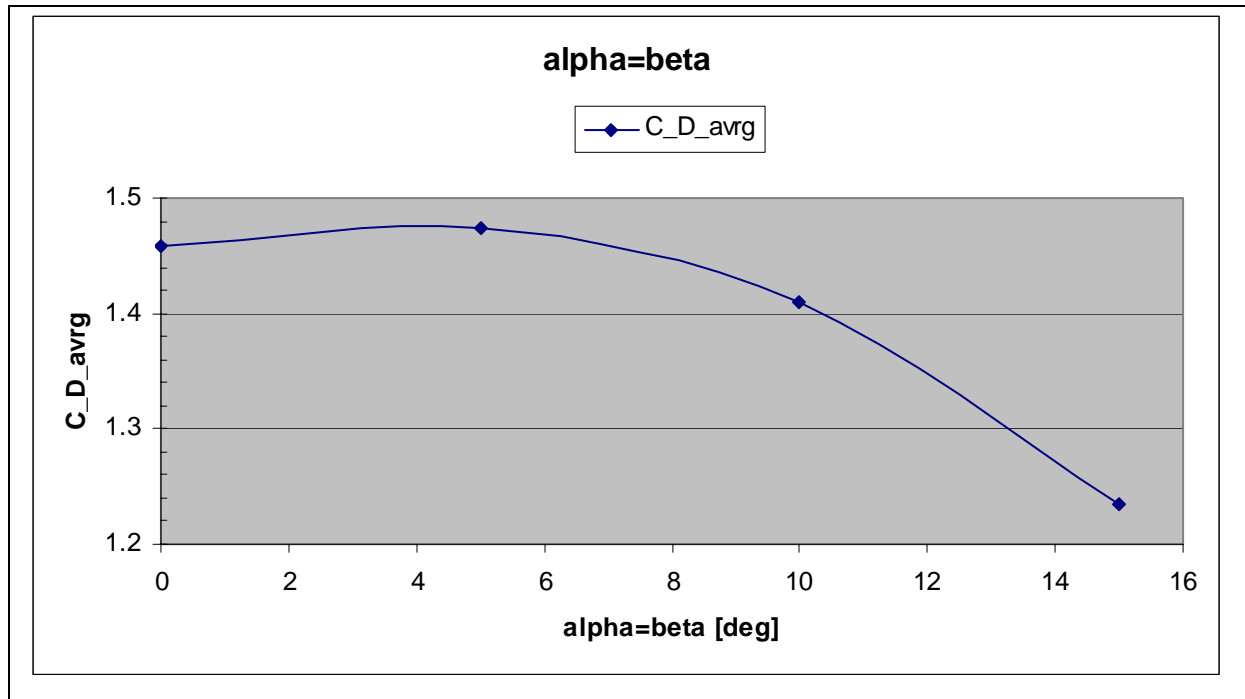
Figure 64 - C_D_avrg for Alpha=Beta

The approach for deriving an expression for $\bar{C}_{D,tTED2}(\alpha,\beta)$ is the very same like before. Starting from chapter 2.4 the reference surface is replaced by the maximum average drag coefficient of $\bar{C}_{D,\max}=1.48$:

$$\bar{C}_{D,tTED2}\left(\alpha,\beta,\bar{C}_{D,\max}\right)=\hat{C}_{D,tTED2}\left(\beta,\bar{C}_{D,\max}\right)\cdot\cos\left(4\alpha\right)+b\left(\beta,\bar{C}_{D,\max}\right) \qquad (4.38)$$

$$\hat{C}_{D,tTED2}\left(\beta,\bar{C}_{D,\max}\right)=\bar{C}_{D,\max}\left[\frac{3}{8}\cos\left(4\beta\right)-\frac{1}{2}\frac{1}{\sqrt{2}}\cos\left(4\beta\right)+\frac{1}{8}\right]$$

$$b\left(\beta,\bar{C}_{D,\max}\right)=\bar{C}_{D,\max}\left[\frac{1}{8}\cos\left(4\beta\right)+\frac{1}{2}\frac{1}{\sqrt{2}}+\frac{3}{8}\right]$$

With eq.(4.38) there is no curve easily creatable because it is an equation of two variables. Instead the measured experimental values will be compared to the functional values within the following table.

$\alpha[°]$	$\beta[°]$	$\overline{C}_{D,analytical}$ from eq.(4.38)	$\overline{C}_{D,exp}$ from measurements	$\overline{C}_{D,analytical} - \overline{C}_{D,exp}$
0	0	1.48	1.459	0.021
5	5	1.454	1.474	-0.02
10	10	1.38	1.41	-0.03
15	15	1.271	1.235	0.036
5	10	1.417	1.433	-0.016
5	15	1.36	1.332	0.028
10	5	1.417	1.4525	-0.0355
10	15	1.325	1.2992	0.0258
15	5	1.36	1.3366	0.0234
15	10	1.325	1.2931	0.0319

Table 21 - Comparison of Calculated and Measured C_D_average for the tTED2

The table shows deviations within a range of about $\Delta\overline{C}_D = \pm 0.036$. Considering the constraints and accuracy of the used balance this is regarded as a strong hint that the hypothesis holds true for any orientation of α and β.

So it is finally argued that the drag coefficient of the Tumbleweed in the box-kite configuration depends at least to a very large extent on the projected surface normal to the free stream direction.

Thus the drag coefficient of the TW will vary between the two extreme values of $\overline{C}_D(\alpha = 0\deg, \beta = 0\deg) = \overline{C}_{D,max}$ and $\overline{C}_D(\alpha = 45°, \beta = 45°) = \frac{1}{2}\overline{C}_{D,max}$. For $\overline{C}_{D,max} = 1.48$ this yields the drag coefficient range of:

$$0.74 \le \overline{C}_D(\alpha, \beta) \le 1.48 \tag{4.39}$$

TECHNISCHE
UNIVERSITÄT
MÜNCHEN

Lehrstuhl für Aerodynamik
Technische Universität München
Univ. Prof. Dr. Ing. N. Adams

aer

4.5.3 Side Force Coefficients for the tinyTED2

As mentioned in chapter 4.5.1 there is a certain range of α, β, q -combinations for that the 6-component-balance is assumed to yield somewhat correct results concerning the side force. The developing of this side force will be shown in terms of the side force coefficient in the following charts.

The side forces are presented as the average values since the developing with increasing Reynolds number showed no difference to the developing of the drag coefficients. That means that also the side force coefficients keep on slightly rising in magnitude with increasing Reynolds number. As a sample the side force coefficient for $\alpha = 15°, \beta = 15°$ is shown.
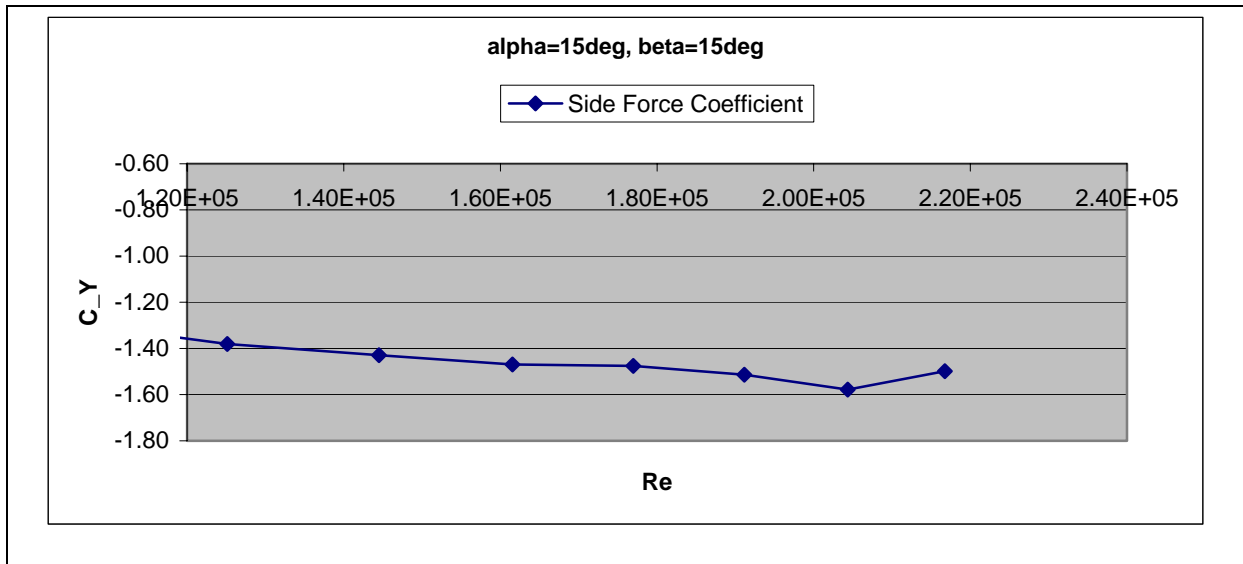
Figure 65 - C_y for Alpha=15deg, Beta=15deg and Changing Re

Hence the same explanations for this behavior hold true for the side force coefficients like for the drag force coefficient.

The 6CB only provided solid data for a yaw angle of $\beta \geq 10°$ and the drag force developing for changing pitch angle can be seen in the following chart.

TECHNISCHE
UNIVERSITÄT
MÜNCHEN

Lehrstuhl für Aerodynamik
Technische Universität München
Univ. Prof. Dr. Ing. N. Adams

aer
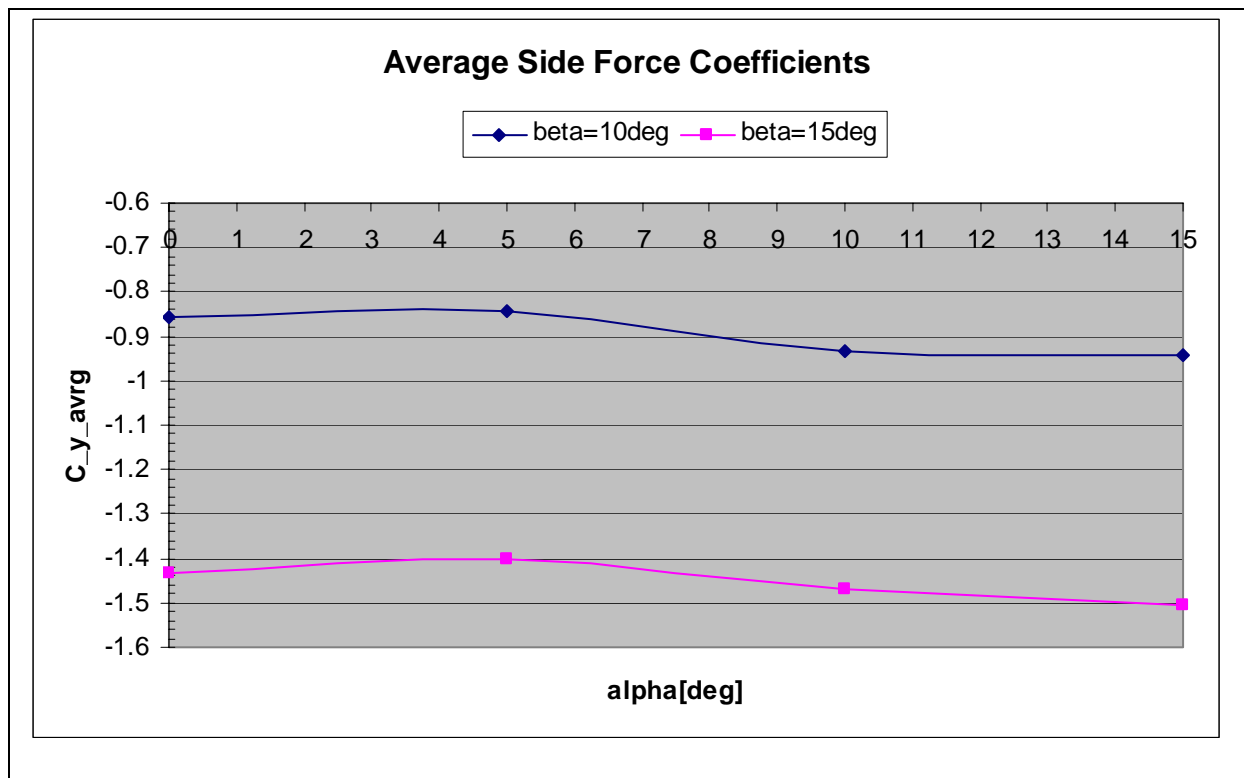
Figure 66 - C_y_avrg for Beta=10 deg, Beta=15deg and Changing Alpha

In the chart the same unexpected developing between $0° \leq \alpha \leq 10°$ is observed like for the drag coefficient. Again this encourages the assumption that some sort of small asymmetry at the tTED2 causes this behavior.

The most striking feature of the chart above is however the big increase in the side force magnitude between $\beta = 10°$ and $\beta = 15°$. In contrast the dependence on the pitch angle seems to be quite small. Therefore the geometry of the tTED2 will be looked into deeper. Like already mentioned when dealing with the OBB in chapter 4.5.2 the yaw angles of $\beta = 0°$ and $\beta = 45°$ represent a symmetric orientation relative to the x-z-plane.

TECHNISCHE
UNIVERSITÄT
MÜNCHEN

Lehrstuhl für Aerodynamik
Technische Universität München
Univ. Prof. Dr. Ing. N. Adams

aer
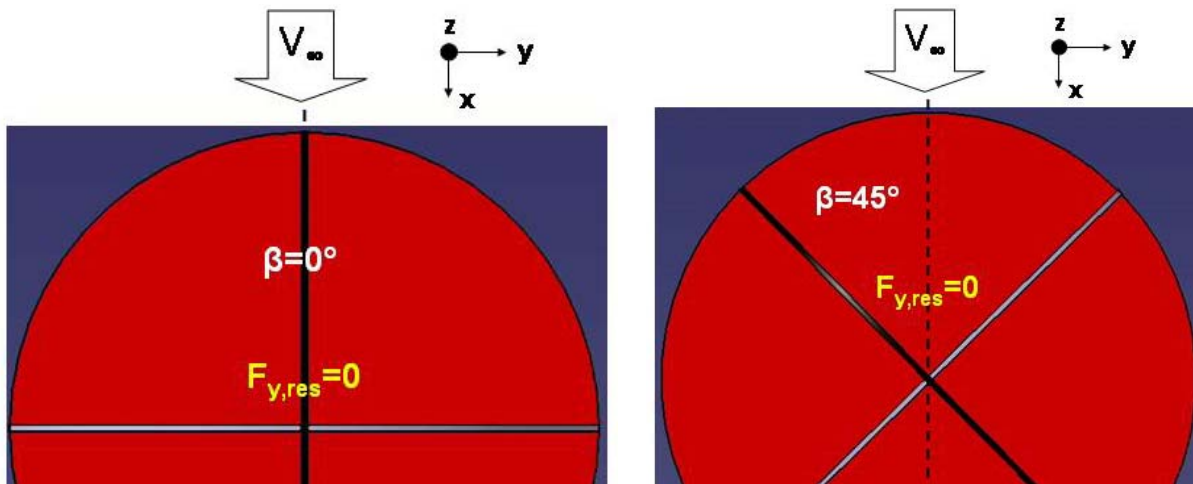
Figure 67 - TW for Beta=0° (left) and Beta=45° (right), Top View

The side force however acts perpendicular to the x-z-plane namely in the y-direction. Hence it is concluded that the pressure distribution over the sails at the two symmetric orientations ideally yield no resulting side force. From this fact in turn it is deduced that the maximum side force is found between those two orientations that is at $\beta = 22.5\,\mathrm{deg}$. Considering the symmetry of the design it can be concluded that there are eight orientations per full yaw revolution for which the side force coefficient is maximum. Those are at :

$$\beta = 22.5°; 67.5°; 112.5°; 157.5°; 202.5°; 247.5°; 292.5°; 337.5°$$

Another noticeable feature of figure 66 is the sign of the side force coefficient which is negative. From the general flow field it is concluded that the point of application of the resulting side force is on the sail surface upstream of the TED center. The sail surfaces downstream of the TED center will already be in its wake region. Therefrom it is concluded that the decisive pressure differences and hence forces concerning the side force will occur on the upstream sail surfaces.

That means that the generated side force will enhance the yaw motion that initially induced the side force. Thus the side force and the yaw motion will be amplified when starting at $\beta = 0°$.

TECHNISCHE
UNIVERSITÄT
MÜNCHEN

Lehrstuhl für Aerodynamik
Technische Universität München
Univ. Prof. Dr. Ing. N. Adams

aer
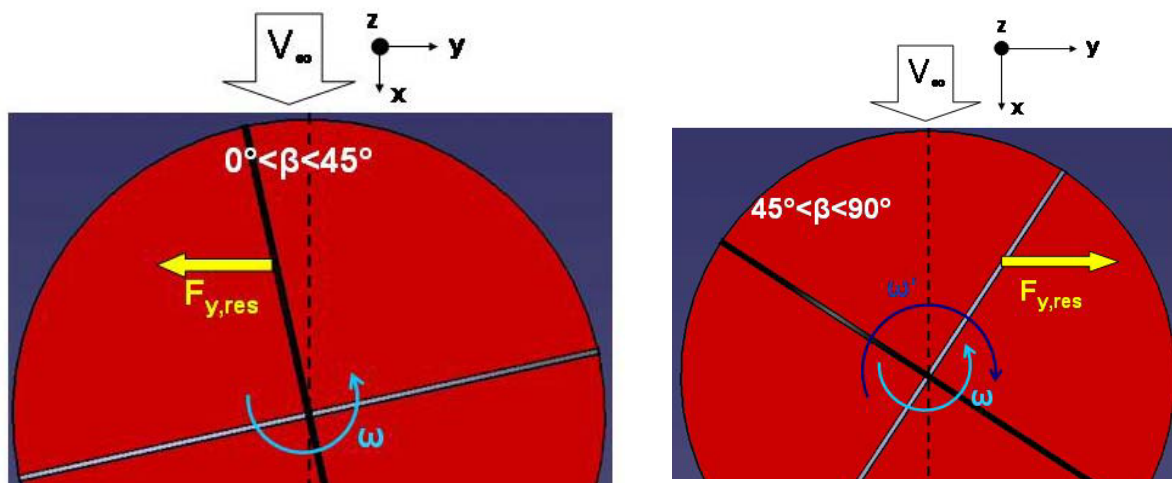
Figure 68 - TW at Beta<45° (left) and Beta>45° (right)

However when passing $\beta = 22.5$ the side force will begin to decrease and finally reach the value of zero again for the next symmetric orientation of $\beta = 45°$. The yaw motion ω however might still go on if the damping influence of the ground friction is not large enough. So the TW will rotate towards the next side force peak at $\beta = 67.5°$. For reasons of symmetry however it is assumed that the side force will act in the positive y-direction this time and thus act against the yaw motion or damp it, respectively. When the yaw motion ω has come to rest and the TW orientation is still at $45° < \beta < 90°$ the side force will induce a yaw motion ω' contrary to the first one. This process might go on until the side force is not strong enough to overcome the ground friction any more or just until the TW keeps its orientation at $\beta = 45°$.

Therefrom it is concluded that the preferred orientation of the rolling TW will be:

$$\alpha = \alpha(t), \beta = 45°; 135°; 225°; 315°$$

The reason for this assumption is that there are always perturbations to the perfect uniform free stream that initiate the process described above. Unfortunately it can be seen from chapter 4.5.2 that this orientation is not very favorable in terms of a maximum drag coefficient.

4.5.4 Flow Separation on the tinyTED2 Sails

In chapter 3.1.4 it is shown that onto the MIS in the center of the gimbal and therefore of the TW an anemometer is mounted. Indeed from airfoil theory it is known that from a certain pitch angle or angle of attack the flow on the suction side will begin to separate. As described

TECHNISCHE
UNIVERSITÄT
MÜNCHEN

Lehrstuhl für Aerodynamik
Technische Universität München
Univ. Prof. Dr. Ing. N. Adams

aer

in chapter 2.1 this boundary layer separation is connected with the creation of vortices and therefore with a flow field that is strongly altered from the uniform external flow. In that case the anemometer is not able to provide reliable data about the relative wind speed any more if it is calibrated only for uniform flow.

Furthermore it might be interesting to know for what pitch and yaw angle the flow separates from the sails. This might provide a deeper comprehension for the unsteady pressure distribution over the sails and hence provide valuable data for aeroelastic research on the TW

On these reasons two sail quarters of the same pocket were equipped with a pattern of tufts. Then the behavior of the tufts were investigated and video-taped for the dynamic pressures of $q = 0.2\,psf$, $q = 0.6\,psf$ and $q = 1.2\,psf$. As described in the previous chapters the measurements for the dynamic pressures of $q = 0.2\,psf$ can be ruled out in the first place.

A video camera was placed next to the test section and the tuft motions were video-taped for all the pitch and yaw angles that were investigated also in the course of the drag measurements.
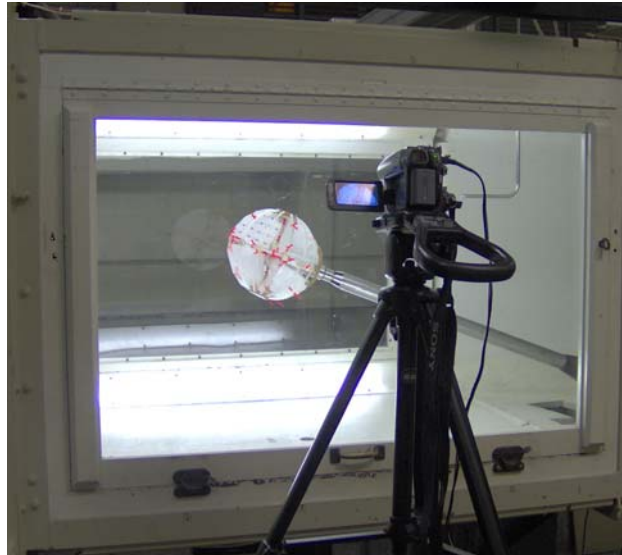
Figure 69 - Video Camera In Front of the Test Section

The tufts were attached to the sails of the upper left front pocket at the x'-y'-plane sail and the x'-z'-plane sail.

TECHNISCHE
UNIVERSITÄT
MÜNCHEN

Lehrstuhl für Aerodynamik
Technische Universität München
Univ. Prof. Dr. Ing. N. Adams

aer
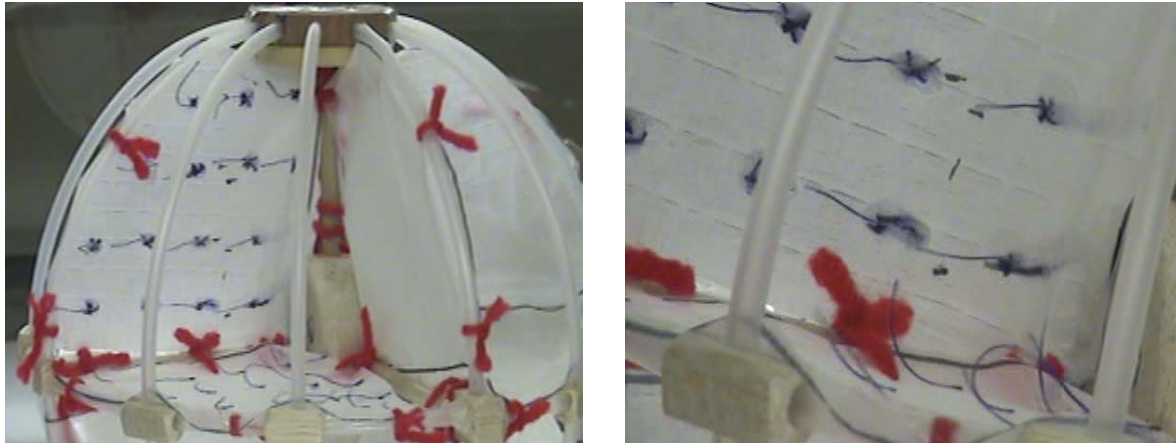
Figure 70 - Tufts on the tTED2 Sails

Unfortunately the analysis of the footage did not yield solid data in terms of the orientation for which the separation occurs first. Some activity of the tufts could be observed. However it was not possible to relate this activity to macroscopic vortices that would indicate the boundary layer separation. In fact the observed activity can also be caused by the tTED2 outer structure and especially on the x'-y'-plane by the pipe connectors. Indeed these parts do not show the geometric similarity and therefore the results are not considered as informative.

Eventually no pitch and/or yaw angles could be determined in the scope of this thesis that mark the onset of boundary layer separation from the sails. To know this orientation may however be important in order to evaluate the accuracy of the anemometer during the rolling. In fact if the separated vortices hit the anemometer it must be expected that anemometer shows wrong values for the relative wind speed. If there are any orientations of the TW for which the vortices do not hit the anemometer some solid data could be gained, though. It might also be possible to calibrate the anemometer mounted in a TW model by extensive wind tunnel tests.

TECHNISCHE
UNIVERSITÄT
MÜNCHEN

Lehrstuhl für Aerodynamik
Technische Universität München
Univ. Prof. Dr. Ing. N. Adams

aer

4.5.5 Summary of Chapter 4.5

Due to the various conclusions of this chapter the most important results will be summarized again. *This time all results will be related to the actual Tumbleweed rover.*

Within the observed Reynolds number range of $1.2 \cdot 10^5 < \text{Re}_{TW} < 2.2 \cdot 10^5$ the Tumbleweed's drag coefficients shows hardly any dependence on the Reynolds number. This verifies the assumption that the TW can be considered as a blunt body.

When spinning about a fixed axis ($\alpha = \alpha(t)$, $\beta = 0$, $\gamma = 0$) the drag coefficient of the Tumbleweed can be calculated with the following two equations, depending on its orientation or time, respectively.

$$\overline{C}_{D,TW}(\alpha) = \frac{1}{2}\left(1 - \frac{1}{\sqrt{2}}\right) \cdot \overline{C}_{D,TW,\max} \cdot \cos(4\alpha) + \frac{1}{2}\left(1 + \frac{1}{\sqrt{2}}\right) \cdot \overline{C}_{D,TW,\max} \tag{4.40}$$

$$\overline{C}_{D,TW}(t) = \frac{1}{2}\left(1 - \frac{1}{\sqrt{2}}\right) \cdot \overline{C}_{D,TW,\max} \cdot \cos\left(4 \cdot \frac{2\pi}{T} \cdot t\right) + \frac{1}{2}\left(1 + \frac{1}{\sqrt{2}}\right) \cdot \overline{C}_{D,TW,\max} \tag{4.41}$$

$$\overline{C}_{D,TW,\max} = 1.48$$

It is assumed that in terms of orientation the drag coefficient only depends on the pitch and yaw angle but not on the roll angle. The reason for this assumption is that changing the roll angle will not change the projected surface perpendicular to the free stream direction. The drag coefficient for every pitch and yaw angle combination can be calculated with the equations:

$$\overline{C}_{D,TW}\left(\alpha, \beta, \overline{C}_{D,TW,\max}\right) = \hat{C}_{D,TW}\left(\beta, \overline{C}_{D,TW,\max}\right) \cdot \cos(4\alpha) + b\left(\beta, \overline{C}_{D,TW,\max}\right) \tag{4.42}$$

$$\hat{C}_{D,TW}\left(\beta, \overline{C}_{D,TW,\max}\right) = \overline{C}_{D,TW,\max}\left[\frac{3}{8}\cos(4\beta) - \frac{1}{2}\frac{1}{\sqrt{2}}\cos(4\beta) + \frac{1}{8}\right]$$

$$b\left(\beta, \overline{C}_{D,TW,\max}\right) = \overline{C}_{D,TW,\max}\left[\frac{1}{8}\cos(4\beta) + \frac{1}{2}\frac{1}{\sqrt{2}} + \frac{3}{8}\right]$$

TECHNISCHE
UNIVERSITÄT
MÜNCHEN

Lehrstuhl für Aerodynamik
Technische Universität München
Univ. Prof. Dr. Ing. N. Adams

aer

The Tumbleweed will have eight yaw orientations for which the side force is maximal. These orientations are: $\beta = 22.5°; 67.5°; 112.5°; 157.5°; 202.5°; 247.5°; 292.5°; 337.5°$

The sign of each maximum side force is alternating between two adjacent maximum orientations and that is why the rolling Tumbleweed will have the preferred yaw orientations of:

$$\beta = 45°; 135°; 225°; 315°$$

However it is not possible to measure the maximum side fore with the means of this thesis. That is why it is not possible to give a solid equation for the side force coefficient. Indeed it should obey a non-displaced cosine-law.

The drag coefficient of this preferred rolling orientation dependent on the pitch angle can be calculated after:

$$\overline{C}_{D,TW}(\alpha) = \frac{1}{2}\left(1 - \frac{1}{\sqrt{2}}\right) \cdot \overline{C}_{D,TW,\max} \cdot \cos(4\alpha) + \frac{1}{2}\left(1 + \frac{1}{\sqrt{2}}\right) \cdot \overline{C}_{D,TW,\max} \tag{4.43}$$

$$\overline{C}_{D,TW,\max} = 1.047$$

The over one rotation averaged drag coefficient at these orientations is equal to the zero shift $b(\beta)$. That is why the average drag coefficient for the Tumbleweed rolling in its preferred orientation is:

$$\overline{\overline{C}}_{D,TW}(\beta = 45°; 135°; 225°; 315°) = 0.893$$

Finally an assessment about the magnitude of the drag coefficient will be given. The measurements of this thesis combined with the results from [29] shown in fig.53 give reason to the assumption that the values are realistic. When comparing the measured magnitudes with the theoretical values from literature however significant differences can be seen.

TECHNISCHE
UNIVERSITÄT
MÜNCHEN

Lehrstuhl für Aerodynamik
Technische Universität München
Univ. Prof. Dr. Ing. N. Adams

aer

In reference [26] the drag coefficient for a flat disk perpendicular to the free stream is given to: $C_{D.flat\,disk} = 1.17$

In the same reference the maximum value for the flat plate is given to: $C_{D,flat\,plate} = 1.98$

The maximum drag coefficient for the TW has been determined to: $C_{D,TW} = 1.48$

As shown in chapter 3.1.3 this deviation from the three-dimensional case seems not be fully explainable by the frictional influence of the sails parallel to the free stream. To proof that an assessment of the contributions of the friction drag and pressure drag will be conducted for a dynamic pressure of $q = 0.5\,psf = 23.94\,Pa$. The theoretical value for the pressure drag of the flat disk yields $D_{form} = 1.17 \cdot 23.94\,Pa \cdot 0.0314\,m^2 = 0.88\,N$. The sails parallel to the free stream and upstream of the tTED2-center are assumed to yield the major contribution to the friction drag. Their wetted surface is $S_{wetted} = 2 \cdot S_{tTED2} = 0.0628\,m^2$. Taking the measured friction drag coefficient of $C_f = 0.053$ yields a friction drag contribution of $D_{friction} = 0.053 \cdot 23.94\,Pa \cdot 0.0628\,m^2 = 0.028\,N$. Adding these contributions up and referencing them again to S_{tTED2} yields a profile drag coefficient for the three-dimensional tTED2 of $C_D = 1.208$. This value is clearly below the measured profile drag of the tTED2 and hence there must be further explanations for the high profile drag of $C_{D,TW} = 1.48$.

Geometrically the flat plate and the flat disk only differ in one space dimension that means that the flat plate is two-dimensional and the flat-disk is three-dimensional. As per [1] there is a general tendency that the drag coefficient of the three-dimensional case is smaller than the drag coefficient of the geometrically analog two-dimensional case. The reason for that is seen in the so-called *three-dimensional relieving effect*. By "giving" a third dimension to the flow it is able to bypass the body more easily than in two dimensions and hence the body does not expose such a big resistance to the flow like in the two-dimensional case.

Recalling figure 11 it is apparent that the TW geometry deviates from the case of a flat disk mainly due to the two more perpendicular sail planes. The three sail planes eventually create eight sail pockets. The reason for the higher drag coefficient is seen in the following procedure. Approaching one of the sail pockets the corresponding flow does not have the full three dimensions in order to pass the perpendicular sail. Instead it is confined on two sides by the both other sail planes. These confinements lead to a weakening of the three-dimensional

relieving effect and hence to a drag coefficient that is between the values of the flat disk and the flat plate.

4.6 Effect of Damaged Sails on the TW Drag Characteristics

In chapter 3.3 it is shown that there are imaginable circumstances that could cause severe damage to the sails of the TW or maybe its SDRS. That is why the effect of one or more damaged sails on the TW drag coefficient will be investigated in this chapter.

In order to simulate the tearing of a sail somewhat realistically a rock-like stone was used. The stone was pressed onto the sail and then the sail was pulled over the stone in a manner like the TW would roll over a rock that reaches into the outer structure.

Figure 71 - Tear Production on a Sail

Due to the sail material "rip-stop nylon" a very similar tear pattern for almost every case could be observed. The material tends to tear apart in a triangular way leaving a hole of pretty accurate triangular area. Thus the hole area could be determined pretty exactly. Additionally one sail was provided with only a single small hole. That is supposed to simulate the hit of a single stone from a rockfall that might be created by the TW when rolling down a ravine or slope. Furthermore one sail was torn apart in the middle and two runs were conducted without one entire sail quarter simulating the failure of a part of the SDRS.
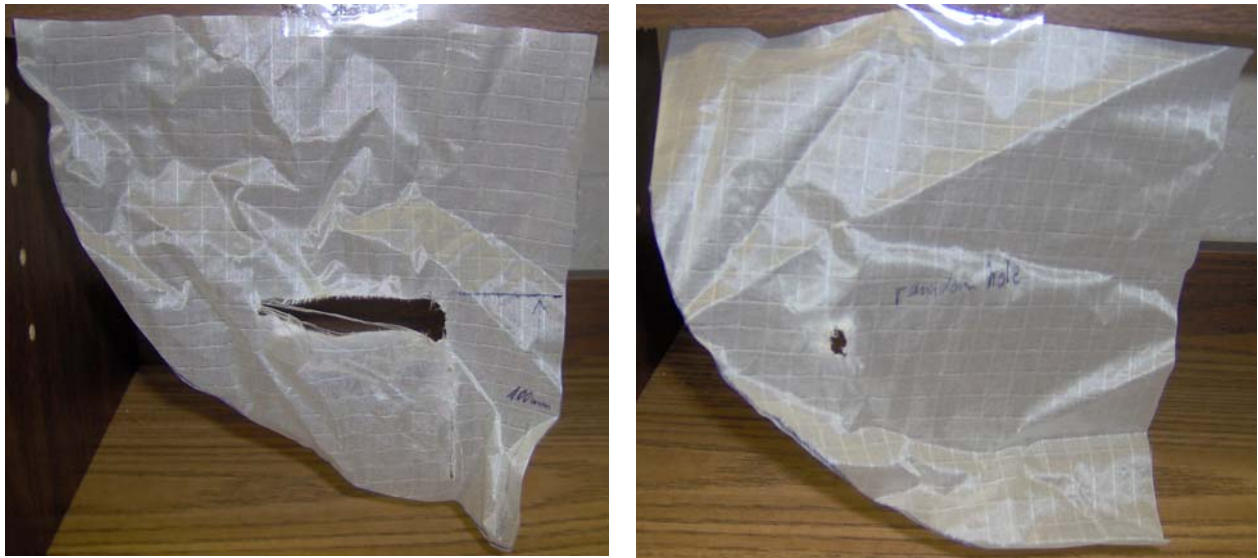
Figure 72 - Sail Hole Geometries

For the tests the tinyTED2 as well as the tinyTED were equipped with damaged sails. Only after the first test run it became clear that the tTED results do not yield realistic drag values. However due to constraints in time and wind tunnel availability there could be no more extensive research on damaged sails for the tTED2. Another issue with the tTED2 will become obvious in the remainder of this chapter. Indeed the results for the tTED seem not to be worthless because the main question for the damaged sail tests was how the drag coefficient changes relative to the undamaged case. This ratio in turn appears to eliminate the exaggerated magnitudes of the tTED measurements and to provide solid data.

All measurements were conducted at $\alpha = 0°$, $\beta = 0°$ and the damaged sails were always mounted in the y'-z'-plane of the model that is the main drag creating sail plane for this orientation. The tTED was tested on the 6CB and the tTED2 on the OBB. The undamaged reference surfaces are:

$$S_{tTED} = 1.2566 \cdot 10^5 \, mm^2 \text{ and } S_{tTED2} = 31416 mm^2 \, .$$

TECHNISCHE
UNIVERSITÄT
MÜNCHEN

Lehrstuhl für Aerodynamik
Technische Universität München
Univ. Prof. Dr. Ing. N. Adams

aer

The applied cases or sails, respectively for the tTED and the tTED2 were:

case #	model	hole area $A_{hole}\left[mm^2\right]$	A_{hole}/S_{model}	notes
1	tTED	19.6	$1.56\cdot10^{-4}$	single hole
2	tTED	2100	0.017	triangular hole
3	tTED	1472+2100=3572	0.028	two damaged sails
4	tTED	31416	0.25	one sail missing
5	tTED2	350	0.011	triangular hole
6	tTED2	about 1784	0.057	sail torn apart
7	tTED2	7853	0.25	one sail missing

Table 22 - Cases of Damaged Sails
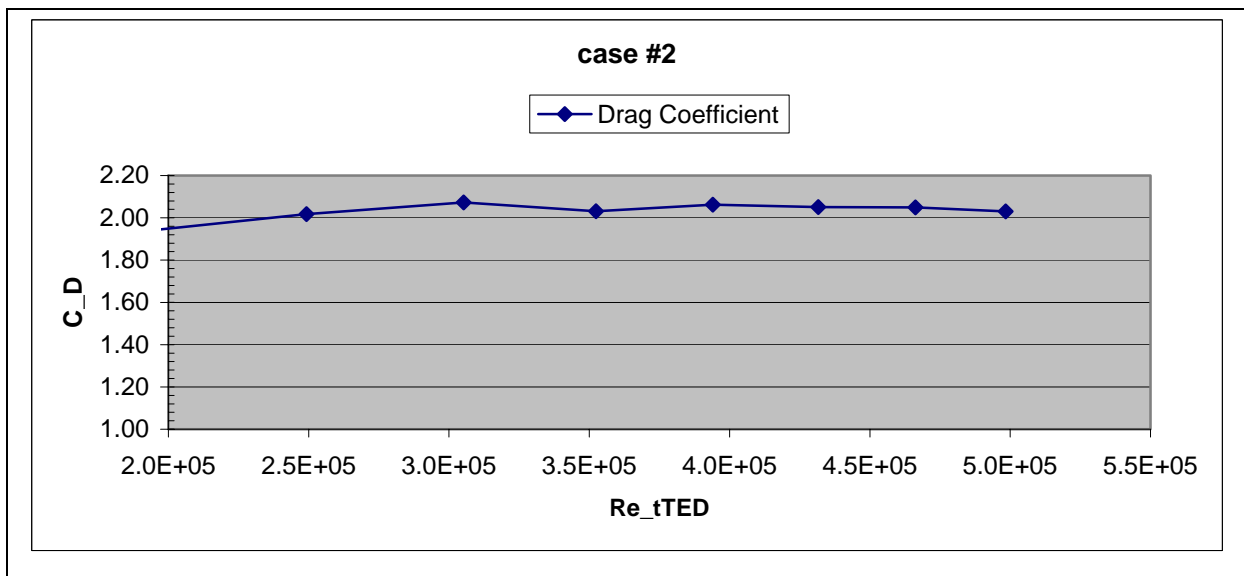
Figure 73 - Damaged Sail Case #4: C_D for Alpha=0deg and Changing Re_tTED

The figure above shows the drag coefficient of case #2 at $\alpha = 0°$ and changing Re_{tTED}. The behavior of the curve is typical for both the tTED and tTED2 at all cases in terms of its apparent lacking dependence on Re_{tTED} and Re_{tTED2}, respectively. That is why the drag coefficients will be shown as averages over the Reynolds number range again.

TECHNISCHE
UNIVERSITÄT
MÜNCHEN

Lehrstuhl für Aerodynamik
Technische Universität München
Univ. Prof. Dr. Ing. N. Adams

aer
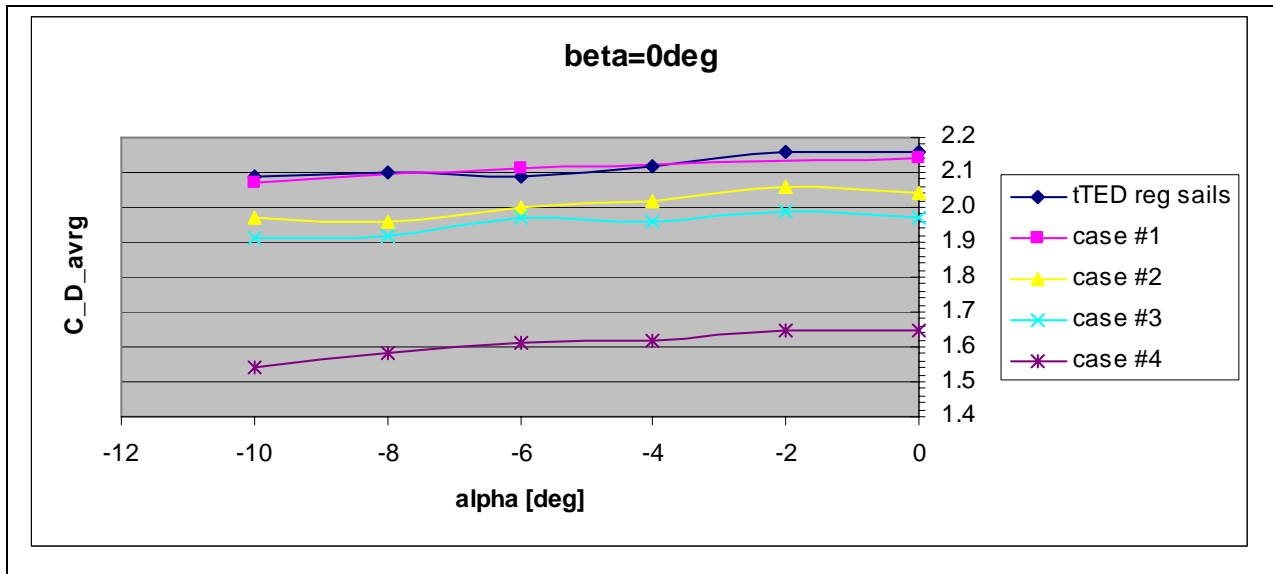
Figure 74 - C_D_avrg for Damaged Sails on the tTED, Beta=0° and Changing Alpha

It becomes obvious that a single relatively small hole hardly affects the tTED drag characteristics. Some drag values are even higher than for the undamaged case. This might be due to slight changes on the tTED geometry when rearming the model with the different sail or due to an effect that is more closely described in the next chapter. Anyway the effect on the drag characteristics is hardly detectible and so this case will be ruled out for the further investigation.

The remaining cases however show a decreasing drag with increasing hole size. Having in mind the dependence of the drag coefficient on the surface perpendicular to the free stream from chapter 4.5 another hypothesis is made: *The drag decreases linearly with increasing hole size*. In order to validate this hypothesis two ratios are made. The area ratio compares hole size and the undamaged sail surface after:

$$area\ ratio = \frac{S_{tTED} - A_{hole}}{S_{tTED}} \tag{4.44}$$

The drag ratio compares the average drag of the damaged sail to the average drag of the undamaged sail that is for the tTED: $\overline{C}_{D,tTED,\max} = 2.16$

$$drag\ ratio = \frac{\overline{C}_{D,tTED,hole}}{\overline{C}_{D,tTED}} \tag{4.45}$$

Apparently the area ratios do not depend on the pitch angle and thus these ratios can be seen as straight lines in the figure below.

TECHNISCHE
UNIVERSITÄT
MÜNCHEN

Lehrstuhl für Aerodynamik
Technische Universität München
Univ. Prof. Dr. Ing. N. Adams

aer
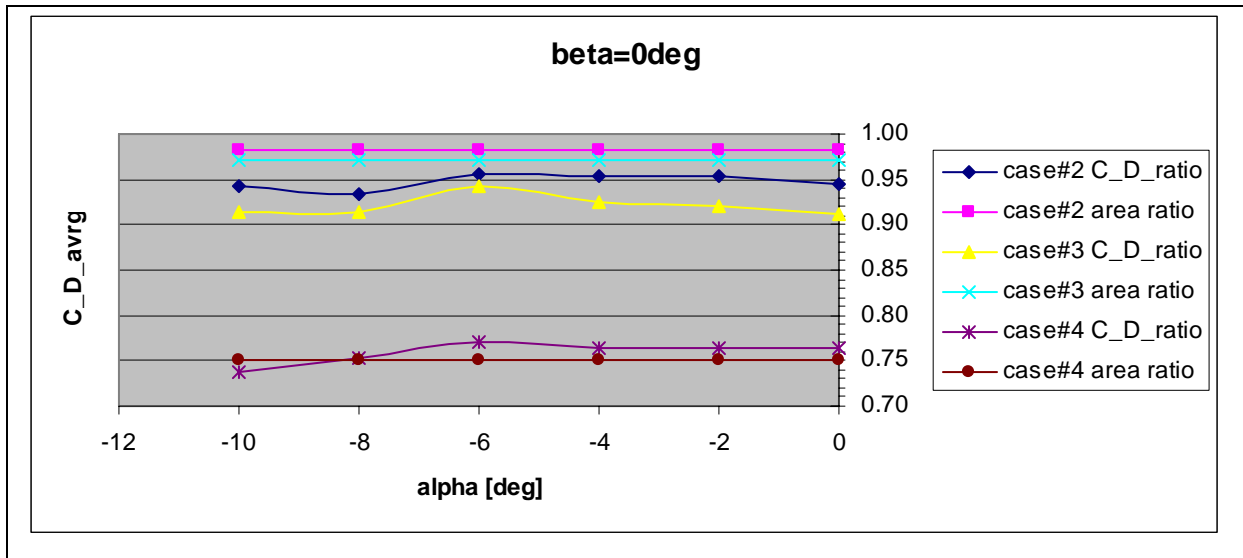
Figure 75 - Comparison between Surface Change and Drag Change for Damaged Sails of tTED

For case #4 the correlations between area reduction and drag drop is pretty good and seems to validate the hypothesis above. However the cases #2 and #3 do not show a clear correlation. Instead the yield even a worse drag drop compared to the decrease in sail surface. The reason for this remains unclear and must be looked after in the complex flow field about the TW. In terms of their magnitude however the drag drops are not disappointing large. So it might be concluded that the chosen sail material and the sail concept in terms of its geometry (box-kite approach) are well able to work under worsened conditions that is with damaged sails.

Three cases of damaged sails were also applied to the tinyTED2 on the OBB. The data can be surveyed easily so it is presented in the form of a table rather than a chart. Again the both ratios are made and the reference drag coefficient of the undamaged case is: $\overline{C}_{D,tTED2,\max} = 1.48$

#	$\overline{C}_D$	$\dfrac{S_{tTED2} - A_{hole}}{S_{tTED2}}$	$\dfrac{\overline{C}_{D,hole}}{\overline{C}_{D,tTED2}}$
5	1.48	0.9889	1
6	1.42	0.9432	0.959
7	1.31	0.7500	0.885

Table 23 - Change in Drag due to Sail Holes for tTED2, Alpha=0° and Beta=0°

The behavior of the tTED2 cases deviates remarkably from the tTED. While case #6 seems to validate the hypothesis made above the cases #5 and especially #7 show a different behavior. This time the pressure drops are less than the decrease in the sail surface. This contradicts the behavior of the tTED and it seems not be realistic that the drag drop gets that much less than

129

Lehrstuhl für Aerodynamik
Technische Universität München
Univ. Prof. Dr. Ing. N. Adams

TECHNISCHE
UNIVERSITÄT
MÜNCHEN

aer

the surface decrease (especially in case #7). The explanation for this behavior may be found in the lack of geometric similarity for the tTED2. The parts of the tTED2 are the same like for the tTED and hence the structural drag coefficient is certainly larger for the tTED2. It is assumed that this unrealistic high drag portion can be seen in the drag coefficients of the cases #5, #6 and #7. That is also why further investigation on damaged sails with the tTED2 are ruled out. It is not expected that they could yield realistic results, neither in terms of magnitude nor in terms of ratios.

Finally it must be mentioned that further tests on damaged sails might be desirable. In order to get realistic drag coefficient magnitudes another test site will probably be necessary. In order to get relative changes the tTED might be used especially at higher stagnation pressures (if the structure can stand them). Hence the force magnitudes on all space directions might be able to meet the minimum force requirement. By comparing these values to the undamaged case solid relative data might be gained. This data in turn might yield interesting insight into the altered orientation change behavior of the TW with damaged sails.

Within the time scope of this thesis these further tests are not feasible any more. In addition it is pointed out again that the applicability of sufficiently high dynamic pressures is with reservation to the structural capability of the tTED.

TECHNISCHE
UNIVERSITÄT
MÜNCHEN

Lehrstuhl für Aerodynamik
Technische Universität München
Univ. Prof. Dr. Ing. N. Adams

aer

5   Sail Performance Optimization

One major purpose of this thesis has been the investigation of different concepts in order to increase the sail performance that is the sail drag.

In reference [25] a pretty extensive research on different sail materials is shown. In this research not only the drag production but also other factors played an important role (like resistance to tear propagation, light transmittance, etc.). The result of this research has been the decision for the material "rip-stop nylon" as the sail material for the TED. It is interesting to note that a TW model at the NASA Langley Research also uses this material. Therefore no further investigations were conducted on the sail material in this thesis. Additionally a large amount of material residues from the TED construction phase were available. So concentrating on "rip-stop nylon" was also an approach exempt from charges.

Two ways were investigated that are supposed to increase the sail performance. The first one is based on an observation that was already made in [25] but was not followed up further. It was observed that punching holes in one of the tested sails could increase the measured form drag of the sail.

The other idea has been inspired from common photographs and images of sail boats. There it can usually be seen that the sails are blown up by the wind pretty often and therefore show a cambered shape rather than the flat-plate-similarity of the present TED sail design.

5.1   Theories for the Drag Increase

5.1.1   Theory for the Drag Increase by Holes

At first glance it seems to be paradox that a decrease in the effective sail surface by holes is supposed to increase the drag force. In fact the form drag is created by the pressure difference between the upstream and downstream side of the immersed body, in this case the sail (see chapter 2.1). This pressure difference Δp is communicated to the body over its surface. Hence the force F on a surface S by a pressure difference Δp can be calculated by:

$$F = \Delta p \cdot S \qquad (5.1)$$

TECHNISCHE
UNIVERSITÄT
MÜNCHEN

Lehrstuhl für Aerodynamik
Technische Universität München
Univ. Prof. Dr. Ing. N. Adams

aer

From this equation it gets obvious that the force can only be increased if the pressure difference rises more than the surface decreases. Thus the optimization takes place between increasing the pressure difference and decreasing the sail surface by the holes.

As per [26] the drag of a disk perpendicular to the free stream does not decrease at first when a hole is put into its center. Provided that the disk outer diameter is d_{Disk}, the hole diameter d_{hole} and taking the non-punched disk area as the reference surface the drag coefficient will not decrease within $\frac{d_{hole}}{d_{Disk}} \leq 0.25$. Taking the then created annular surface as reference the coefficient even rises steadily with increasing d_{hole} having an again pronounced rise from $\frac{d_{hole}}{d_{Disk}} = 0.6$ on.

Figure 30.   Drag coefficient of annular plates (rings), as reported in (34,d), at $R_{d_o} = 10^5$.
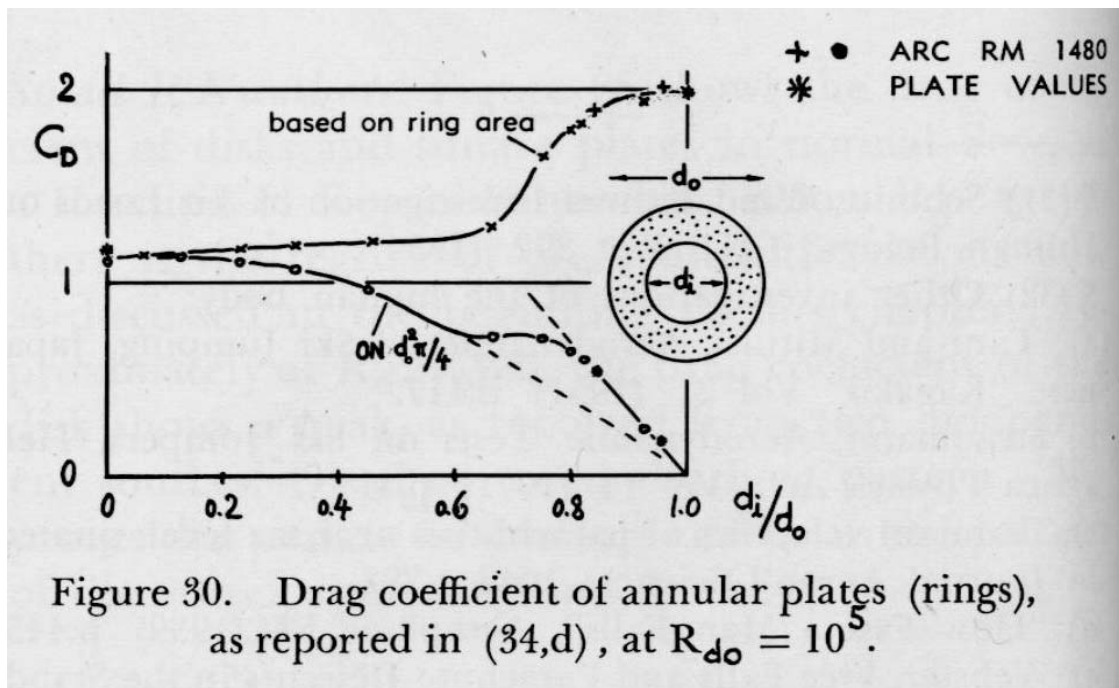
Figure 76 - C_D for a Disk with a Centered Hole from [26], Re_Disk=10e5

In order to increase the drag, however it is necessary that the drag coefficient with respect to the non-punched disk surface even rises instead of only not decreasing. The mechanism for this desired behavior may be gained from an analogy to the internal orifice flow. When a perforated plate is inserted into a duct the internal flow will experience a pressure drop when passing this orifice.

TECHNISCHE
UNIVERSITÄT
MÜNCHEN

Lehrstuhl für Aerodynamik
Technische Universität München
Univ. Prof. Dr. Ing. N. Adams

aer

In chapter 2.1 it is shown that the flow can be assumed to be incompressible so as per [31] the pressure loss can be calculated after:

$$\Delta p = \left(\frac{Q}{K \cdot A_{orifice}} \right)^2 \cdot \frac{1}{2} \rho \tag{5.2}$$

ρ density of the flow

K   flow coefficient

Q volume flow through the duct

orifice area $A_{orifice} = \frac{\pi}{4} d^2_{orifice}$

Increasing the volume flow will also increase the pressure drop. However the volume flow cannot be determined by design because it is assumed to depend on the free stream that is the wind. The same is true for the density that depends on the atmospheric conditions. Decreasing the orifice area A_o will increase the pressure drop. Finally the so called flow coefficient also depends strongly on the orifice geometry. A decreasing flow coefficient will also increase the pressure drop. Its developing can be seen from the following chart taken from [31].

TECHNISCHE
UNIVERSITÄT
MÜNCHEN

Lehrstuhl für Aerodynamik
Technische Universität München
Univ. Prof. Dr. Ing. N. Adams

aer
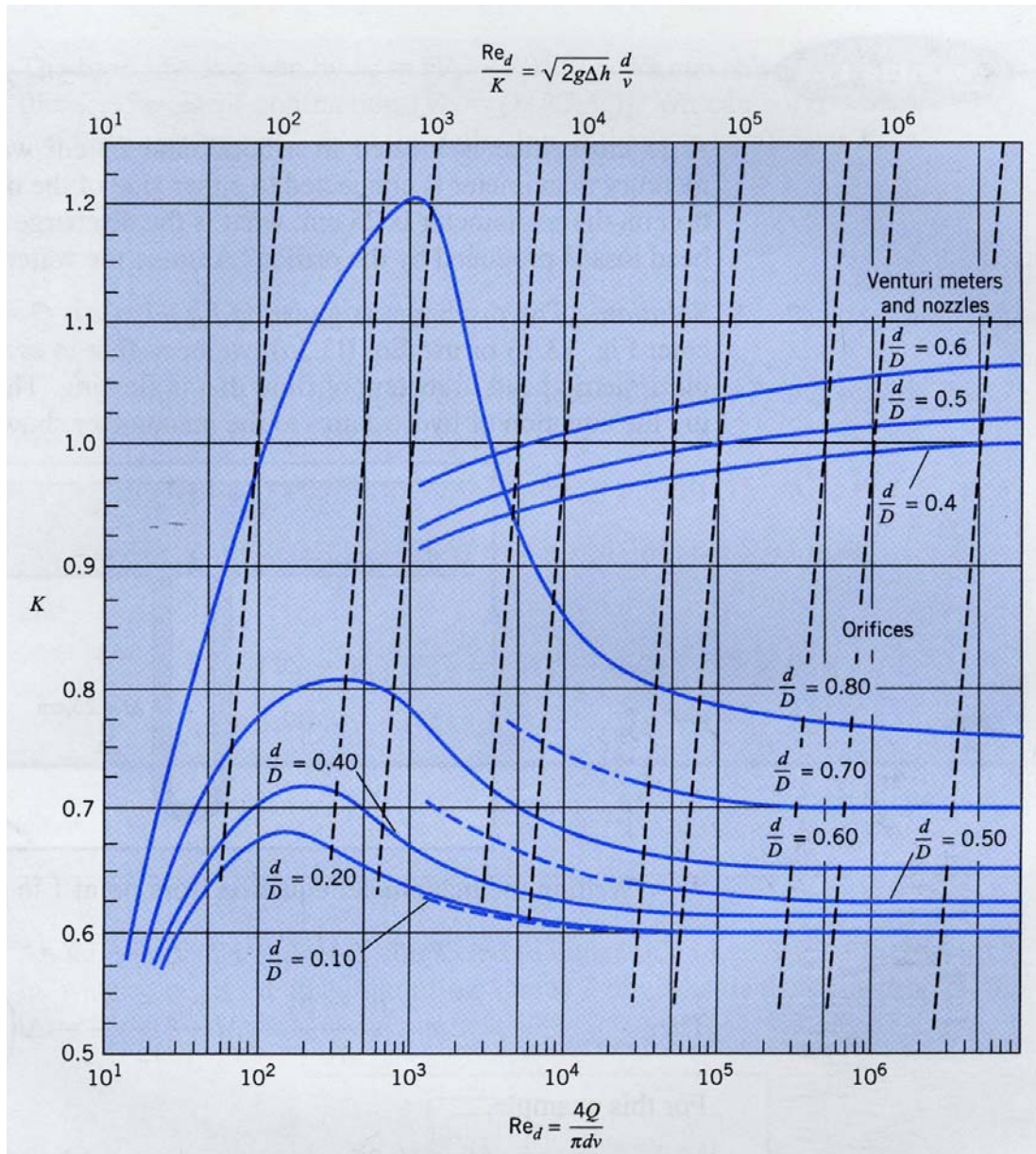
Figure 77 - Developing of the Flow Coefficient K from [31]

(Note: $d = d_{orifice}$, $D = d_{duct}$, ν : kinematic viscosity)

From the chart above it can be seen that the flow coefficients declines with decreasing $d_{orifice}$.

So it is finally concluded that in order to get a high pressure drop a low orifice diameter or a low sail hole diameter, respectively is desirable.

The physical explanation for the pressure drop is as follows. As described in chapter 2.1 a flow may separate from its confinements if there is a frictional force and a adverse pressure

TECHNISCHE
UNIVERSITÄT
MÜNCHEN

Lehrstuhl für Aerodynamik
Technische Universität München
Univ. Prof. Dr. Ing. N. Adams

aer

gradient. Both requirements are met downstream of the orifice. When the internal flow approaches the orifice it has to accelerate in order to the mass conservation that requires:

$$V_{orifice} = V_{duct} \cdot \frac{A_{duct}}{A_{orifice}}$$

After Bernoulli's theorem the static pressure will drop with increasing flow velocity. After having passed the orifice the flow cross section widens again, the flow will decelerate and the static pressure rises. So there is an adverse pressure gradient. In addition a frictional force will act due to the duct walls and the orifice. Thus a pressure drag is created like explained in chapter 2.1.
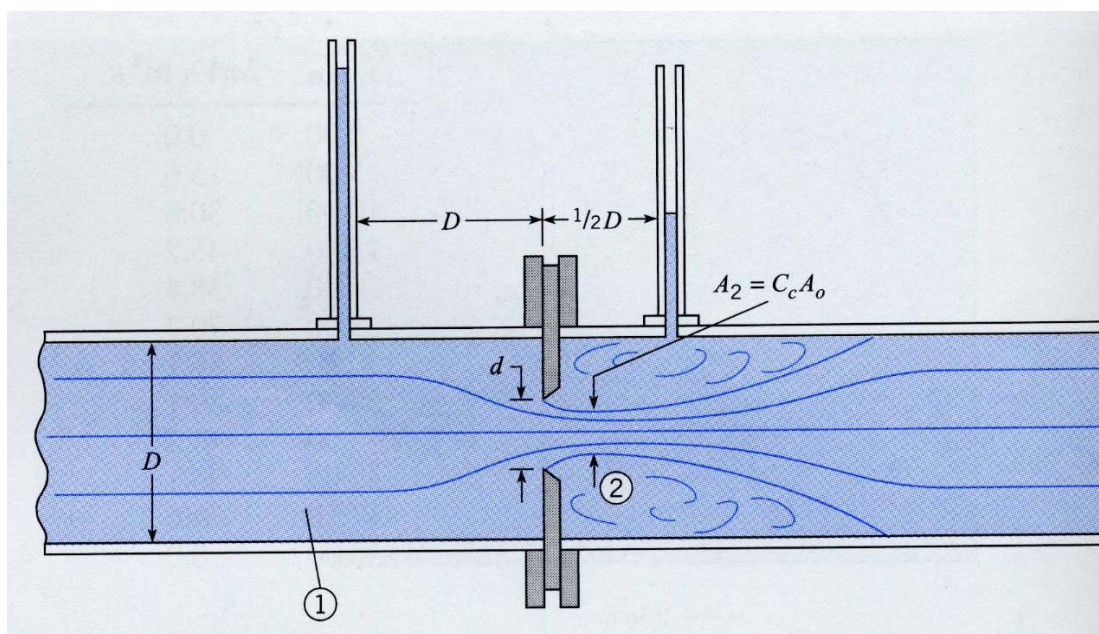
Figure 78 - Flow Separation at an Orifice Flow from [31]

Finally it must be mentioned that both analogies do not describe the case of a perforated sail completely. The holes are distributed all over the sail surface and not only in its center. Moreover there is no internal flow but an external one. That means that it cannot be determined easily what part of the flow really passes through the holes and what part just flows past the sail like in the none-perforated case.

5.1.2   Theory for the Drag Increase by a Cambered Sail

From many pictures about sail boats it is well known that the sails are often blown up by the wind. In fact as per [26] the flat plate or disk is not the shape that yields the highest aerodynamic drag. Bodies that show the shape of a cup or cap may yield remarkably higher drag values. In the figure below the geometry for such a body is shown in two dimensions.

TECHNISCHE
UNIVERSITÄT
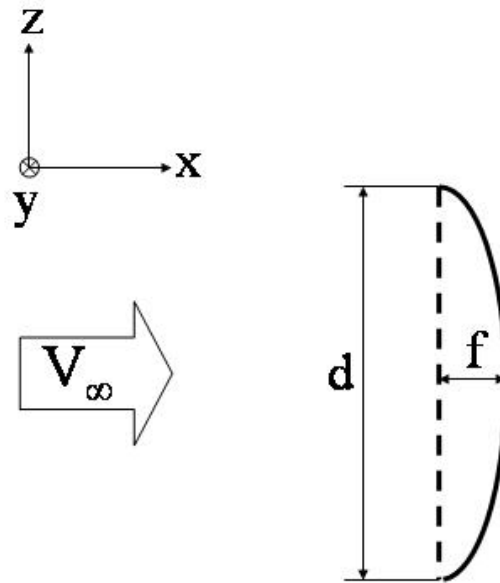MÜNCHEN

Lehrstuhl für Aerodynamik
Technische Universität München
Univ. Prof. Dr. Ing. N. Adams

aer

Figure 79 - Geometry of the Cambered Sail

The camber for such a body is defined to:

$$c = \frac{f}{d} \tag{5.3}$$

The drag coefficient of these bodies is given relative to the area which is projected on the y-z-plane:

$$S = \frac{\pi}{4} d^2 \tag{5.4}$$

In accordance with [26] the maximum drag coefficient for such a body shape is given for a camber of $c = 0.5$ which yields a somewhat hemispherical body. When exceeding this value the body rear side will more and more take the shape of a fairing and hence decrease the downstream pressure drop. Reference [26] also yields the following values for two- and three-dimensional cup-like bodies. They are compared to the values of the flat plate.

Case	$C_{D,2D}$	$C_{D,3D}$
flat plate or disk	1.98	1.17
cup-like body $(c = 0.5)$	2.30	1.42

Table 24- Drag Coefficients for the Flat Plate and the Cup-Like Body from [26]
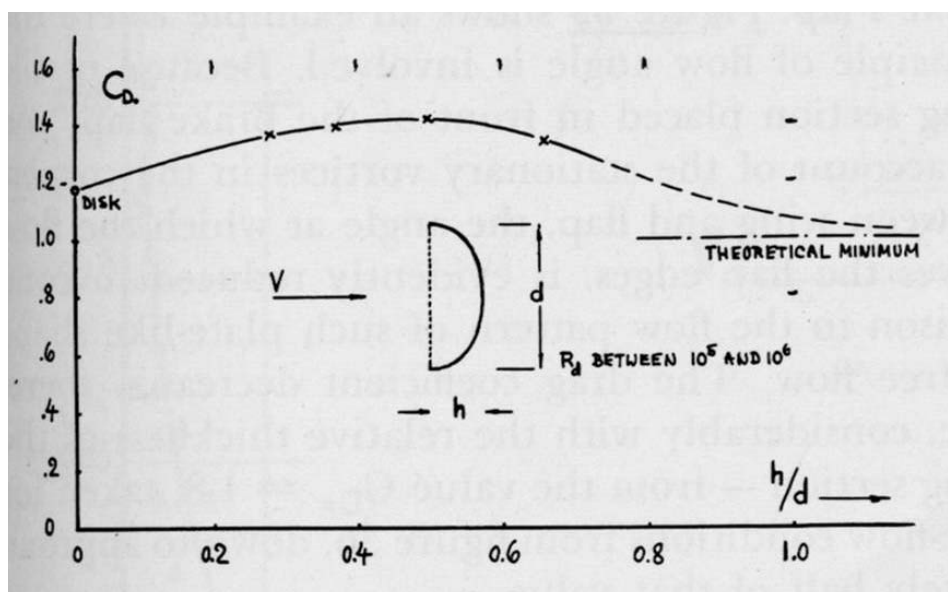
Figure 80 - Drag Coefficient of Different Cambered Cup-like Bodies in 3D from [26]

5.2 Sail Frame and Tested Sails

In order to realize the testing of different sails the standard 6-component-balance is inappropriate. The article has to be mounted on the balance metal sleeve. That is why it would have been very complicated to design and construct a proper frame that is attachable to the balance. Arming the three dimensional model with the different sails would have taken too much time and work.

On these accounts the approach from reference [25] has been copied and advanced. The senior space design team of 2004/2005 used a plastic frame on a metal rod in order to place the sail in the wind tunnel. This metal rod reached through the baseplate and was mounted to the floor.

TECHNISCHE
UNIVERSITÄT
MÜNCHEN

Lehrstuhl für Aerodynamik
Technische Universität München
Univ. Prof. Dr. Ing. N. Adams

aer

Figure 81 - Sail Frame Placed in the Wind Tunnel from [25]

A strain gage was attached to the rod by which the drag of the sail was measured. The frame consisted of two parts so the sail material could be clamped in the frame.

The very same kind of frame was also used for this thesis. Again a metal rod was attached to the frame using the glue substance "J-B-Weld®". The metal rod has the same diameter like the metal center struts of the tinyTEDs. Thus the OBB could also be used for the sail frame. In order to determine the lever arm length it is assumed that the drag force attacks in the very center of the frame.

Figure 82 - Sail Frame with Attached Metal Rod

In order to fix the yaw angle of the frame relative to the balance again a hole was drilled in the end of the metal rod and so the rod was fixed by a bolt and the yaw-fixing-device of the OBB (see chapter 4.2).

TECHNISCHE
UNIVERSITÄT
MÜNCHEN

Lehrstuhl für Aerodynamik
Technische Universität München
Univ. Prof. Dr. Ing. N. Adams

aer

The geometry of the frame is:

$$d_{frame\ inner} = 244mm$$

$$d_{frame\ outer} = 262mm$$

The reference surface is calculated with the outer diameter because the whole frame surface contributes to the drag production:

$$S_{sail\ frame} = \frac{\pi}{4}d^2_{frame\ outer} = 53912.87mm^2$$

Thus the sail frame orientated perpendicular to the free stream yields and blockage factor of:

$$BF_{frame} = \frac{S_{frame}}{A_{test\ section}} = 0.058 \qquad (5.5)$$

Again this blockage factor is slightly above the assumed maximum allowed blockage factor of $BF_{max} = 0.05$ what could be an error source for the measurements.

The frame was mounted to the rod manually. Hence it cannot be guaranteed that the frame is completely aligned with the metal rod. Therefore an initial pitch angle might exist in the first place. With increasing stagnation pressure the drag force and hence the bending moment on the rod will increase. Thus the frame will change its pitch angle with increasing stagnation pressure. Finally the used "J-B-Weld®" is actually meant to attach steel on steel. In the present case however steel is attached to plastic decreasing the rigidity of the assembly.

On these accounts the dynamic pressure had to be limited. The senior space design class of 2004/2005 used a dynamic pressure range of $0.1psf \le q \le 0.5$ and hence this range was also chosen for the frame tests at hand. However the later assessments of the wind tunnel free stream at low stagnation pressures (see chapter 4.5.1) yielded that in this range the flow cannot be considered to be really uniform. For a trade-off between these conflicting constraints figure 49 is consulted again. Here the curve for the tTED indicates that the flow between $q = 0.3psf$ and $q = 0.6psf$ is converging to the state of uniform flow which is considered to be at hand from $q = 0.6psf$ on. So the decision was made to investigate the stagnation pressure range of $0.3psf \le q \le 0.5psf$.

All these constraints and problems do not allow to expecting that the measured values have an accurate magnitude. However like in the case of the tTED and the damaged sails the most interesting feature of these tests is not the absolute change of properties but the relative

change compared to the case of a tight flat sail. That is why it is believed that the measurements. Eventually this concept includes some error sources but it is relatively easy and inexpensive. That is why it was applied.

On the base of the two presented theories of chapter 5.1 various sails were produced. In order to produce the *perforated sails* different tools of different diameters were used. It turned out that the material "rip-stop nylon" is not perfectly appropriate to punch holes in. For many of the used tools the holes have taken an unexpected namely rectangular shape although the used tools had a circular cross section. The four used tools were a small pin, a nail, a screw and a kind of pliers that allows to punching in holes of different sizes.

Figure 83 - Tools Used for Punching in the Holes

In addition to the unexpected shape the holes were also different to the tool diameter. Therefore the hole area was approximated by measuring a sample of holes each. The produced sails are:

Tool	N	$\overline{d}_{hole}$ [mm]	$\overline{A}_{hole}\left[mm^2\right]$	$A_{holes\ total}/S_{sail\ frame}$
Pin	630	0.5	0.196	0.00229
Double Pin	1260	0.5	0.196	0.00458
4 x Pin	2520	0.5	0.196	0.00916
Nail	610	-	3	0.0339
Screw	290	-	12	0.0645
Pliers large	42	10	78.54	0.0612
Pliers medium	610	-	9	0.1018
Pliers small	610	-	6	0.0678

Table 25 - Produced Perforated Sails

TECHNISCHE
UNIVERSITÄT
MÜNCHEN

Lehrstuhl für Aerodynamik
Technische Universität München
Univ. Prof. Dr. Ing. N. Adams

aer

In order to produce the *cambered sails* several circular areas were cut out that exceeded the frame's inner diameter. The overhang $l_{clamp\ excess}$ for clamping the sail into the frame had to be accounted for, too. The actual shape that the sail will adopt when blown up was not known before. In order to have an easy design tool the sail shape was approximated to be linear and by this "design camber" c' the required sail diameter d_{sail} was calculated.
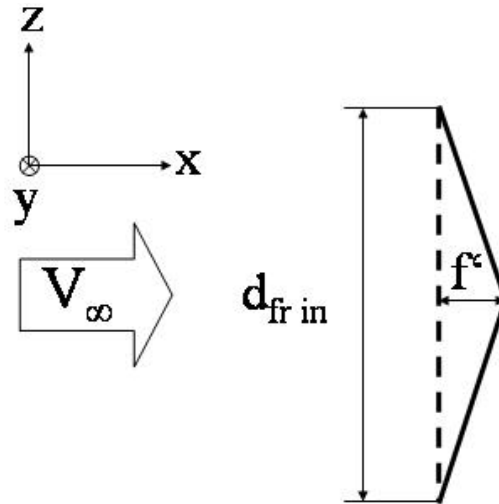

Figure 84 - Definition of "design camber" c'

$$c' = \frac{f'}{d} \tag{5.6}$$

$$d_{sail} = 2\left[\sqrt{\left(\frac{d_{frame\ inner}}{2}\right)^2 + f'^2} + l_{clamp\ excess}\right] \tag{5.7}$$

$$l_{clamp\ excess} = 28mm$$

Using this design equation (5.7) the following sails were produced and tested:

sail shape or design camber c'
flat sail
0.21
0.27
0.38
semi-sphere

Table 26 - Cambered Sails

TECHNISCHE
UNIVERSITÄT
MÜNCHEN

Lehrstuhl für Aerodynamik
Technische Universität München
Univ. Prof. Dr. Ing. N. Adams

aer

After the first tests the sail appeared to adopt the shape of a somewhat round shell. With that assumption the final cambered sail was produced in order to adopt the shape of a semi-sphere and hence to yield the maximum drag. The diameter to cut out was chosen so that it would cover half of the surface of a spherical shell with the diameter $d_{frame\ inner} = 244mm$.

Figure 85 - Semi-Sphere Sail

Concerning the cambered sails another error source must be attended. As stated above the actual shape of the blown up sail cannot be predicted easily. The OBB however still is based on the assumption that the drag force attacks in the very center of the sail frame. Considering the real shape it can happen that the pressure distribution about the sail deviates from the ideally symmetric state and hence the resulting force attacks not in the center of the frame. This leads to somewhat falsified measurements of the OBB.

Finally it was also investigated if the effects of holes and camber may be superimposed and yield an even higher drag. The same techniques as described above were used to produce the following sail.

Tool	N	$\overline{d}_{hole}$ [mm]	$\overline{S}_{hole}\left[mm^2\right]$	$S_{holes}/S_{sail\ frame}$	c'
Nail	610	-	3	0.0339	0.38

Table 27 - Sail for Investigating the Superimposition of the Two Concepts

TECHNISCHE
UNIVERSITÄT
MÜNCHEN

Lehrstuhl für Aerodynamik
Technische Universität München
Univ. Prof. Dr. Ing. N. Adams

aer

5.3 Results of the Sail Frame Tests

(Note: Again in this chapter there are average drag coefficients whose average is taken over the Reynolds number range.)

The mentioned sails were tested in the NCSU Subsonic Wind Tunnel. The frame was placed in the test section so that its surface was perpendicular to the fee stream. The Reynolds number is calculated with the outer frame diameter:

$$\mathrm{Re}_{frame} = \frac{\rho_\infty \cdot V_\infty \cdot d_{frame\ outer}}{\mu_\infty} \tag{5.8}$$

As described in the previous chapter the initial dynamic pressure range included again the attempt to simulate Reynolds numbers as low as possible. The chart of the case "flat sail" at this Reynolds number range can be seen in the figure below.
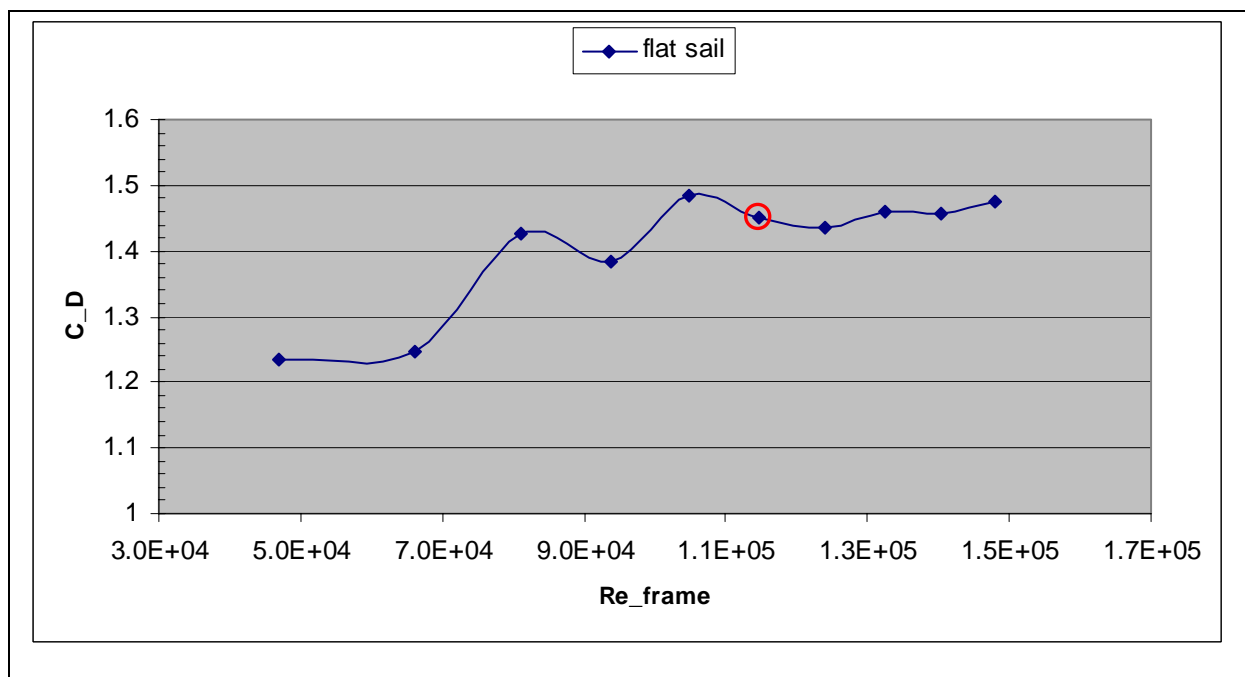

Figure 86 - C_D for the Case "Flat Sail" versus a Large Re_frame Range

In the previous chapter the assumption was made that the flow within the dynamic pressure range of $0.3\,psf \leq q \leq 0.6\,psf$ is converging toward a uniform state. In the chart above the corresponding data point for $C_D\left(q = 0.3\,psf\right)$ is marked red. The developing of the C_D values to the right of this marked data point seems to validate the assumption and hence in the remainder of this chapter the measurements are investigated for the dynamic pressures of:

$$0.3\,psf \leq q \leq 0.5\,psf \tag{5.9}$$

143

This corresponds to a Reynolds number range of about:

$$1.1 \cdot 10^5 \leq \mathrm{Re}_{frame} \leq 1.5 \cdot 10^5 \qquad (5.10)$$

The measurements of the perforated sails have yielded the following charts. As a reference the case "flat sail" is also included.
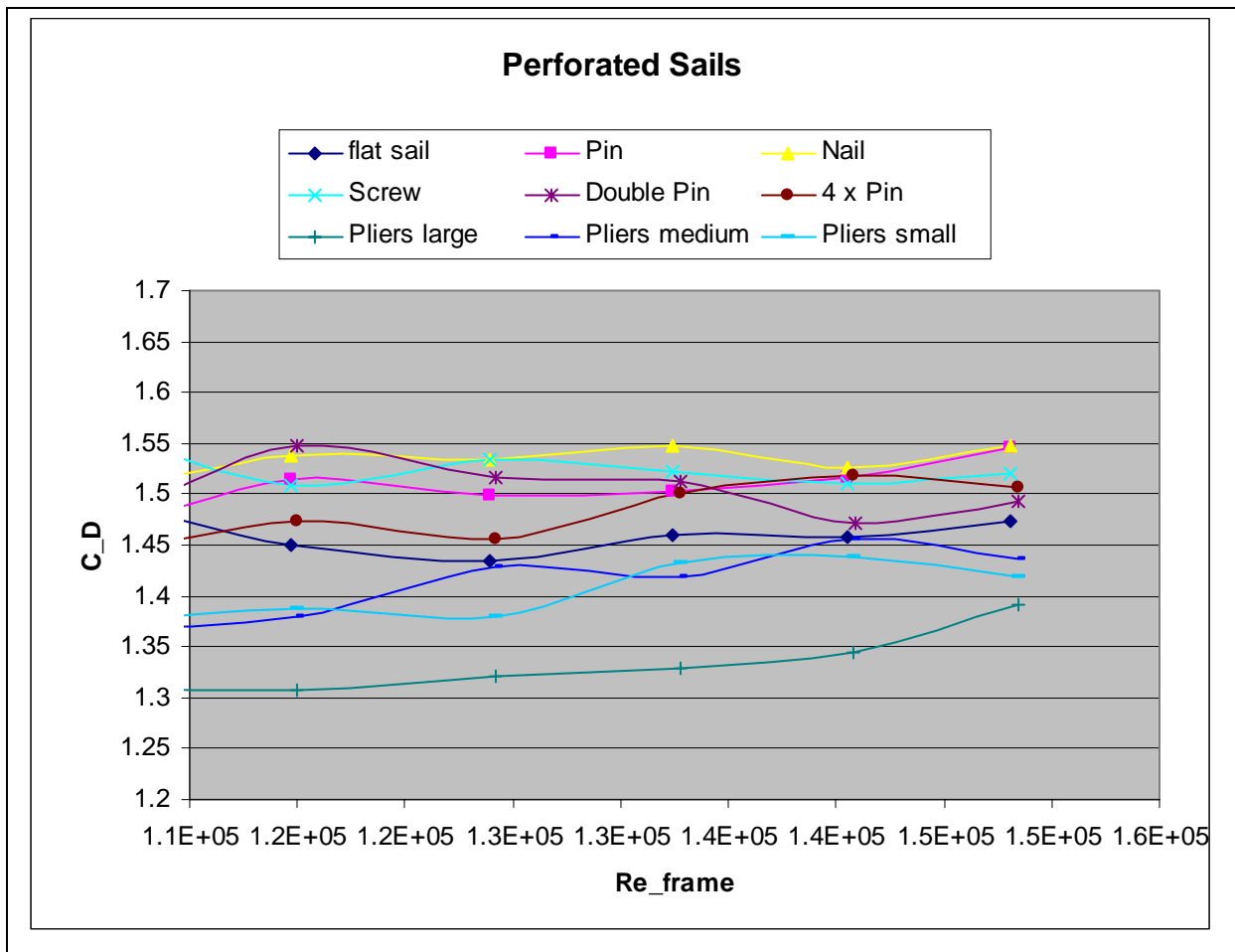

Figure 87 - C_D versus Re_frame for Perforated Sails

From the chart above it becomes obvious that all cases in which the holes were punched in with the pliers yield a lower drag than the reference case of the flat sail. That is why they are ruled out for the further investigation.

In the next chart the drag coefficients are depicted relative to the reference case of the flat sail which consequently appears as a horizontal line at the value of one.

$$C_{D,relative} = \frac{C_{D,i}}{C_{D,flat\ sail}} \qquad (5.11)$$
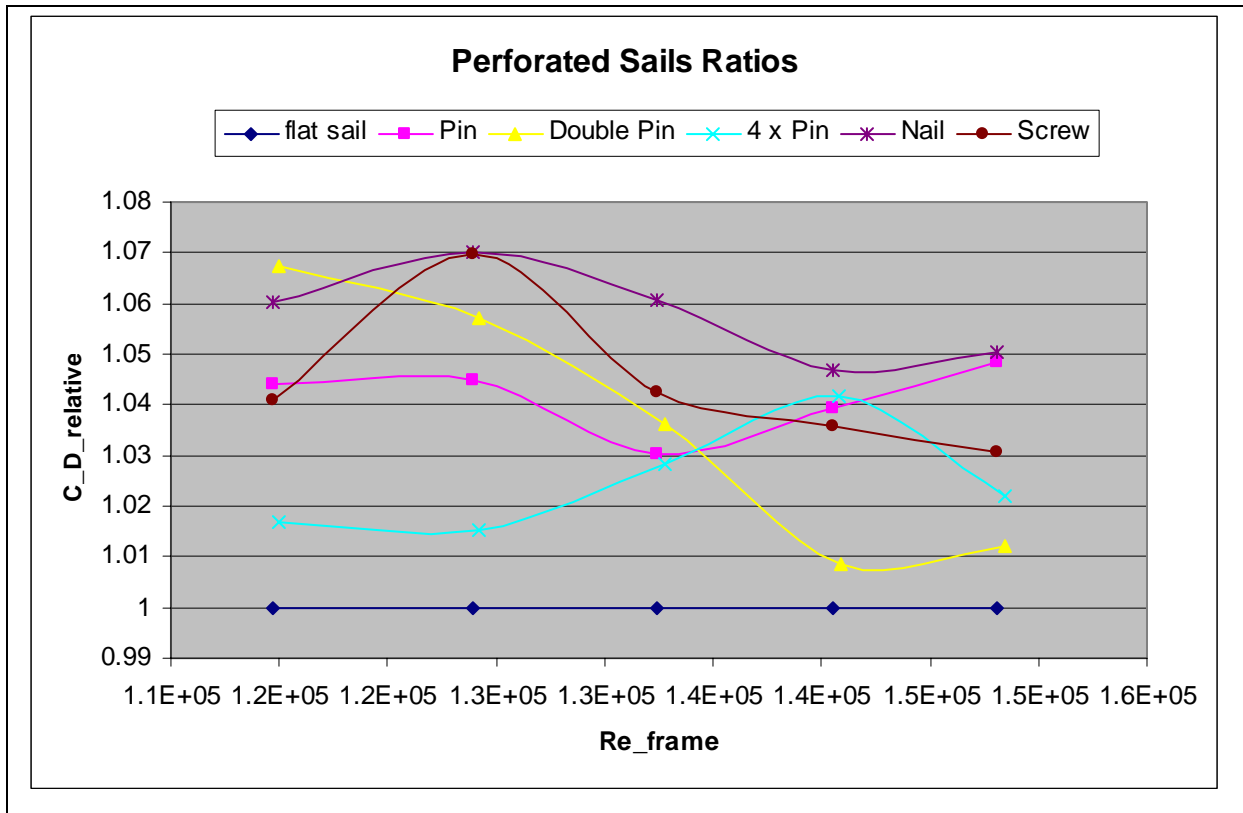
i = case of perforated sail

TECHNISCHE
UNIVERSITÄT
MÜNCHEN

Lehrstuhl für Aerodynamik
Technische Universität München
Univ. Prof. Dr. Ing. N. Adams

aer

Figure 88 - Relative C_D versus Re_frame for Perforated Sails

From this chart is gets obvious that the case "Nail" yields the highest drag increase. Taking the average over the relative drag coefficient provides $\bar{C}_{D,relative,nail} = 1.058$. Hence on average the nail holes increase the drag of the sail about 5.8%.

This result is somewhat surprising when the assumed theory of chapter 5.1 is considered. There it was assumed that the drag would increase the more the smaller the holes are. However comparing the pin holes with the nail holes already falsifies this assumption. It was then supposed that more small holes would also produce a larger pressure drop and therefore a larger drag increase. However the comparison between the pin hole cases also falsifies this assumption. Neither of these cases is able to reach the drag increase of the nail holes. Hence it is finally concluded that there may also be hole diameters that are too small in order to produce the desired effect. The explanation for that might be found in eq.(5.2). Here the pressure difference will rise with increasing volume flow. If the punched holes are too small they might not be able to pass a volume flow big enough to produce a big pressure difference. On the other hand especially the case "Pliers large" also indicates that there are also too large hole diameters. The theoretical limit for the surface decrease by the holes is gained by

TECHNISCHE
UNIVERSITÄT
MÜNCHEN

Lehrstuhl für Aerodynamik
Technische Universität München
Univ. Prof. Dr. Ing. N. Adams

aer

reducing all holes to a single hole in the center of the sail. Then the condition $\frac{d_{hole}}{d_{Disk}} \leq 0.25$.

can be applied which yields

$$\left.\frac{A_{holes\ total}}{S_{sail}}\right|_{max} = \frac{\pi/4\,d_{hole}^2}{\pi/4\,d_{sail}^2} = \frac{\left(0.25 \cdot d_{sail}\right)^2}{d_{sail}^2} = 0.0625 \qquad (5.12)$$

In table 25 it can be seen that the cases "Screw", "Pliers large" and "Pliers small" show an area ratio close to that assumed limiting value. However it was established in figure 87 that all Pliers cases are not able to increase the drag of the sail.

Actually it would then be concluded that the area of a single hole of these cases is too large. Indeed the case "Screw" shows an even bigger single hole area but an drag increase. Form this fact it may be concluded that not only the total hole area matters but also the pattern of the holes. In fact the screw holes had a larger mutual distance than the "Pliers small" holes because they were only about half of the amount of the "Pliers small" holes. The single hole diameter of the case "Pliers large" however seems to mark or exceed the upper diameter limit.

Table 25 shows that perforated sail of the case "Nail" has not yet reached the limit of the assumed maximum total hole area of $\left.\frac{A_{holes\ total}}{S_{frame}}\right|_{max} = 0.06$. Consequently a "Nail" case with more namely N=1078 holes might yield an even higher drag. However this fact was only found after the analysis of the experimental data. Due to limitations in the availability of the wind tunnel (it was use during the hole period of the thesis also by classes and students from other projects) this case could not be tested any more. It is therefore passed over to a later point in time or the application of a CFD tool.

In any case it seems to be very desirable go on with the optimization research with an appropriate CFD tool that allows to investigating various cases more easily than this experimental approach. The experimental data however seems to be very useful for validating the results of such a CFD tool.

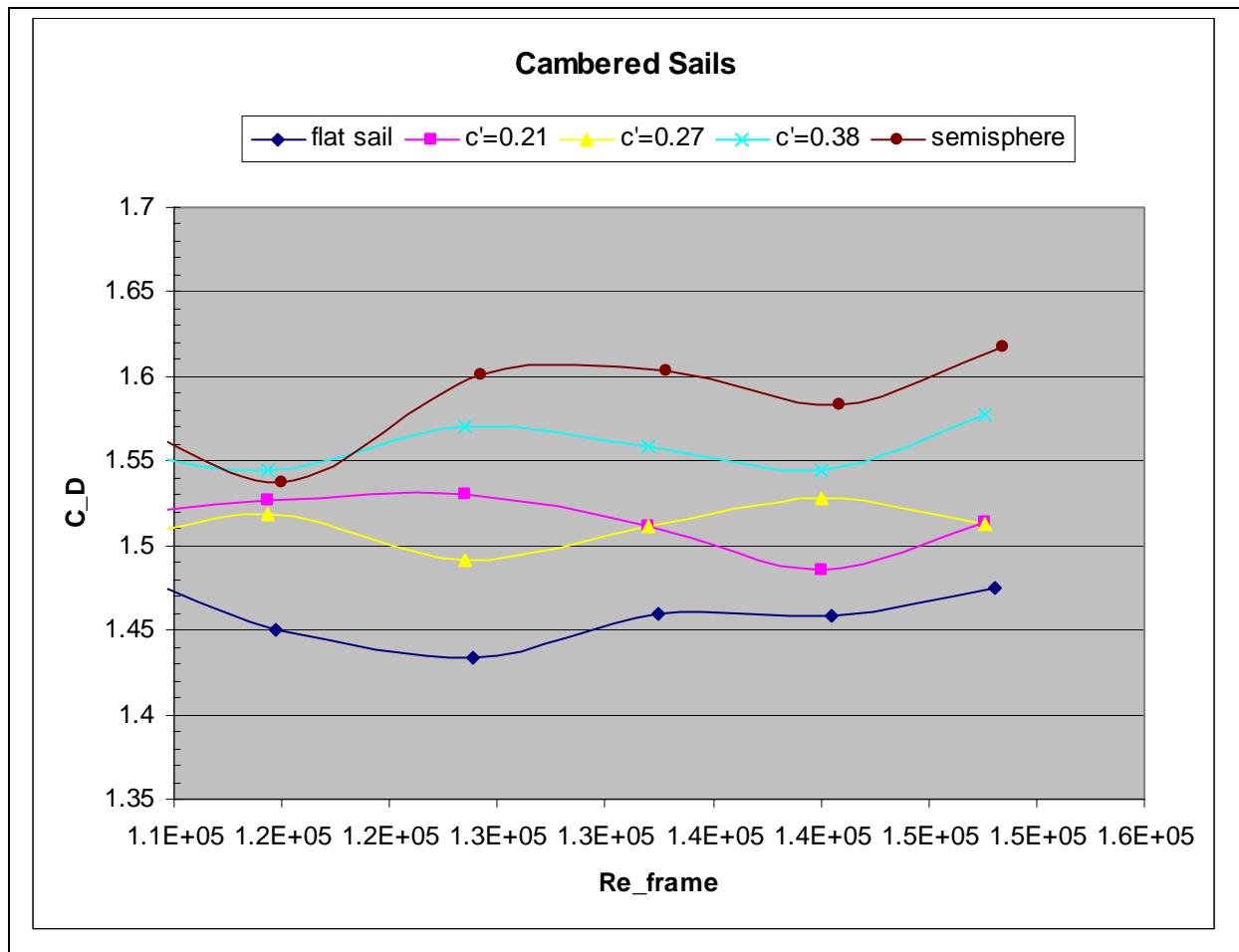The testing of the *cambered sails* has provided the following results.

Figure 89 - C_D versus Re_frame for Cambered Sails

For the sake of further clarity also these results are depicted in terms of the relative drag coefficient just like the perforated sails:

$$C_{D,relative} = \frac{C_{D,i}}{C_{D,flat\ sail}}$$
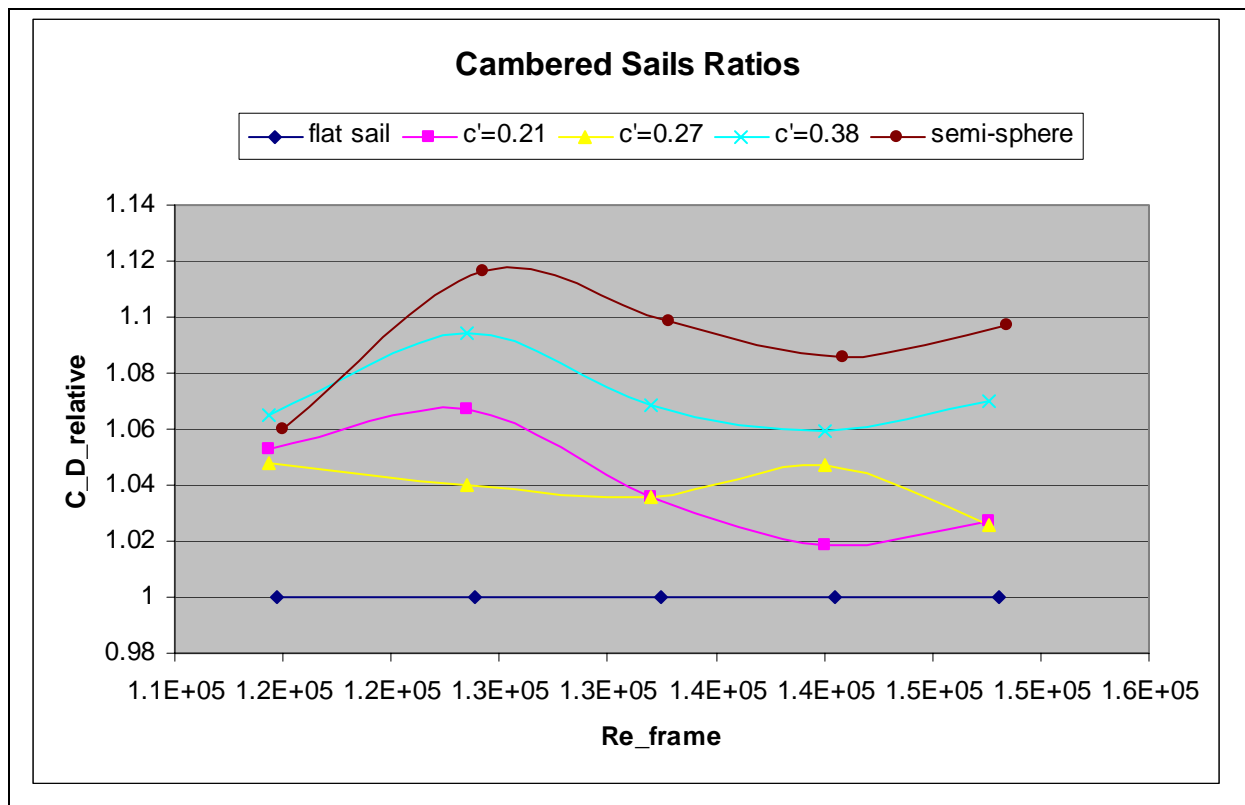
(5.13)

i = cambered sail

Figure 90 - Relative C_D versus Re_frame for Cambered Sails

In contrast to the perforated sails the cambered sails yield little surprise. The largest average drag coefficient is provided by the semi-sphere-like sail with $\overline{C}_{D,relative} = 1.092$ or a drag increase of 9.2%. Hence the trend seems to be confirmed that up to the camber of $c = 0.5$ (semi-sphere) the drag coefficient is rising steadily.

TECHNISCHE
UNIVERSITÄT
MÜNCHEN

Lehrstuhl für Aerodynamik
Technische Universität München
Univ. Prof. Dr. Ing. N. Adams

aer

Finally the test of the sail with camber and holes yielded an unexpected result. In the figure below this case is shown compared to the sails with the single feature each.
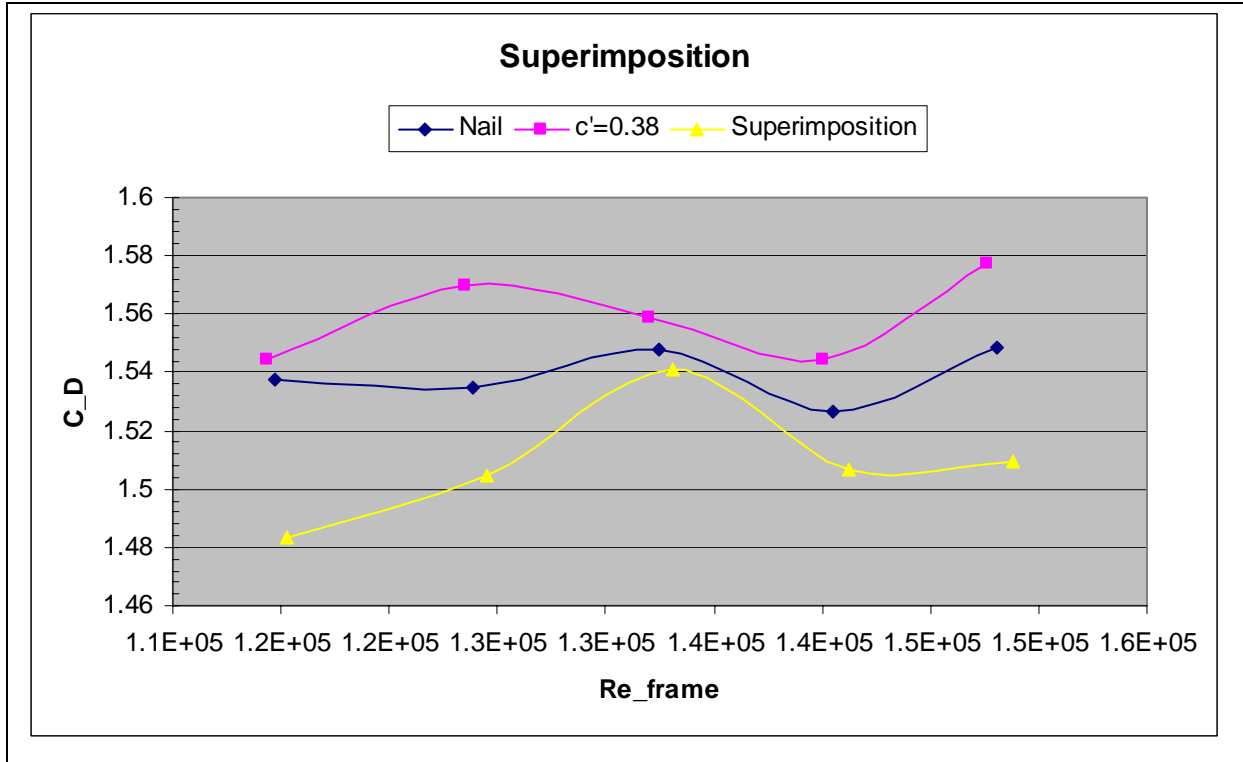

Figure 91 - Superimpostion of Sail Camber and Sail Perforation

Quite obviously the superimposition not only is not able to increase the drag further but both effects seem to affect each other negatively. So the drag for the perforated and cambered sail is lower than for the sails that show only a single effect each.

The reason for that is hard to conclude. Certainly the sail camber alters the flow field downstream of the sail compared to the case of a flat sail.

In spite of punching in the holes only to the center surface that is equivalent to the flat sail $\left(S_{center} = \frac{\pi}{4} d_{frame\ inner}^2 \right)$ most of the holes will not be aligned with the free stream direction due to the camber. Thus many created pressure differences will not point in the drag direction and consequently contribute less to the resulting drag force. The drag gain by the orifice flows is decreased thereby.

On the other hand the holes decrease the sail surface that produces the drag in combination with the pressure difference. That is why the drag increasing camber effect cannot work as effectively as with a non-perforated sail.
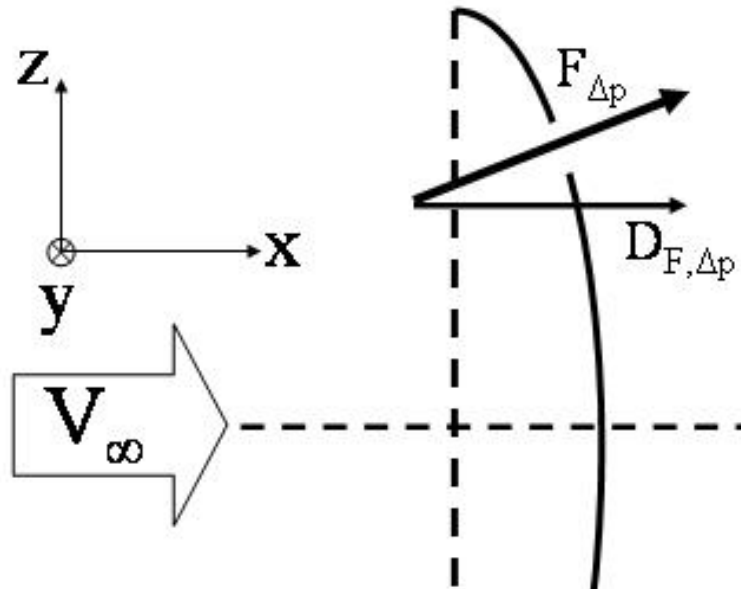
TECHNISCHE
UNIVERSITÄT
MÜNCHEN

Lehrstuhl für Aerodynamik
Technische Universität München
Univ. Prof. Dr. Ing. N. Adams

aer

Figure 92 - Sketch for Explaining the Superimpostion Effect

Eventually it is concluded that superimposing the perforated sail and the cambered sail will not yield in a higher drag for the TW. The final reasons however should be again investigated by a proper CFD tool.

5.4 Conclusion and Application on the tTED2

In figure 45 the drag coefficient for the flat disk is given to $C_{D,disk} = 1.17$ and from [26] the maximum drag coefficient for the cup-like hemispherical three-dimensional body is known to be $C_{D,semi-shpere} = 1.42$. Compared to the Reynolds number averaged magnitudes of the sail frame experiments these values show differences of:

$$\Delta C_{D,disk} = \overline{C}_{D,flat\ sail} - C_{D,disk} = 1.46 - 1.17 = 0.29$$

$$\Delta C_{D,semi-sphere} = \overline{C}_{D,semi-sphere} - C_{D,semi-sphere} = 1.59 - 1.42 = 0.17$$

That shows that the measurements apparently exaggerate the real magnitude of the sail frame drag. Besides of the error sources of the OBB described in chapter 4.2 also the blockage factor of the frame might play a role. As mentioned in chapter 5.2 this factor is $BF_{frame} = 0.058$ and therefore above the assumed maximum of $BF_{max} = 0.05$. Hence the drag coefficient increases relative to the real case as described in chapter 2.2. Nevertheless especially the relative values for the drag increase seem to yield reasonable data.

TECHNISCHE
UNIVERSITÄT
MÜNCHEN

Lehrstuhl für Aerodynamik
Technische Universität München
Univ. Prof. Dr. Ing. N. Adams

aer

The final obvious step in this chapter is the application of the improved sails on the tTED2. For reasons of drag increase this actually would be the semi-spherical cambered sail. However one important system aspect argues against this choice. In chapter 3.1.4 it is described that the TW energy supply is supposed to consist of a solar array mounted on the MIS and therefore in the center of the TW. Of course the solar cells will only produce electrical energy when illuminated by the sun rays. Indeed there are more imaginable orientations of the TW, its sails and the sun that lead to a shading of the solar cells in case of the cambered sails than in case of the flat sails. That is why unless the sail material is not changed to a transparent material the usage of cambered sails is ruled out.

So it was chosen to produce a set of "Nail" sails for the tTED2. The hole density thereby was kept constant with respect to the smaller sail area of the tTED2 compared to the sail frame.

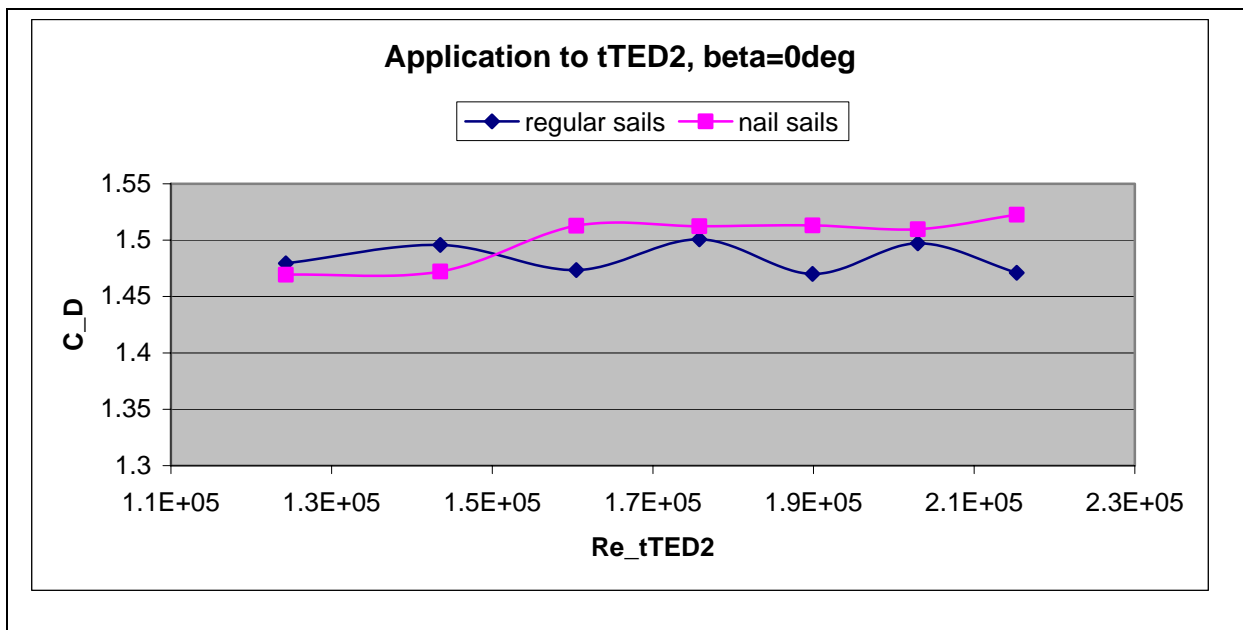The application of the "Nail" sails on the tTED2 has yielded the following results.

Figure 93 - C_D tTED2, "Nail" Sails and Regular Sails, Beta=0°

TECHNISCHE
UNIVERSITÄT
MÜNCHEN

Lehrstuhl für Aerodynamik
Technische Universität München
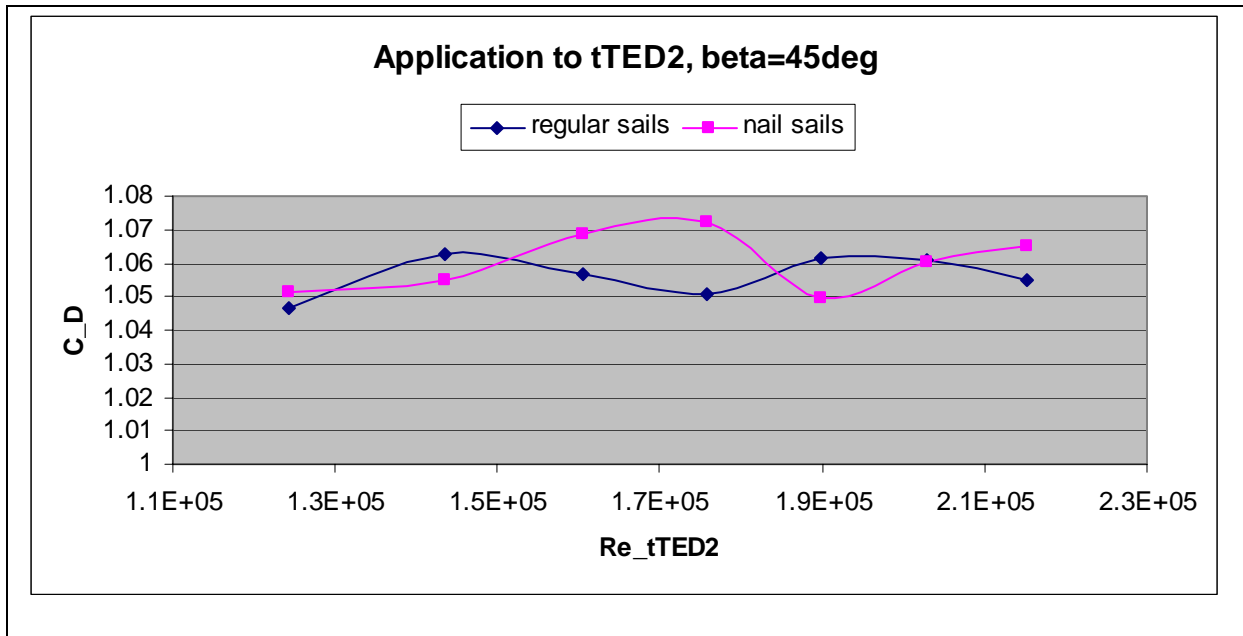Univ. Prof. Dr. Ing. N. Adams

aer

Figure 94 - C_D tTED2, "Nail" Sails and Regular Sails, Beta=45°

The ratios between the average drag coefficients of the "Nail" sails and the regular sails are:

$$\frac{\overline{C}_{D,nail}}{\overline{C}_{D,reg}}\left(\beta = 0°\right) = 1.012$$

$$\frac{\overline{C}_{D,tTED2,nail}}{\overline{C}_{D,tTED2,reg}}\left(\beta = 45°\right) = 1.0037$$

So the drag could be increased between 1.2% and 0.37% what is far less compared to the sail frame increase of 5.8%. The reasons for this are hard to assess.

One issue might be the large contribution of the tTED2 structure to the total drag that was already observed in connection with the damaged sails in chapter 4.6. Apparently this part of the drag production is not affected by a different type of sails.

The lower increase for a higher yaw angle might be explainable with the analogy to the orifice flow. When changing the yaw angle the free stream will not approach the sails and their holes perpendicular any more. So the flow through the holes might be decreased.

Altogether these final results of the sail optimization research again point towards the application a CFD analysis. The flow field of the three-dimensional model together with the orifices is expected to be pretty complex. That is why a further systematic experimental investigation appears to be very time, work and maybe cost intense.

TECHNISCHE
UNIVERSITÄT
MÜNCHEN

Lehrstuhl für Aerodynamik
Technische Universität München
Univ. Prof. Dr. Ing. N. Adams

aer

6 Investigation of the Tumbleweed's Wake Flow

During the tests on the beach in the summer 2005 the wake flow about the resting TED was investigated. First field measurements provided some hints that there is a vortex flow downstream of the Tumbleweed (see chapter 3.2.2). In order to further investigate this wake flow and its vortices the visualization of this flow region is necessary. It is hoped that the dimensions of the wake flow and the frequencies and sizes of the vortices and their shedding can be looked into. Additionally the ability would be very desirable if not only the resting but also the rolling TW could be investigated. In fact the rolling TW is expected to yield an altered namely unsteady flow field.

6.1 Improvised Smoke Channel

The NCSU subsonic wind tunnel does not provide the ability to visualize a wake flow field by means of smoke or similar visualizing techniques. Additionally there is no device at hand that could simulate a boundary layer flow, either. In order to get the models spinning in the tunnel a shear flow is necessary, though.

On these accounts it was decided to build an improvised smoke channel and use the model tinyTED in order to simulate the TW wake field. The nomenclature for this channel and the remainder for this chapter can be seen from the figure below.
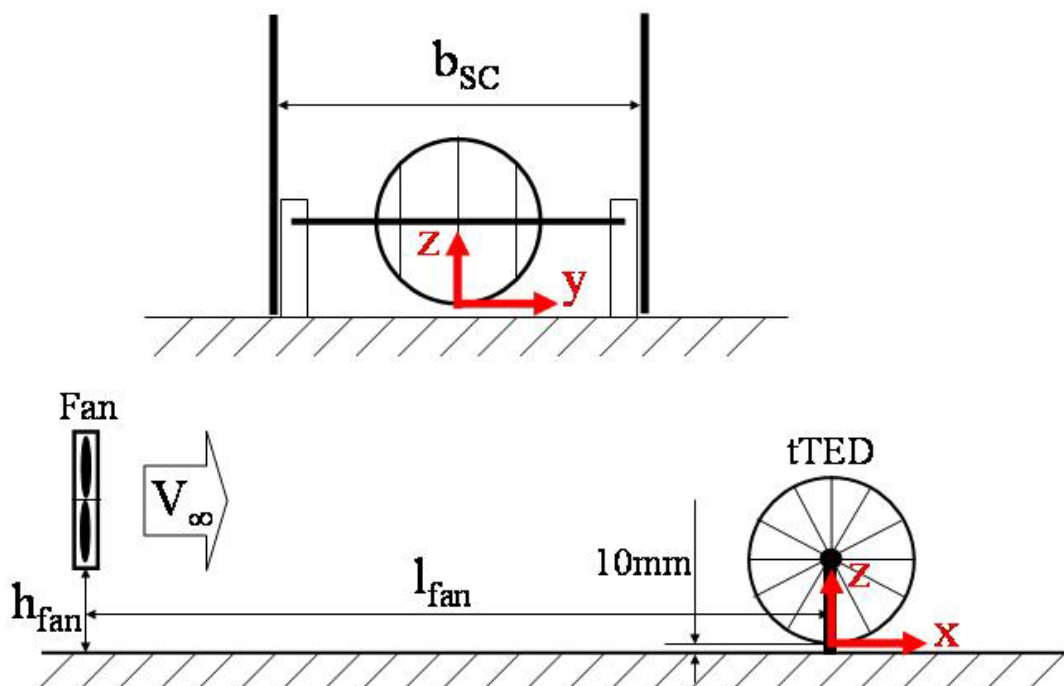

Figure 95 - Nomenclature for the Improvised Smoke Channel

TECHNISCHE
UNIVERSITÄT
MÜNCHEN

Lehrstuhl für Aerodynamik
Technische Universität München
Univ. Prof. Dr. Ing. N. Adams

aer

A metal rod was stuck through both of the tTED hubs and two simple wooden supporting stands have been constructed. To each of these stands a ball bearing has been attached by using a metal shackle. The height of the ball bearings was chosen so that there is a gap of about 10mm between the tTED and the ground. By this construction the tTED can spin freely about its center strut. In addition a metal sheet with an attached nut was mounted laterally to each wooden stand. The nut approximately aligns with the ball bearing and thus an axial force can be exerted on the tTED center strut by a bolt that is screwed through the nut. Thus the revolution velocity can be decreased. Moreover this device ensures the center strut will not slide out of the ball bearings while spinning. In order to fix the pitch angle and simulate the resting TED a wooden wedge was stuck between the stand and the center strut.
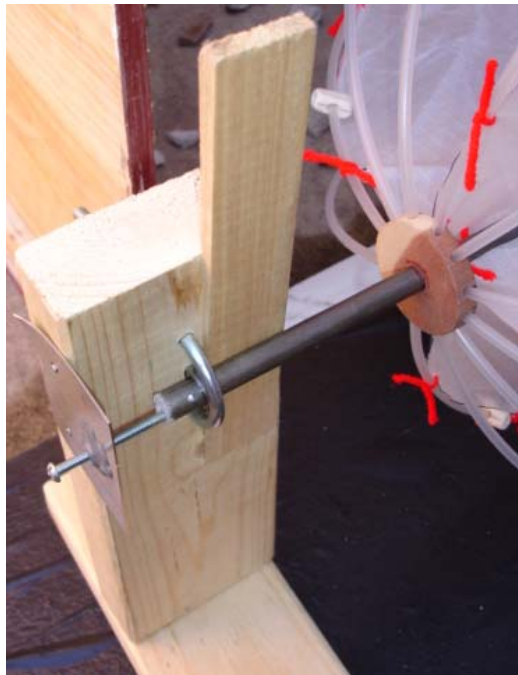
Figure 96 - Wooden Supporting Stand with Ball Bearing, Axial Screw, Pitch Angle Fixing Wedge

The general concept is to use a COTS fan to generate a somewhat defined flow velocity profile. Two parallel boards were put on the ground in order to form a channel in front of the tinyTED. Another board could be used to confine the channel to the top if necessary. However the final design did not require this top board.

In order to force the fan flow into a shear flow that somehow resembles a boundary layer profile some research in the appropriate literature has been conducted. Thereby several concepts could be identified that were first applied in the 1950s and 1960s. Additionally it was also considered to apply the chosen concept to the NCSU Subsonic Wind Tunnel. These concepts are described in the references [11], [14] and [15].

TECHNISCHE
UNIVERSITÄT
MÜNCHEN

Lehrstuhl für Aerodynamik
Technische Universität München
Univ. Prof. Dr. Ing. N. Adams

aer

The approach of reference [11] is to place an obstacle on the floor upstream of the test section. Immediately downstream of this obstacle some vortex generators are placed in order to mix the created velocity non-uniformity to the upper flow layers and thus create a shear profile. However this concept requires a fetch length upstream of the test section that cannot be provided by the NCSU Subsonic Wind Tunnel.

In reference [15] it is suggested to use a grid of unevenly spaced plates. The spacing between the plates grows towards the top. Onto the plates two wooden pieces are glued in spanwise direction near the leading edge and the trailing edge in order to impress a desired turbulence level in the flow. This approach again has requirements that cannot be matched by the NCSU Wind Tunnel. In the case of reference [15] it was possible to roll a plate rack in front of the test section of the wind tunnel. Of course that is not possible in the NCSU Subsonic Wind Tunnel and every other imaginable method to mount the plates in the tunnel turned out to be very complicated if not unfeasible.

Therefore the attention was finally focused on the approach of reference [14]. Herein and in some subsequent papers that are not referenced in this thesis it is suggested to use a grid of circular rods. These rods are also unevenly spaced with increasing spacing towards the top. The disadvantage however is that no defined turbulence may be impressed on the flow. Additionally the created flow that is described in [14] is a linear shear flow rather than a logarithmical boundary layer profile (see chapter 2.2.2). However it was supposed that by the appropriate rod spacing a boundary layer profile might be approximated.

A rack was constructed that basically consists of two metal bars mounted on two wooden plates. Several metal angles are clamped on the bars with small clamps thus the spacing between the rods is freely adjustable to some extent. For the first tests three sets of wooden rods were purchased having the diameters of $d_{rod,1} = 12.7mm\left(0.5"\right)$, $d_{rod,2} = 9.525mm\left(3/8"\right)$ and $d_{rod,3} = 6.35mm\left(1/4"\right)$. All components could be purchased from a local DIY-store and hence this first grid could be constructed for relatively low costs.

Figure 97 - Shear Grid in the Improvised Smoke Channel

The next step was to determine the velocity profile that develops in the plane where the tinyTED is supposed to be placed. Therefore the pitot-static-tube that is regularly mounted in the wind tunnel's test section was used. The stagnation pressure can be read off from an older water scale that has to be leveled out on the floor with the help of two water levels. This readout device is a pretty large and heavy one and it could therefore hardly be transported to another place. That is why the flow measurements had to be carried out in the NCSU Wind Tunnel room.

Knowing the current ambient air density allowed to calculating the flow velocity from the dynamic pressure after eq(2.6). In order to know the height in which the current velocity was measured the pitot-static-tube was equipped with several marks. The mark for the reference height $z=0$ was placed so that the pitot-static-tube's tip orifice was 10mm above the ground. This height is equivalent to the very bottom of the supported tinyTED. The tube was then fixed by a clamp that in turn was placed on a beam that was finally supported on the channel boards.

TECHNISCHE
UNIVERSITÄT
MÜNCHEN

Lehrstuhl für Aerodynamik
Technische Universität München
Univ. Prof. Dr. Ing. N. Adams

aer

Figure 98 - Pitot-Static-Tube Read-Out Device (left), Marks (center) and Mounting (right)

The pitot-static-tube works on the following principle. On its very tip an orifice is drilled in. If the tube is orientated so that this orifice faces the free stream normally the total pressure may be detected by this drilling. At some distance downstream of this tip orifice some more and smaller orifices are drilled in radially. Thus their inlet areas will be parallel to the flow and therefore will measure the static pressure of the flow. By comparing the total and the static pressure the stagnation pressure can be gained. From this working principle it gets obvious that the pitot-static-tube must be aligned with the free stream that is the pitch and yaw angle must be zero.

In the case at hand this requirement is met by two different measures. The pitch angle is determined by a water level. Since no finite value has to be measured but it has only to make sure that the pitch angle is zero this approach was considered to be sufficient. In order to

adjust the yaw angle three red lines were drawn on the floor. Theses red lines were perpendicular to the y-z-plane. Moreover one line was drawn in the center of the channel (y=0mm) and the two others were displaced to y=100mm and y=200mm, the latter marking one end of the tinyTED. The pitot-static-tube was aligned with these lines in order to adjust its yaw angle at zero degree.

Figure 99 - Adjustment of the Pitot-Static Tube Pitch Angle (left) and Yaw Angle (right)

Two different fans were used in order to simulate the shear flow towards the tinyTED. They were placed at various distances upstream of the tinyTED and also their height was changeable. The first one has a rectangular cross section of $546.1mm \times 546.1mm$ (consequently the blades are slightly smaller than this) and is therefore bigger than the tinyTED. Its revolution velocity can be switched between three stages. After the first runs however it was found that this fan can not provide the desired flow field at all. The shear grid was not able to alter the undisturbed flow field positively enough, either and when using a simple obstacle at some distance downstream of the fan the tinyTED even spun in the wrong direction namely against the wind. It was concluded that the fan provides a much too non-uniform flow field due to its large blades. In combination with the confinement through the ground the flow is faster near the ground than further above what seems to be even enhanced by the obstacle. A measured flow velocity profile for the undisturbed flow can be seen in the figure below. The measurements were conducted at $l_{fan} = 1.83m \left(6\,ft. \right)$ and $h_{fan} = 0$.

TECHNISCHE
UNIVERSITÄT
MÜNCHEN

Lehrstuhl für Aerodynamik
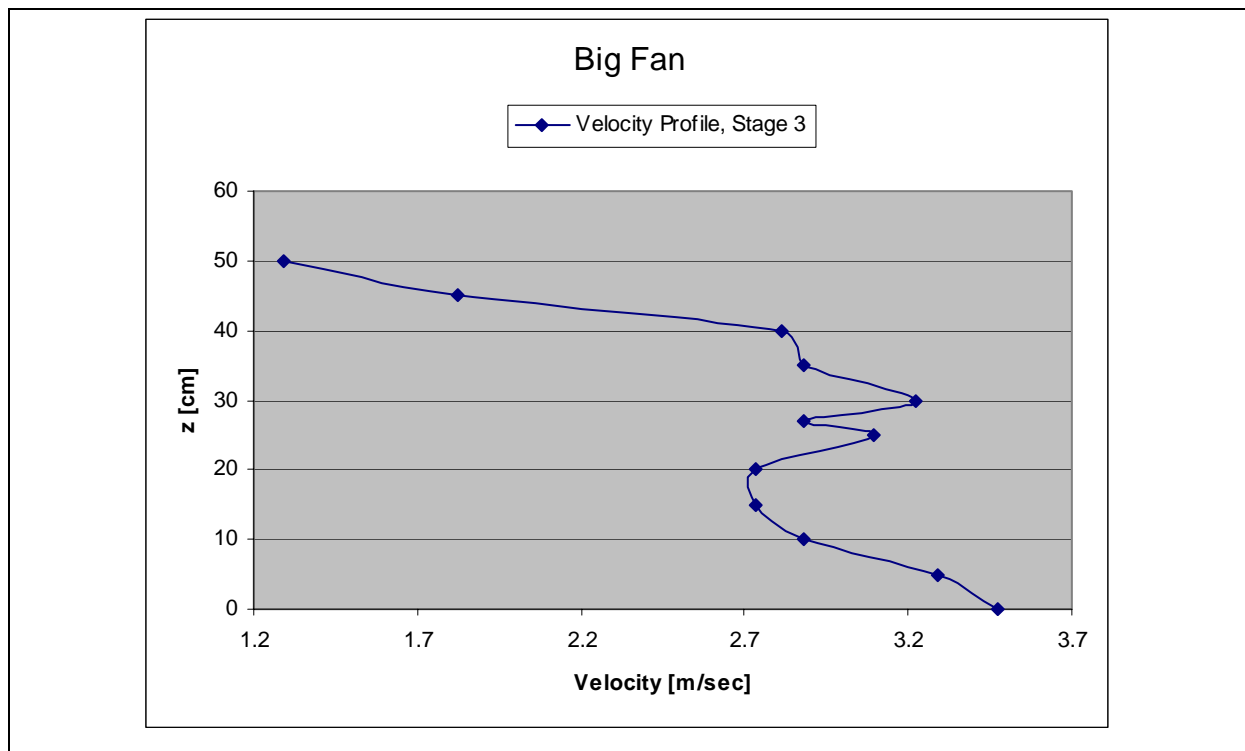Technische Universität München
Univ. Prof. Dr. Ing. N. Adams

aer

Figure 100 - Velocity Profile of the Big Fan at l_fan=1.83m

Due to these results a smaller fan was chosen. It only has got a diameter of $d_{fan,small} = 220mm$ and hence the velocity of its blade tips is smaller than for the big fan. The fan is placed on the center line of the channel (y=0) and the flow field of this fan is expected to be more uniform.

Figure 101 - Tested COTS Fans

Unfortunately the next tests that included the smaller fan and the shear grid yielded again that the grid is not able to create the desired shear flow. Two reasons come into questions for that. First the described tests in reference [14] were conducted at a flow velocity of $V = 22.86\,m/\text{sec}$. This value cannot be provided by the small fan at all. Second in [14] tests

TECHNISCHE
UNIVERSITÄT
MÜNCHEN

Lehrstuhl für Aerodynamik
Technische Universität München
Univ. Prof. Dr. Ing. N. Adams

aer

were conducted in a wind tunnel that means that the flow upstream of the grid is assumed to be uniform. This assumption is not valid for the COTS fan, either. The fan will impress a swirl on the flow that might decay to some extent until reaching the shear grid but certainly the flow will not change to a completely uniform flow. On all theses accounts the usage of the shear grid was eventually abandoned for the improvised smoke channel.

Instead another approach was chosen that relied strongly on a trial-and-error process. The small fan was placed at several heights and distances upstream of the plane of measurement. Thereby the flow leaving the fan should get the opportunity to diffuse in a way that yields a somewhat uniform flow and the desired boundary layer profile in the plane of measurement. The desired velocity profile was derived from the ideal Martian profile that is described in chapter 2.2.2. It is described mathematically by the equation:

$$V_{\infty,M}\left(z\right) = \frac{u_*}{k}\ln\left(\frac{z}{z_0}\right) \tag{6.1}$$

In order to keep the geometrical similarity the surface roughness is down-scaled by the diameter ratio of the tTED and the TW:

$$z_{0,SC} = \frac{d_{tTED}}{d_{TW}} \cdot z_0 = \frac{1}{15} \cdot 0.03m = 0.002m \tag{6.2}$$

The friction velocity from chapter 2.2.2 for Martian conditions is transformed to the smoke channel conditions by using the Reynolds number. The "friction velocity Reynolds numbers" of the TW and the tTED are set equal:

$$\mathrm{Re}_{TW,*} = \frac{\rho_M \cdot u_{*,M} \cdot d_{TW}}{\mu_M} = \frac{\rho_E \cdot u_{*,SC} \cdot d_{tTED}}{\mu_E} = \mathrm{Re}_{tTED,*} \tag{6.3}$$

$$u_{*,M} = 0.55\frac{m}{\sec}, \; \rho_M = 0.0156\frac{kg}{m^3}, \; \mu_M = 1.1 \cdot 10^{-5} Pa\sec, \; d_{TW} = 6m$$

The Martian friction velocity of $u_{*,M} = 1\frac{m}{\sec}$ creates a velocity profile that corresponds to the published average wind speed of $V_{\infty,M} = 10\frac{m}{\sec}$. Hence the Martian friction velocity was adjusted in order to provide a velocity profile that represents an average Martian wind speed within the published range of $2\frac{m}{\sec} \le V_{\infty,M} \le 10\frac{m}{\sec}$.

The eq.(6.3) can be solved for the friction velocity that defines the ideal velocity profile in the smoke channel:

$$u_{*,SC} = \text{Re}_{TW,*} \cdot \frac{\mu_E}{\rho_E \cdot d_{tTED}} \qquad (6.4)$$

$$\mu_E = 1.824 \cdot 10^{-5} \, Pa\sec, \ \rho_E = 1.19 \frac{kg}{m^3}, \ d_{tTED} = 0.4m$$

$$u_{*,SC} = 0.1815 \frac{m}{\sec} \qquad (6.5)$$

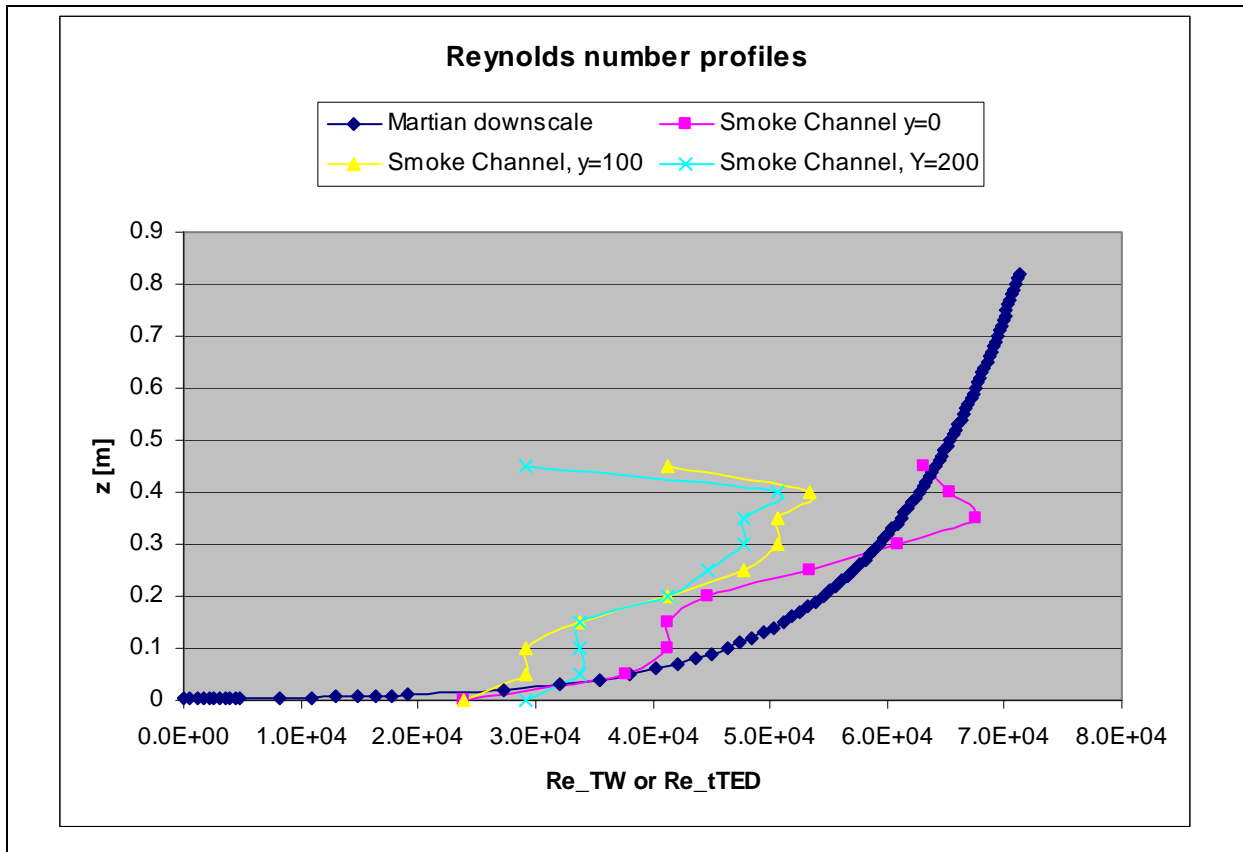$$V_{SC,ideal}(z) = \frac{0.1815 \, m/\sec}{0.4} \ln\left(\frac{z}{0.002m}\right) \qquad (6.6)$$

During the trial-and-error phase several combinations of the fan-tTED-distance and the fan-height have been tested. Thereby one goal was to locate the fan as far as possible upstream of the tTED in order to give the flow enough time to develop. The limiting case therefore was the distance for which the tTED would not spin about its center strut any more.

The final smoke channel setup that has been found in this trial-and-error process is:

l_{fan} [mm]	1524
h_{fan} [mm]	238
b_{SC} [mm]	500

Figure 102 - Final Smoke Channel Setup with the Small Fan

The measured velocity profiles of this setup in x=0 and y=0, y=100mm and y=200mm can be seen in the chart below. The profiles are compared to the model profile of eq.(6.6). Moreover the decisive parameter for dynamic similarity is rather the Reynolds number than the actual flow velocity. That is why the profiles are depicted in terms of the Re_{tTED} and Re_{TW}, respectively.

TECHNISCHE
UNIVERSITÄT
MÜNCHEN

Lehrstuhl für Aerodynamik
Technische Universität München
Univ. Prof. Dr. Ing. N. Adams

aer

Figure 103 - Flow Profile for the Improvised Smoke Channel versus the Martian Model Profile

The flow field shows some similarity to the model profile. Especially at the channel center line y=0 the profile matches the desired one to some extend. Considering that the tTED reaches up to about z=0.41m the achieved flow profile seems to be acceptable. Furthermore the tTED is spinning steadily about its center strut when exposed to this flow profile.

Through a smoke source the flow is loaded with smoke particles. These particles are supposed to visualize the streamlines / flow pattern about the tTED and thus provide the possibility to determine the appearance and dimensions of the wake flow.

Finally some stones were placed upstream and downstream of the tTED in order to simulate Martian ground conditions. The prevailing rock size thereby was $h_{rock,M} = 0.25m$ that was downscaled with the diameter ratio $\dfrac{d_{tTED}}{d_{TW}} = \dfrac{1}{15}$ to about $h_{stone,E} \cong 17mm$.

TECHNISCHE
UNIVERSITÄT
MÜNCHEN

Lehrstuhl für Aerodynamik
Technische Universität München
Univ. Prof. Dr. Ing. N. Adams

aer

The wind profile in figure 103 is equivalent to the Martian wind profile of $V_{\infty,M}(z) = \frac{0.55\,m/\sec}{0.4}\ln\left(\frac{z}{0.03}\right)$. The arithmetic average wind speed of this Martian profile between z=0 and z=6m is $\bar{V}_{\infty,M}\big|_{0m}^{6m} = 5.98\frac{m}{\sec}$. The goal is to determine the corresponding TW translational velocity at this wind speed. From this velocity its rotational frequency and hence its Strouhal number can be determined. The Strouhal number in turn will ideally be matched by the spinning tTED. The spinning tTED however is stationary that means that the smoke channel flow profiles represent the relative wind on the TW. Consequently the average Martian wind of $\bar{V}_{\infty,M}\big|_{0m}^{6m} = 5.98\frac{m}{\sec}$ is the relative average wind on the TW: $\bar{V}_{r,1,TW} = 5.98\frac{m}{\sec}$.

In order to determine the rotation velocity of the TW the equilibrium between aerodynamic drag force and rolling resistance is investigated:

$$D_{TW} = F_{R,TW} \tag{6.7}$$

$$\bar{C}_{D,TW}(\beta = 45°) \cdot q_M \cdot S_{TW} = \mu_{R,M} \cdot m_{TW} \cdot g_M \tag{6.8}$$

$$q_M = \frac{\rho_M}{2}\bar{V}_{r,2,TW}^2 = \frac{\rho_M}{2}\left(\bar{V}_{\infty,M,2}\big|_{0m}^{6m} - W_{TW}\right)^2$$

$$\bar{V}_{r,2,TW} = \bar{V}_{\infty,M,2}\big|_{0m}^{6m} - W_{TW} = \sqrt{\frac{\mu_R m_{TW} g_M}{\bar{C}_D(\beta = 45°)\cdot\frac{\rho_M}{2}\cdot S_{TW}}} \tag{6.9}$$

$$S_{TW} = 28.274m^2,\ g_M = 3.72\frac{m}{\sec^2},\ \rho_M = 0.0156\frac{kg}{m^3}$$

From reference [32] the values for the medium rolling resistance coefficient and the desired maximum TW mass are:

$$\mu_{R,M} = 0.075,\ m_{TW} = 20kg$$

From chapter 4.5 the average drag coefficient for the rolling TW and its preferred rolling orientation is:

$$\bar{C}_D(\beta = 45°) = 0.893.$$

So the wind speed that is needed to keep the TW (with the properties described above) rolling is:

$$\bar{V}_{r,2,TW} = 5.32\frac{m}{\sec}$$

TECHNISCHE
UNIVERSITÄT
MÜNCHEN

Lehrstuhl für Aerodynamik
Technische Universität München
Univ. Prof. Dr. Ing. N. Adams

aer

That means that the created relative flow profile deviates from the physical necessary flow profile about $\Delta \bar{V}_{r,TW} = 0.66 \frac{m}{\sec}$. The created flow profile is slightly too high. Taking into account the hassles to create this flow profile however it seemed not feasible to adjust the profile with a reasonable effort in time, work and money. So the tests were conducted with the flow profile at hand.

In eq.(6.9) it can be seen that the translational velocity of the TW is not easy to determine because the absolute average Martian wind $\bar{V}_M \big|_{0m}^{6m}$ speed is not known. Hence an assumption has to be made. As per chapter 2.2.2 the Martian wind range near the ground is $2\frac{m}{\sec} \leq \bar{V}_M \leq 10\frac{m}{\sec}$. The relative flow velocity in order to keep the TW rolling is $\bar{V}_{r,2,TW} = 5.32\frac{m}{\sec}$. Hence the translational speed of the TW can be between the differences of the wind speed range and this relative flow velocity: $0 < W_{TW} < 4.68\frac{m}{\sec}$. Apparently a steady rolling motion will only occur for values distinctly larger than zero. For this thesis an arbitrary value of 1m/sec is chosen: $1\frac{m}{\sec} \leq W_{TW} \leq 4.68\frac{m}{\sec}$. For this velocity range it is possible to determine a frequency and hence a Strouhal number range.

The circumference of the TW is $c_{TW} = \pi \cdot 6m = 18.85m$. The period for one rotation is:

$$T_{TW} = \frac{c_{TW}}{W_{TW}} \tag{6.10}$$

Thus the period range is:

$$4.02\sec \leq T_{TW} \leq 18.85\sec$$

The time period and the frequency are related after:

$$f_{TW} = \frac{1}{T_{TW}} \tag{6.11}$$

Thus the frequency range is approximately:

$$0.05\frac{1}{\sec} \leq f_{TW} \leq 0.25\frac{1}{\sec}, \; 3.2rpm \leq f_{TW} \leq 15rpm$$

Lehrstuhl für Aerodynamik
Technische Universität München
Univ. Prof. Dr. Ing. N. Adams

TECHNISCHE
UNIVERSITÄT
MÜNCHEN

aer

The similarity parameter that governs the unsteady flow field is the Strouhal number that is defined in chapter 2.1 and is also known as the dimensionless frequency. The Strouhal number for the TW is:

$$Sr_{TW} = \frac{f_{TW} \cdot d_{TW}}{\bar{V}_{r,2,TW}} \tag{6.12}$$

Thus the Strouhal number range is:

$$0.056 \leq Sr_{TW} \leq 0.282$$

The Strouhal number of the spinning tTED is supposed to match the Strouhal number of the rolling TW in order to achieve the similarity of both unsteady flow fields. From the assessment of the TW geometry and the drag coefficient it is expected that the unsteady flow field will have a periodicity of four repeats per TW rotation. However the same is true for the TED so the number of four will be canceled on both sides of the equation. Eventually the required frequency range of the spinning tTED can be determined with this requirement.

$$Sr_{TW} = Sr_{tTED} = \frac{f_{tTED} \cdot d_{tTED}}{\bar{V}_{tTED}} \tag{6.13}$$

The value for the average flow velocity on the tTED $\bar{V}_{tTED}$ is determined by calculating the arithmetic average of the three measurement rows of y=0, y=100mm and y=200mm and then averaging these gained averages mutually again. So the average flow velocity on the tTED is $\bar{V}_{\infty,tTED} = 1.65\frac{m}{\sec}$. With this value the required rotational frequency range for the tTED can be determined to:

$$f_{tTED} = Sr_{TW} \cdot \frac{\bar{V}_{\infty,tTED}}{d_{tTED}} \tag{6.14}$$

$$0.231\frac{1}{\sec} \leq f_{tTED} \leq 1.16\frac{1}{\sec}, \ 13.86rpm \leq f_{tTED} \leq 69.6rpm$$

TECHNISCHE
UNIVERSITÄT
MÜNCHEN

Lehrstuhl für Aerodynamik
Technische Universität München
Univ. Prof. Dr. Ing. N. Adams

aer

6.2 Smoke Tests and Results

Several test runs were conducted with the improvised smoke channel and the tTED in the loading bay just outside of the workshop of Research Building II on Centennial Campus. The tests were conducted with a COTS fireworks smoke grenade and a so-called smoke-pen. This smoke-pen is normally used for the testing of ventilation, air balancing, smoke detectors etc..

Figure 104 - Smoke Grenade, Smoke Pen (left) and Smoke Duct, Smoke-Pen on a Stick (right)

After the first grenade applications it got apparent that the produced smoke is not very focused but rather diffusive. That is why from one of the PVC-pipes a duct was constructed that has a nozzle-like outlet at one end. The smoke pen was taped to a metal stick in order to place it inside of the wake field without generating major disturbances of the flow.

The location was chosen because there the smoke did not bother the fire detection devices that are present in every university building. Moreover the smoke could drain off much more easily than in any room inside a building. A disadvantage of this outside location is the potential disturbance of the flow field by wind gusts. That is why the test area was confined to some extent by the building walls and wooden boards. However this confinement in turn enhanced the accumulation of the smoke especially for the smoke grenade application and consequently from each smoke grenade test run only the first few seconds could be reasonably analyzed for solid data. After this period of time the distinction between the smoke in the wake field and the accumulated smoke residuals was very hard if not impossible.

TECHNISCHE
UNIVERSITÄT
MÜNCHEN

Lehrstuhl für Aerodynamik
Technische Universität München
Univ. Prof. Dr. Ing. N. Adams

aer

The test runs were recorded with different digital video cameras from a side view and from a top view. Then the footage was analyzed with the Software "Ulead Video Studio 9 ®" in order to alter the footage features like color and contrast and in order to get single pictures out of the movies.

The tests were conducted with a resting tTED at $\alpha = 0°, \beta = 0°$, $\alpha = 45°, \beta = 0°$ and with a spinning tTED $\alpha = \alpha(t), \beta = 0°$. The spinning frequency could be altered a little. However it turned out that the constructed device to exert a retarding axial force on the spinning center strut did not have the desired level of sophistication to adjust a large frequency range.
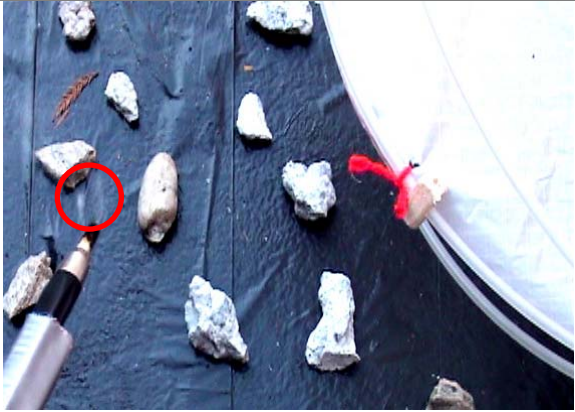
In general it turned out that unfortunately both means of smoke generation could not provide a fully satisfactory flow visualization. While the smoke grenade produced a very dense smoke even with the constructed smoke duct it was not possible to generate a nicely defined smoke streak. For every grenade application the wake field was filled with a more diffusive smoke pattern than with clearly defined streamlines. That is why it was not possible within this thesis to investigate the frequencies of the vortex shedding properly. Furthermore the dimensions of the wake field could not be determined satisfactorily, either. These tasks must be turned over to other aerodynamic experimental sites that have more sophisticated flow visualization capabilities.
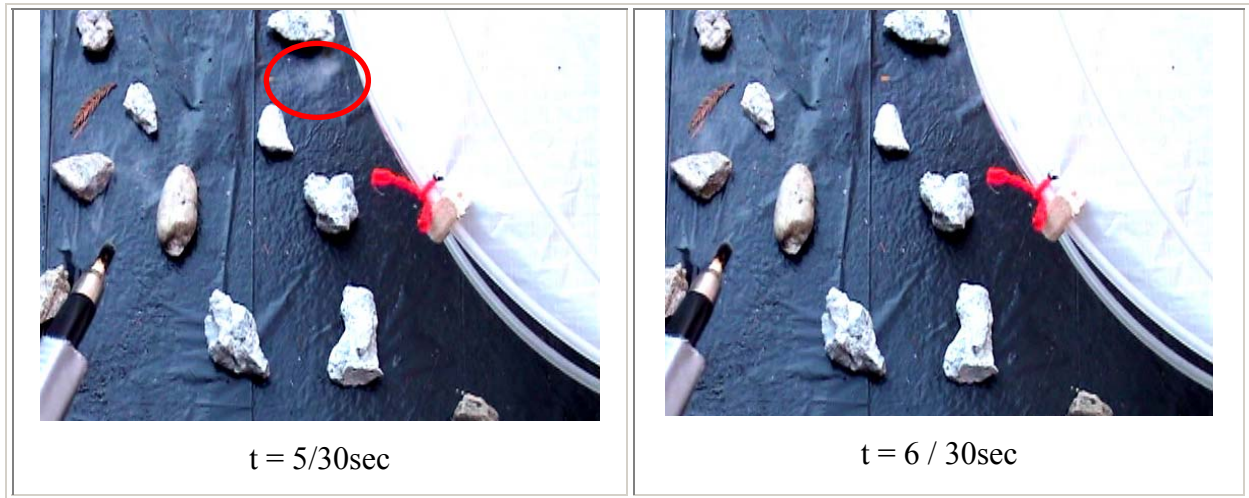
Eventually the results of the conducted tests are all constrained to approximations.

6.2.1   Resting tTED

In chapter 3.2.2 it is assumed that the resting TED is comparable to a flat plate perpendicular to the free stream direction. In figure 26 the wake pattern of this case is shown and the field measurements with the TED on the Outer Banks gave the first indications that this assumption holds true. The flow velocities on the center axis downstream of the TED all pointed towards the TED that is against the free stream direction. In figure 25 this velocities are marked yellow.
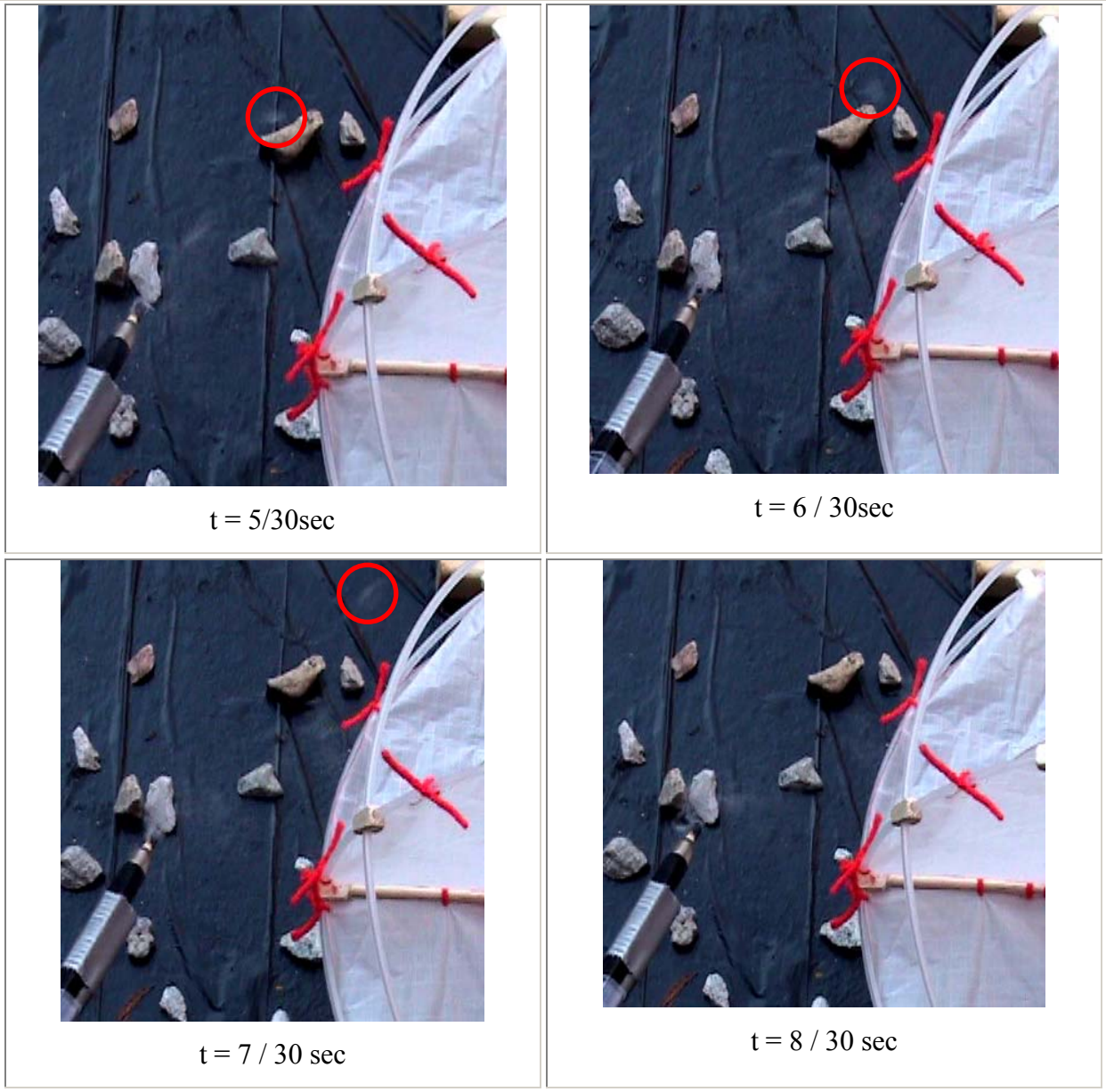
Sequence #1 gives further hints that this assumption is correct. The small fluid element within the red circle is flowing towards the tTED with increasing time and hence against the free stream direction.

TECHNISCHE
UNIVERSITÄT
MÜNCHEN

Lehrstuhl für Aerodynamik
Technische Universität München
Univ. Prof. Dr. Ing. N. Adams

aer

Sequence #1	
Smoke Source	smoke pen
View	top
Free Stream Direction	from right to left
fixed tTED pitch angle [°]	0
time period [sec]	6/30 = 0.2
smoke pen position [mm]	x=230; y=150; z=200

t = 0sec

t = 2/30sec

t = 3/30sec

t = 4/30sec

TECHNISCHE
UNIVERSITÄT
MÜNCHEN

Lehrstuhl für Aerodynamik
Technische Universität München
Univ. Prof. Dr. Ing. N. Adams

aer

| t = 5/30sec | t = 6 / 30sec |

Furthermore the theory for the flat plate in figure 26 predicts two vortex regions next to the center axis. In sequence #2 a small fluid element is marked red again. It is clearly moving form the center axis laterally towards the tTED edge indicating the existence of a vortex similar to figure 26. Sequence #3 shows the very same behavior for the opponent side relative to the center axis. Moreover a smoke streak evolves for a very short time that gives an impression of the streamlines of the vortex.

TECHNISCHE
UNIVERSITÄT
MÜNCHEN

Lehrstuhl für Aerodynamik
Technische Universität München
Univ. Prof. Dr. Ing. N. Adams

aer

Sequence #2	
Smoke Source	smoke pen
View	top
Free Stream Direction	from right to left
fixed tTED pitch angle [°]	0
time period [sec]	7/30 = 0.2333
smoke pen position [mm]	x=230; y=0; z=200

t = 0sec

t = 1/30sec

t = 2/30sec

t = 3/30sec

t = 5/30sec

t = 6 / 30sec

t = 7 / 30 sec

t = 8 / 30 sec

TECHNISCHE
UNIVERSITÄT
MÜNCHEN

Lehrstuhl für Aerodynamik
Technische Universität München
Univ. Prof. Dr. Ing. N. Adams

aer

Sequence #3	
Smoke Source	smoke pen
View	top
Free Stream Direction	from right to left
fixed tTED pitch angle [°]	0
time period [sec]	10/30 = 0.333
smoke pen position [mm]	x=230; y=0; z=200

t = 0sec

t = 1/30sec

t = 4/30sec

t = 5/30sec

TECHNISCHE
UNIVERSITÄT
MÜNCHEN

Lehrstuhl für Aerodynamik
Technische Universität München
Univ. Prof. Dr. Ing. N. Adams

aer

t = 6/30sec

t = 7 / 30sec

t = 8 / 30 sec

t = 9 / 30 sec

t = 10/30sec

Finally in sequence #4 also one vortex for the side view could be captured. It exists only a very short period of time before diffusing but from the sequence two things can be concluded. First for the resting TW there are not only vortices with a vertical rotational axis but also vortices with a horizontal rotational axis. Second there are horizontal vortices with a length scale of $d_{vortex,tTED} \cong 66.67mm$. Translated to the TW this means $d_{vortex,TW} \cong 1000mm$.

Sequence #4	
Smoke Source	smoke pen
View	side
Free Stream Direction	from left to right
fixed tTED pitch angle [°]	45
time period [sec]	4/30 = 0.1333

t = 0sec

t = 1/30sec

t = 2/30sec

t = 3/30sec

TECHNISCHE
UNIVERSITÄT
MÜNCHEN

Lehrstuhl für Aerodynamik
Technische Universität München
Univ. Prof. Dr. Ing. N. Adams

aer

t = 4/30sec

A sequence #11 is also attached to this thesis on CD-ROM as "sequence#11.mpg". It was not possible to get solid pictures out of this sequence but the movie might provide a good impression of the horizontal vortices downstream of the resting tTED.
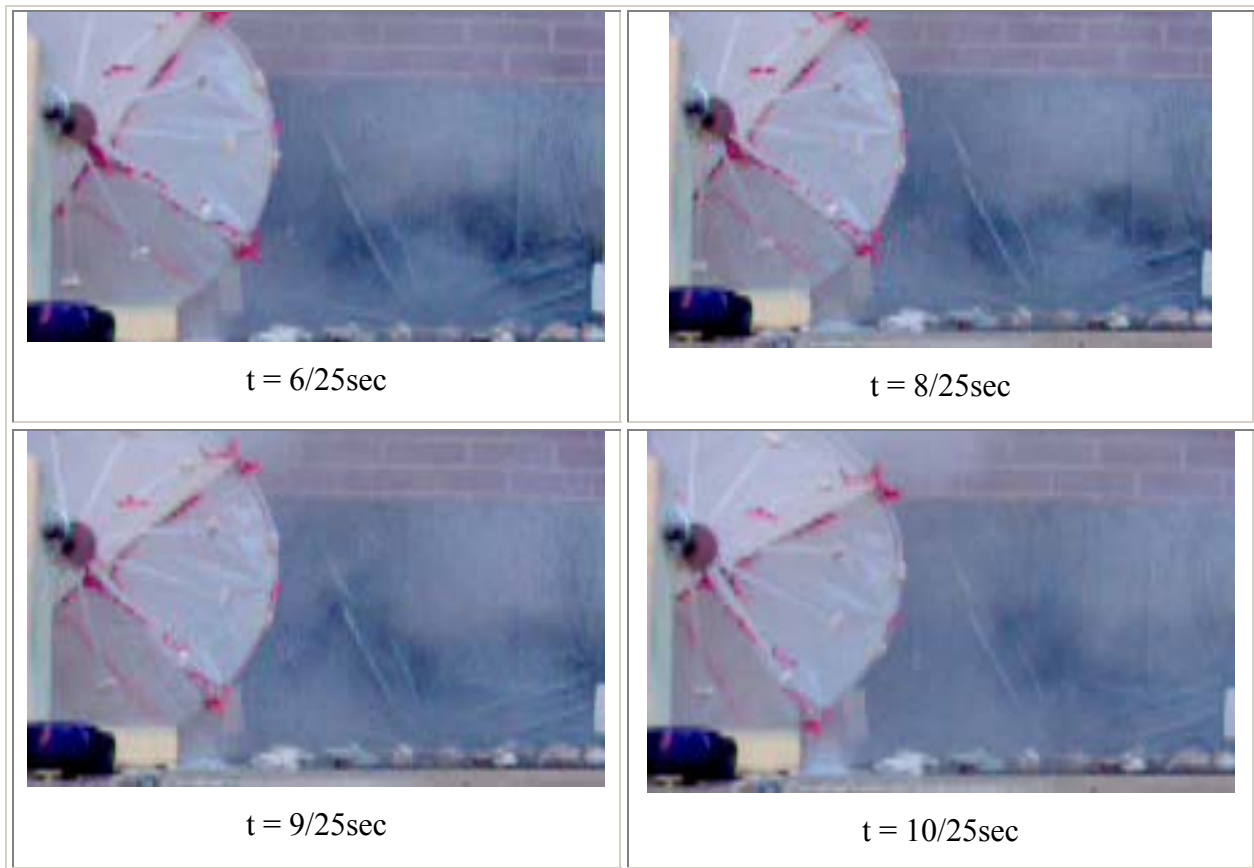
6.2.2   Spinning tTED

Before presenting the results for the spinning tTED a statement must be made considering the rotational frequency. As mentioned above a decisive similarity parameter for the unsteady flow field is the Strouhal number. In order to match the TW Strouhal number for the corresponding Martian conditions a rotational frequency range of about 14 to 70rpm would be necessary for the tTED.

It was tried to match different spinning frequencies with the axial force device described in chapter 6.1. The achieved frequencies are within the required range but it was not possible to adjust the frequency to every desired value. The axial force could not be adjusted as accurate as desired. As can be seen from the low time periods of the sequences it was furthermore not possible to judge during the tests if the run was successful in terms of solid footage or not. So it turned out that it was not possible within the scope of this thesis to forecast solid video footage for a desired rotational frequency. In fact the revealing footage was only found during the analyzing phase using the video editing software. That is why a systematical investigation of the influence of frequency on the flow field was not possible, unfortunately.

TECHNISCHE
UNIVERSITÄT
MÜNCHEN

Lehrstuhl für Aerodynamik
Technische Universität München
Univ. Prof. Dr. Ing. N. Adams

aer

In sequence #5 the evolution of alternating vortices for the spinning tTED is indicated. It seems as if the vortices evolve alternately on two different levels in the region below the center plane at z=200mm. The both heights of the horizontal vortex pivots seem to be at $z_{vortex\ axis,1} \cong 125mm$ and $z_{vortex\ axis,2} \cong 75mm$. Translated to TW conditions: $z_{vortex\ axis,1,TW} \cong 1875mm$ and $z_{vortex\ axis,2,TW} \cong 1125mm$.

Sequence #5	
Smoke Source	smoke grenade
View	side
Free Stream Direction	from left to right
tTED frequency [rpm]	26
Strouhal number Sr_{tTED} [-]	0.105
time period [sec]	10/25 = 0.4
t = 0sec	t = 1/25sec
t = 2/25sec	t = 4/25sec

TECHNISCHE
UNIVERSITÄT
MÜNCHEN

Lehrstuhl für Aerodynamik
Technische Universität München
Univ. Prof. Dr. Ing. N. Adams

aer

t = 6/25sec	t = 8/25sec
t = 9/25sec	t = 10/25sec

Sequence #6 reveals one pretty well defined vortex in the very same region as in sequence #5 namely just below the center plane of z=200mm. From both of theses sequences the translational velocity of the horizontal vortices is approximated to

$W_{vortex\ horizontal,\#5,\#6} = 0.312 \frac{m}{\sec}$ and the vortices diameter to $d_{vortex,\#5,\#6} \cong 83mm$. Transformed to

the actual TW dimensions this means a horizontal vortex diameter of about

$d_{TW,vortex} \cong 1250mm$ and a translational velocity relative to the TW of $W_{r,vortex,TW} = 1.13\frac{m}{\sec}$.

The vortex translational velocity was up-scaled with the ratio of the average velocities for the Martian equivalent to the smoke channel profile and the profile of the smoke channel. This ratio is:

$$\frac{5.98\,m/\sec}{1.65\,m/\sec} = 3.65$$

TECHNISCHE
UNIVERSITÄT
MÜNCHEN

Lehrstuhl für Aerodynamik
Technische Universität München
Univ. Prof. Dr. Ing. N. Adams

aer

Sequence #6	
Smoke Source	smoke grenade
View	side
Free Stream Direction	from left to right
tTED frequency [rpm]	26
Strouhal number Sr_{tTED} [-]	0.105
time period [sec]	3/25 = 0.12

t = 0sec

t = 1/25sec

t = 2/25sec

t = 3/25sec

TECHNISCHE
UNIVERSITÄT
MÜNCHEN

Lehrstuhl für Aerodynamik
Technische Universität München
Univ. Prof. Dr. Ing. N. Adams

aer

Sequence #7 again shows vortices below the center plane of z=200m. Again this time their average diameter is about $d_{vortex,\#7} \cong 83mm$. Additionally one vortex seems to run just above the ground and therefore lower than in the sequences #5 and #6. Its translational velocity seems to be not constant but within a range of $0.1\frac{m}{\sec} \leq W_{vortex,\#7} \leq 0.833\frac{m}{\sec}$. Translated to Martian conditions that means a vortex diameter of $d_{TW,vortex} \cong 1250mm$ and a vortex translational velocity relative to the TW of about $0.363\frac{m}{\sec} \leq W_{r,vortex,TW} \leq 3.02\frac{m}{\sec}$.

Sequence #7	
Smoke Source	smoke grenade
View	side
Free Stream Direction	from left to right
tTED frequency [rpm]	26
Strouhal number Sr_{tTED} [-]	0.105
time period [sec]	9/25 = 0.36
 t = 0sec	 t = 2/25sec
 t = 4/25sec	 t = 5/25sec

TECHNISCHE
UNIVERSITÄT
MÜNCHEN

Lehrstuhl für Aerodynamik
Technische Universität München
Univ. Prof. Dr. Ing. N. Adams

aer

t = 7/25sec	t = 9/25sec
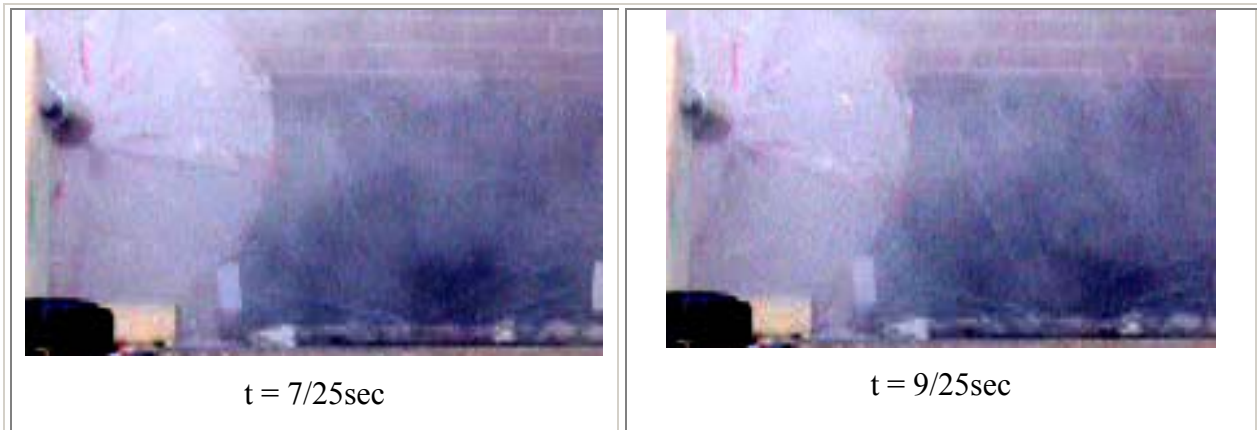
From sequence #8 on the view is changed to the top. The sequence shows a small fluid element marked red that flows against the free stream direction towards the tTED just like in the resting case.

Sequence #8	
Smoke Source	smoke pen
View	top
Free Stream Direction	from right to left
tTED frequency [rpm]	38
Strouhal number [	0.154
time period [sec]	8/25 = 0.32
smoke pen position [mm]	x=250; y=150; z=200

t = 0sec	t = 2/25sec

TECHNISCHE
UNIVERSITÄT
MÜNCHEN

Lehrstuhl für Aerodynamik
Technische Universität München
Univ. Prof. Dr. Ing. N. Adams

aer

t = 3/25sec

t = 4/25sec

t = 6 / 25sec

t = 7/25sec

t = 8/25sec

Sequence #9 shows the formation of a vertical vortex just downstream of the tTED. Unfortunately the smoke pattern is very faint and it one might get a better impression from the attached video "sequence#9.mpg". During the first slides the smoke flows towards the tTED but then changes directions and follows a somewhat circular trajectory.

The sequence #10 shows the same behavior. Indeed this time the smoke is so faint that only the video reveals something of the effect described above. Again this video "sequence#10.mpg" is attached to this thesis.

Sequence #9	
Smoke Source	smoke pen
View	top
Free Stream Direction	from right to left
tTED rotational frequency [rpm]	30
Strouhal number Sr_{tTED} [-]	0.121
time period [sec]	4/25 = 0.16
smoke pen position [mm]	x=230; y=0; z=200

t = 0sec

t = 1/25sec

t = 2/25sec

t = 3/25sec

t = 4/30sec
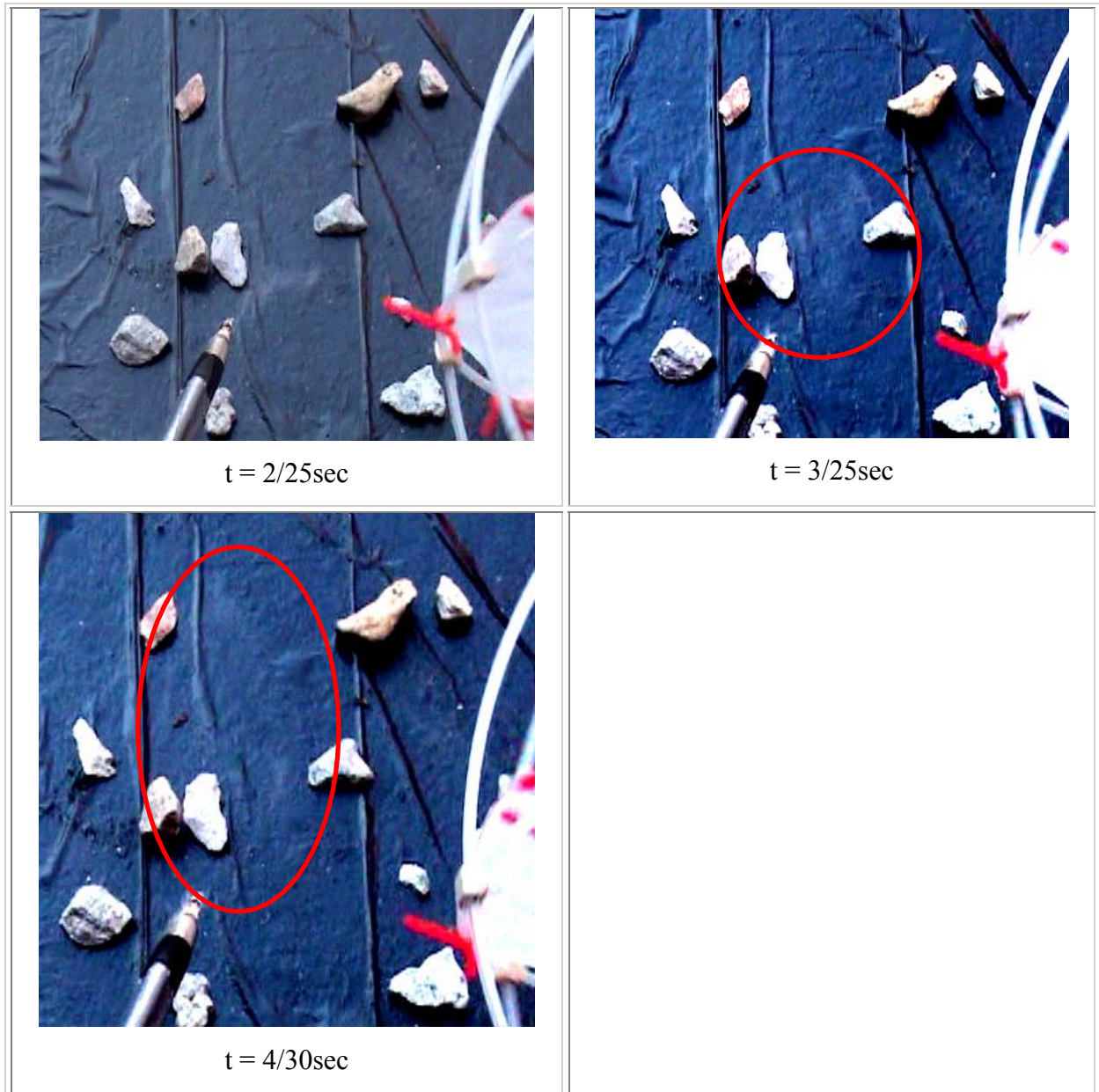
Finally it is obvious that the conducted tests can hardly provide more than further hints about the vortex flow downstream of the TW. The resting tTED seems to approve the analogy made in chapter 3.2.2. However for the resting and the spinning TW it is very desirable to conduct further tests in a more capable aerodynamic test facility. (see chapter 7).

TECHNISCHE
UNIVERSITÄT
MÜNCHEN

Lehrstuhl für Aerodynamik
Technische Universität München
Univ. Prof. Dr. Ing. N. Adams

aer

6.3   Summary of Chapter 6.2

Again it must be pointed out that the following statements can only be considered as approximations and assumptions that must be validated at more sophisticated flow visualizing experiments. However the following phenomena are expected for the TW wake flow.

In case of the resting TW it seems to be confirmed that it can be compared to a flat disk perpendicular to the free stream pretty well. From the top view (on the x-y-plane) the typical flow pattern is observed that means a backflow on the center axis and two vortex flows next to the center axis. Hence vortices with vertical pivots are observed. They seem to have a diameter of about $d_{vortex,TW} = 3m$. The side view reveals also a vortex with a horizontal pivot and a diameter of $d_{vortex,TW} = 1m$.

In case of the rolling TW a flow pattern is expected that reminds to some extent on a so-called vortex street. From the side view it is observed that on the two heights of $z_1 = 1.125m$ and $z_2 = 1.875m$ alternating vortices are flowing downstream with a velocity of about $W_{r,TW,vortex} = 1.13 \frac{m}{\sec}$. They have a diameter of $d_{vortex,TW} = 1.25m$.

Vortices of the same diameter are also expected near the ground. Indeed their translational velocity varies within $0.363 \frac{m}{\sec} \leq W_{r,vortex,TW} \leq 3.02 \frac{m}{\sec}$. The reason for this might be the frictional influence of the ground and especially the rocks.

Finally from the top-view it is concluded that there are also vortices with a vertical pivot. The flow pattern like for the resting TW could not be observed. There is no steady backflow and no somewhat stationary vortices next to the center axis.

TECHNISCHE
UNIVERSITÄT
MÜNCHEN

Lehrstuhl für Aerodynamik
Technische Universität München
Univ. Prof. Dr. Ing. N. Adams

aer

7   Conclusion and Outlook

During summer 2005 three 1/2-subscale models of the Tumbleweed Mars Rover were constructed and tested at the NCSU and in the state of North Carolina, respectively. These tests revealed the operability of the chosen concept and further aerodynamic research demands.

Therefore two subscale wind tunnel models were designed and built, the so called tinyTED and tinyTED2. The comparison of their test results revealed two minimum constraints for the NSCU Subsonic Wind Tunnel. Its flow can be considered as somewhat uniform from a dynamic pressure range of $0.3\,psf \leq q_{\min} \leq 0.6\,psf$ on. The standard 6-component balance displays solid force data for a minimum force of $F_{\min} = 2N$ for the corresponding space direction.

Another strain gage balance was build in order to get rid of the wake interference by the standard balance.

Applying the determined minimum test conditions to the measured data of the 6-component-balance and using the self-made strain gage balance has yielded the following results. The drag coefficient of the tTED2 and thus of the TW depends to a very large extent on the projected surface that is perpendicular to the free stream. Two equations for predicting this behavior were derived. Moreover assessing the aerodynamic forces the rolling TW will prefer a yaw orientation of 45 degrees.

Some damaged sails were applied to the wind tunnel models. The results are not definite. Indeed they indicate that also the effect of a damaged sail on the drag properties may be described by the loss in sail surface.

The self-made balance was also used to look into the optimization of the sail performance that is the sail drag. The two chosen concepts were a perforated sail and a cambered sail. Both approaches are able to increase the sail drag. However in case of the cambered sail a system aspect might argue against its application. This issue is the shading of the solar cells by a potentially non-transparent sail material.

TECHNISCHE
UNIVERSITÄT
MÜNCHEN

Lehrstuhl für Aerodynamik
Technische Universität München
Univ. Prof. Dr. Ing. N. Adams

aer

Amazingly it seems not to be able to superimpose the both effects. A try is given to explain this phenomenon. However some CFD investigations on this subject seem to be very desirable.

The application of a perforated sail yields a far lower drag increase than for the sail frame only. The reason for that is hard to assess without further analysis. This analysis is recommended to be carried out by a CFD tool rather than experimentally.

Finally it was tried to visualize the wake field downstream of the tTED or TW, respectively. Some major issues were faced during the preparation and conduction of the experiments. Hence the presented results are rather qualitative than quantitative and the found values are all approximations. However it seems to be confirmed that the resting TW is similar to a flat disk perpendicular to the free stream in terms of its wake field. The spinning tTED shows a flow pattern similar to a so-called vortex street and for both cases the length scale of the vortices could be assessed.

During the making of this thesis the opportunity arose to conduct tests the TED in the Langley Full Scale Tunnel that is currently run by the Old Dominion University. In order to seize this opportunity a proposal for the potential tests was written. It is attached to this thesis. The proposal was accepted and so tests with the TED in the LFST are scheduled. Unfortunately for the author the appointments will be earliest at the beginning of the year 2006 and consequently after the date of his return to Germany. Nevertheless there are some interesting test scenarios that can be derived from this thesis.

The two derived functions for $\bar{C}_D(\alpha)$ and $\bar{C}_D(\alpha, \beta)$ can be validated or falsified. In the case of $\bar{C}_D(\alpha)$ or $\bar{C}_D(t)$, respectively the full dynamic drag profile should be measurable with a appropriate TED-support in the LFST. Using the yaw ability of the LFST test section also various static α, β-orientations should be measurable in order to assess the function $\bar{C}_D(\alpha, \beta)$ from chapter 4. A fully dynamic simulation of this case seems not to be feasible because the pivot of the supported TED will change its orientation with the yaw motion of the test section.

TECHNISCHE
UNIVERSITÄT
MÜNCHEN

Lehrstuhl für Aerodynamik
Technische Universität München
Univ. Prof. Dr. Ing. N. Adams

aer

The subscale models tTED and tTED2 are not able to provide a wealth of solid data in terms of magnitude for the cases of damaged sails. The reasons are described in chapter 4.6. Hence it will be very interesting to investigate the influence of damaged sails on the TED in the LFST.

It will also be interesting to see if the perforated sails yield a larger drag increase for the TED than for the smaller tTED2. If that is the case this would indicate that there are some scale effects to consider when designing the appropriate sails for Martian conditions.

Finally the flow visualizing capabilities of the LFST are much better than the opportunities available for this thesis. Hence it is expected to get a better understanding of the TW wake in terms of dimensions, shape and frequencies. It will also be interesting if the approximations and conclusion of chapter 6 can be confirmed by the full-scale tests.

The results of this thesis and the expected results of the LFST experiments appear to be a good validation base for CFD simulations. The issues to overcome in this thesis in terms of flow uniformity and balance accuracy have shown that it would be desirable to have an analyzing tool that is independent of these constraints. CFD simulations could provide this independence and especially in cases like the sail optimization or damaged sails a further systematic experimental investigation would be very work, time and maybe cost intense. Therefore it is recommended to go for a CFD tool in the future that would ease the aerodynamic research on the TW and TED a lot once it has been developed.

Lehrstuhl für Aerodynamik
Technische Universität München
Univ. Prof. Dr. Ing. N. Adams

TECHNISCHE
UNIVERSITÄT
MÜNCHEN

aer

8 Appendices

8.1 Appendix 01

EA-06-240LZ-120

EA-06-240LZ-120	
Gage Type	
120.0 ±0.3%	
Resistance in ohms at 24°C	
2.075±0.5%	
Gage Factor at 24°C	
(+0.2 ±0.2)%	
Transverse Sensitivity at 24°C	
E	
Option	
A44AD593	
Lot Number	
133314-6833	
Code	

≡M≡M≡

Micro-Measurements
Division

**MEASUREMENTS
GROUP, INC.**

P.O. Box 27777

Raleigh, North Carolina 27611
(919) 365-3800

SELF-TEMPERATURE COMPENSATION: These gages have been manufactured with self-temperature compensation (STC) characteristics to minimize thermal output (see Tech Note TN-504). Thermal output data given below are valid only for the indicated test material, since thermal output is a function of the thermal expansion properties of the test specimen.

$$\varepsilon_{TO} = -1.52 \times 10^{2} + 3.92 \times 10^{0}T - 3.04 \times 10^{-2}T^{2} + 7.47 \times 10^{-5}T^{3} - 4.79 \times 10^{-8}T^{4} \ (°F)$$

$$\varepsilon_{TO} = -5.51 \times 10^{1} + 3.96 \times 10^{0}T - 7.61 \times 10^{-2}T^{2} + 4.00 \times 10^{-4}T^{3} - 5.03 \times 10^{-7}T^{4} \ (°C)$$

TESTED ON: 1018 STEEL   TEST PATTERN: T004R   CODE: 112819   ENG.: JP
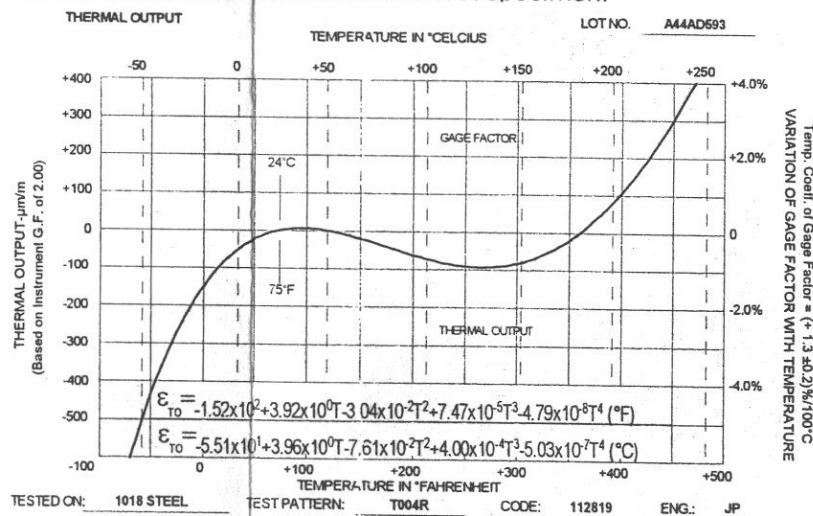
GENERAL INFORMATION
SERIES EA STRAIN GAGES

GENERAL DESCRIPTION: Student Gages are EA Series gages. This series is a general-purpose family of constantan alloy strain gages widely used in experimental stress analysis. EA gages are constructed with a 0.001 inch *(0.03 mm)* tough, flexible polyimide film backing. All Student Gages include Option E, a polyimide encapsulation of the grid face, with exposed solder tabs. See Tech Note TN-505 for assistance in gage selection.

TEMPERATURE RANGE: Normal use temperature range for static strain measurement is -100°F to +350°F *(-75°C to +175°C)*. For special or short-term exposure, an expanded range of -320°F to +400°F *(-195°C to +205°C)* may be used.

STRAIN LIMITS: Approximately 5% for 0.240 in *(6 mm)* gage length and approximately 3% for 0.120 in *(3 mm)* and 0.060 in *(1.5 mm)* gage lengths for single cycle use. See Tech Tip TT-605 for high elongation measurements.

FATIGUE LIFE: Dependent on gage length and method of cycling; 10^8 cycles at $\pm1200\mu\epsilon$, 10^6 cycles at $\pm1500\mu\epsilon$. Derate 10% for nonzero mean strains of same absolute (peak-to-peak) values. See Tech Note TN-508 for additional data.
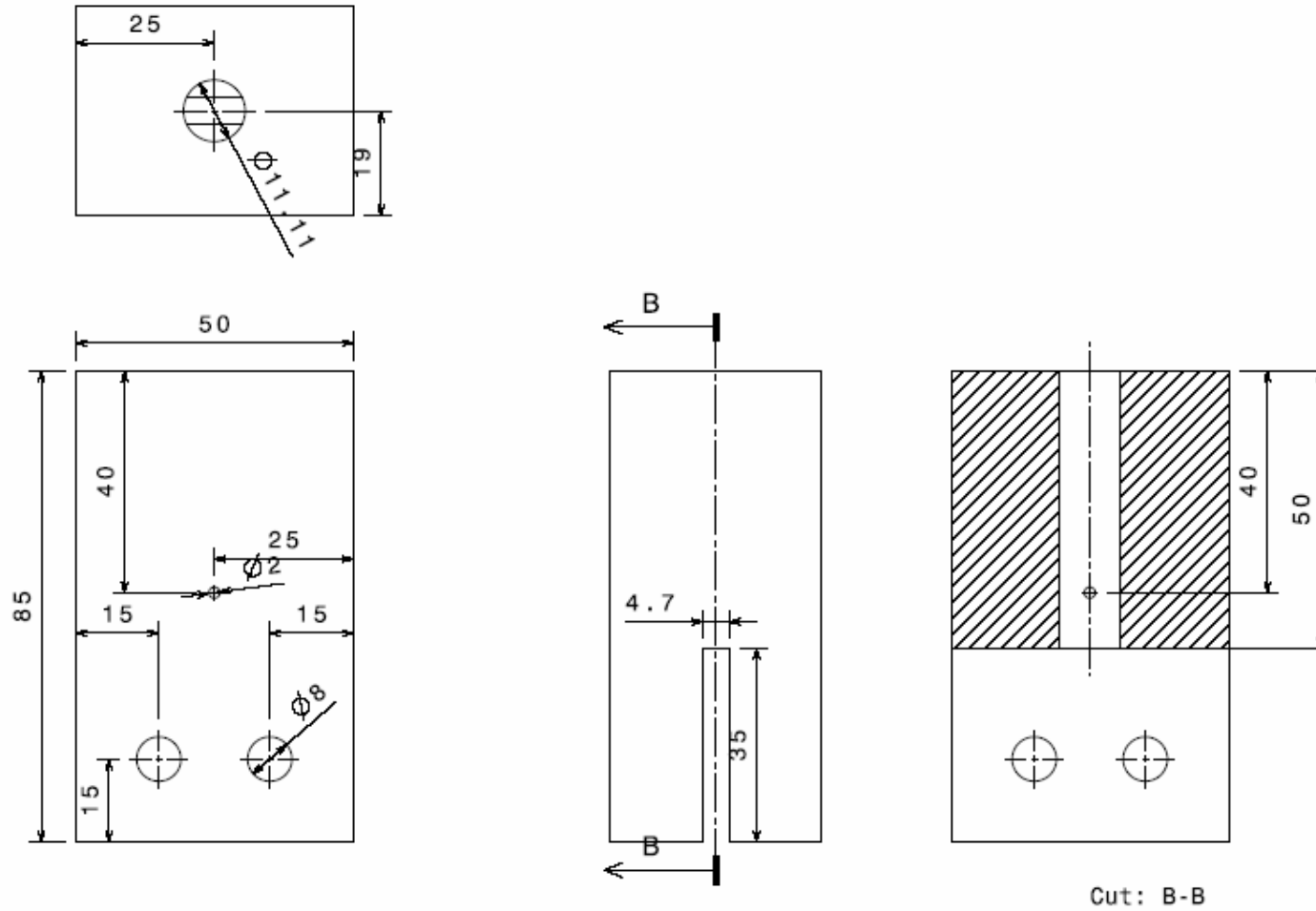
ADHESIVES: M-Bond 200 is an excellent, general purpose adhesive for those learning to bond strain gages (see Instruction Bulletin B-127). M-Bond AE-10 may be used when a wider range of bonding properties is needed (see Instruction Bulletin B-137). Refer to Instruction Bulletin B-129 for proper surface preparation, and to Catalog A-110 for other bonding agents.

SOLDER: M-Line solder type 361 is recommended for leadwire attachment when operating temperatures do not exceed +300°F *(+150°C)*. See Catalog A-110 for higher temperature solders.

PROTECTIVE COATINGS: Because of Option E encapsulation, Student Gages require no further protection under most laboratory conditions. When further protection is required, refer to Catalog A-110 for M-Coat protective coatings information.

NOTE: The backing of Student Gages has been specifically treated for optimum bond formation with all appropriate gage adhesives. No further cleaning is necessary if contamination of the prepared surface is avoided during handling. Should contamination occur, clean with a cotton swab slightly moistened with a low residue solvent such as isopropyl alcohol. Allow the gage to dry for several minutes before bonding.

8.2 Appendix 02

Cut: B-B

Lehrstuhl für Aerodynamik

Technische Universität München
Univ. Prof. Dr. Ing. N. Adams

8.3   Appendix 03

Scale: 1:1

Cut A-A
Scale: 2:1

TECHNISCHE
UNIVERSITÄT
MÜNCHEN

Lehrstuhl für Aerodynamik
Technische Universität München
Univ. Prof. Dr. Ing. N. Adams

aer
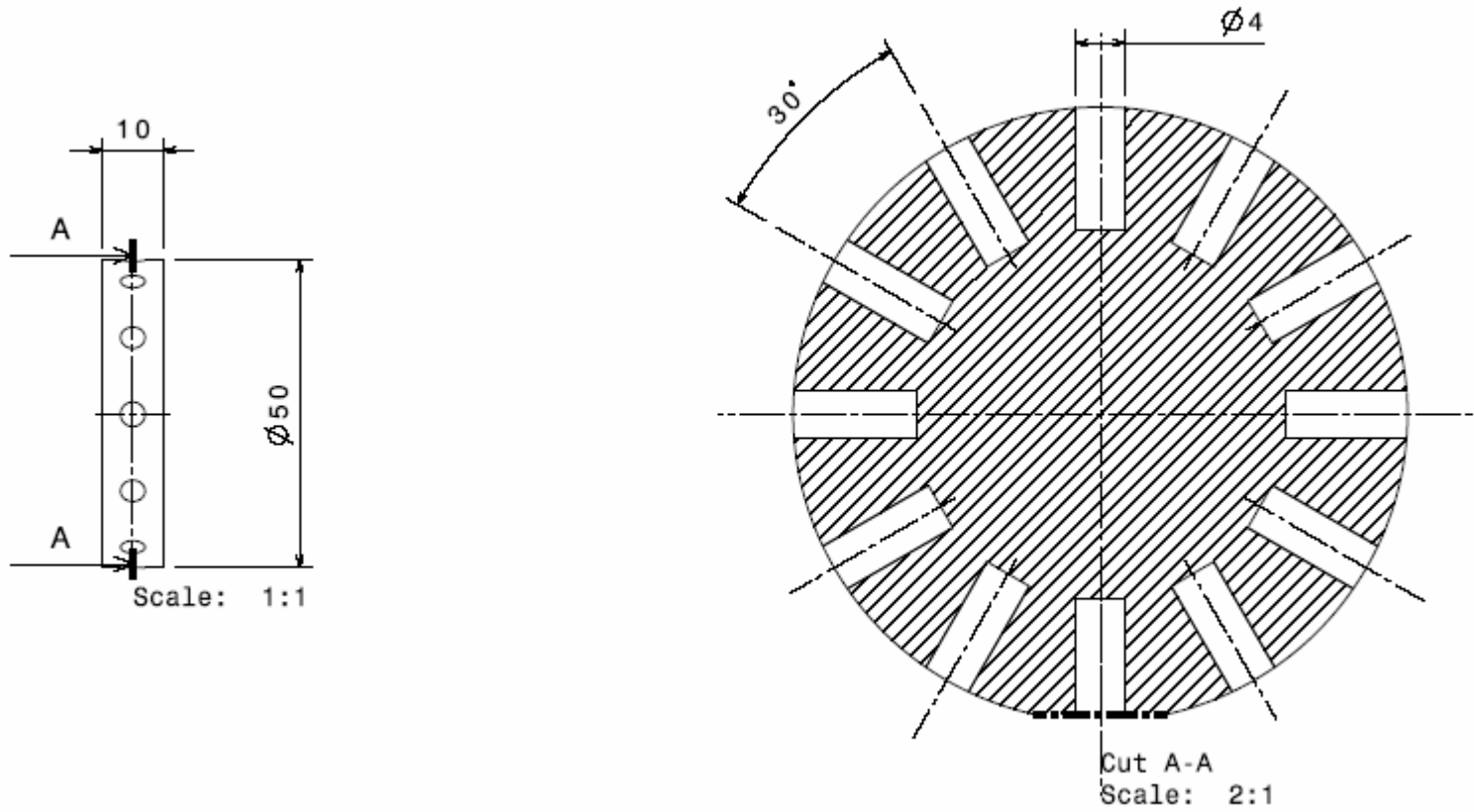
8.4 Appendix 04

Here the derivation of the function for determining the surface of the TW and its models normal to the free stream $S_\perp$ will be shown. Like in chapter 2.4 the denomination will refer to the TED but is true for the actual TW and the wind tunnel models, too.

The initial position is the cosine-function and for the beginning only the change of the pitch angle is considered:

$$S_\perp(\alpha) = S_{TED} \cdot \cos\alpha \qquad (8.1)$$

The surface S_{TED} is just the area of one sail plane. The normal surface will obviously never become negative but oscillate between the two values of S_{TED} and $\frac{1}{\sqrt{2}} S_{TED}$. Hence the cosine function must be scaled and displaced. The general form for this procedure is:

$$y = f(x) \rightarrow \frac{y-b}{B} = f\left(\frac{x-a}{A}\right) \qquad (8.2)$$

Applied to the cosine-function this yields:

$$S_\perp(\alpha) = B \cdot S_{TED} \cdot \cos\left(\frac{\alpha-a}{A}\right) + b \qquad (8.3)$$

The geometry of the TED will return to its initial state at four times during one TED rotation. That is why the pitch angle scaling factor A is:

$$A = \frac{1}{4}$$

Assuming that the TED starts from $\alpha = 0°$ there is not phase shift:

$$a = 0$$

As mentioned earlier the new amplitude $\hat{S}$ will vary between S_{TED} and $\frac{1}{\sqrt{2}} S_{TED}$ and can be described with:

$$\hat{S} = \frac{1}{2}\left(S_{TED} - \frac{S_{TED}}{\sqrt{2}}\right)$$

TECHNISCHE
UNIVERSITÄT
MÜNCHEN

Lehrstuhl für Aerodynamik
Technische Universität München
Univ. Prof. Dr. Ing. N. Adams

aer

This leads to the amplitude scaling factor after:

$$\hat{S} = B \cdot S_{TED}$$

$$\frac{1}{2}\left(S_{TED} - \frac{S_{TED}}{\sqrt{2}}\right) = B \cdot S_{TED}$$

$$B = \frac{1}{2}\left(1 - \frac{1}{\sqrt{2}}\right)$$

Finally the zero line will be shifted to the middle between the two new maximum and minimum values:

$$b = \frac{S_{TED}}{\sqrt{2}} + \frac{S_{TED} - S_{TED}/\sqrt{2}}{2} = \frac{S_{TED}}{2} + \frac{1}{2}\frac{1}{\sqrt{2}}S_{TED}$$

$$b = \frac{1}{2}S_{TED}\left(1 + \frac{1}{\sqrt{2}}\right)$$

Combining everything yields the final equations for the surface normal to the free direction dependent on the pitch angle:

$$S_{\perp}(\alpha) = \frac{1}{2}\left(1 - \frac{1}{\sqrt{2}}\right)S_{TED} \cdot \cos(4\alpha) + \frac{1}{2}\left(1 + \frac{1}{\sqrt{2}}\right)S_{TED} \tag{8.4}$$

The angle may also be depicted with the rotational period of the TED T and the time coordinate t after $\alpha = \frac{2\pi}{T} \cdot t$. Therewith the normal surface may also be described in terms of time:

$$S_{\perp}(t) = \frac{1}{2}\left(1 - \frac{1}{\sqrt{2}}\right)S_{TED} \cdot \cos\left(4\frac{2\pi}{T} \cdot t\right) + \frac{1}{2}\left(1 + \frac{1}{\sqrt{2}}\right)S_{TED} \tag{8.5}$$

The angle-dependent equation (8.4) is also the starting point for the derivation of the normal surface that depends on the pitch and the yaw angle. The situation however gets more complex because the changing of the yaw angle β will alter the amplitude and the zero shift of the function. Therefore its general form is:

$$S_{\perp}(\alpha, \beta) = \hat{S}(\beta) \cdot \cos(4\alpha) + b(\beta)$$

The amplitude can be depicted as:

$$\hat{S}(\beta) = \frac{S_{\perp,max}(\beta) - S_{\perp,min}(\beta)}{2} \qquad (8.6)$$

The maximum value $S_{\perp,max}(\beta)$ will vary between $S_{\perp}(\alpha = 0°, \beta = 0°) = S_{TED}$ and $S_{\perp}(\alpha = 0°, \beta = 45°) = \frac{1}{\sqrt{2}} S_{TED}$. These conditions however are equal to the alpha-oscillation described above and hence the maximum normal surface can be described after:

$$S_{\perp,max}(\beta) = \frac{1}{2}\left(1 - \frac{1}{\sqrt{2}}\right) S_{TED} \cdot \cos(4\beta) + \frac{1}{2}\left(1 + \frac{1}{\sqrt{2}}\right) S_{TED} \qquad (8.7)$$

The minimum value $S_{\perp,min}(\beta)$ will vary between $S_{\perp}(\alpha = 45°, \beta = 0°) = \frac{1}{\sqrt{2}} S_{TED}$ and $S_{\perp}(\alpha = 45°, \beta = 45°) = \frac{1}{2} S_{TED}$. Applying the approach of eq.(8.2) on these boundary conditions yields the new scaling and zero shift values of:

$$B' = \frac{1}{2}\left(\frac{1}{\sqrt{2}} - \frac{1}{2}\right)$$

$$b' = \frac{1}{2}\left(\frac{1}{2} + \frac{1}{\sqrt{2}}\right) S_{TED}$$

Consequently the minimum surface normal to the free stream can be calculated after:

$$S_{\perp,min}(\beta) = \frac{1}{2}\left(\frac{1}{\sqrt{2}} - \frac{1}{2}\right) S_{TED} \cdot \cos(4\beta) + \frac{1}{2}\left(\frac{1}{2} + \frac{1}{\sqrt{2}}\right) S_{TED} \qquad (8.8)$$

The equations (8.7) and (8.8) can now introduced into the equation (8.6) yielding a pretty long term. The brackets of this term have to be dissolved and the proper terms must be summed up. After a longer but basic calculation the amplitude dependent on the yaw angle can be depicted with:

$$\hat{S}(\beta) = \left(\frac{3}{8}\cos(4\beta) - \frac{1}{2}\frac{1}{\sqrt{2}}\cos(4\beta) + \frac{1}{8}\right) \cdot S_{TED} \qquad (8.9)$$

TECHNISCHE
UNIVERSITÄT
MÜNCHEN

Lehrstuhl für Aerodynamik
Technische Universität München
Univ. Prof. Dr. Ing. N. Adams

aer

The zero shift $b(\beta)$ is conveniently presentable with the just derived functions for the minimum and maximum surfaces normal to the free stream direction:

$$b(\beta) = S_{\perp,\min}(\beta) + \frac{S_{\perp,\max}(\beta) - S_{\perp,\min}(\beta)}{2} \qquad (8.10)$$

Again equation (8.10) requires a longer calculation in terms of dissolving the brackets and summing up the proper terms. This finally leads to the expression for the yaw-angle dependent zero shift:

$$b(\beta) = \left(\frac{1}{8}\cos(4\beta) + \frac{1}{2}\frac{1}{\sqrt{2}} + \frac{3}{8} \right) \cdot S_{TED} \qquad (8.11)$$

So the general function in order to calculate the surface perpendicular to the free stream is:

$$S_{\perp}(\alpha, \beta) = \left(\frac{3}{8}\cos(4\beta) - \frac{1}{2}\frac{1}{\sqrt{2}}\cos(4\beta) + \frac{1}{8} \right) S_{TED} \cdot \cos(4\alpha) + \left(\frac{1}{8}\cos(4\beta) + \frac{1}{2}\frac{1}{\sqrt{2}} + \frac{3}{8} \right) S_{TED} \qquad (8.12)$$

TECHNISCHE
UNIVERSITÄT
MÜNCHEN

Lehrstuhl für Aerodynamik
Technische Universität München
Univ. Prof. Dr. Ing. N. Adams

aer

8.5 Appendix 05

In the following table it is shown which measured force components fulfill the requirement $F \geq 2.0N$ for which dynamic pressure. A dash means that the component does not reach the minimum for all of the applied dynamic pressures. A letter indicates the lowest dynamic pressure for which the value is reached first. The dynamic pressures are denominated by:

q5=1.0psf, q6=1.2psf, q7=1.4psf, q8=1.6psf, q9=1.8psf

$\alpha[°]$	$\beta[°]$	$F_{x'}$	$F_{y'}$	$F_{z'}$
0	0	q5	-	-
0	5	q5	-	-
0	10	q5	q8	-
0	15	q5	q5	-
5	0	q5	-	-
5	5	q5	-	-
5	10	q5	q8	-
5	15	q5	q5	-
10	0	q5	-	-
10	5	q5	q8	-
10	10	q5	q8	-
10	15	q6	q5	-
15	0	q6	-	-
15	5	q6	-	-
15	10	q6	q7	-
15	15	q6	q5	-
20	0	q6	-	-

For the drag force the force $F_{x'}$ was taken as the criterion and for the side force the force $F_{y'}$ was taken as the criterion if and from which dynamic pressure on the 6-component-balance was expected to yield solid data.

9 References

[1]   John D. Anderson Jr.: Fundamentals of Aerodynamics, Third Edition
McGraw-Hill, International Edition; 2001

[2]   Jewel B. Barlow, Wiliam H. Rae,Jr., Alan Pope: Low-Speed Wind Tunnel Testing,
Third Edition
John Wiley & Sons; 1999

[3]   A.Kliore: The Mars Reference Atmosphere
Pergamon Press, Advance in Space Research; 1982

[4]   http://en.wikipedia.org/wiki/Strain_gage
09-15-2005

[5]   R.L. Hannah and S.E. Reed: Strain Gage Users' Handbook
Elsevier Science Publishers Ltd. and Society for Experimental Mechanics, Inc.; 1992

[6]   Vishay Measurement Group Educational Program: Student Manual for Strain Gage
Technology
Vishay Measurement Group, Inc.; 1992

[7]   C. A. Marchaj: Sail Performance – Techniques to Maximize Sail Power
International Marine / McGraw-Hill; 1996/2003

[8]   Dr. Hermann Schlichting: Boundary Layer Theory
Springer, Eigth Revised and Enlarged Edition; 2000

[9]   Jürgen Dankert, Helga Dankert: Technische Mechanik; Statik, Festigkeitslehre,
Kinematik/Kinetik
B.G. Teubner Verlag / GWV Fachverlage GmbH; 2004

[10] Robert Sullivan, Ronald Greeley et al.: Results of the Imager for Mars Pathfinder
Windsock Experiment
Journal of Geophysical Research, Vol. 105, No.E10,pp.24,547-24,562; 2000

[11] J. Armitt, J. Counihan: The Simulation of the Atmospheric Boundary Layer in a Wind
Tunnel
Atmospheric Environment, Pergamon Press, Vol.2, pp.49-71, 1968

[12] Roland B. Stull: An Introduction of Boundary Layer Meteorology
Kluwer Academic Publishers; 2001

TECHNISCHE
UNIVERSITÄT
MÜNCHEN

Lehrstuhl für Aerodynamik
Technische Universität München
Univ. Prof. Dr. Ing. N. Adams

aer

[13] Erich J. Plate: Aerodynamic Characteristics of Atmospheric Boundary Layers
      USAEC Technical Information Center, Oak Ridge, Tennessee; 1972

[14] P.R. Owen and H. K. Zienkiewicz: The Production of uniform shear flow in a wind
      tunnel
      Journal of Fluid Mechanics, Vol. 2, pp.521-531; 1957

[15] A. Lloyd: The Generation of Shear Flow in a Wind Tunnel
      Quarterly Journal of the Royal Meteorological Society, Vol. 93, pp.79-96; 1966

[16] Scott E. Ross, Cody B. Moody et al.: Drag Measurement and Dynamic Simulation of
      Martian Wind Driven Sensor Platform Concepts
      43rd AIAA Aerospace Science Meeting, Reno, Nevada, USA; January 10-13, 2005

[17] Dennis Baldocchi: Wind and Turbulence, Part 2, Surface Boundary Layer: Theory and
      Principles
      Lecture in Biometeorology, University of California, Berkley, USA; October 2004

[18] Kuzman Raznjevic: Handbook of Thermodynamic Tables and Charts
      Hemisphere Publishing Corporation; 1976

[19] E. Plate (editor): Engineering Meteorology
      Elsevier Scientific Publishing Company; 1982

[20] Clayton T. Crown, Donald F. Elger, John A. Roberson: Engineering Fluid Mechanics
      John Wiley & Sons, Inc.; 2001

[21] NCSU Senior Design Team of 2001/2002: Mars Tumbleweed Final Design Report
      NCSU, Department of Mechanical and Aerospace Engineering; 2002

[22] John J. Flick, Matthew D. Toniolo: Preliminary Dynamic Feasibility and Analysis of a
      Spherical Wind-Driven (Tumbleweed), Martian Rover
      AIAA-2005-0250, 43rd AIAA Aerospace Sciences Meeting and Exhibit, 10-13 January
      2005, Reno, Nevada

[23] Bronstein, Semendajew et al.: Taschenbuch der Mathematik
      Verlag Harri Deutsch; 2000

[24] Paul K. Chang: Separation of Flow
      Pergamon Press, 1970

[25] Space Senior Design Team of 2004/2005: Mars Tumbleweed Final Report
North Carolina State University, April 2005

[26] Sighard F. Hoerner: Fluid-Dynamic Drag
Published by the author, 1958

[27] T.C. Duxbury, R.L. Kirk et al.: Mars Geodesy/Cartography Group Recommendations
On Mars Cartographic Constants and Coordinate System
Symposium on Geospatial Theory, Processing and Application, Ottawa, 2002

[28] http://berlinadmin.dlr.de/Missions/express/marsfacts/marsfactsheet.shtml, 11-21-05

[29] Christopher V. Strickland, Jennifer P. Keyes: Wind Tunnel Tests to Determine Drag
Coefficients for the Mars Tumbleweed
43rd AIAA Aerospace Sciences Meeting and Exhibit, 10 - 13 January 2005, Reno,
Nevada

[30] http://en.wikipedia.org/wiki/Wheatstone_bridge, 11-22-05

[31] Clayton T. Crowe, Donald F. Elger and John A. Roberson: Engineering Fluid
Mechanics
John Wiley & Sons, Inc., 7th edition, 2001

[32] John J. Flick, Matthew D. Toniolo: Prelimineary Dynamic Feasibility and Analysis of a
Spherical Wind-Driven (Tumbleweed), Martian Rover
AIAA-2005-0250, 43rd AIAA Aerospace Science Meeting and Exhibit, 10 - 13 January,
2005 Reno, Nevada, USA

[33] Emil Simiu, Robert H. Scanlan: Wind Effects on Structures, Fundamentals and
Applications to Design
John Wiley & Sons, Inc., Third Edition, 1996